2005-12-12

Laser beam interaction with materials for microscale applications

Krzysztof A. Nowakowski
Worcester Polytechnic Institute

Laser beam interaction with materials for microscale applications

A Dissertation
submitted to the Faculty of the

Worcester Polytechnic Institute

in partial fulfillment of the requirements for the
Degree of Doctor of Philosophy in
Mechanical Engineering

by

Krzysztof A. Nowakowski

22 November 2005

Approved:

Prof. Ryszard J. Pryputniewicz, Major Advisor

Prof. Cosme Furlong, Member, Dissertation Committee

Prof. Richard D. Sisson Jr., Member, Dissertation Committee

Dr. Thomas F. Marinis, Draper Laboratory, Cambridge, MA
Member, Dissertation Committee

Prof. John M. Sullivan, Jr., Graduate Committee Representative

This Dissertation

is dedicated

to my Wife and Children

Nomenclature

a	is spot size if the collimated beam exiting the laser
a_i	coefficients of the least-square fit function
b	the focused beam size of the lease beam on the fiber face
c	specific heat, or speed of light, or the desired fiber fill factor
$c(T)$	specific heat
c_p	specific heat at constant pressure
c_{pl}	specific heat at constant pressure for liquid state
c_{pv}	specific heat at constant pressure for vapor state
c_s	velocity of sound in the solid
d	minimum fiber optic diameter
dA	differential area
d_{min}	size of the minimum spot
dt	the infinitesimal time step
dx	spatial increments in x direction
dy	spatial increments in y direction
dz	spatial increments in z direction
e_{cc}	eccentricity
erf	error function
$erfc$	complementary error function
f	laser pulse frequency, or focal length, or fraction of electron energy
fcf	focusing correction factor
fs	femtoseconds
ffp	focal plane position
fps	frames per second
g	gravitational constant, or the gravitational acceleration
g_e	degeneracy factors for electrons
g_i	degeneracy factors for ions
g_0	degeneracy factors for neutral atoms
h	melt thickness, or specific enthalpy, or Planck's constant
h_c	convective heat transfer coefficient
h_{ch}	convective heat transfer coefficient inside the hole
h_{pl}	plasma plume-affected focusing radius
h_r	radiative heat transfer coefficient
h_{rh}	radiative heat transfer coefficient inside the hole
$h^t_{i,j,k}$	the value of nodal enthalpy at time t
i	number of phase steps
$\hat{i}, \hat{j}, \hat{k}$	the unit vectors along each of the Cartesian coordinate directions
$ierfc$	complementary error function
k	thermal conductivity, or imaginary part of the refractive index, or

	extinction coefficient
$k(T)$	thermal conductivity
k_{air}	thermal conductivity of the air surrounding the workpiece
k_B	Boltzmann's constant
k_g	the thermal conductivity of the assist gas
k_l	thermal conductivity in liquid state
k_s	thermal conductivity in solid state
k_v	thermal conductivity in vaporization state
l	thermal diffusion length, or mode number, subscript used in representation of the heat transfer coefficients refer to the sample's surface with surface normal pointing in the negative (or left) direction of the coordinate axes
l_d	diffusion length
l_s	penetration skin depth
l_{th}	thermal penetration depth
$lbwp$	laser beam waist position
$\overline{m}$	average mass of an evaporation atom, or mass of an electron, or the absolute value of the magnification of the imaging system
m_e	mass of melt ejection, or electron mass
m_m	the mass of melted metal that was ejected
m_s	mass of melting of solid metal
m_v	mass of evaporation
n	real part of the refractive index, or density of a weakly ionized plasma or integer indicating number of orbits in the atom, or the order of the least-squares fit polynomial
n_1	index of refraction
n_2	index of refraction
ns	nanosecond
n_a	the electron number density
$n_{a,g}$	atom number density of gas g
n_{ec} or n_{ec}	critical electron density
n_e	electron density or plasma density
n_g	flow velocity of the assist gas
n_i	density of singly ionized atoms
n_0	total gas density or the neutral ion atom density inside the plasma
$n_{Z,g}$	Z-charged ion number density of gas g
$\overline{n}$	complex index of refraction
p	perimeter of the workpiece, or pressure, or mode number, or position factor or the transform variable
$p(\tau)$	the normalized beam power
ps	picoseconds
p^{in}	pressure component enters the finite element volume
p^{out}	pressure component exits the finite element volume

p_b	the pressure within the bubble
p_c	the assist gas pressure at the nozzle exit
p_e	the external pressure exerted on the material by evaporating atoms
p_{eff}	the effective static gas pressure
p_i	the assist gas pressure inside the nozzle
p_r	evaporation recoil pressure
p_s	saturated vapor pressure
$p_{sat}(T_s)$	saturated vapor pressure as a function of temperature
$p(\tau)$	normalized total beam power as a function of normalized time into the pulse
ps	picosecond
q	heat flux or lens shape factor
q_c	convection heat flux
q_n	the magnitude of the heat flux in the n-direction
q_r	radiation heat flux
q_{rad}	the magnitude of radiation flux
r	radial coordinate, or direction along the melt surface, or subscript used in representation of the heat transfer coefficients refer to the sample's surface with surface normal pointing in the positive (or right) direction of the coordinate axes
r_0	the radial distance at which the surface temperature is equal to the boiling point
r_b	the radius of critical bubble
r_{blur}	the blur introduced because of diffraction effects
r_c	correlation length
r_g	the assist gas density
r_m	the melt puddle radius
r_{pl}	half axis width of the plasma plume
s	the transform variable
t	time
t_{disp}	melt displacement time
te	the electron cooling time
t_{ej}	the time for melt displacement from the melt puddle
tl	the lattice heating time
t_{max}	the maximum time
t_p	laser pulse duration
t_{pulse}	the total time of the power meter measurement
u	dummy variable, or internal energy
u_o	welding speed
v	linear vaporization rate, or collision frequency
v_c	electron-atom/ion-phonon collision frequency
v_d	drilling velocity
v_{de}	"drilling" velocity due to ejection of the melt
v_{dm}	melt surface velocity determined by melt ejection

v_{dv}	"drilling" velocity due to evaporation of the melt
v_{dvs}	velocity at which the surface of the condensed phase recedes due to loss of material by vaporization
v_e	melt-ejection velocity
v_l	specific volumes for liquid state
v_m	melt velocity
v_r	radial melt flow velocity averaged over the melt layer thickness
v_v	evaporation velocity, or specific volumes for vapor state
v_s	speed of sound in the solid
w	diameter of the core of fiber optic cable
w	beam radius
$wsp^t_{i,j,k}$	a record of the number of vaporized nodes above the node (i,j,k)
x,y,z	Cartesian coordinates
z	direction normal to the melt surface, or the spatial Cartesian coordinate
z_0	axial coordinate of defocusing beam
$(z)_{eq}$	the equilibrium distance
z_f	the location of the focal plane
z_F	laser material interaction area
z_{pl}	half axis length of the plasma plume
z_{thresh}	depth threshold
A	surface area, or surface absorptivity, or optic absorbtance
A_{amb}	an ambient pressure dependent coefficient
A_{eff}	the effective area of flow entering the hole
A_l	the area of the incident laser beam
Ar_F	laser material interaction area
B	the jet plate distance
B_0	the evaporation constant
C	arbitrary constant
CAZ	chemical affected zone
CW	continuous wave
CP	critical point
CPA	chirped pulse amplification
D	diameter of the lens, or beam diameter on the focusing lens or microscopic displacement or arbitrary constant
DOF	depth of focus
D_ave	average diameter of the hole
$D\_entrance$	entrance spot diameter on the top surface
D_F	diameter of the laser beam in the focal plane of the focusing lens
D_L	laser beam size when it propagates to the front side of the focus objective lens
D_m	minimum hole diameter
D_{min}	minimum beam diameter that can be achieved

D_n	is the beam size at location Z_n
D_exit	exit spot diameter on the bottom surface
D_0	diameter of laser beam on the lens, or diameter of the beam waist
DH	digital holography
E	energy, or modulus of elasticity, or electric field, or phasor amplitude of the EM field
E_0	maximum electric field intensity on axis
$E_{\zeta,t}$	energy of electrons a considered region
$E_{z,t}$	energy of phonons a considered region
EM	electromagnetic field
EMW	electromagnetic wave
E_a	an activation energy evaporation per atom
E_{disp}	the displacement threshold energy
E_{dr}	drilling threshold energy
$E_{b,\lambda}$	blackbody monochromatic emissive power
E_f	an electron at the final continuum state
E_i	ionization potential for the neutral atoms in the gas at the initial continuum state
E_m	the melting threshold energy
E_{phonon}	mean energy of phonon
E_{req}	energy required for micromachining process
E_s	electric field intensity
F	the focal length of the last focusing optical lens on the path of the laser beam, peak load, or focal number of focusing optic, or factor that depends on the characteristic of the fiber
F_{th}	fluence breakdown threshold
FDM	finite difference model
FO	Fiber optic
G	collection of time and space terms of finite difference equation
HAZ	heat affected zone
H_f	the latent heat of fusion
H_v	the latent heat of vaporization
H_{v0}	is the latent heat vaporization at absolute zero
I	intensity
$I(z)$	the intensity of the incident radiation at a given distance, z, into the absorbing medium from the irradiated surface
I_A	numerical approximation of laser beam intensity of the normalized area
$I_0(x,y,0,t)$	is laser radiation intensity at the material surface
I_{abs}	absorbed laser intensity
$I_0(\tau)$	is the laser beam temporal characteristic
I_{mach}	the optimal power density
$I_R(x,y,z)$	is the spatial laser beam characteristic
I_t	fiber optic threshold irradiance

I_v	threshold intensity
K	the aberration of the fiber optics
$K(n,q,p)$	the factor dependent on the refractive index
L	the characteristic length
L_r	the characteristic length
LASER	light amplification by stimulated emission of radiation
LSC	laser supported combustion
LSD	laser supported detonation
LSR	laser supported radiation
LST	laser-sonic-technique
LTE	local thermodynamic equilibrium
M	mass of a neutral atom, or expansion factor of the beam expander, or the atomic mass
M_a	atomic mass
M^2	quality of the laser beam
M_{exp}	the expulsion fraction of material removed in laser drilling
$M_{r,oe}$	the relative atomic mass of the metal element
Mt	the total mass of material in laser drilling zone
MASER	microwave amplification of stimulated emission of radiation
MAZ	mechanical heat zone
MEF	melt ejection fraction
MEMS	micro-electronic
N	number of laser pulse or number of atoms, or the number of free electrons per unit volume
NA	numerical aperture of the fiber
N_a	Avogadro's number
N_G	the number of atoms evaporated per unit time per unit area
N_u	Nusselt number
N_z	the number density of electrons which transfer energy to dz
Ob	the perimeter of the workpiece
OP	optical path
P	laser power or dipole moment per unit volume
PCM	phase conjugated mirrors
P_c	the power loss from elastic collisions
P_e	the Peclet number
P_L	the power loss from inelastic collisions
P_{max}	maximum total beam power during a laser pulse
P_{lcond}	output power per unit length of the molten layer due to conduction
P_{lconv}	output power per unit length of the molten layer due to convection
P_{levp}	power per unit length spent for the evaporation
P_{lin}	input power per unit length of the molten layer
P_{lrad}	output power per unit length of the molten layer due to radiation
P_L	power loss from inelastic collisions
$P(\infty)$	normalized total power of the laser beam

P_0	constant power during a laser pulse, or the ambient pressure
Pr	Prandt number of the assist gas
P_{rp}	the reactive power generated due to oxidation
$P(T)$	saturated vapor pressure defined by Clausius-Clapeyron equation
Q	the rate of laser energy absorbed per unit volume in the irradiated medium, or a volumetric term accounting for the internal generation of heat
Q_c	convective cooling rate per unit area
$Q_{cond,conv,rad}^{x,y,z}$	the heat transfer due to conduction, convection, and radiation to the ambient regions in the x, y, and z direction
R	reflectivity, or radius of wavefront curvature, or universal gas constant, or the recoil force
R_a	Raleigh number
R_d	electron diffusion rate
Re	the Reynolds number at jet exit
R_i	electron production rate
R_{oe}	the absolute reaction rate
R_r	electron recombination rate
R_x	laser beam radius along the x-axis
S_2	distance from lens
$S_{i,j,k}^{x}$	scaling factors describing the length of the element in the x direction
$S_{i,j,k}^{y}$	scaling factors describing the length of the element in the y direction
$S_{i,j,k}^{z}$	scaling factors describing the length of the element in the z direction
$SOTA$	state-of-the-art
SST	stainless steel
T	temperature, or the power transmission
TAS	thermal analysis system
TEM	transverse electromagnetic modes of the laser beam
T_a	ambient temperature or room temperature
T_b	boiling temperature
T_c	critical temperature
T_e	plasma temperature or electron temperature
T_l	temperature in liquid state
T_m	melting temperature
T_{plmax}	maximum plasma temperature
T_s	surface temperature of the workpiece, or temperature in solid state
T_v	vaporization temperature
T_0	initial temperature, or the peak temperature at time t
T^{0}_{0}	the peak temperature just prior to irradiation

$T_{i,j,k}^{wall}$	temperature of wall surface grid point (i,j,k)
$T_{i,j,k}^{SS}$	steady-state temperature
T^*	the average temperature in the melt layer
ΔE	discrete units of energy or phonon energy
ΔE_{pulse}	average energy delivered per pulse
ΔE_{total}	the total change in energy of the meter
$\Delta P(r)$	the difference between the local equilibrium vapor pressure and the atmospheric pressure
ΔS_v	vaporization entropy
ΔT	change in temperature
Δt	time increment
Δz_f	dislocation of the focal plane
U	energy of evaporation per atom, or thermal displacement
V	volume of the melted material or recession velocity
V_0	a coefficient of the order of magnitude of the sound velocity
Z	average ionic charge in the plasma, or the charge number
Z_0	the beam waist location
α_e	coefficient of thermal expansion
β	pulse parameter, or the coefficient of volumetric thermal expansion
δ	molten layer thickness, or the interval separating the two values of function u
δ_m	melt-layer thickness at the edge of the laser spot
$\left.\dfrac{\partial T}{\partial z}\right\|_z$	the temperature gradient at the surface along the normal (z- axis)
ε	emissivity, or component in total strain vector or permittivity
ε_0	the elementary charge, or the permittivity of free space
$\bar{\varepsilon}$	the average electron energy
ξ	dimensionless parameter to express the position coordinate x
$\zeta_{i,j,k}$	geometrical coefficient
γ	the kinematic viscosity, or pulse parameter
θ	divergence of a laser beam, or the half-angle laser divergence or atomic constant
κ	thermal diffusivity
κ_m	thermal diffusivity of the melt metal
κ_s	thermal diffusivity of the solid metal
κ_v	thermal diffusivity of the vaporized metal
λ	wavelength
μ	bulk absorption coefficient, or the dynamic viscosity of the gas
μ_m	the melt viscosity
μ_s	bulk absorption coefficient in solids
μ_v	bulk absorption coefficient in vapor
η	is the fraction of recondensing atoms

Θ_a	angular fault (half angle) of the beam
θ_{act}	real beam divergence
v	melt viscosity
υ	phonon frequency
ρ	density
σ	Stefan-Boltzmann constant, or stress, or root-mean-square surface roughness, or surface tension of the liquid-vapor interface
ψ	dimensionless parameter to express the position coordinate y
τ	thermal time constant, or normalized time relative to the pulse length
τ_l	laser pulse width
τ_e	laser pulse width
φ	optical phase, or angle of incidence
$\varphi_{i,j,k}$	geometrical coefficient
φ_0	preexponential factor
ω	laser beam radius at the surface of a workpiece, or the laser frequency, angular frequency
ω_0	laser beam radius where the intensity is reduced from its maximum value at the beam center by a factor of $1/e^2$, or the laser beam radius at the beam waist
ω_e	electron collision frequency
$\omega_{ea,g}$	the electron-atom collision frequency of gas g
ω_{lens}	the laser beam radius measured at the lens
ω_p	plasma frequency
$£^{-1}$	the inverse Laplace transform
Φ	the absorbed laser power density, or divergence of the laser beam
$\Phi(z,t)$	the temperature of the lattice site atoms in dz
$\Theta(\zeta,t)$	the temperature of the electrons when they arrive at dz
∇	gradient operator

Acknowledgment

First of all I would like to thank Professor Ryszard J. Pryputniewicz for giving me the opportunity to work with Him at the Center for Holographic Studies and Laser micro-mechaTronics (CHSLT), and for supporting and advising me throughout my graduate studies.

Support came in many ways and forms, always appreciated and remembered from CHSLT's members. I would like to thank Professor Cosme Furlong for his help and understanding, special thanks goes to Peter Hefti, Dr Wei Han, Adam Klempner, Ryan Marinis, and Shivananda P. Mizar.

I would like to express my gratitude to my family for their love and encouragement, and for supporting me in many ways throughout my academic career.

Finally, a very special thanks to my wife, Ela, who has been with me every step of the way, for her love, support, and patience. I thank you and love you.

Table of contents

List of figures

List of tables

Dissertation summary

The objective of this Dissertation is to study laser beam interaction with materials for microscale applications.

Laser micromachining is essential in today's advanced manufacturing, of e.g., printed circuit boards and electronic components, especially laser drilling (Duley, 1985; Treusch and Herziger, 1986, Chryssolouris, 1991; El-Batahgy, 1997; Solana et al., 2001). Demand for circuit miniaturization, and small MEMS components and their packaging, (Cheng et al., 1998) have created the need for smaller holes and microvias, smaller lands, narrower lines and spaces, tighter registration, and smaller and more controllable spot-weld than ever before. All that requires more accurate and controlled production process, (Bruggemann, 1996) smaller taper of the microholes, and more stable and controlled laser micromachining process than currently available. Therefore much more attention must focused on the laser parameters that determine critical specifications such as the accuracy of the hole size, shape, and taper angle. According to Karnakis et al. 2003 "Thermal management of microdrilling process has become increasingly important and needs to be carefully considered. In brief, current requirements in laser micromachining are for the laser sources with better energy stability, higher average power, which emit at short wavelengths with short pulse durations".

Although laser micromachining has become widely used in microelectronics and packaging industry, a full understanding of various phenomena involved is still a matter of trials and speculations. Laser micromachining is a very complex process which involves variability in shape and properties of keyhole welds (Chryssolouris, 1991;

Marley, 2002; Jin and Li, 2003) or laser drilled holes (Batteh et al., 2000; Low et al., 2002) due to the very complex phenomena including, but not limited to, heat transfer, fluid flow, plasma effect, lattice-phonon vibration, and metallurgical problems (Bulgakova and Bulgakov, 2001a).

Lastly, study of laser beam interaction with materials enables us to explore the physical processes involved, better understand the micromachining processes, and maybe eliminate some unwanted side effects as well as increase efficiency of the micromachining processes. Determination of process parameters in laser micromachining is done mostly by trial and error. This Dissertation attempts to reduce the experimental time and cost associated with establishing process parameters in laser micromachining.

The research for this Dissertation has been done at the Center for Holographic Studies and Laser micro-mechaTronics (CHSLT) laboratories of Mechanical Department at Worcester Polytechnic Institute in Worcester, Massachusetts.

To avoid duplications and so called reinventing the wheel, a collection of current state-of-the–art (SOTA) work and prior study done in the field of laser micromachining has been evaluated first (Duley, 1985; Christensen and Tillack, 2003).

The investigations performed in this Dissertation are based on analytical, computational and experimental solutions (ACES) methodology (Pryputniewicz, 1993). More specifically, the studies will be focused on the development of equations governing interaction of the laser beam with materials, where analytical solution of these equations

based on Fourier heat conduction using the Laplace integral transform (Yilbas and Shuja, 1999) method will be utilized.

Solutions obtained by finite difference method (FDM) and experimental demonstration of laser micromachining will be presented, and correlation of the analytical, computational, and experimental results will be determined (Pryputniewicz, 1998). Some of the tasks to be performed will include measurements of temperature distribution in the workpiece, characterization of the thermal deformations, and investigation of shape and profile of microdrilled holes. Furthermore, systematic investigations will be performed to study the effects of specific laser parameters on the results of laser micromachining processes, and optimization is proposed for the specific applications.

Experimental and theoretical investigations were performed to study properties of the laser beam impinging on the surface of the material under consideration. The temporal and spatial characteristic of the laser beam are presented.

To reduce size of microholes, researchers have started using short laser pulses, down to 10^{-9} s (following optical Raleigh law) (Dausinger et al., 2003). As the pulse length reduces further ($< 10^{-9}$) and intensity increases ($> 10^{13}$ W/m^2), the kinetic theory predictions (Yilbas et al., 2000) deviate considerably from the Fourier theory results, basically because these assumptions do not account for the effects that electron movements in the solids have in the laser micromachining processes using ultrashort pulses. Consequently, new models of the laser interaction with materials based on revised assumptions and approximations are needed. The modeling of laser microdrilling

30

process is essential for better understanding of the physical phenomena occurring during laser beam interaction with materials (Wang and Chen, 2003). Absorption of laser energy takes place through photon interaction with bound and free electrons in the material structure, which raises them to the higher energy levels. Energy conversion takes place through various collision processes involving electrons, lattice phonons, ionized impurities, and defect structures. This Dissertation examines pulsed laser heating process by considering both Fourier conduction and electron-phonon kinetic theory approaches. More specifically, this Dissertation focuses on development of equations governing interaction of a Gaussian laser beam with materials, where analytical solution of these equations based on both the Fourier heat conduction theory and kinetic theory approach using a Laplace integral transformed method are utilized (Yilbas et al., 2000). A comparison of the analytical solution of the Fourier theory and closed form solution of the kinetic theory approach is also presented in this Dissertation.

Study in this Dissertation is concentrated on one of the most popular laser processes used in the microelectronics industry, which is laser microdrilling. Further more, the expulsion of molten material from the hole has an important role in microdrilling efficiency.

The samples that are considered in this Dissertation are made out of two materials, first very popular in MEMS technology – silicon (Cytrynowicz et al., 2003), and second, being used in MEMS devices and electronic industry, alloy 304 stainless steel (Cheng et al., 1998; News, 2004).

The hope is that this research will facilitate improvements and optimizations of SOTA laser micromachining techniques.

Complete results are presented in the Dissertation.

The contributions of the Dissertation include:

1. Investigation of the effects of laser operating parameters on the profiles and dimensions of the laser microdrilled holes.

2. Calculations of the temperature profiles during laser micromachining using program developed for the purpose of this Dissertation using finite difference method. The program has capability of handling 3D slab of nonlinear material properties, temperature dependent coefficient of energy absorption, with preliminary calculations of the fluid dynamic phenomena involved in laser microdrilling. The program uses experimentally obtained spatial and temporal laser beam characteristics.

3. Experimental investigation of laser beam micromachining using a fast camera (18000 frames per second) to record laser beam interaction with materials, especially to measure speed of liquid expulsion during microdrilling and plasma formation.

4. Considerations of thermal and laser beam conditions and their effect on laser micromachining processes.

5. Initial investigation of the effect of ultrasonic operating parameters on the results of profiles and dimensions of the laser microdrilled holes, which will provide guidelines and will advance currently existing laser microdrilling processes.

6. Correlation between computational and experimental results of the microdrilled holes; explanation and improvements of the model based on the mechanisms of laser micromachining process.

The investigations presented in the Dissertation show practicality of laser micromachining process and explain some problems occurring during set ups of those process. This knowledge should improve quality of microdilled holes and manufacturing processes. They will also provide guidelines, which will help to explain and will provide better understanding of the existing laser micromachining process. Results of the Dissertation will facilitate improvements and optimization of the SOTA laser micromachining processes.

1. Literature review

While there have been a significant number of papers published on the subject of interaction of laser energy with materials only a few of these papers present unique information. Some of the references included herein are of historical value, while others are quite comprehensive in addressing the mechanisms of interaction of laser energy with materials. A discussion of the findings from selected relevant literature follows. Because the primary objective of this chapter is to summarize the existing literature relating to laser microdrilling, phenomena like a normal evaporation, liquid droplet ejection, and the hydrodynamic effects will be of interest and will be discussed. Generally, the entire field

of laser beam interaction with materials can be divided into two groups: (i) resonant and (ii) nonresonant interaction.

The resonant group includes selective excitation processes in systems with photon discrete spectra, multiphoton ionization of atoms and molecules, multiphoton photoelectron emission, and nonlinear optical phenomena in solids and liquids. as discussed later. The following parameters affect these excitation processes: coherence, polarization, and spectral characteristics of laser radiation.

In the nonresonant interactions, laser-induced thermo-chemical and thermo-physical phenomena can be related to each other, as well as to laser breakdown of gases and solids and laser plasma generation.

In the Dissertation, the main study concentrates on the nonresonant laser beam interaction with materials. For this group phenomena like coherence and spectral characteristic are not very important. Principal effects are connected to the heating of materials, and important factors are: the laser intensity, pulse duration, and focusing conditions. We consider laser heating, melting, and vaporization of solid materials and related instability of these processes. We also consider the dynamics of vapor plume expansion, with an emphasis on hydrodynamic instabilities of vapor expansion.

Many theoretical, analytical, and experimental works with the lasers have been developed and published. Summary of the methods used and results obtained by selected researchers in chronological order are presented below.

The beginning of laser's history started in 1916 based on Einstein's theory of light emission and concept of stimulation emission (Thompson, 2003). In 1917, Einstein

proposed the concept of "photon" (Einstein, 1917). We can say that light is composed of individual particles called photons which posses a discrete amount of energy or quanta. Einstein (1917) also predicted that when there exists the population inversion between the upper and lower energy levels among the atom systems, it would be possible to realize amplified stimulated radiation, i.e., laser light. Quantum Mechanics was developed to explain these new phenomena since 1920 (Kittel, 1987).

1951 Townes, the inventor of the MASER –microwave amplification of stimulated emission of radiation, at Columbia University – first device based on stimulated emission, was awarded Nobel prize in 1964 (Towns, 2002).

1960 - Maiman – invented first working LASER based on Ruby rod as the lasing medium, May 16th, 1960, Hughes Research Laboratories, New York (Maiman, 1960).

1968 - Anisimov developed a theoretical model to predict a temperature profile in the material on which the laser beam is impinging, (Anisimov et al., 1971). He considered temperature, pressure, and density discontinuities across the Knudsen layer in vacuum to solve analytically heat transfer equations the Knudsen discontinuity is modeled by a Mott-Smith type solutions.

1972 - Paek and Gagliano (1972) developed a theoretical model to predict a temperature profile assuming the laser beam of circular cross section and uniform intensity. They found that the absorptivity along with beam intensity were the most important factors during the laser drilling process.

1974 - Wagner (1974) presented a quantitative model, which predicts the depth and shape of a hole, drilled in alumina ceramic by a ruby laser. Experimental and

theoretical results indicated that the drilling mechanism for this application is not surface absorption or conduction, but one in which laser energy is absorbed throughout the bulk of the ceramic. Wagner (1974) based on experimental evidence, developed a mathematical model including material removal due to pressure caused by laser radiation. The shape and depth of holes drilled in ceramic have been rather accurately predicted from the measured beam energy density distribution. He showed that the radiation pressure of the focused beam plays an important role in the removal of molten material from heated zone.

1975 - Andrews and Atthey (1975), developed a useful framework of the drilling phenomena. They developed a model for complete analysis of the drilling speed as one-dimensional. They predicted a continues growth of a hole depth with time.

1975 – Sparks (1975) developed a theory of laser heating of metals and derived exact analytical solutions. He calculated the transient and steady-state temperature rise of a laser irradiated metals. Sparks had evidence for plasma formation and his theoretical work suggested that the temperature rise caused by ordinary heating of solids by laser is orders of magnitude too small to ignite the plasma, but that thermally isolated surface imperfections could cause ignition.

1976 – von Allmen (1976) established an analytical model taking into account liquid expulsion. The development of models incorporating melt ejection really began with von Allmen's equations, which allow calculating drilling velocity and drilling efficiency as functions of the absorbed laser beam intensity. Equations are based on a 1D

steady-state "piston-like effect" of recoil pressure driving molten material away from the ablation front.

1977 – Anthony and Cline (1977) study thermal analysis of laser heating and melting of materials. They stated that during laser surface melting and alloying, temperature gradients on the melt surface (interaction line of the solid-liquid interface) generate surface tension gradients that sweep liquid away from laser beam impact line. The resulting flow of liquid creates a depression of the liquid surface beneath the beam and ridging of the liquid surface elsewhere. As the beam passes to other areas of the surface, this distortion of the liquid surface is frozen in, creating a roughened rippled surface. They show that rippling from surface-tension gradients can be avoided if during surface melting, the laser beam velocity exceeds a critical velocity. Experiments were presented for stainless steel 304.

1979 - Mazumder and Steen (1979) worked on 3D heat transfer model for continuous wave laser material processing. They developed 3D heat transfer model with moving Gaussian heat source using finite difference method. In their work, the system is considered to be in a quasi-steady-state condition after the keyhole initiation time, which was treated as instantaneous.

1980 - Veiko (1980) discussed laser-induced formation of submicron holes in thin films. The qualitative concepts of melt surface evaporation and of melt motion under the action of the reactive vapor pressure of surface tension forces and of adhesion was shown. The basic equations describing the removal process were solved numerically. It

was shown that evaporation or liquid phase motion plays a principal role in the film removal mechanism.

1986 - Ursu et al. (1986) worked on high intensity laser radiation of metallic surfaces. An analysis on the role of the periodic structures induced by laser radiation on metallic surfaces was given a great deal of attention. One important aspect was the influence of metallic periodic structures on the optical characteristics of the surface. Discussion was presented based on experimental and theoretical results. They concluded that at certain conditions of metallic surface, the absorptivity of a metal surface could decrease with temperature.

1986 - Herziger (1986) demonstrated laser-induced plasma by the optical feedback control by on-line diagnostics. He also presented 3D heat flow calculations for different energy coupling. Herziger investigated the vapor breakdown and resulting plasma formation by high-speed photography in the framing and streak mode of operation. He concluded that the plasma assisted transport of processing material as vapor, or melt, have to be adapted to characteristic time constant of the involved physical process and to the thermo-physical properties of the processing materials in order to yield maximum heat input and efficient machining. He concluded that high efficiency of materials processing could be achieved only in a narrow intensity range between the thresholds of plasma generation and plasma shielding, which can be influenced by gas controlling the plasma properties. Herziger el at. (1986) improved laser efficiency by applying in line the pulse separation process, in a way that plasma absorption has

diminished between two successive pulses, and the pulse halfwidth has to be adjusted so no substantial plasma absorption during the interaction time will occur.

1986 - Treusch and Herziger (1986) studied precision laser drilling. They calculated threshold intensity for Gaussian laser beam and melt deposition at the hole entrance during drilling. They observed that accurate adjustments of absorbed laser power and heat losses are important to control the process of material drilling as well as the laser induced plasma. For a reproducible material removal by lasers the following parameters are critical: pulse power, pulse duration, duty cycle of pulses, intensity distribution, and intensity time slope, protection of the optics and thermal lensing of the laser medium.

1987 - Chan and Mazumder (1987) developed a 1D steady-state analytical model for damage by vaporization and liquid expulsion due to laser material interaction. They found that the radiation plays an insignificant role in determining the surface temperature, rate of material removal in both vapor and liquid form. Results were compared for conditions both with and without radiative heat loss. The vaporization process produces a recoil pressure that pushes the vapor away from the target and expels the liquid, so material is removed in both vapor and liquid phases. The total material removal rate is equal to the sum of vaporization and liquid expulsion rates. The speed of the solid-liquid or liquid-vapor interface is a direct measure of the material removal rate. They predicted that the liquid expulsion rate goes through a maximum as the power density varies. At lower power, the vaporization temperature is slow. Consequently, the expulsion rate is low because of low recoil pressure. With low intensities producing a low liquid ejection

rate, due to a lower rate of vaporization and hence recoil pressure. At high power, the vaporization temperature is high. Very high intensity thinning the molten layer, and again reducing the rate of liquid expulsion. Results indicated peak in the rate of material removal by melt ejection, as a function of power density. At low beam power the dominant form of material removal is liquid expulsion, at high power vaporization was the dominant form of materials removal. The vapor phase is assumed optically thin so its absorption of the laser beam is negligible. Close-form analytical solutions were obtained for three different materials: aluminum, superalloy and titanium.

1989 - Armon et al. (1989a) measured and analyzed aluminum plates drilled with a CO_2 laser beam and the following was analyzed: penetration time, the spatial intensity profile of the beam, the temperature-dependent absorptivity, evaporative material removal, heat conduction within the workpiece, crater radius, melted zone using theoretical approach. Assumption for absorption of liquid metal, attenuation by metal vapor and heat exchange with vapor were made. 3D time dependent formulation for metal drilling with a laser beam was presented and 1D solution for penetration rate was the upper limit solution that led to rather realistic prediction in small aspect ratio cases at short pulses.

1989 - Finke and Simon (1989) discussed in the 1D steady-state analytical model properties of steady evaporation of metals during irradiation of metal surface by a high radiation laser beam. They distinguished three regimes: Knudsen layer adjacent to metal surface, condensation regime, and hydrodynamic regime. Estimates of temperature,

density, average velocity, degree of condensation, and decrease of pressure along the jet were presented.

1989 – Postacioglu et al. (1989) investigated natural frequencies of oscillation of weld pool when in its molten state: these frequencies were studied by a combination of analytical and numerical methods inner and outer boundaries of the weld pool as well as the finite depth of the pool and the dependence of the surface tension on temperature were considered.

1990 - Kar and Mazumder (1990) developed a 2D model for material damage during laser melting and vaporization: Crank – Nicholson method was used. The problem was formulated by using energy conservation equation (the Stefan condition) at the phase interfaces. The effect of curvature of solid-liquid and liquid-vapor interfaces was taken into account and solved numerically. The effect of laser power, time, number of pulses, and laser beam diameter on depth and radius of the crater during laser irradiation were also examined. Linear relationship between the maximum crater depth and the laser intensity was derived phenomenologically and verified numerically.

1991 - Armon et al. (1991) employed a time-dependent axisymetric heat conduction model and used the enthalpy method to determine the transient cavity shapes and penetration velocities.

1991 - Chryssolouris (1991) suggested that for laser power densities below threshold value (e.g., for copper about 300 J/cm^2) the surface for most metals shows a high reflectivity to beam energy and no material removal occurs. The surface reflectivity is time dependent since the slope of the hole wall changes rapidly with time. During this

stage most of the incident laser energy is reflected from the erosion front, as time progresses, absorptivity increases and reaches the maximum, because the slope of the hole does not change much. For energy greater then threshold, drilling occurs, but efficiency may have been lowered by two phenomena. First is a plasma formation and the second laser supported detonation (LSD) waves.

1991 - Kar et al. (1991) introduced a 2D model for laser-induced material damage and effects of assist gas and multiple reflections inside the cavity were studied.

1992 - Olson and Swope (1992) demonstrated laser drilling with focused Gaussian beams. A computational model for drilling holes with Gaussian laser beams was presented and compared with experimental results. The beam divergence near the focus was taken into account and was shown to strongly affect the hole profile. The model correctly represents experimental observations, including moving of the beam waist from the target surface. Dependence of the hole profile on beam divergence was demonstrated as well as the optical conditions needed to drill cylindrical or conical holes.

1995 – Ho et al. (1995) further developed Kar and Mazumder's model considering effects of gas dynamics and Knudsen layer discontinuity during the ablation process. These models assume 1D heat transfer in target material, recognizing that the machining depth is much smaller than the diameter of hole, which is reasonable for relatively large holes (a few hundred micrometers in diameter). The effects of beam profiles and cavity profiles were not considered. These factors are important when the size of the hole is comparable to the drilling depth.

1995 – Tokarev et al. (1995) have proposed an analytical thermal model of ablation by UV lasers. The approximation used to describe the absorption of the incident beam in excimer laser induced ablation plasma, for the case of single-photon absorption. The changing (increasing or decreasing) slope of the curve of etches depth, z, versus logarithmic fluence.

1996 - Modest (1996) developed a transient 3D heat conduction model for material volume being machined. The model assumed that vaporization occurs in a single step without melting. Gas dynamics and discontinuity layer were not taken into account. This is not suitable for laser machining of metals on nanosecond time scale.

1996 – Luft et al. (1996) studied mechanical and thermal distortions in laser drilling of metals. Hole shape was investigated as well as composition of material in the edge region of the drill. Increasing mechanical loads on the material due to the higher pressure in the drill channel was a limiting factor for accuracy of the processing. Surface of the entrance channel was relatively smooth and contained a high number of sub-microscopic boiling pores. Extensive material bulging upon drilling was observed, which was attributed to the direct mechanical effect of the high pressure in the drilling channel. This pressure results from the recoil of ablated material and the expanding cloud of vapor and plasma. They concluded that heat diffusion into the bulk of the material in the direction of drilling is comparatively lesser problem than heat diffusion into the side walls of the hole and is unclear which processes contributed most: deposition of melts, plasma erosion, or multiple reflections to the lateral heat diffusion.

1996 - Niedrig and Bostanjoglo (1996) investigated ablation of metal films. Chronological order of ablation was observed in nanoseconds time frame. Ablation revealed threshold behavior. Above a laser energy density of 5-6 J/cm^2 the irradiated film region was completely evaporated during the laser pulse. At the beginning of laser heating, the surface evaporation occurred and after the energy reached its threshold, a bulk evaporation was observed. Below this threshold, evaporation was marginal and the film disintegrated mainly by liquid flow. Model was developed based on Herzt-Knudsen-Langmuir relation of rate of ablated atoms per area. They have also shown that vaporization enthalpy must be considered as a function of temperature for correct modeling of evaporation by short laser pulses. The differential equations were integrated using 4th order Runge-Kutta scheme. Prediction of shape of the drilled hole was introduced for the higher than threshold energy density, successfully.

1996 - Ganesh el al. (1996) have developed a 2D numerical model to predict overall material removal rates that compared well with experimental data. The coupled conduction heat transfer in the solid and the advection-diffusion heat transfer in the liquid metal, the fluid dynamics of melt expulsion and the tracking of solid–liquid and liquid–vapor interfaces have been mathematically modeled for the 2D axisymmetric case. The donor–acceptor cell method using the volume of fluid approach was used. It takes into account all thermo-physical properties including latent heat of vaporization, gravity, and surface tension driving forces. The novelty of this model was to treat the melted pool surface as a deformable free surface. It was found that resolidification of melt (recast formation) occurred throughout the pulse interval and had significant influence on the

developing of hole geometry, while the effect of vaporization material removal on the hole geometry was found to be small. Comparison of the simulated results indicated the material removed per Joule of energy absorbed appears to be inversely proportional to the square root of the peak beam intensity and the drilling rate appeared to be proportional to the square root of the surface pressure.

1997 - Yilbas and Sami (1997) were analyzing liquid layer with a presence of nucleate boiling mechanisms. Experimental study of liquid ejection mechanism and theoretical study of saturated nucleate boiling were presented. In experimental study they used streak photography. Kinetic theory for heat transfer model and transport of energy through electron-phonon (elastic) collisions were adopted. They found that the time measured for the liquid expulsion from the heated zone was identical with time computed corresponding to possible saturated nucleate boiling. They calculated the degree of superheat required for nucleation to occur using the Claussius-Clapeyron equation. The particle velocity measured using the streak photography method agreed with the theoretical calculations with 10% error, due to measurement error and/or the assumption made in the analysis.

1997 - Semak and Matsunawa (1997) carried out a theoretical analysis of the energy balance in the laser-meal interaction. The heat transfer due to the recoil-pressure-induced melt flow was taken into consideration. This melt flow carries away from the interaction zone a significant portion of the absorbed laser intensity (about 70–90% at low laser intensities); thus, convection-related terms can neither be ignored in

calculations of the energy balance in the interaction zone nor in calculations of the thermal field in the vicinity of the weld pool or cutting front.

1998 – Cheng et al. (1998) developed 3D finite difference model that simulates heat flow and material removal by volatilization. This model was used to determine hole profiles and thermal fields. In addition to monolithic specimens, drilling of layered materials was modeled.

1999 - Tokarev and Kaplan (1999) developed 1D time dependent heat conduction equation for surface heating and phase boundary. Analytical solution has been made for rectangular pulse shape and temperature independent material parameters. Intensity dependence of melt depth was investigated. The authors distinguished two melting regimes: slow and fast Stefan problem and kinetic boundary conditions were applied at the liquid-vapor interface.

1999 - Solana et al. (1999) attempted to determine time dependence of melt ejection by incorporating two distinct mechanisms of molten ejection. First occurring early in the pulse period as a result of rapid pressure build up. Second at a later stage by a more progressive process resulting from the pressure gradient associated with the radial decay in beam power. Some high-speed photography observations were presented to support this theory.

2000 - Voisey et al. (2000) considered a material removal during laser drilling. Most of the material removal during laser drilling of blind holes is displaced by melt ejection, depending on the beam power density and type of metal. Comparisons were made between hole dimensions and predictions from heat flow model. A technique was

developed to collect the ejected materials to determine the proportion of the hole volume removed by melt ejection. A trend was noticed that the melt ejection fraction (MEF) to rise initially as the beam power density was raised, but then fall. That fall maybe associated with a reduction in the thickness of the molten layer at high beam powers.

2001 - Bulgakova and Bulgakov (2001b) utilized experimental results to show the transition from normal vaporization to explosive phase change. They determined numerically that surface heating could be significant for non-metal materials. Subsurface heating could lead to explosive boiling. No experimental data were obtained to support boiling mechanism.

2001 - Solana el al. (2001) further incorporated two distinct mechanisms of melt ejection. Initial burst of melt ejection was modeled as the flow of molten material once pressure gradients in the drilled hole were great enough to overcome surface tension forces. This was followed by the flow, driven by the radial pressure gradients that resulted from radial intensity gradients in the incident beam. No experimental evidence was given for the second type of melt ejection on radial varying intensity distribution.

2001 - Zhang el al. (2001) reported experimental and numerical investigation of micromachining of copper using a frequency tripled Nd:YAG laser with 50 ns pulse duration. They have developed an axisymmetric model with laser beam distribution consideration and its coupling with the target material. This model used the enthalpy method to track the solid-liquid interface Stefan and kinetic boundary conditions were applied at the liquid-vapor interface. Discontinuity across Knudsen layer was considered. The Marangoni effect was neglected. Experimental results were presented and compared

well with model predicted results. The range of thermal vaporization dominated machining of copper using nanosecond time scale lasers was studied. Optimum laser intensity for micromachining of copper was suggested.

2002 – Xu and Willis (2002) proposed phase explosion as a mechanism for liquid droplet formation and discussed the physics of metastable liquids. Their experimental data showed a jump in vapor front velocity, vapor transmisivity, and ablation depth at the threshold laser fluence. With a heating rate on the order of 10^9 K/s, or higher, the surface layer melted by laser irradiation can reach a temperature higher than the normal boiling point. The vapor pressure does not build up as fast and thus falls below the saturation pressure at the surface temperature, resulting in a superheated, metastable state. As the temperature of the melt approaches the thermodynamic critical point, the liquid undergoes a phase explosion that turns the melt into a mixture of liquid and vapor. The time required for nucleation in a superheated liquid, which determines the time needed for phase explosion to occur, was also investigated from both theoretical and experimental viewpoints.

2002 – Low et al. (2002) introduced a hydrodynamic Physical Modeling of Laser drilling. 1D hydrodynamic physical model was created based on realistic material removal mechanisms (including melt vaporization and vaporization-induced recoil pressure). The effect of O_2 gas assist (exothermic reaction) and forced convective cooling were incorporated in this study – but were proven to be insignificant.

2003 – Semak et al. (2003) defined microwelds as having fusion zone dimensions of < 100 μm. The theoretical criteria defining threshold pulse energy and beam intensity

for melt displacement for welding or drilling were proposed. They presented the results of numerical simulation as dependence of threshold pulse energy and beam intensity as function of laser pulse duration and beam radius.

2003 - Further work by Golosnoy et al. (2003a) has improved determination of shape of the hole profile by introduction of an interface tracking technique that accounts for changing proportion of liquid and solid phases in each cell. The beam was assumed to have a Gaussian spatial distribution. Defocusing and multiple reflection effects were not taken into account. Convective and radiative heat losses from substrate surface were simulated via a surface heat transfer coefficient. The substrate was effectively modeled to be semi-infinite in all in-plane directions.

2004 – Voisey and Clyne (2004) used 2D finite difference mathematical model developed by Cheng et al. (1998), that simulates heat flow and material removal by volatilization, to predict hole profile and thermal fields. In addition to uniform monolithic substrate, they divided a modeled material into a number of layers. The heat flow at the interface was being handled by an interfacial heat transfer coefficient. They used improved determination of the hole profile which was done by Golosnoy et al. (2003b), by introducing the interfacing tracking technique that takes into account the changing proportion of liquid and solid phases in each cell. The convective and radiative losses from the substrate surface were simulated via a surface heat transfer coefficient.

1.1. Mechanisms for liquid formation and melt ejection during laser microdrilling

The mechanisms involved in melt ejection are rather complex and (at this time) poorly understood. There are two important aspects of laser drilling not fully yet explained.   The first is the laser induced reflectivity drop. The second, and probably the most important for practical purposes in microdrilling, is the quantitative connection between the absorbed laser energy and the extracted volume of material. Because several mechanisms may contribute to the interaction of rapidly heated workpiece, to correctly model that interaction one has to know which mechanism occurs. The energy flux of the laser source and physical characteristics of the affected material may determine which mechanisms occurs. The extent to which melt ejection occurs depends on both material properties and laser conditions. Since mechanisms may be temperature and/or time dependent it is possible that removal of the laser material during laser micromachining occurs in steps, or simultaneously, during an energy pulse. Below is a summary of research on expulsion of material during laser drilling, which will support the development of a mathematical model in the Dissertation. A brief description of several possible mechanisms found in the literature follow.

The majority of the recent literature dealing with liquid droplet ejection has focused on phase explosion. Anisimov et al. (1971) stated that the expulsed liquid must come from the bottom of the holes and not from the walls. The expulsed liquid jet forms the envelope of a cone. This can be seen by collecting the liquid on a thin transparent sheet in front of the target surface, where a ring of droplets is formed. In 1976, von Allmen delivered considerable experimental evidence that for expulsion of metal in

liquid form exists a mechanism involving radial liquid movement caused by the evaporation pressure. Direct measurements of metal drilling efficiency by a Nd:YAG laser over a broad intensity region for metal drilling have shown that optimal results can be expected only in a quite narrow intensity region – for most metals it varies from 5 to 50 MW/cm^2. For lower intensities heat conduction and reflection losses are dominant. For higher intensities, effects such as beam defocusing in the vapor cloud or even induced air-breakdown severely degrade the drilling efficiency and reproducibility of the drilling process. The shape of the drilled holes showing a regular and nearly polished surface, so von Allmen (1976) suggested a rather laminar flow of liquid. Contrary to von Allmen a series of explosions were proposed by Dabby and Paek (1972) and later by Miotello and Kelly (1995). Korner et al. (1996) discussed different regimes of laser drilling. For example, they have stated "As pulse intensity increases the laser-material interaction regime can change from threshold to stationary evaporation and then to melt ejection." The proportion of removed material increases with the increase of laser intensity. The concept is that there is an intermediate range of pulse energies, for a given pulse duration over which melt ejection is most pronounced. However, Korner et al. (1996) showed very little reliable experimental data in this area. Low et al. (2002) exploit the expression between melt ejection and pulse intensity. Grad and Mozina (1998) controlled melt ejection by temporally shaping pulsed or pulse trains. Murthy el al. (1994) reported, using streak photography method, velocities of melt ejected droplets on the order of 100 m/s for drilling. Sami and Yilbas (1997) claimed typical ejection velocities of about 130 m/s with ejection velocities increasing with pulse width. They

also reported two types of melt ejections, an initial burst of slow particles, attributed to radial pressure gradient expelling material. Then, after about 10 percent of the pulse width (100 μs), finer, faster moving particles, followed by larger, slower-moving particles. The temporal variation in melt ejection described by Rodden et al. (2000) corresponds with the second type of behavior reported by Sami and Yilbas (1997), who suggested explanation of this 2nd type of melt ejection as a nucleate boiling occurring in the molten layer. They did not report any microstructure evidence though. Luft el at. (1996) reported submicroscopic boiling pores. Later work proved that nucleate boiling would occur about 120 μs after the start of the pulse, matching well with the observed start time of the second type of melt ejection. They reported that using shorter pulses (pulses with higher intensity) causes the nature of melt movement to change from continuous liquid flow to atomization, with inhibition of recast layer near the hole entrance and ultimately to suppression of ejection. Luft et al. (1996) also noticed that increased pulse intensity increases the pressure generated; hence increase the flow velocity of molten material. Murthy el al. (1994) have explained variation in drilling velocity prior to reaching steady-state conditions in terms of melt ejection. After the initial burst of melt ejection, there is an approximately exponential decay, in drilling velocity from about 12 m/s as the molten layer forms and thickens until an equilibrium is reached between the absorbed intensity and energy loss via material expulsion, resulting in a steady-state drilling velocity of 1.0-1.5 m/s after 100-125 μs. The initial drilling velocity would be therefore higher then that predicted by steady-state models. According to Voisey et al. (2004) for melt ejection to occur, a molten layer must form and the

pressure gradients acting on the surface vaporization must be sufficiently large to overcome surface tension forces and expel the molten material from the hole. Since the latent heat of vaporization does not need to be absorbed when melt occurs, this is very efficient way of removing material. The energy required to remove material via melt ejection is about one quarter of the energy needed to vaporize the same volume. Christensen and Tillack (2003) developed the first model for the mechanism of liquid droplet formation and ejection, as well as prediction of the ejected droplet rate, size, and velocity. They were the first to consider heterogeneous boiling and homogeneous boiling and phase explosion mechanisms.

1.2. Normal evaporation

Normal evaporation, or heterogeneous evaporation, is the escape of molecules or atoms from a liquid surface (i.e., region of high concentration of matter) to the ambient gas in contact with the liquid surface (i.e., region of low concentration of matter). Normal evaporation occurs whenever vapor pressure in the ambient gas is less than the saturation pressure of the liquid at the liquid temperature (Xu and Willis, 2002). Christensen and Tillack (2003) stated: "As liquid temperature increases, so the saturation pressure of the liquid and the rate of evaporation also increases with the temperature; Evaporation from the liquid surface causes a decrease in liquid temperature". They determined mass of evaporated material as a function of saturated pressure at the liquid

surface temperature with aid of the Claussius-Claperon equation. Similar determinations

of mass removal mechanisms for normal evaporation is utilized in the Dissertation.

1.3. Homogeneous boiling

For laser beam interaction with materials, when the liquid is heated slowly, during

phase change process, the process is shown in Fig. 1.1, as binodal. However, if the heat

rate is fast, then the liquid may become superheated, i.e. the liquid temperature can

exceed the boiling temperature. A superheated liquid is in metastable state. If the

temperature continues to increase, the spinodal (Fig. 1.1.) is reached and the liquid

becomes unstable and relaxes to a liquid-vapor mixture. A process that prevents a liquid

from reaching the spinodal is called homogenous boiling (or nucleation). It consists of

the spontaneous creation of vapor nuclei within the liquid, without the help of preexisting

nucleation sites.
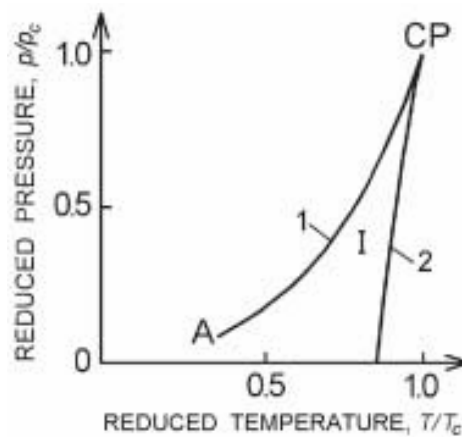
Fig. 1.1. A pressure-temperature diagram showing: (1) the binodal, (2) the spinodal.
The area I is the metastable region (Bulgakova and Bulgakov, 2001b).

A typical $p-T$ phase diagram of a substance in the neighborhood of the critical point (CP) is shown in Fig. 1.1. The line of equilibrium for the system 'liquid–vapor' (the binodal) originates at the triple point A (a point of coexistence of solid, liquid and vapor) and ends at the CP. To provide a clearer insight into the mechanisms of phase explosion and its possible manifestations, we recall here the basics of the theories of metastable liquids and critical state of matter (Xu and Willis, 2002, Christensen and Tillack, 2003).

(1) As the CP is approached, the fluctuations of the matter parameters are increasing. The density and the entropy thereof undergo the greatest fluctuations as compared to the other parameters *(p, T)*. The matter takes on a fine-grained structure, scattering light (the opalescence phenomenon). Simplifying the picture, one may say that the critical state is "a gas of droplets", whose characteristic size r_c (or a correlation length) increases when approaching the CP.

(2) If the liquid, being heated, has enough time to relax to a definite equilibrium state (far from the CP, the relaxation time is normally 1–10 ns (Christensen and Tillack, 2003), the matter is stable and its state follows the binodal. In other words, if the system is heated through the sequence of the equilibrium states, one may use the theory of equilibrium thermodynamics and the Clausius–Clapeyron equation is still valid. However, with increase of the correlation length, the fluctuation theory should be used instead of the classical approach.

(3) The rapidly heated system may undergo superheating. In other words, the temperature of the liquid becomes higher than that of boiling under the given pressure. If

so, the system shifts from the binodal into the region I of the metastable states (Fig. 1.1) and, as the heating rate increases, approaches the spinodal. This leads to a decrease of the lifetime of the system and to an uncertainty of its thermodynamic parameters near the spinodal. The system seeks for equilibrium that results in its return to the binodal through explosive boiling (sharp increase of homogeneous nucleation).

(4) The rate of homogeneous nucleation increases dramatically with superheating. The average time for formation of the critical vapor nucleus (a vapor sphere that will grow rather than decay) can drop by 3–4 orders of magnitude with superheating by 1ºC, which is conditioned by a fast decrease of both the critical nucleus size and the free energy for formation of a stable nucleus. At the same time, the rate of the vapor sphere growth increases drastically. The increasing nucleation prevents the liquid from approaching the spinodal, resulting in decay of the highly superheated liquid into a mixture of gas and droplets (phase explosion or explosive boiling). It maybe said that the liquid 'is torn into droplets' by growing the numerous gas bubbles.

(5) One of the possible mechanisms for formation of a new phase is a rise of the density gradients inside a small volume of superheated liquid (density fluctuations) that leads to the loss of stability and to the appearance of a vapor bubble. If the metastable region is close to the CP ($T \geq 0.9\ T_c$) the density gradient necessary for the nucleation due to fluctuations decreases. This is why the closer matter approaches the CP the more possible is superheating and phase explosion.

(6) For a given superheating, the critical nucleus size is much greater for metals than for organic liquids and water. As a result, spontaneous nucleation in liquid metals is

56

not obtained even for large superheating. On fast heating, the metals can be heated very close to the critical temperature and only then does phase explosion occur.

(7) Metals loose their metallic properties near the CP. Particularly, the electric conductivity drops because of the disruption of the conductivity zone due to increasing density fluctuations.

A variety of methods were proposed to estimate the thermodynamic critical temperature of materials. Most of them are based on the relation between the critical and boiling temperatures, which was first revealed by Guldberg for a number of substances (Bulgakova and Bulgakov, 2001b). The literature on the estimations of T_c is reviewed in (Reid and Sherwood, 1966), where different modifications of the Guldberg law and some other methods are given. A generalization of the Guldberg law for inorganic liquids was proposed as $T_c=T_b/\theta$, where θ is determined by the vaporization entropy, ΔS_v, as $\theta=a+b/\Delta S_v$ with the coefficients a and b depending on the polarity of the substance molecules. Normally, the θ value is in the range 0.45−0.55 for ionic compounds and 0.25−0.5 for metals.

1.4. Heterogeneous boiling

In many of the papers that address phase change mechanisms of liquid droplet ejection, heterogeneous boiling has been neglected.

Evaporation and boiling each involves liquid-vapor phase change at the liquid-vapor interface. Boiling includes the development of vapor bubbles at discrete locations

below the liquid surface, whereas in evaporation the vapor escapes from the interface between the liquid and the ambient gas (Kandlikar et al., 1999). Once boiling occurs, the temperature of the liquid remains approximately constant, because at commencement of boiling, energy that is added to the heated melted material is primarily used for the liquid-vapor phase change and not for rising the liquid temperature. The presence of moving vapor bubbles slows down the formation of temperature gradient.

Heterogeneous boiling occurs when vapor bubbles are formed below the surface at a nucleation site. A nucleation site may consist of: a) a scratch or pit at a solid-liquid interface in which gas or vapor is trapped, or b) foreign gas bubbles existing in the liquid. When the temperature exceeds the saturation temperature of the liquid, vapor bubble formation and growth will occur.

Miotello and Kelly (1995) suggest that the nucleation site density may be too low for significant heterogeneous boiling to occur. With only a small number of nucleation sites the nucleation and growth of vapor bubbles would not have the ability to produce sufficient amount of liquid droplets observed during ablation. Craciun et al. (2002) suggested that heterogeneous boiling might occur when a high fluence laser beam causes a "thick" liquid pool. The authors argue that neglecting heterogeneous boiling based on a small nucleation site density may be in error. It is suggested that this error is a result of the constant nucleation site density proposed by previous authors. It is proposed that nucleation site density should be calculated as a function of superheat, which would increase the number of nucleation sites. Three papers are referenced by Craciun et al. (1998). The authors suggest that a bubble must reach a critical size before it can burst,

58

and the liquid layer that confines the bubble must also reach a critical size. They might provide insight into droplet size for heterogeneous boiling or explosive boiling. Craciun et al. (2002) questioned the explosive boiling theory on the basis that small liquid droplets ejected into a plume with superheated temperatures would have time to evaporate, therefore no droplets would be found on witness plates. Overall, the proposals by Craciun et al. (2002) are interesting and offer an alternative view of what is taking place, but they offered no theoretical basis.

1.5. Phase explosion

Much of the evidence for phase explosion caused by rapid laser heating is based upon an observable jump in ablation rate when the laser fluence reaches a threshold value. For these researchers the threshold fluence marks a transition from normal vaporization to phase explosion. Bulgakova and Bulgakov (2001a) give an excellent theoretical and experimental handling of this subject. They developed a theoretical model for normal evaporation as a function of the laser fluence in 1D form. These observations suggest a transition from normal vaporization to a more vigorous mass removal mechanism. The liquid droplets have been explicitly imaged as bright sparks; droplets have also been observed by placing a collection plate in the ablation plume. The obvious change in ablation rate is attributed to explosive boiling.

Similar experiments were performed in this Dissertation to establish droplets size and which mass removal mechanism occurs during laser beam interaction with matter.

Xu and Willis (2002) reported similar results for laser ablation of nickel. While

the same basic results are obtained, (i.e., normal evaporation occurs for laser fluences

below the threshold value, while explosive occurs above the threshold value) some

important points are included in their treatment. They pointed out that the properties of a

material as it approaches the spinodal, changed drastically. These changes in material

properties could affect the absorption of laser irradiation, the electrical conductivity, and

the formation and ejection of liquid droplets. The difficult task of obtaining properties

such as surface tension and density near the spinodal may be required in order to

accurately predict the ejected droplet size. In order for a nucleation to occur a vapor

embryo must exist, and grow to a critical size. Once critical size is achieved the bubble

will continue to grow in order to minimize free energy. The time lag for nucleation is the

time necessary for an embryo to grow to the critical size. Xu and Willis (2002) utilized

experimental data that show a jump in vapor front velocity, vapor transmisivity, and

ablation depth at the threshold laser fluence. Saturation of these values occurs for laser

fluence above the threshold. The jump in these values suggests a transition from normal

vaporization to some other form of ablation, namely explosive boiling. The saturation of

the vapor front velocity also indicates a saturation of the surface temperature of the

target. One may wonder what happens to the additional energy resulting from increased

laser fluence, if a significant increase in surface temperature does not occur. Saturation

of the surface temperature is attributed to the decrease in material absorptivity as the

spinodal is approached. This decrease in absorptivity results in laser energy penetrating

deeper into the material. An additional reason is that once nucleation is initiated, energy added to the system is used for nucleation and growth of vapor bubbles.

1.6. Subsurface heating

Subsurface heating may occur when a thin layer of liquid is heated volumetrically, while the evaporation of atoms or molecules at the liquid–vapor interface removes heat from the liquid surface, and by doing it, decreases the surface temperature. The combination of evaporation and volumetric heating can result in the existence of temperature maximum below the surface of the liquid.

Dabby and Paek (1972) were among the first to propose subsurface heating as the mechanism of liquid droplet ejection. Miotello and Kelly (1995) pointed out that the assumption of a constant vaporization temperature at the liquid surface was incorrect, because inappropriate boundary conditions were used. Miotello and Kelly (1995) and Yoo el at. (2000) concluded that subsurface heating would not be significant and showed that explosive boiling (or phase explosion) remained the primary thermal mechanism of laser interaction with metals at high fluencies. However, Bulgakova and Bulgakov (2001a) determined numerically that subsurface heating could be significant for non-metal materials. As discussed earlier, subsurface heating could lead to results similar to explosive boiling. While these suggestions were made, no experimental data were obtained to verify the existence or effect of subsurface heating in metals. Based on latest findings, in transparent or semitransparent (non-metal) materials like single crystal

silicon, the subsurface heating process is main phenomenon occurring during laser beam

interaction and will be facilitated in the Dissertation.

2.   Modeling of laser interaction with materials

A complete understanding of laser interaction with materials is still a matter of

trials and adjustments. The real physical processes of laser beam interaction (drilling,

cutting, or welding) with materials are very complex. Problem of laser interaction with

materials presents many difficulties, both from modeling as well as from experimental

sides. One would expect a reasonable description of the main phenomena occurring

during laser interaction, but this is complicated because many of physical processes

equally contribute to the development of conservation equations, producing draw back

because of a great complexity of the equations to be solved. In most instances, this leads

to formulation of a model needed to be solved numerically. A lack of pertinent

experimental data to compare with, forces one to simplify some equations and use

previous analytical and computational work done in this filed.

2.1. Introduction

Laser micromachining is based on the interaction of laser light with matter. As a

result of a complex process, small amounts (depending on the process used) of material

can be removed from the surface of a workpiece. Two different phenomena may be

recognized: pyrolithic and photolithic processes. In both cases short pulses are applied in order to remove material in a controlled way. Pyrolithic process is based on breaking of the chemical bonds by photon energy. It is applied mostly in polymers by use of ultraviolet lasers characterized by wavelengths of 157 to 351 nm. Photon energy is converted directly in breaking chemical bonds and there is very little thermal interaction with the workpiece itself. Photolithic processes are based on a rapid thermal cycle heating, melting, and partly evaporation of the heated volume.

In general, one can say that laser is focused on the material surface and is partly absorbed. The first step in laser micromachining is laser absorption. The absorptivity depends on the material, surface structure, material defects, power density, and wavelength. For non-UV wavelengths, the absorption mechanisms are different for absorbing materials such as metals and semiconductors and transparent dielectric materials such as glasses and plastics.

For opaque materials, nonlinear absorption can become dominant at ultrashort pulse widths with high intensity. For transparent materials, absorption has to come from nonlinear processes through laser-induced optical breakdown. This process is described in more details in Section 2.3.3.

The absorbed energy transfers into bulk material by conduction. The laser energy absorbed by the material starts heating, melting the workpiece, and then vaporization occurs. The vapor flux generates a recoil pressure on the evaporating surface. There also exists a large temperature gradient at the liquid-vapor interface due to spatial distribution of the laser beam energy, which generates a thermo-capillary force. The recoil pressure

63

and the thermo-capillary force together provide the driving force for the liquid ejection. Thus, the material is removed from the workpiece both in vapor and liquid phases. Depending on the laser intensity, the liquid-vapor interface temperature may rise far beyond the normal boiling point. However, there exists a maximum temperature, called a critical temperature that a liquid material can attain. Critical temperature is the temperature below which a gas can be liquefied by applying pressure and above which no amount of pressure is sufficient to bring about liquefaction. At the critical temperature the distinction between liquid and gas vanishes. The high vaporization rate causes a shock wave and high vapor pressure at the liquid surface, which considerably increases the boiling temperature. Finally, the material is removed as a vapor by the expulsion of melt, as a result of high pressure and by an explosive boiling of the superheated liquid after the end of the laser pulse. In metals a rim of resolidified material caused by laser micromachining is clearly seen. In plastics, however, the process is different. The material is removed by breaking the chemical bonds of the macromolecules, and is dispersed into gas or small particles.

Modeling of micromachining process requires multidisciplinary approach (Dowden, 2001) involving heat transfer, fluid mechanics, phase transformation physics as well as the tracking of the liquid-vapor or solid-liquid interfaces. Research efforts can be divided in two groups. One group concentrates on the energy transport taking into account heat transfer in the materials and latent heat of vaporization (Allmen, 1976; Andrews and Atthey, 1975). The other group concentrates on kinetics of the vaporization process (Anisimov et al., 1971; Knight, 1979).

There are many laser-material interaction models, but none of them has yet considered all of the relevant process physics. This Dissertation is another attempt to develop such a model. Process of modeling of laser impinging on a 3D workpiece, Fig. 2.1, can be described in five steps:

1. Define the laser energy;

2. Characterize the laser energy coupling with the target material;

3. Find necessary properties of the materials;

4. Analyze and simplify the physical phenomena to develop the governing equations;

5. Setup boundary conditions, write the governing equations, and develop a computer program.
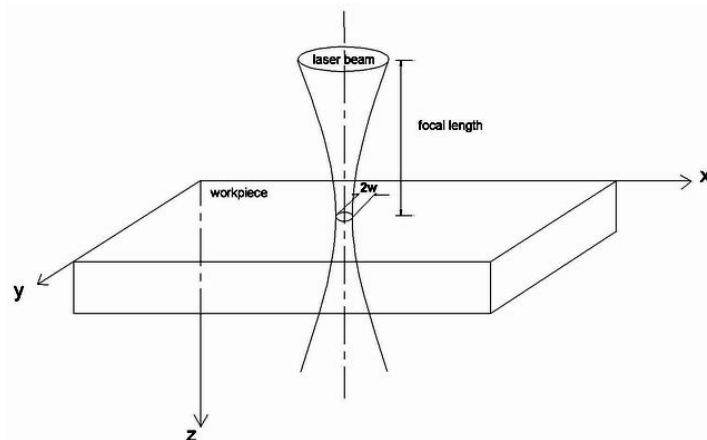
Fig. 2.1. Schematic of laser beam impinging on a workpiece.

In case of microdrilling, the basic quantities like the drilling rate, the vaporized material, the hole diameter, or heat affected zone (HAZ), can be directly measured very accurately, but the difficult part is to describe the laser beam interaction inside the hole. A preliminary theoretical model of laser drilling process can be formulated in two different approaches: (i) in terms of absorbed laser intensity and drilling velocity, and (ii)

65

in terms of absorbed energy and integrated depth of hole. In most publications researchers employ the first approach. The latter approach is of lesser interest because it depends on the specific temporal pulse shape. However, if temporal envelope is varying too rapidly, then the intensity vs. velocity concept cannot be utilized. In this Dissertation the second concept is of interest. The laser beam intensity absorption and redistribution inside the hole can be measured only indirectly as part of many interacting phenomena such as: fluid motion, hole instabilities, plasma formation, and multiple reflections on the hole wall.

2.2. High power laser system

For experimental study for this Dissertation a Nd:YAG class 4 pulsed laser, model KLS 126, manufactured by Lasag Industrial Lasers Corporation was used, Fig. 2.2. The characteristic parameter values, which should never be exceeded are: laser is rated at a maximum average output power of 200 W, with a single pulse capability up to 130 J, voltage up to 370 V, and wavelength $\lambda = 1.064$ μm. The pulse duration is variable between 0.1 to 10 ms, (Lasag, 1997).

Lasers have been discussed since Einstein proposed their existence in his theory of stimulated emissions in 1917. Yet, they did not come into existence until late 50's. Today lasers have evolved to be a powerful tool and at the lead of technology front in various applications. Lasers have revolutionized the word of mechanical machining practices and have introduced new capabilities into micromachining.

Fig. 2.2. High power laser system used in this study.

The word LASER stands for "Light Amplification by Stimulated Emission of Radiation". The laser energy source is introduced into a specified mass of a solid, gas, or liquid material, depending on the type of laser. With the Nd:YAG - Neodymium Yttrium Aluminum Garnet, solid-state laser, the YAG material is the host material that contains a small fraction of neodymium, the active element. The substitution of the yttrium ions with neodymium ions is called doping, and typically, the doping percentage is about 1-1.5 %. The YAG crystal is an ideal host for the lasing material Nd_3+, being physically hard stable, optically isotropic, and has good thermal conductivity that permit laser operation at high average power levels. Neodymium is an excellent lasing material as it produces the highest level of powers of any doping elements. The dimensions of the laser rods are selected for power and optical quality, with the maximum rod size limited

to about 15 mm diameter and 200 mm in length for reasons of crystal quality and thermal management (Lasag, 1997).

The active medium requires external energy input or "pump source" in order for lasing to occur. The Nd:YAG is solid state laser, meaning that the medium is solid crystal, and it uses light energy as the pump source coming from flash lamps. The source of the pumping energy is a plasma flash lamp (electrical discharge in a quartz tube filled with inert gas).

The generation of a laserbeam is essentially a three-step process that occurs almost instantaneously:

1. The pump source provides energy to the medium exciting the laser medium atoms such that electrons held within the atoms are elevated temporarily to higher energy states. The electrons held in this excited state cannot remain there indefinitely and drop down to a lower energy level. In this process the electrons loose the excess energy gained from the pump energy by emitting a photon. This is called spontaneous emission and the photons produced by this method are the seed for laser generation.

2. The photons emitted by spontaneous emission strike other electrons in the higher energy states. The incoming photons releasing the electrons from the excited states to a lower energy level creating another photon. These two photons are coherent meaning they are in phase, of the same wavelength, and traveling in the same direction, this is called stimulated emission.

3. The photons are emitted in all directions, however some travel along the laser medium to strike the resonator mirrors (located at both ends of the medium) to be

reflected back through the medium. The resonator mirrors define the preferential amplification direction for stimulated emission. In order for the amplification to occur there must be a greater percentage of atoms in the excited state than in the lower energy levels. This "population inversion" of more atoms in the excited state leads to the conditions required for laser generation.

The photon emissions are trapped between two reflective mirrors, one being semitransparent and the other 100% reflective, defining the optical resonator. When an adequate level of energy is created and stored within the leasing material, a collimated beam of light will expel through the semi-transparent mirror. This phenomenon is described as a laserbeam.

Design of the resonator has a significant impact on the equality and the spatial power distribution of the emitted laserbeam. The most commonly used resonator design is composed of two spherical or flat mirrors facing each other with the medium between them. The beam propagation properties are determined by the curvature of the reflective mirrors and the distance these mirrors are apart. As the laser absorbs the pump energy the laser rod heats up. If the frequency of the pump energy exceeds the thermal relaxation time of the crystal, the temperature of the crystal increases. This includes temperature gradients in the laser rod crystal that give rise to thermal lensing (Bronski, 2003), whereby the crystal acts as a lens to diffract the laser , which reduces power, so the cooling is required. The cooling is provided for both the flash lamp and the laser rod by flooding the entire cavity with flowing water.

When this laserbeam is focused to a small spot then we can cut, melt, and burn through any materials (including diamonds). This interaction of laser energy with various materials is a subject of this Dissertation.

2.3. Interaction of electromagnetic radiation with matter

The physical processes in laser material interaction are important for understanding the capabilities and limitations of laser micromachining processes. Laser radiation is an electromagnetic (EM) radiation and can be represented as an electric vector field and magnetic field, Fig. 2.3.
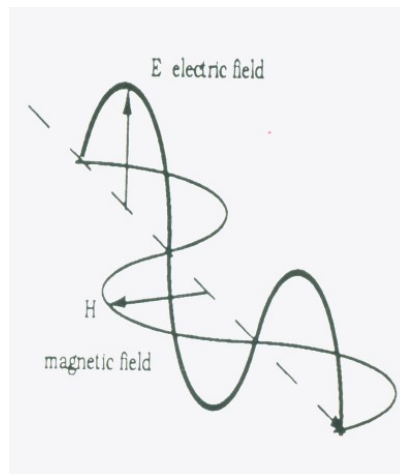
Fig. 2.3. The electric and magnetic filed vectors of EM radiation.

When EM wave radiation (laserbeam) strikes a surface (air/solid interface) it undergoes a reflection and transmission. Some radiation is transmitted, some reflected and, some absorbed. As it passes through a new medium it is absorbed according to Beer Lambert's law,

$$I = I_0 e^{-\mu \cdot z},$$
(1)

where, the absorption coefficient μ, depends on the medium, wavelength of the radiation and the intensity I, temperature, and the plasma formation above the target. Section Chapter 4.3.1 is dedicated to establish the value of μ.

When EM wave passes through a small elastically bound charged particle, the particle will be set in motion by the electric force from the electric field, E. The force is very small and is incapable of vibrating an atomic nucleus. This process of photons being absorbed by electrons is known as the "Inverse Bremsstrahlung Effect". Bremsstrahlung effect is the emission of photons from excited electrons. As the electron vibrates it will either reradiate in all directions or be restrained by the lattice phonon. Before considering the wave equation any further, one has to define two previously mentioned phenomena: plasma and phonon.

2.3.1. Phonon consideration

Considering the regular lattice of atoms in a uniform solid material, one would expect there to be energy associated with the vibrations of these atoms. However, they are tied together with bonds, so they cannot vibrate independently. The vibrations take the form of collective modes, which propagate through the material. Such propagating lattice vibrations can be considered to be sound waves, and their propagation speed is the speed of sound in the material. The vibrational energies of molecules, (e.g., a diatomic molecule, the lowest vibrational transitions of diatomic molecules approximate the

quantum harmonic oscillator and can be used to imply the bond force constants for small oscillations) are quantities treated as quantum harmonic oscillators. Quantum harmonic oscillators have equally spaced energy levels with separation ΔE so the oscillators can accept or lose energy only in discrete units of energy $h\upsilon$. where h is Plank constant and, υ is phonon frequency.

Evidence on the behavior of vibrational energy in solids is that the collective vibrational modes can accept energy only in discrete amounts, and these quanta of energy have been labeled phonons. Like the photons of EM energy, they obey Bose-Einstein statistics.

Considering a solid to be a periodic array of mass points, there are constraints on both the minimum and maximum wavelength associated with a vibrational mode, Fig. 2.4. By associating phonon energy

$$\Delta E = h \cdot \upsilon = \frac{h \cdot v_s}{\lambda} = \frac{h \cdot v_s \cdot n}{2L} \quad , \tag{2}$$

with the modes and summing over the modes, Debye was able to find an expression for the energy as a function of temperature and derive an expression for the specific heat of the solid. In this expression, v_s is the speed of sound in the solid.
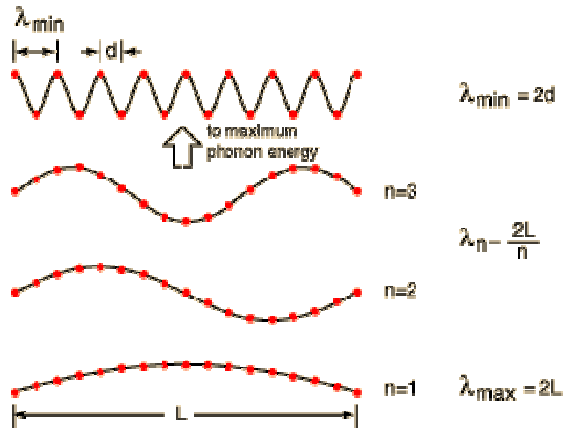
Fig. 2.4. Phonon vibrations.

Debye's approach was to consider a sphere in "n-space" which would give the same number of atoms. Taking n as a vector and allowing the components to take only positive values gives 1/8 of the sphere volume.

$$N = \frac{1}{8}\frac{4}{3}\pi \cdot n_{max}^3 \quad , \tag{3}$$

$$n_{max} = \sqrt[3]{\frac{6}{\pi}N} \quad . \tag{4}$$

A phonon is a quantized mode of vibration occurring in a rigid crystal lattice, such as the atomic lattice of a solid. The study of phonons is an important part of solid state physics, because they contribute to many of the physical properties of materials, such as thermal and electrical conductivity. For example, the propagation of phonons is responsible for the conduction of heat in solids.

There are two important properties of phonons. First, phonons are bosons, and second, each phonon is a "collective mode" caused by the motion of every atom in the lattice.

73

The speed of propagation of a phonon, which is also the speed of sound in the lattice, is given by the slope of the dispersion relation, $\partial\upsilon/\partial k$. At low values of k (i.e. long wavelengths), the dispersion relation is almost linear, and the speed of sound is independent of the phonon frequency, υ. As a result, packets of phonons with different wavelengths can propagate for large distances across the lattice without breaking apart. This is the reason that sound propagates through solids without significant distortion. It should be noted that the physics of sound in air is different from the physics of sound in solids, although both are density waves. This is because sound waves in air propagate in a gas of randomly moving molecules rather than a regular crystal lattice.

2.3.2. Lattice wave

Due to the connections between atoms, the displacement of one, or more, atoms from their equilibrium positions will give rise to a set of vibration waves propagating through the lattice. One such wave is shown in Fig. 2.5. The amplitude of the wave is given by the displacements of the atoms from their equilibrium positions. The wavelength λ is marked in Fig. 2.5.
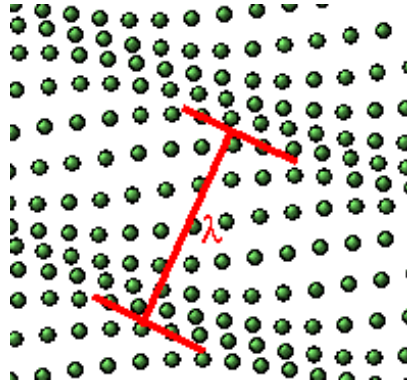
Fig. 2.5. Phonon wave.

In real solids, there are two types of phonons: "acoustic" phonons and "optical" phonons. "Acoustic phonons" have frequencies that become small at the long wavelengths and correspond to sound waves in the lattice. "Optical phonons," which arise in crystals that have more than one atom in the unit cell, always have some minimum frequency of vibration, even when their wavelength is large. They are called "optical" because in ionic crystals (like sodium chloride) they are excited very easily by light (in fact, by infrared radiation, e.g., Nd:YAG). This is because they correspond to a mode of vibration where positive and negative ions at adjacent lattice sites swing against each other, creating a time-varying electrical dipole moment.

2.3.3. Laser-induced optical breakdown

Laser-induced breakdown is a process where a normally transparent material is first transformed into absorbing plasma by the strong laser pulse. Subsequent absorption by the plasma of the laser energy causes heating that leads to irreversible damage to the

75

host material. The nonlinear processes that cause breakdown are avalanche ionization and multiphoton ionization.

2.3.3.1. Avalanche ionization

The avalanche ionization process is illustrated in Fig. 2.6. In a transparent dielectric material, the bound valence electrons have an ionization potential or bandgap greater than the laser photon energy. The bound electrons do not absorb the laser light at low intensities. However, in all real materials there are always some free or conduction electrons present, and they are the seed electrons for avalanche ionization. These seed electrons can come from metallic impurities, as well as from thermal or linear optical ionization of shallow energy levels of inclusions. A free electron, when simply wiggling in the oscillating laser field, does not gain energy when averaged over an optical cycle, thus does not absorb the laser energy. However, the free electron can absorb laser energy when it collides with the bound electrons and the lattice through dephasing. This is the Joule heating process, also known as inverse Bremsstrahlung.

The seed electron can be accelerated enough that its kinetic energy exceeds the ionization potential of the bound electron. Therefore the next collision with a bound electron will result in an ionization event if the free electron transfers nearly all its energy to the bound electron, resulting in two free electrons with low kinetic energies. This is called impact ionization.

This process will repeat itself, leading to an avalanche where the free-electron density grows exponentially from the very low seed electron density. When enough bound electrons are ionized by this avalanche process, a plasma with a "critical density" is produced, and the transparent material is broken down and becomes absorbing (the absorption by the initial seed electrons is negligible due to the very low density). This critical density is customarily taken to be 10 cm for nanosecond or longer pulses, since this is considered the density at which significant optical absorption occurs for irreversible damage to take place. For shorter pulse durations, the real plasma critical density for the laser wavelength, defined as (in cgs units), where is the electron mass and is the laser frequency, may be a more appropriate choice. This is the plasma density at which the plasma oscillation frequency equals the laser frequency, and the transparent material becomes totally opaque. For visible and near-IR wavelengths, 10 cm. Laser-induced breakdown is accompanied by emission of acoustic waves and optical plasma radiation (a spark) from the focus.
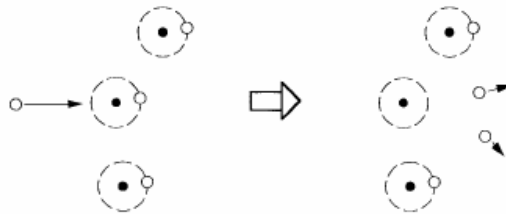
Fig. 2.6. Schematic of electron avalanche by collisional impact ionization. Secondary free electrons are generated during collisions with electrons whose kinetic energy is greater than the bound electrons binding energy.

2.3.3.2. Multiphoton ionization

When the laser field strength is very high, as in the case of ultrashort-pulse laser–matter interaction, bound electrons of the transparent material can be directly ionized through multiphoton absorption. This process is schematically shown in Fig. 2.7. A bound electron can be lifted from its bound energy level or valence band to the free energy level, or conduction band, by simultaneously absorbing photons in the laser pulse such that, where is the energy of the photon, and is ionization potential or bandgap.
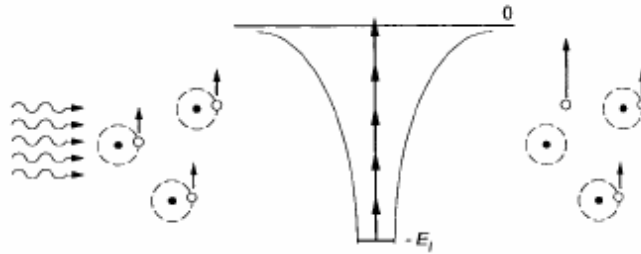
Fig. 2.7. The multiphoton ionization process. The bound electron is ionized by simultaneously absorbing *m* photons.

This is called multiphoton ionization. Only at very high field strength is multiphoton ionization significant. Therefore, for long pulse widths where the field strength at breakdown is lower, the multiphoton ionization contribution is negligible, and laser-induced breakdown is dominated by avalanche ionization. However, at ultrashort pulsewidths, multiphoton ionization plays an important role: it determines the breakdown threshold behavior.

The laser-induced breakdown process takes time to build up and depends on the laser field strength. It exhibits a threshold behavior: at a given laser pulsewidth, only when the laser field strength exceeds a certain threshold can the plasma density grow to

the critical value where irreversible breakdown takes place. The threshold is customarily expressed as a laser fluence threshold (in unit of energy per unit area) as a function of pulsewidth.

2.4. Analysis of laser energy

Developing an clear overall physical model first it is important to exploit and better understand laser energy under consideration. Analyzing laser energy one can distinguish four attributes: time, spatial distribution, frequency, and amplitude. Analysis of energy phenomena is very helpful for our research and modeling.

2.4.1. Time consideration

Temporal modulation of energy field has been proven to be an effective way to improve machining quality. This Section mainly illustrates the time scale effects, continuous/discrete effects and the relativity effects of time attribute.

The temporal distributions of energy fields at different time scales, can greatly affect the interaction between energy and material. Heat Affected Zone (HAZ) for pulsed laser processing is usually smaller than that of continues wave (CW) laser processing. More striking phenomena were found when pulsed lasers progressed from ns scale (10^{-9} second) to under ps (10^{-12} second). For fs (10^{-15} second) scale laser processing changes that are even more radical happened. HAZ decreased to almost zero at different

wavelengths for the same material. These were attributed to the ultra-short laser pulse duration. One can briefly explain this as follows. When laser beam acts on a material, laser energy is first absorbed by electrons. The absorbed energy propagates through the electron subsystem, and then is transferred to the lattice. In this way laser energy is transferred to the ambient target material, Fig. 2.8. One can distinguish three characteristic time scales: te - the electron cooling time, which is in the order of 1ps; tl - the lattice heating time; and t_p - the duration of laser pulse. te and tl are proportional to their heat capacity divided by a same constant, and the heat capacity of electron is much less than that of lattice, so $te << tl$, te and tl are material dependent, t_p, time duration of laser pulse one can choose to according to the application. For different ranges of t_p, we can distinguish three cases to occur.
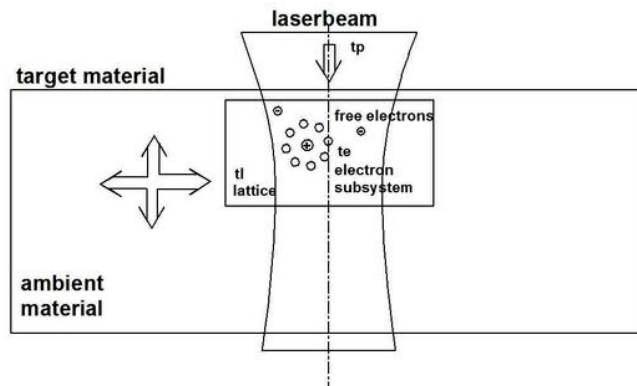
Fig. 2.8. Energy flow in laser-material interaction.

Case one: $t_p > 1$ ns $>> tl >> te$. In this case, electron absorbed laser energy has enough time to be transferred to lattice, electron and lattice can reach thermal equilibrium, the main energy loss is the heat conduction into the solid target. Material is first melted, when the beam is strong enough, evaporation occurs from liquid state. The

existence of melting layer makes precise material removal using laser pulses above nanosecond very complicated.

Case two: t_p is in fs range and $<< te << tl$, laser pulse duration t_p in this case is shorter than the electron cooling time. Electrons are heated instantly, then in about 1 ps electrons transfer their energy to their positive lattice ions. When this energy intensity is high enough, which is often true for ultra-fast pulsed lasers, those ions get energy high enough to break the bonding of lattice structure, they break off instantly without having time to transfer their energy to their neighboring lattice ions, thus direct solid-vapor transition occurs. Heat conduction into the target can be neglected, heat affected zone is greatly reduced. For melting-free ablation to be possible, two conditions must be met: ultra-short pulse duration and high enough pulse energy.

Case three: $tl >> t_p >> te$, t_p is of ps time scale. This is a transitional situation, melting layer exists in laser ablation. The temporal distributions of energy fields can be continuous or discrete, both have their advantages and disadvantages relative to their applications.

An important time duration effect is that when the energy field intensity and energy pulse duration reach certain extent, something unusual may happen. One should also be aware of the relativity of time effects. Relative to very fast events such as very short energy pulses, the event varying at normal speed can be treated as static. Below a corresponding time scale, objects usually demonstrate very abnormal properties. For example, the property of liquid can change for different time scales, below 10^{-12} second, water can not be treated as a Newtonian fluid anymore.

2.4.2. Spatial consideration

Spatial distribution of energy field is directly related to energy acting area, acting location and relative position between tool/energy sources and parts.

Laser beam can be transmitted over long distances with very small divergence, laser beam spot size can vary from 1 μm to 10 mm. Highly focused beams can act locally with high intensity, which are used for precision material removal, defocused laser beams are used for surface treating, laser forming, etc. In laser machining the relative position between laser source and parts is important. Optical fibers have been used in communication for a long time, now they are used to carry high power laser beams in manufacturing, they add valuable flexibility in laser energy transmission. It's the refractive index difference in the fiber system that makes low loss light energy transmission feasible. Spatial adjustments of energy fields are widely used to achieve various objectives. Telescope or microscope is representative example.

Why are pulse duration time and focus spot size so important in laser processing? Peak power of the laserbeam equals pulse energy divided by pulse duration time, intensity is the area average of peak laser power. When the interaction between energy field and target is not continuous, energy intensity is usually the deciding factor. Let the absolute energy in a laser pulse be 0.1 J, fixed. Let pulse lasting time be dt seconds, let pulse repetition rate be f=1 Hz, ($1/f > dt$). Let the beam focused spot size be D cm in diameter. If pulse repetition rate can vary in the range of 1-4 kHz, then average power is $f*E = 0.1\sim400$ W. One can vary pulse length and acting area, compute the peak power

and intensity. One sees clearly from Fig. 2.9, peak intensity of a 10 fs pulse with $D=1$ μm is 10^{22} W/cm^2, while the intensity of a 1 μs pulse with $D=1$ mm is 10^7 W/cm^2.
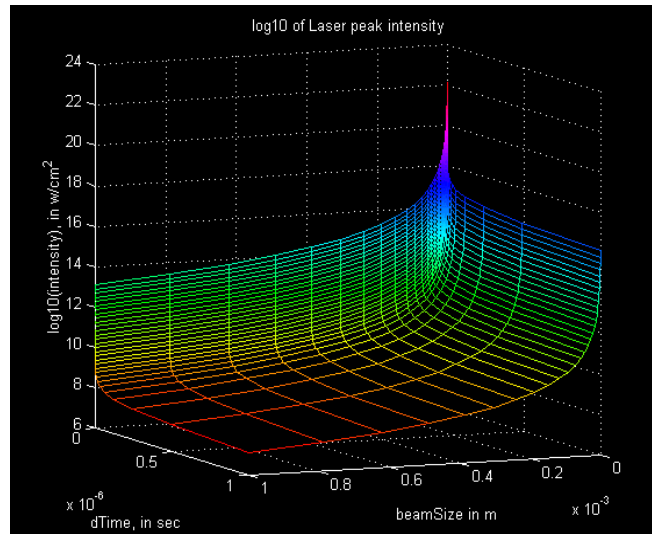
Fig. 2.9. Interrelationship between laser intensity, beam size and pulse duration, (Columbia, 2005).

2.4.3. Frequency consideration

Frequency is the characteristic frequency of energy field, which is different from Pulse Repetition Rate. Radio wave, microwave, sound wave, mechanical vibration, lattice vibration, gas molecule collision, etc., all have their respective characteristic frequencies. Thermal radiation has spectral distribution, many other energy forms or material properties are also related to frequencies. Lasers usually have very narrow spectral width, while other energy forms may have very broad and complex frequency distributions. Characteristic frequency of some energy fields is not obvious, such as gravitation field, medium field, thermal energy, stress energy, vacuum field, fluid pressure field, etc.

The characteristic frequency of energy field is important because materials may responded very differently to energy fields at different frequencies. UV laser ablation of organic polymers is very different from infrared or visible laser ablation, because their ablation mechanisms are very different. The infrared and visible laser ablation is mainly photo-thermal degradation, while UV laser ablation involves direct photo-chemical dissociation. The emissivity of copper varies with wavelength that is the main reason why lasers at different wavelengths are used to process different materials.

2.4.4. Amplitude consideration

Amplitude or magnitude is a direct measure of energy field intensity, deciding what amplitude is proper, or optimal, is a challenge. For energy field method one is interested in effective ways of amplitude modulation and the direct or indirect amplitude effects of various energy fields. In optics, optical filters, polarizers, attenuators, beam expanding and focusing systems are used to modulate laser intensity and spatial distribution. With their help, one can match the laser power output to very different applications in the same time without disturbing the laser source.

There is a certain value for the interaction between material and energy field, below which, the interaction mechanism may be of simple linear relationship, but beyond this value, the mechanism becomes nonlinear, and at extreme conditions, abnormal phenomena may happen. This indicates that some kind of transition mechanism between frequency and amplitude exists, or one can say, the effect of amplitude adjustment is to a

certain extent equivalent to the effect of frequency adjustment. An example is self-

focusing of laser light. When laser intensity is high enough, media refractive index

changes, the higher the intensity, the bigger the refractive index. Since the center of a

Gaussian laserbeam has higher intensity than the rims, when the beam passes through

optical medium, central area has bigger refractive index, this is equivalent to a new laser

source whose wavelength has been reduced to about 1/5 of the original.

Diffraction free focus spot size of the laserbeam is proportional to light

wavelength. For circular beams, the focal spot size is

$$\omega_{min} = 2.44 \cdot \frac{f \cdot \lambda}{D_L} \quad , \tag{5}$$

where, f is the lens focus length, λ is the light wavelength, D_L is the unfocused beam

diameter. This is the upper limit of laser processing precision at a specific frequency.

Theoretically, laser should be free of limitations. The ideal laser should produce

an intense, perfectly collimated beam of light that could be focused to a very small spot

size. That tiny intense spot of light could be used to cut any shape in any materials.

Unfortunately, such a well-focused high intensity laser was hard to find before 1990, and

even present ones are impractical for some laser cutting. The problem can be explained

through the following equation:

$$D_F = M^2 \frac{4}{\pi} \cdot \lambda \cdot \frac{f}{D_L}, \tag{6}$$

where, D_F is the diameter of the laser beam in the focal plane of the focusing lens; M^2 the

beam quality factor, λ is wavelength of the laser light, f is the focal length of the focusing

lens, D_L is the diameter of the collimated laser beam on the focusing lens.

Analyzing Eq. 6, if we want to have small diameter of the laser beam, D_F, then we should make small the ratio f/D_L, or make f small and D_L very large. However, one should also consider the laser's Raleigh length R_L,

$$R_L = D_F \cdot \frac{f}{D_L} , \qquad\qquad (7)$$

which is the distance above and below the focal plane where diameter of the beam has increased by $\sqrt{2}$ and the beam intensity has dropped by 2. In practice, one can cut very thick materials, which are as thick as Raleigh lengths. To cut thicker materials one would need large f/D_L ratio, so the only parameters left is the wavelength and beam quality M^2 to be adjusted to reduce the spot diameter D_F for the purpose of cutting very small objects with very small laserbeam as a cutting tool.

Ultrafast laser oscillators generate pulse energy initially at nJ (i. e., 10^{-9}J) scale, amplification to mJ level is needed in micromachining, but one knows, when pulse lasting time is very small, peak energy intensity goes up far beyond the safe operation range of normal optical amplification systems. Ultrashort pulsed lasers successfully solved this difficulty using Chirped Pulse Amplification (CPA) and Pulse Compression techniques. The energy of ultrafast lasers are highly concentrated in time domain, but their frequency distributions are much broader than normal laser systems. Light at different frequencies travel at different speeds through optical mediums. This is a bad thing at first glance, but contrary to one's intuition, this forms the base for the final solution. In free space, different components in a broad band laser pulse travel at nearly same speed. When normal optical components are in the optical path, long wavelength

light components travel through the medium faster than short wavelength components, thus pulse lasting time is stretched and energy intensity is lowered. Special optical devices such as chirped mirrors or special prism pairs are used to compensate the pulse spreading, they allow short light components pass through faster than long wavelength components, so they compress pulse lasting time.

2.4.5. Non linear optical effects

A new exciting area of physics has been opened up by the laser since the focused beam can generate huge EM fields affecting the atomic dipoles. At normal level of radiation (several W/m^2) the dipoles respond in one to one ratio with the driving force – linearly. Thus, we have linear effects of reflection, refraction, scattering, and absorption, all of which occur at this same frequency. That is, frequency of the light is not altered by the process.

However, in 1961 Peter Franken and others at the University of Michigan focused a high powered ruby laser (red light) onto a quartz crystal and generated ultra violet light mixed with the transmitted light. This was the birth of the new era of nonlinear optics. At high levels of radiation (several MW/m^2) the dipoles no longer respond linearly, but exhibit a variety of harmonic oscillations. Via such effects it is possible to mix the frequency of light waves. This was against all the principals of the super positioning of waves, known at that time light theory.

Today, many electro-optic devices depend on non-linear optical effects. Those effects include: second harmonic generation, Pockel's electro-optic effect, the Kerr electro-optic effect, third harmonic generation, general four wave mixing, stimulated Brillouin scattering, stimulated Roman scattering, optical Kerr effect, phase conjugation, self focusing, self phase modulation, and two photon absorption: ionization and emission.

2.4.5.1. Stimulated Raman scattering

When low intensity light is transmitted through a transparent material, a small fraction is converted into light at longer wavelengths with a frequency shift corresponding to optical phonon frequency in the material. This process is called Raman scattering. At higher intensities, Raman scattering becomes stimulated, and from the spontaneous scattering a new light beam can be built up. Under favorable conditions, the new beam can become more intense than the remaining original beam. The amplification is equally high in both directions: forward and backward. This may lead to situations when a large fraction of a new beam can be redirected towards the source of the original beam rather than towards the target. This could be a problem especially when fiber optic cable is used. Then a detection techniques like LIDAR could be employed to prevent damage of the system.

2.4.5.2. Stimulated Brillouin scattering

The same process takes place with the acoustical phonons. However, corresponding frequency shift is much smaller. Acoustical phonons are based on sound wave propagation and the frequency shift exists only for wave in the backward direction. At high intensities the Brillouin effect becomes a stimulated process, and the wave may get much more intense than the original beam. Almost the entire beam is reflected back towards the laser source.

2.4.5.3. Second harmonic generation

In a case of non-linear interaction the non-linear radiation itself couples the energy from one beam to another. This would not be possible in a vacuum. In the second harmonic generation the non-linear polarization wave moves through the structure at one end at one velocity and the primary refracted wave at another. For them to interact constructively the phase velocities of two waves must match. This can be done by using birefringent crystals, such as Lithium niobate ($LiNbO_3$), whose refractive index depends on the direction and polarization of propagating light. If a polarized light wave passes through a birefringent crystal at just the right angle, the phase velocities of the induced polarization wave and the second harmonic wave can be made equal. This is done in environment with maintaining the right temperature and correct angle of incidence. Example can be frequency doubling Nd:YAG lasers, where laser beam is shone into

LiNbO$_3$ crystal held in a temperature controlled enclosure at correct angle and an IR beam emerges with some 30% converted to green light beam.

2.4.5.4. Optical Kerr effect

The third order non linear polarization effect can cause a change in the refractive index of the material subject to high intensity radiation. One of the strangest effects, using this Kerr effect is optical phase conjugation. In one form, called degenerate four wave mixing two beams converge in material and set up a form of a grating within the material. The third wave couples nonlinearly with the others to form a phase conjugated wave. This principle is applied to phase conjugated mirrors, PCM. PCMs return the light to the source, any distortion between the source and the PCM is automatically compensated because of the phase reversal. Self focusing fibers are also a possibility using this effect.

2.4.6. Physical laser beam characteristics

The energy from a laser is in the form of a beam of EM radiation. Apart from power, it has the properties of wavelength, coherence, mode/diameter, and polarization. Let us briefly discussed those as follows.

2.4.6.1. Wavelength consideration

Wavelength depends on the transitions taking place by stimulated emission. If one wishes to achieve a very short pulse of light, for example of a femto second (10-15s, i.e., a beam of light about 0.3 um long) it is not possible without first making a laser with a broader waveband, as is required by the Fourier series, which defines such a short pulse waveform.

2.4.6.2. Coherence consideration

The stimulated emission phenomenon means that the radiation is generating itself and, in consequence, a continuous waveform is possible with low order mode beams. The length of the continuous wavetrain may be many meters long. This long coherence length allows some extraordinary interference effects with laser light (e.g., speckle interferometry, holography and Doppler velocity measurements).

2.4.6.3. Mode/diameter consideration

A laser cavity is an optical oscillator. When it is oscillating there will be standing EMW set up within the cavity and defined by cavity geometry. Modes are the standing oscillating EM waves, which are defined by the cavity geometry. If the cavity is of closed form, i.e., both the mirrors and sidewalls are reflective, there will be large amounts of longitudinal modes oscillating inside the cavity, a typical value can be 10^9 modes for a

He:Ne laser. People had thought closed form could improve the output power, but it

turns out that the output beam can not be well focused for closed cavities with so many

modes. So, open oscillators are used, whose lateral walls are not reflective. That is, light

incident on this part is absorbed. This can reduce the possible longitudinal modes. When

these modes oscillate, they interfere with each other, forming the transverse standing

wave pattern on any transverse intersection plane. This mechanism decides the

Transverse Electromagnetic Modes (TEM) of the laser beam, which is the wave pattern

on the output aperture plane. We use the sign TEM_{pq} to specify a TEM mode, where p is

the number of radial zero fields, q is the number of angular zero fields, q is the number of

longitudinal fields, and we usually use TEM_{pq} to specify a unambiguous TEM mode,

without the third index. Representative TEM patterns are shown Fig. 2.10. Clearly, the

mode pattern affects distribution of the output beam energy, which affects the machining

process. Then what is the diameter of a laser beam? Usually this diameter is defined as

the distance within which $1/e^2$ of the total power exists. The higher the order of the

mode, the more difficult it is to focus the beam to a fine spot, since the beam of higher

order is not from a virtual point, but from patterns as those in Fig. 2.10, Columbia, 2005.
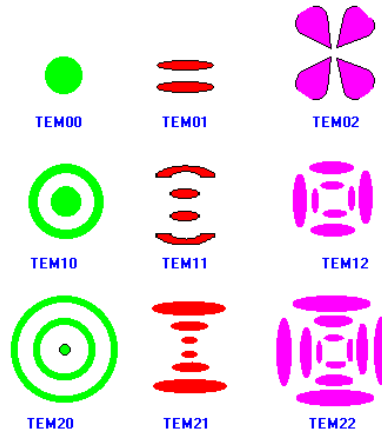
Fig. 2.10. Representative TEM modes (Columbia, 2005).

Although assuming Gaussian beam profile is reasonable if the laser outputs pulses at TEM_{00} mode, it will cause intolerable error if one assumes the laser beam propagate as perfect Gaussian beam, the error can easily go beyond 50%-100%. But it is usually very difficult to directly measure the focused beam, especially for cases when the focused spot size is below 10 microns. One solution is to combine experimental measurement with optical calculations to overcome this difficulty.

2.4.6.4. Polarization consideration

When electric vectors of traveling EMW are lineup thus the beam is polarized. Many modern laser systems do not have a fold in a cavity, will produces randomly polarized beams. In this case the plane of polarization of the beam changes with time and machining quality may reflect it. To avoid this it is necessary to introduce into the cavity a fold mirror of some form. Outside the cavity, such a fold would make no noticeable

difference, but inside the cavity it is a different matter since the cavity is an amplifier and hence the least loss route is the one being amplified in preference to the other – in fact almost to its total exclusion. Polarized beams have a directional effect in certain process for example cutting due to the reflectivity effects.

2.4.7. Focal spot size consideration

Focal spot size determines the maximum energy density that can be achieved when the laser beam power is set, so the focal spot size is very important for material processing. In order to adjust the beam, to guide it to the workpiece and shape it, there are many devices. These devices will be discussed together with the basic theory of their design in Section . In nearly all of them the simple laws of geometric optics are sufficient to understand how they work. However, to calculate the precise spot size and depth of focus one needs to refer to Gaussian optics and diffraction theory.

2.4.7.1. Diffraction limited spot size

A beam of finite diameter is focused by a lens onto a plane as shown in Fig. 2.11. When a beam of finite diameter D is focused by a lens onto a plane, the individual parts of the beam striking the lens can be imaged to be point radiators of new wavefront. The light rays passing through a lens will converge on the focal plane and interfere with each other, thus constructive and destructive superposition will take place and light energy is

distributed as shown in Fig. 2.11. The central maximum contains about 86% of the total power. The focusing diameter is measured between the points where the intensity has fallen to $1/e^2$ of the central peak value.
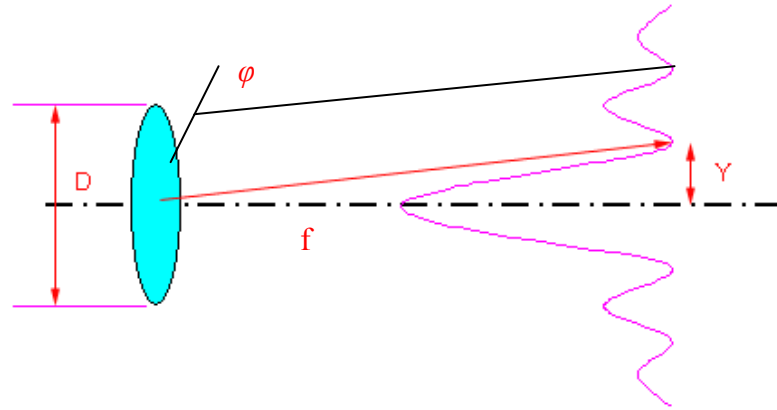
Fig. 2.11. Focus pattern of parallel light (Columbia, 2005).

For a circular beam with a plane wavefront, the diffraction limited beam diameter, which is the smallest focal diameter, is given by Eq. 5, and the smallest possible focal spot size in this case is (Columbia, 2005)

$$\omega_0 = 2.44 \frac{f \cdot \lambda}{D}(2p + l + 1) \quad , \tag{8}$$

where f is the lens focal length, D is the beam diameter at the lens, λ is wavelength of the light, p, l are the mode numbers. From Eq. 8, we can clearly see the influence of modes on the focal property.

There are other factors that affect focal spot size, such as spherical aberration and thermal lens effects. Most lenses are made with a spherical shape, but they cannot be of perfect shape because there exists spherical aberration. Lenses in laser systems transmit or reflect high power laser radiation. However, laser power variations can cause shape

95

changes of the lenses, so the focal point will change when the radiation power changes, thus affecting the focal spot size.

According to Lasag, manufacturer of Nd-YAG laser system, the spot diameter of laser beam focused onto the workpiece, Fig. 2.1, can be approximated as (Lasag, 1997)

$$2\omega \approx \frac{2 \cdot f \cdot \theta}{M} \quad , \tag{9}$$

where f is the focal length of the lens, θ is the divergence of the laser beam before the expander, and M is the expansion factor of the beam expander.

For laser micromachining small focal spot size is preferable. Based on the previous discussion one can learn that the focal diameter is related to beam mode, wavelength, beam diameter, and focus.

2.4.7.2. Depth of focus consideration

The laser light is first converged at the lens focal plane, and then diverged to a wider beam diameter again. The depth of focus (DOF) is the distance over which the focused beam has about the same intensity. This is also called beam waist, Fig. 2.12. It is defined as the distance over which the focal spot size changes $\pm 5\%$. The equation for DOF is (Lasag, 1997)

$$DOF = \frac{8 \cdot \lambda}{\pi} \cdot \left[\frac{f}{D}\right]^2 = 2.44 \cdot \lambda \cdot \left[\frac{f}{D}\right]^2 \quad , \tag{10}$$

where λ is the wavelength, f is the lens focal length, and D is the unfocussed beam diameter. Usually longer depth of focus is preferred, because equal energy density along the beam is preferred when using the laser to process materials.

Position of the focal plane is known to have an effect on final shape of the hole as well as degree of penetration. As the laser focusing spot moves up and down, the laser material interaction area Ar_F varies too, according to expression (Semak and Matsunawa, 1997)

$$Ar_F = n\omega_0 \left[1 + \left(\frac{z - z_\omega}{2 \cdot \omega_0 f / D} \right)^2 \right]^{\frac{1}{2}} , \tag{11}$$

where ω is the laser beam radius at the beam waist equals to ω_0 which is the minimum radius of the laser beam. In our analytical and numerical calculations, Eq. 11 was proved to be the most accurate and is used in this Dissertation.

While calculating the drilled hole profiles defocusing of the laser beam effects should be taken into account. As a rule, the divergence of the laser beam would increase the radial heat flux on the hole walls, by decreasing energy at the entrance of laserbeam of the evolving hole. However, multiple reflections inside the hole will accumulate the energy at the bottom of the drilled hole, which is described in detail later.
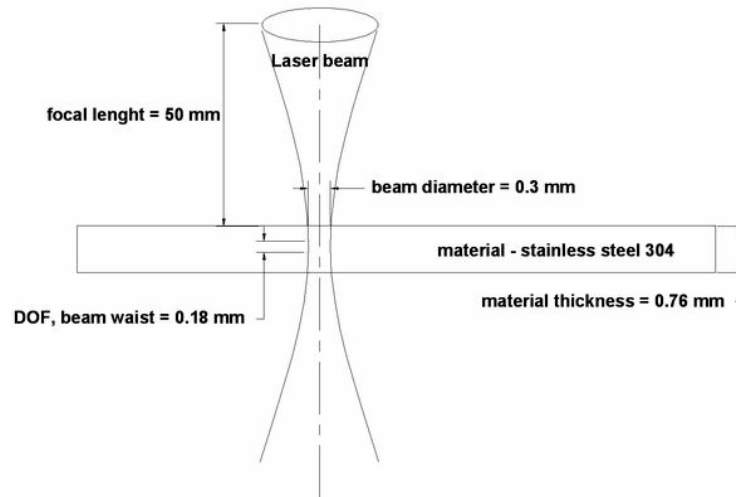
Fig. 2.12. Laserbeam focusing onto the sample.

2.4.7.3. Quality of laser beam

The concept of M^2 is important to describe actual propagation of laser beams. M^2 is a beam quality that measures the difference between the actual beam and the Gaussian beam. In order to find out the M^2 of a laser system, we need first measure the spot size along the laser optical axis.

Edge method is used if beam profilometer is not available. Edge method uses a knife-edge to block the laser beam, a powermeter measures the power after the blocking of the knife-edge, by recording the 86% and 14% location of the full power. Subtracting the two values one gets the beam spot size at that point. This method measures the $1/e^2$ radius of the laser beam. Because the laser spot size is rather small, the relative measurement error for such dimension using edge method can be large. Usually a beam expander, or a collimator, is used to expand and "parallel" the beam, the spot size out of

the collimator is several millimeters. For such dimension, knife-edge method can easily

reduce the relative measurement error to less than 2%. As illustrated by Fig. 2.13, six

measurements at three different distances from the collimator are taken, Z_n, D_n, where

n=1, 2, 3. The distance from any chosen point along the optical axis and the spot size at

that location are recorded.
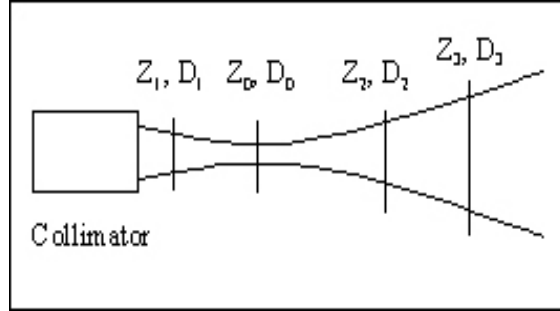
Fig. 2.13. Measurement of beam properties.

The beam size at location Z_n, satisfies the following equation:

$$D_n^2 = D_0^2 + \left[\frac{4M^2\lambda}{\pi}\right]^2\left[\frac{Z_n - Z_0}{D_0}\right]^2, n = 1,2,3 \quad,$$ (12)

where, D_n is the beam size at location Z_n, D_0 is the beam waist, Z_0 is the beam waist

location, λ is the wavelength, M^2 is the beam quality parameter which is unknown. In

this relation, λ is known, D_n and Z_n can be measured, M^2, D_0 and Z_0 are unknowns.

Taking the measured data into Eq. 6, we get three highly nonlinear equations for three

unknowns. One can solve these equations using, e.g., MathCAD. Knowing M^2, one can

calculate the beam divergence, focused spot size, and depth of focus (DOF) as follows:

$$D_{min} = \frac{4 \cdot f M^2 \lambda}{\pi \cdot D_L} \quad , \tag{13}$$

$$\theta_{Gaussian} = \left[\frac{Af}{\pi D_0} \right] \quad , \tag{14}$$

$$\theta_{act} = \frac{M^2 \lambda}{\pi \cdot D_0}, \qquad \theta_{inf\ inity} = \left[\frac{D_3 - D_2}{2(Z_3 - Z_2)} \right] \quad , \tag{15}$$

$$DOF = \pm 0.08 \cdot \lambda \cdot \left[\frac{D_{min}}{M^2 \cdot \lambda} \right]^2 \quad , \tag{16}$$

where D_L is the laser beam size when it propagates to the front side of the focus objective

lens, f is the focus length, D_{min} is the minimum beam diameter that can be achieved. θ_{act} is

the real beam divergence. It can be verified that the equations are solved with an error

less than 10^{-10}. In practical cases, one should first measure the pulse energy or average

power of the laser beam, then measure the beam spot size along the optical axis. Using

Eqs 13 and 14 one can calculate the beam waist and beam waist location, and one can

find M^2 of the beam, then can calculate the other indexes in Eq. 16. Knowing DOF one

can calculate M^2 value as

$$M^2 = \left[0.08 \frac{(D_{min})^2}{DOF \cdot \lambda} \right]^{1/2} \quad , \tag{17}$$

where D_{min} is the minimum beam diameter that can be achieved. Knowing diameter at

any location, one can determine the intensity of the laser beam at that location.

2.4.7.4. Spherical aberration

There are two reasons why a lens will not focus to a theoretical point. First is the diffraction limited problem discussed in Section 2.4.7.1, and the second is that lens is not of a perfect shape. Most lenses are made with a spherical shaped since this can be accurately manufacture without too much cost and alignment of the beam is not so critical as with a perfect aspheric shape. The net result is that the outer ray entering the lens is brought to a shorter axial focal point than the rays nearer the center of the lens. This leaves a blur in the focal point location. The plane of best geometric focus is a little short of the plane wavefront (paraxial point). The size of the minimum spot, d_{min} is given by

$$d_{min} = K(n,q,p)\left(\frac{D_L}{f}\right)^3 S_a = 2\Theta_a S_2 \quad , \tag{18}$$

where, Θ_a is angular fault (half angle), S_2 is distance from lens, D_L is diameter of top hat beam mode on lens, f is the focal length of the lens, $K(n,q,p)$ is the factor dependent on the refractive index n, q is the lens shape, and p is lens position,

$$K(n,q,p) = \frac{1}{128n(n-1)}\left[\frac{n+2}{n-1}q^2 + 4(n+1)pq + (3n+2)(n-1)p^2 + \frac{n^3}{n-1}\right] \quad , \tag{19}$$

where q is the lens shape factor $= (r_2+r_1)/(r_2-r_1)$, r_1, r_2 are the radii of curvature of the two faces of the lens and p is position factor $= 1 - 2f/S2$.

2.4.7.5. Thermal lensing

In optical elements, which transmit or reflect high power radiation there will be some heating of the component, which will alter its refractive index and shape (Bronski, 2003). As the power, or the absorption, changes so will the focal point and spot size. The two main elements usually concern are the output coupler and the focusing lens. The beam guidance mirrors could also be of concerned if adequate cooling is not supplied (water cooling or dry air cooling).

Thermal lensing is mainly caused by the rise in temperature increasing the refractive index (dn/dT) and thus shortening the focal length. A lesser effect is the thermal distortion (dl/dT). The focal length shift for thin lenses can be calculated to be

$$\Delta F = \frac{2A\ P\ F^2}{\pi\ k\ D_L^2}\frac{dn}{dT} \quad ,$$ (20)

where, A is the optic absorbtance, k is the thermal conductivity, T is the temperature, P is incident power of the laser beam.

Uneven heating causes further complications. The approximate Gaussian power distribution of the incident beam heats the middle more than the edge causing a radial temperature gradient (usually the edge of the lens is being cooled). A typical temperature difference would be 14 degrees for a 1,500 W beam of 38 mm diameter passing through an optic with 0.2% absorbtance.

At this time let us mention another problem. During laser micromachining, from the fact that the absorption is on the surface of the lens, there is also going to be a temperature gradient in the depth direction. The thicker the optic the more bowed will be

the internal isotherms. Such an aberrations will affect the M^2 value, transverse mode, and on the spatial distribution of the laser beam, which will be discussed and verified experimentally in Section 4.2.4.

2.5. Theoretical consideration of laser absorption

This chapter describes different effects of the laser beam physical and optical properties on the material's absorption of the electromagnetic wave.

The absorption of the laser energy takes place through photon interaction with bound and free electrons in the material structure, which raises them to the higher energy levels. Energy conversion takes place through various collision processes involving electrons, lattice phonons, ionized impurities and defect structures.

If the surface being machined reflects too much light energy, the absorbed energy is decreased, the operation efficiency is lowered, and the reflected light may do harm to the optical systems. Reflection and absorption of laser beams is closely related to laser micromachining. The value of absorption and reflection is related by

Reflectivity = 1- Absorptivity - Transmisivity (for transparent materials).

In metals, the radiation is predominantly absorbed by free electrons in an "electron gas". These free electrons are free to oscillate and reradiate without disturbing the solid atomic structure. As a EM wave-front arrives at a surface of the target then all the free electrons in the surface vibrate in phase generating an electric filed 180° out of phase with the incoming beam creating "electron gas". This "electron gas" within the

metal structure means that the radiation is unable to penetrate metals to any significant depth, only one to two atomic diameters (or free paths), thus metals are opaque and they appear shiny. According to Fig. 2.14 reflectivity decreases as wavelength becomes shorter, while absorption increases when photon energy increases.
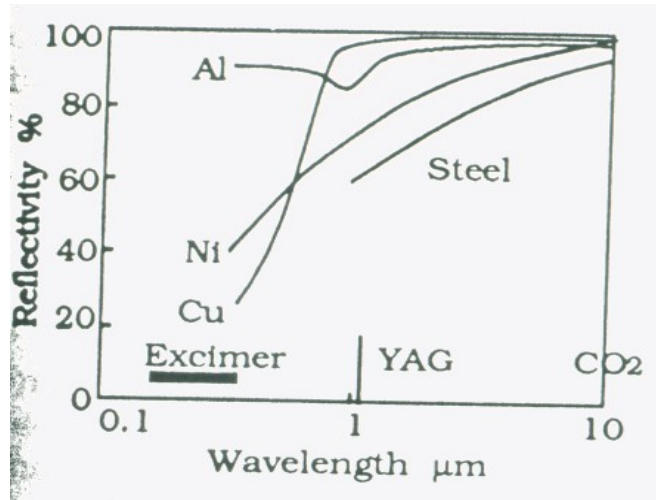
Fig. 2.14. Reflectivity as a function of wavelength for different metals (Han, 2005).
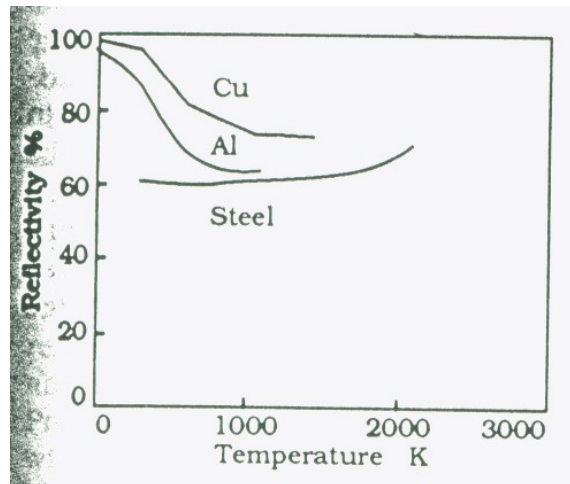
Fig. 2.15. Reflectivity as a function of temperature for 1.064 μm radiation (Han, 2005).

If sufficient energy is absorbed then the vibration becomes so intense that the molecular bonding is stretched so far that it is no longer capable of exhibiting mechanical strength and the material is said to have melted. On further heating the bonding is further loosened due to the strong molecular vibrations and the material is said to have evaporated. The vapor is still capable of absorbing the radiation, but only slightly since it will only have bound electrons. The exception occurs if the gas is sufficiently hot so that electrons are shaken free and the gas is then said to be a plasma.

2.5.1. Heat diffusion and pulse length considerations

For absorbing materials, such as metals and semiconductors, there is a large density of free electrons and valence electrons with an ionization potential less than the photon energy. For long pulses, linear absorption dominates, and the material is heated through Joule heating (Inverse Bremsstrahlung effect) (Liu et al., 1997). When melting or vaporization temperature is reached, the material is considered broken down and damaged. The breakdown is also accompanied by acoustic waves and optical radiation. The rate of heating is determined by the rate of laser energy absorption and the rate of energy loss from the focus, mainly through thermal conduction away from the focus. The rate of laser energy absorption is approximately constant before the breakdown. The energy is deposited in a surface layer whose thickness is given by the absorption or penetration skin depth (Anisimov and Khokhlov, 1995)

$$l_s = \frac{1}{\mu} \quad , \tag{21}$$

where, μ is the absorption coefficient.

Another characteristic length is the heat diffusion length during the laser pulse, which gives the heat penetration depth due to thermal conduction. This diffusion length is given by

$$l_d = \sqrt{\kappa \cdot \tau_l} \qquad (22)$$

where κ is the thermal diffusivity and τ_l is the laser pulse width. For long pulses, $l_d > l_s$ and the volume of the material heated by the laser pulse, hence the temperature, is determined by the heat diffusion length during the laser pulse. Therefore, for long pulses, the fluence breakdown threshold varies with laser pulse width as $F_{th} \propto \sqrt{\tau_l}$. However, as the laser pulse width decreases to a value τ_e such that $l_d = \sqrt{\kappa \cdot \tau_e} < l_s$, the skin depth determines the heated volume during the laser pulse, not the heat penetration depth (Liu, 1997). The breakdown threshold becomes independent of the pulse width (Anisimov and Khokhlov, 1995). The above argument also applies to transparent materials once significant absorption due to plasma generation occurs, and it has been used to explain the observed $\sqrt{\tau_l}$ scaling of the breakdown threshold.

For long pulses where the heat diffusion length is larger than the skin depth, a large volume is heated and melted, the ablation and material removal is accomplished through melt expulsion driven by the vapor pressure and the recoil of the light pressure. This is a very unstable process, since the fluid dynamics of the fluid phase and the driving vapor conditions are quite complicated. In hole drilling and cutting applications, the resolidification of the melt after the ablation can lead to very irregular shapes in the

106

holes and cuts. The localized energy heats the material very quickly past the liquid phase to the vapor phase with high kinetic energy (way above the vaporization temperature). The material removal is by direct vaporization away from the surface (into vacuum or air). Most of this is accomplished after the laser pulse irradiation is finished. The material is still heated by the heat diffusion over a longer time scale. However, the resulting melt layer thickness will be small because most of the heated material reaches vaporization temperature, and there is rapid cooling due to the steep temperature gradient. The heating of the material by heat diffusion is further reduced by the fact that a large amount of the absorbed laser energy is carried away by the direct vaporization. Because little liquid is involved, ablation and material removal become highly precise, in contrast to the long pulse case.

There is a great diversity in absorptivity and reflectance data found in the literature. Indeed these values are bulk properties, but in practice metal surfaces usually show lower reflectance than the bulk, due to contamination (absorbents, oxide layers) or macroscopic defects (flakes, pits craters, etc). Optical behavior is almost completely dominated by surface effects. Surface defects and impurities have a great importance in the laser-material coupling because they decrease the laser intensity threshold needed to initiate vaporization of the surface. The initiation mechanism is probably associated with the presence of surface defects such as flakes, which are thermally uncoupled from the bulk material. Before a flake vaporizes an electron density can be as high as 10^{13} created by thermionic emission. More details on this subject are in Section 2.6.

2.5.2. Optical functions

The standard optical functions are the complex refractive index

$$n' = n + ik = \varepsilon / 2 \quad .$$

(23)

where, n and k are the refractive index and the extinction coefficient, respectively, and ε denotes the permittivity. The surface absorptivity, A is

$$A = \frac{4\pi k}{\lambda} \quad .$$

(24)

The fundamental response of a solid to an EM field is described by

$$D = \varepsilon E = E + 4\pi P \quad .$$

(25)

where, D, E, and P are the microscopic displacement, electric field, and the dipole moment per unit volume, respectively.

Reflectivity R, for normal angles of incidence from dielectric or metal surface may be calculated from the real part of refractive index, n, and the extinction coefficient, k

$$R = \frac{(1-n)^2 + k^2}{(1+n)^2 + k^2} \quad .$$

(26)

For opaque materials such as a metal surface absorptivity, A, can be computed using the following formula

$$A = 1 - R = \frac{4n}{(1+n)^2 + k^2}$$

(27)

Some values of theses constants are given in Table 1.

The variation of amplitude, A_m, with depth, z, is given by Beer-Lambert's Law for a wavelength, λ, in vacuum

$$A_m = A_{m0} \exp\left(\frac{2\pi \cdot \mu \cdot z}{\lambda}\right) \quad . \tag{28}$$

Simple analytical representation for ε, such as the Drude expression for free carriers (EMIS, 1988)

$$\varepsilon = 1 - \frac{(35.1\,eV)^2}{E(E + i8.2\,eV)} \quad . \tag{29}$$

or the Sellmeier expression for dispersion in regions of transparency, permit efficient calculation of optical functions to supplement tabulated values.

Energy E, to wavelength, λ, conversion is done according to

$$E(\lambda) = \frac{h\,c}{n} = 1.2395086 \quad 1eV(1\,micron) \quad . \tag{30}$$

where, $\lambda=550$ nm, $h=6.626176x10^{-34}$ J s, $c=2.99792458x10^{10}$ cm/s, $1\,eV=1.6021892x10^{-19}$ J, and ordinary refractive index of dry air, $n=1.000277$ at 15 C, 760 mmHg, (CRC Handbook, 1983), so for Nd:YAG laser beam $E(\lambda=1.064)=1.165\,eV$. Based on this value, n and k, the real part of refractive index and the extinction coefficient for single crystal silicon are as follows: $n=3.55$, and $k=8.9x10^{-5}$, and surface absorptivity, $A=112/cm$.

Intensity is proportional to the square of amplitude and hence the variation of intensity with depth is given by:

$$I = I_0 \exp\left(-\frac{4\pi \cdot \mu \cdot z}{\lambda}\right) \quad . \tag{31}$$

Please note that the optical properties are functions of radiation wavelength and vary with temperature.

Table 1. Complex refractive index and reflection coefficient for some material's optical properties (1.06 μm radiation).

Materials	k	n	R
Al	8.50	1.75	0.91
Cu	6.93	0.15	0.99
Fe	4.44	3.81	0.64
Mo	3.55	3.83	0.57
Ni	5.26	2.62	0.74
Pb	5.40	1.41	0.84
Ti	4.00	3.80	0.63
W	3.52	3.04	0.58
Zn	3.48	2.88	0.58
Sn	1.60	4.70	0.46
Glass	0	1.50	0.04

2.5.3. Effect of wavelength

The shorter the wavelength, the more energetic the photons are. Photons with shorter wavelengths are easier to be absorbed by the materials than photons with longer wavelengths. Thus reflectivity, R, normally decreases as wavelength becomes shorter, while absorption increases when photon energy increases, Fig. 2.14. As the sample thickness approaches 1 mm, the ablation rate becomes strongly wavelength dependent, Fig. 2.16c. At similar laser fluence, UV laser beam provides almost an order of magnitude faster drilling than an IR beam.
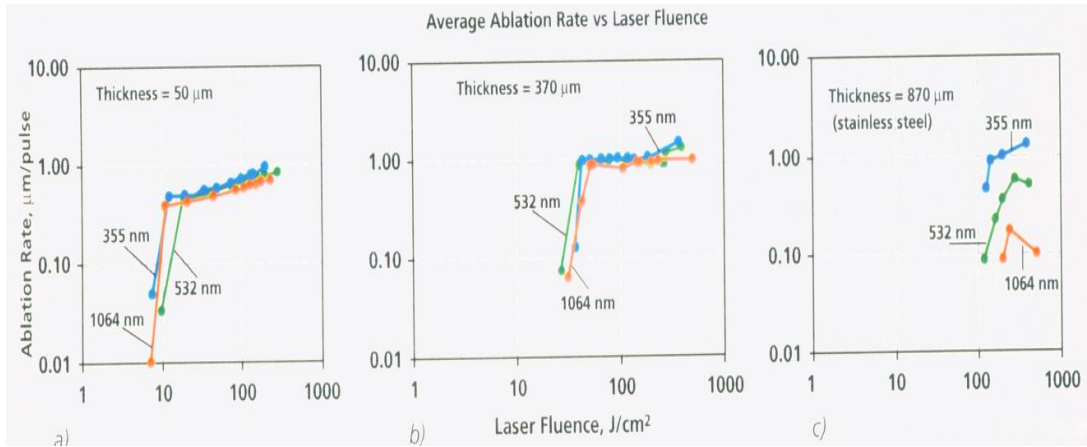
Fig. 2.16. Ablation rate as a function of sample thickness at different wavelengths.

This trend is summarized in Fig. 2.17. The characteristic sample thickness at which average ablation rate starts decreasing, is greater for shorten wavelength. Apparently, in the thicker samples, beams of different wavelength are attenuated to different degree inside the hole. Although ablation rates at the surface are similar for all three wavelengths, Fig. 2.16a. Attenuation of the beam towards the exit of the hole and subsequent reduction in material removal in thick samples lead to reduction of average ablation rate, Fig. 2.17.
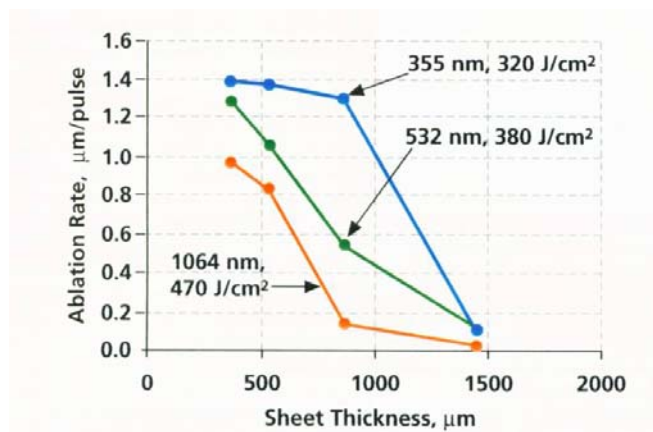
Fig. 2.17. Average ablation rate vs laser fluence.

111

One possible mechanism responsible for such drastic wavelength dependence is inverse Bremsstrahlung effect. Simple estimate of plasma absorption using formula

$$\beta = 1.37 \cdot \lambda^3 \cdot n_e^2 \cdot T_e^{-1/2} \quad . \tag{32}$$

Assuming plasma density $n_e = 1.4 \cdot 10^{19} \ cm^{-3}$ and plasma temperature $T_e = 20000 \ K$ leads to extinction lengths: L(1064) = 0.5 mm at 1064 nm, L(535) = 4 mm at 532 nm, and L(355)=13 mm at 355 nm wavelength. Additionally one has to account for an avalanche-like increase of n_e, T_e for longer wavelength due to radiation heating of plasma. More on plasma absorption can be found in Section 2.6.1.

2.5.4. Effect of temperature

As the temperature of the structure rises, there is an increase in the phonon population causing more phonon-electron energy exchanges. Electrons are more likely to interact with the structure rather than with the incident photons. Thus a fall in the reflectivity and an increase in the absorptivity with a rise in temperature should be observed, Fig. 2.18. Detail considerations on the relationship between absorption and temperature is described in Section 2.6.1.
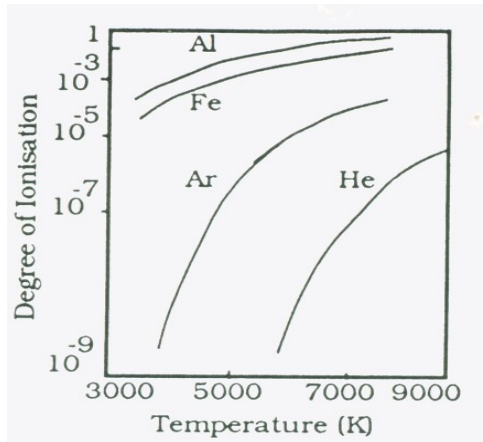
Fig. 2.18. Ionization vs. temperature.

2.5.5. Effect of surface films

The reflectivity is essentially a surface phenomenon so surface films may have a large effect. For interference coupling the film must be around *[(2n+1)/4]λ* to have any effect, where *n* is any integer. The absorption variation for CO_2 radiation by a surface oxide film is shown in Fig. 2.19 and Fig. 2.20. One form of these surface films may be plasma provided that plasma is in thermal contact with the surface.
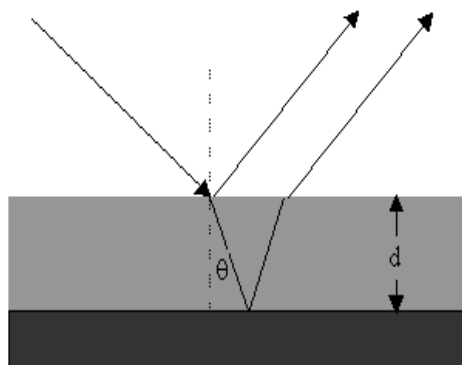
Fig. 2.19. A surface film acting as an interface coupling, "anti-reflection" coating.

113
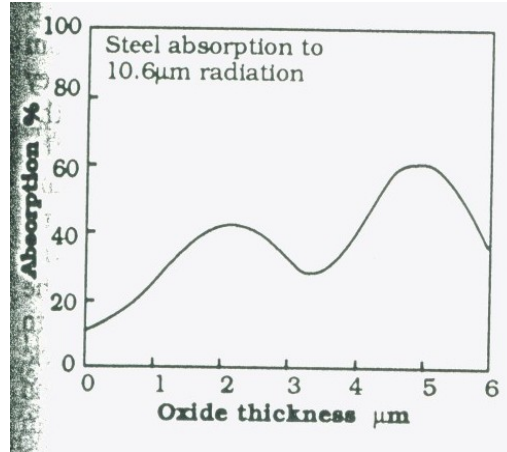
Fig. 2.20. Absorption as a function of thickness of an oxide film on steel for 10.64 μm radiation.

2.5.6. Effect of angle of incidence

A full theoretical analysis of the reflectivity allowing for angle of incidence shows a variation both with angle and with the plane of the electric vector, the plane of polarization. If the plane of polarization is in the plane of incidence the ray is said to be a "p" ray (parallel); if the ray has its plane of polarization at right angles to the plane of incidence it is said to be an "s" ray (senkrecht = perpendicular) (Steen, 2003). The reflectivities for these two rays reflected from perfectly flat surface are given by

$$R_p = \frac{\left(n - \dfrac{1}{\cos\varphi}\right)^2 + \kappa^2}{\left(n + \dfrac{1}{\cos\varphi}\right)^2 + \kappa^2} \quad , \tag{33}$$

$$R_s = \frac{\left(n - \cos\varphi\right)^2 + \kappa^2}{\left(n + \cos\varphi\right)^2 + \kappa^2} \quad , \tag{34}$$

where φ is angle of incidence and other parameters are as previously defined.

114

A variation of the reflectivity with angle of incidence is shown in Fig. 2.21. At certain angles the surface electrons may be constrained from vibrating. Otherwise electrons would have to leave the surface and they would be unable to do that (collective vibrational modes) without disturbing the matrix, i.e., absorbing the photon. Thus, if the electric vector is in the plane of incidence, the vibration of the electron is inclined to interfere with the surface and absorption is thus high. While if the plane is at right angles to the plane of incidence then the vibration can proceed without reference to the surface and reflection is preferred. There is particular angle – the "Brewster" angle – at which the angle of reflection is at right angles to the angle of refraction. When this occurs it is impossible for the electric vector in the plane of incidence to be reflected since there is no component at right angles to itself. Thus the reflected ray will have an electric vector only in the plane at right angles to the plane of incidence. At this angle the angle of refraction = 90°, which is the angle of incidence and hence by Snell's law the refractive index, n=tan(Brewster angle. Any beam, which has only, or principally, one plane for the electric vector is called a "polarized" beam.
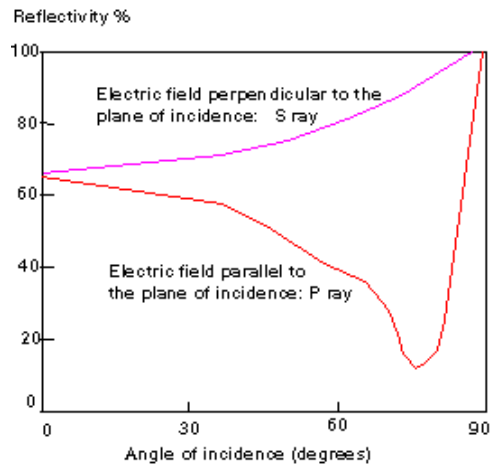
Fig. 2.21. Reflectivity of steel to polarized 1.064 μm radiation (Columbia, 2005)).

2.5.7. Effect of materials and surface roughness

Roughness has a large effect on absorptivity due to the multiple reflections in the undulations. There may also be some "stimulated absorption" due to beam interference with sideways reflected beams. Provided that roughness is less than the beam wavelength the radiation will not suffer these events and hence will perceive the surface as flat. Though the reflected phase front formed from the Huygens wavelets will no longer be the same as the incident beam and will spread in all directions as a diffuse reflection. It is interesting to note that it should not be possible to see the point of incidence of a red He:Ne beam on a mirror surface, if the mirror is perfect.

2.5.8. Effect of high aspect ratio drilling

Fig. 2.22 illustrates how the high aspect ratio of a hole for the thicker materials becomes a limiting factor. This relationship is shown comparing the average ablation rate in 1.46 mm thick stainless steel sheet at different wavelengths and laser spot diameters. The laser fluence at the surface was maintained constant. For each given wavelength higher aspect ratio led to a significant in lower ablation rate.
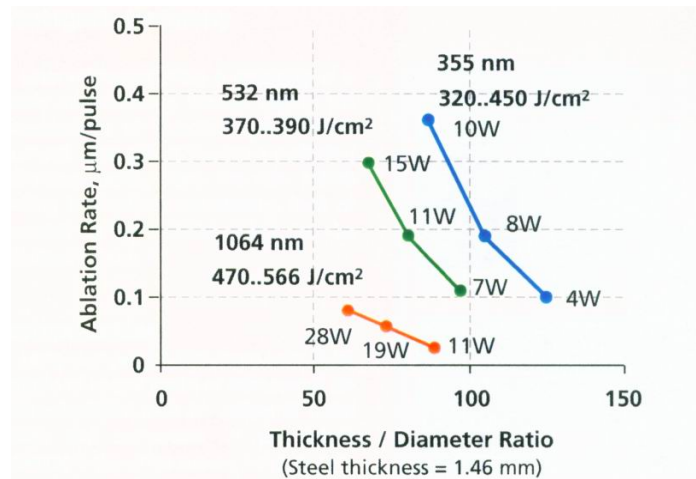
Fig. 2.22. Average ablation rate in stainless steel sample as a function of aspect ratio.

Besides evident aspect-ratio dependence, even more pronounced is the dependence of ablation rate on wavelength. A shorter wavelength allows the drilling of higher aspect ratio holes at a higher speed for the sample thickness exceeding 1 mm

2.5.9. Effect of polarization

Any beam, which has only, or principally, one plane for the electric vector is called a "polarized" beam. Most lasers produced beams, which are polarized due to the

117

nature of the amplifying process within the cavity, which will favor one plane. Any plane will be favored in random manner unless the cavity has folding mirrors, in which case the electric vector which is at right angles to the plane of incidence on the folded mirrors will be favored because that is the one suffering the least loss.

Light is a transverse EMW, normally the direction of the electric field of light beam is randomly distributed, no direction is dominant, we say such light is not polarized. If the light electric field is not evenly distributed, some directions dominate, we say the light is polarized. The plane of the polarized light electric field is called the plane of polarization.

Present laser systems generate polarized light. It is realized by using fold mirrors inside the cavity. The fold mirrors select the direction of the resonant light, since only light with the preferred direction can build up in the cavity, the output laser is highly polarized. If the light is not properly polarized, machining quality may change with time because laser polarization plane changes with time and the plane direction affects the machining quality.

Polarized beams have a directional effect in machining due to reflectivity effect, hence in material machining, lasers are usually designed first to generate highly polarized beam, then they are adjusted to the required direction changes using depolarizers.

The beam out of a depolarizer is a "circularly polarized" beam. To summarize, one can say, to avoid the negative effects of polarization, one lets the laser generate highly polarized light first, then use depolarizers to change the beam into the desired form.

2.6. Plasma consideration

The role of plasma during laser interaction with materials has been debated for over two decades. Some researchers reported a considerable loss of transmitted laser energy through the plasma onto the target, whereas others reported enhanced coupling due to re-radiation from plasma. Some report that plasma can alter the laser beam propagation path and affect the energy distribution transmitted to the surface or bulk of the target. Definitely plasma is one of the most important aspects of laser interaction with materials and still is not fully understood.

Plasma is a fourth state of matter well known to physicists, other three states of matter being solid, liquid, and gas. Plasma is a loosely bound matter of highly charged atoms and electrons containing so much energy that the forces that hold the material together are obliterated. Lasers can produce this state of matter because they pack so many particles of light called photons during small time interval that when they interact with the atoms in the surface of the material, they strip as many as 15 electrons off the atom.

According to Duley (1999), in laser micromachining a plume is usually produced as the result of ejection of material from the micromachined area. The vaporized material is ejected and moves through the incident beam where it may be heated to temperatures in excess of the vaporization temperature. This heating arises, in large part, through collisions with energetic electrons. Under certain conditions, the overall effect is to produce a rapid increase in the level of ionization within the plume with the formation of the plasma.

The optical coupling of a metal is dominated by the conduction electrons. Only electrons in states close to the Fermi level, referred to as 'free electrons', contribute to the optical properties. There are two main mechanisms for electron generation. The first, called multiphoton ionization, involves simultaneous absorption by an electron of a sufficient number of photons to be ejected from the conduction band. The second mechanism is the absorption of laser radiation by free electrons: the thermionic process.

The multiphoton absorption process is more effective at low laser wavelengths because photons then have a larger energy (few eV) and ionization can be achieved with the simultaneous absorption of only few photons. Thus the multiphoton absorption process is important only at laser wavelengths $< 1\ \mu m$. For CO_2, laser irradiation (10.6 μm), the simultaneous absorption of a few tens of photons (0.1 eV) is needed to eject an electron from a metallic conduction band.

Plasma formation requires vaporization of the material surface as a first step. When laser radiation is absorbed at the surface of the target, light energy is transformed into heat and the surface temperature increases. Simultaneously heat conduction takes place into the interior of the target, thus increasing the thickness of the heated layer. While it is understood that evaporation usually occurs from a liquid, the solid-liquid transition is generally neglected, since the latent heat of fusion is a small fraction of the latent heat of vaporization of material at the evaporation temperature.

Plasma is formed for higher laser intensity. If the plasma density is low, laser energy can still be transmitted to the material without obvious absorption, if the plasma density is high enough, absorption by the plasma should be considered. This absorption

is related to the electron density in the plasma. When the plasma density reaches certain value, high absorption and reflection happens. Then laser energy cannot be effectively transmitted to the target material, thus laser and material interaction is decoupled. When the plasma expands, dissipates, and rarefies, then laser energy can reach the surface again, another cycle of plasma generation, decoupling, and dissipation happens. In this process, shock wave is generated, so the highest laser intensity is optimum for laser machining. Laser machining works in the range below strong plasma generation. Laser shock waves can be used for material processing, it is called Laser Shock Processing, which is used to improve surface hardness and stress distribution.

The evolution of the plasma follows three major paths depending on irradiance, spot size, and ambient gas conditions. One can distinguish the three major types of laser absorption waves commonly known as

(i) laser supported combustion (LSC) wave,

(ii) laser supported detonation (LSD) wave,

(iii) laser supported radiation (LSR) wave (for $I > 1$ GW cm^{-2}).

Velocity, pressure, and the effect of radial expansion on the subsequent plasma evolution are the primary characteristics of a wave. LSC waves occur at low irradiance (10^4-10^7 W/cm^{-2}), the precursor shock is separated from the absorption plasma - laser absorption zone. The front edge of the plasma (laser absorption zone) propagates into the shocked gas (10^5 cm/s). Freshly shocked gas ingested by the LSC wave rapidly heats up. During expansion maintains the pressure that drives the shock wave. This process propagates layer by layer. The LSC wave velocity is lower than that of the shock wave;

this permits the laser energy to be channeled into heating a small mass to very high temperature rather than a large mass to low temperature (Root, 1989). The plasma stays confined to the vapor and surrounding ambient gas.

LSD waves occur at an intermediate irradiance (10^7-10^9 W/cm^2). The precursor shock is sufficiently strong for the shocked gas to be hot enough to begin absorbing the laser radiation without requiring additional heating by energy transport from the plasma.

The laser absorption zone follows directly behind the shock wave and moves at the same velocity (10^5-10^6 cm/s). The LSD wave is typically observed to form ahead of a target before it has even started to evaporate. Breakdown plasmas tend to be strongly absorbing. After an LSD wave is ignited, it begins to travel away from the surface along the laser beam and eventually degenerates into a plasma column (Root, 1989), a reheating front moves towards the surface. The plasma kinetics wave propagation for LSC, schematically illustrated in the upper part of Fig. 2.23, and in the lower part of the picture for LSD wave propagation.
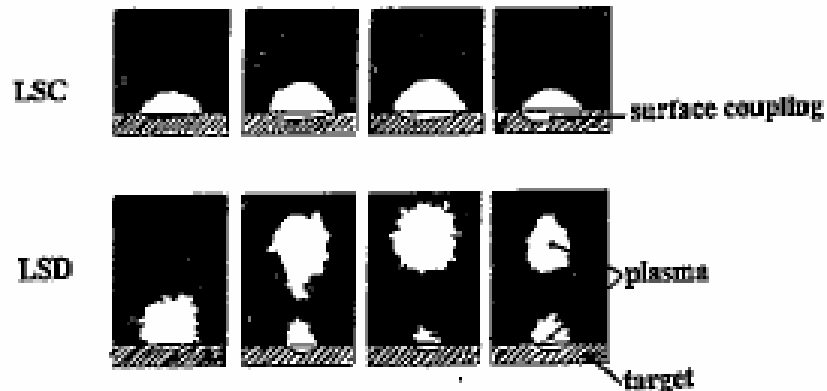
Fig. 2.23. Plasma kinetics for LSC and LSD wave propagations
(Boulmer, 1993; Herziger, 1986).

122

Laser beams have been used as the high-flux energy source for a wide range of industrial materials processing, such as laser welding, cutting, drilling, etc. The interaction of the laser beam with the evaporated metal vapor often leads to the partial ionization of metal vapor, and thus induces plasma inside the keyhole (referred to hereafter as keyhole plasma) and above the workpiece surface (referred to hereafter as plasma plume).

As a good energy transfer medium, the plasma inside the keyhole or near the keyhole top will help the energy transport from the laser beam to the workpiece. On the other hand, the plasma plume that emanates from the workpiece surface may heat the laser head and affect the micromachining process through laser absorption, scattering, and refraction. In order to protect the laser head from thermal damage, a shielding gas is usually injected coaxially with the laser beam. Interaction between the plasma plume, laser beam, and shielding gas induces a complicated picture of fluid flow and heat/mass transfer, and a part of the incident laser beam power will be absorbed by the plasma plume through an inverse Bremsstrahlung mechanism. When the absorbed laser energy is great enough to balance the energy loss due to conduction, convection, and radiation from the plasma plume, the plume can be maintained in a stationary form with respect to the laserbeam. The spatial distributions of gas temperature and electron number density in the plasma plume are always non-uniform. The existence of electron density gradients within the plasma plume will cause refraction and defocusing of the laser beam, reduce the power density of the laser beam arriving at the workpiece surface, and thus affect the laser micromachining process. Sometimes undesirable unsteadiness and intermittence of

the laser micromachining process may occur at high laser beam intensities. In order to suppress the unfavorable effect of the plasma plume on the micromachining process, a laterally injected assisting gas is often employed. The laser-induced plasma plume has been the subject of numerous studies (Herziger, 1986), summarized some research results up to the middle of the 1980s on laser-induced plasma plume characteristics in laser welding. Experimental results were reported about the plasma plume temperatures, but the electron (or plasma) temperatures measured by various authors differed significantly. For example, the reported maximum values of the measured temperatures for the plasma plume encountered in continuous-wave CO_2 laser welding of steel workpiece were from around 5,000 K to over 20,000 K, and corresponding electron densities varied in a wide range from 10^{21} to 10^{24} m^{-3} (DebRoy et al., 1991) Table 2. They showed that the laser intensity at the light spot was reduced mainly due to defocusing, and only to a minor degree due to absorption in the plasma plume.

Experimental investigations (e.g., Beck et al. 1995) show a highly frequent modulation of the plasma temperature. Since the plasma-affected focusing diameter depends on this temperature, it obviously also fluctuates during processing. Whenever the plasma temperature varies within the temperature range 6,000-22,000 K, the focus diameter can temporarily change by a factor of two, even at a shielding gas content of 90% He. This might be one cause for process instabilities. To increase process stability, therefore, the temperature-dependence of the focusing diameter should be suppressed as much as possible. This can be achieved by applying appropriate shielding mixtures to reduce the temperature-dependence of the plasma's optical properties.

Location of the plasma in laser micromachining is time and intensity dependent. Under certain conditions, the plasma appears to evolve from inside the keyhole into the ambient medium.

Table 2. Experimentally determined temperatures and electron densities.

Power density (10^8 W cm^{-2})	Plasma temperature (10^3 K)	Electron density (10^{16} cm^{-3})	Metal	Shielding gas flow rate (l min^{-1})	Welding speed (m min^{-1})
3–6	5–10	1–10	Fe		
2.8	8–12	1–20	Fe	Ar, 30	0.5
1–5	5.2–6.8	2.5–8.5	Fe	He, 50	1.2
4	8.5–9.2	0.41–25	Steel	Ar, 3	0.3
4	7.5	0.2–0.8	Fe	He, 40	
		12		None	
		11–12		N$_2$, 5–30	
6		8–16 (peak values)		He, 0–40	
4	16.68	4.6	Al	He, 30	3
	17.64	6.2		O$_2$, 40	
	18.00	6.5		N$_2$, 60	

At a relatively low laser intensity, the plasma remains attached to the entrance of the hole and is not important in attenuating incident laser radiation. At higher laser intensity, the plasma separates from the surface, but still is relatively stable.

The properties of the laser induced plasma are described by applying the theory for a plasma in local thermodynamic equilibrium (a LTE plasma). For such a LTE plasma, the degree of ionization can be calculated according to the Saha-Eggert equation (Verwaerde et al., 1995)

$$\frac{n_e n_i}{n_0} = \frac{g_i g_e}{g_0} \frac{(2\pi m_e k_b T_e)^{3/2}}{h^3} \exp\left(\frac{-E_i}{k_b T_e}\right) \quad , \tag{35}$$

where n_e, n_i, and n_0, are respectively, the electron, ion, and neutral atom densities, and T_e, is the electron temperature, g_e, g_i, and g_0 are the degeneracy factors for electrons,

ions, and neutral atoms, respectively, E_i is the ionization potential for the neutral atoms in the gas, and m_e is the mass of the electron, k_b, E_i are, respectively, the Boltzmann constant, and the ionization potential of the atom. Moreover, because the plasma is neutral and the atoms are at most singly ionized, then $n_e = n_i$, Equation 35 can be rewritten as

$$n_e = An^{\frac{1}{2}}T_e^{\frac{3}{4}}\left[\exp(-\theta/T_e)\right]^{\frac{1}{2}} \quad . \tag{36}$$

Numerical values for A and θ for several elemental gases are given in Table 3. Equation can be used to estimate the initial concentration of electrons that are the seed electrons that initiate plasma heating via inverse Bremsstrahlung.

Table 3. Atomic constants for various atoms and ions and values for A and θ.

Element	g_i	g_0	A (cm$^{-3/2}$ $^\circ$K$^{-3/4}$)	θ ($^\circ$K)
He	2	1	9.8×10^7	285,300
Ar	2	1	9.8×10^7	182,900
Al	1	6	2.8×10^7	69,400
Fe	30	25	7.6×10^7	91,700
Zn	2	1	9.8×10^7	109,000

One can assume that the plasma is an ideal gas with its pressure in equilibrium with the ambient atmosphere, p. Because the neutral ion atom density n_o inside the plasma plume is rather high, all the present particles have the same temperature, T_e, then the equation of state for this vapor is

$$p = (n_o + n_i + n_e)kT_e \quad . \tag{37}$$

Since the plasma is weakly ionized ($n_e < n_o$) one can neglect contribution of the charged particles to the pressure. Then, substituting Eq. 37 into the Saha-Eggert, Eq 35, the electron density can be related to the square root of the pressure and in case of an ion gas gives the relation

$$n_o(cm^{-3}) = 2.16x10^{17} \sqrt{p(Torr)}T_e^{1/4}(K) \cdot \exp\left(\frac{-45.65 \cdot 10^3}{T_e(K)}\right) \quad . \tag{38}$$

Equation 38 can be compared with the measured electron density. Variation of the electron density according to Eq. 38 versus the pressure is displays Fig. 2.24, where the experimentally observed electron temperature T_e measured by spectroscopy, has been used. The spread of the data results from taking into account the experimental uncertainties in T_e. The rather good agreement observed between the experimentally measured electron density n_e and the computed one (maximum difference of about 2-3) is remarkable, given the strong sensitivity of n_e with T_e in Eq. 38, a 5% variation of T_e induces a 40% variation of n_e.
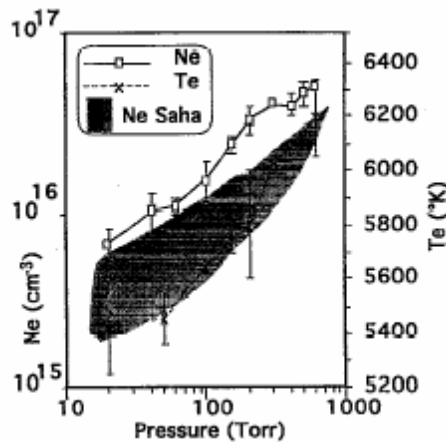
Fig. 2.24. Variation of the electron density and temperature as a function of the ambient pressure for an incident laser power of 10.5 kW. Shaded area: electron density calculated from the Saha-Eggert equation using the measured temperature (Verwaerde et al., 1995).

127

Verwaerde et al., (1995), performed experimental study of continuous CO_2 laser welding at sub-atmospheric pressures and metallic vapor ejected by the keyhole, for different helium pressures, Fig. 2.25.

This luminosity decreases when the helium pressure is reduced, and seems to disappear between 20 and 60 Torr. A similar evolution was observed earlier by Arata et al. 1984, and Kabasawa et al., 1992. Thus, the electron density is principally controlled by the ambient pressure. An important significance of this study is that, at low pressure, the perturbing effects of the plasma plume (the lensing effect and absorption by inverse Bremsstrahlung are completely suppressed by the one order of magnitude reduction of the electron density.
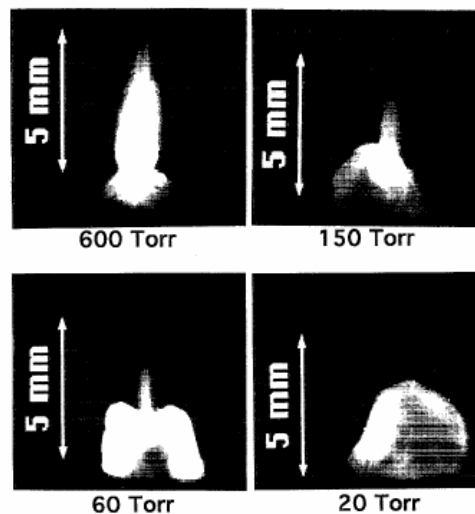
Fig. 2.25. Examples of plasma photographs under different pressure conditions for a laser power of 10.5 kW. A droplet of liquid metal is always visible at the target surface (Verwaerde et al., 1995).

Moreover, according to experimental investigations showing that expansion velocities of the plasma outside the keyhole are about 100-200 m/s, one can assert that this flow is subsonic (Verwaerde et al., 1995). Therefore, when the ambient pressure is

reduced, the electron density of the plasma inside the keyhole follows the same variation

as that of the plasma plume. This plasma reduction inside the keyhole has strong

consequences for the laser energy deposition. These are readily observed in the

metallographic studies described further, in which one analyzes the energy deposition and

determines a local absorption coefficient. The absorbed power is the same at every

pressure, but the melted profiles are different. Hence, the energy deposition mode of the

laser beam inside the keyhole is different at high pressure than at low pressure. The

energy deposition mode can be understood qualitatively from the evolution of plasma

with decreasing pressure. Density and temperature of the plasma decrease when the

pressure is reduced and the plasma disappears at low pressures. Therefore, the absorption

inside the keyhole becomes quite different. At atmospheric pressure and for low welding

speeds the main mechanisms of energy absorption inside the keyhole are inverse

Bremsstrahlung and Fresnel absorption along the keyhole wall. The energy deposition

can therefore be described, to the first approximation, by a bulk absorption coefficient μ.

By analyzing weld seam profiles and using a thermal model of the keyhole, μ is

determined to range from 1.4 to 1.7 cm^{-1} for such welding conditions. A consequence of

this high absorption coefficient is that much more laser energy is deposited near the top

of the keyhole than at its bottom; the energy deposition law follows a quasi-inverse

exponential dependence. In contrast, when the pressure is reduced, a similar derivation

of the absorption coefficient gives a value of about 0.4-0.5 cm^{-1}, for a 5 Torr pressure

experiments. The plasma being almost entirely suppressed, the absorption inside the

keyhole is only due to the Fresnel absorption, and the total local absorption coefficient becomes much smaller.

Propagation of an EMW is described by the wave equation (Beck el al., 1995)

$$\left(\nabla^2 + k^2 \bar{n}^2\right)E = 0 \quad,$$
(39)

where E is phasor amplitude of the EM field, k is propagation vector of the optical field, and the optical properties defining the propagation media are represented by the complex index of refraction, $\bar{n}$. For plasmas, in which electrons that are not bound to the atomic shell dominate the interaction with the EMW, the index of refraction can be calculated from the dispersion relation

$$\bar{n} = 1 - \frac{\omega_p^2}{\omega\ (\omega_p + i\omega_e)} \quad,$$
(40)

where ω_p is plasma frequency, ω_e is electron collision frequency, and ω is the laser frequency. The dispersion relation describes the close connection between the laser frequency and the plasma properties, represented by the plasma, ω_p, and the electron collision frequency.

Using a ray tracing method (Rockstroh et al., 1987; Ducharme et al., 1994), described the effect of plasma plume on propagating laser beam. These authors showed that properties of the beam are modified not only by absorption, but also by refraction due to the spatially varying optical properties within the plasma plume. The major drawback of the ray-tracing method used by those authors is that it is not applicable to describe the beam propagation in the focal area. Other authors (Beck el al., 1995) performed numerical and experimental analysis for a focused laser beam conditions.

They have studied intensity distribution in the focal plane and its exact position

dependent on the plasma plume and also with regard to the properties of the focusing

optics (especially its *F*-number). Optical properties of the plasma were derived in terms

of their dependencies on plasma pressure and temperature as well as on shielding gas

composition and laser wavelength. In the calculations, properties of the plasma plume

(spatial temperature distribution and shielding gas content) were pre-set and

parametrically modified, corresponding to experimental results documented in the

literature.

The total number density of all particles within the plasma depends on

temperature and pressure and is given for a mixture of different particles by Dalton's law

$$p \ = \left[n_e + \sum_\varepsilon \left(n_{a,g} + \sum n_{Z,g} \right) \right] k_b T \quad , \tag{41}$$

where $n_{a,}$ is electron number density, $n_{a,g}$ is atom number density of gas g, and $n_{Z,g}$ is Z-

charged ion number density of gas g. Since the LTE plasma is quasi-neutral, the number

densities of electrons and ions are related by

$$n_e = \sum\sum Z n_{Z,g} \quad , \tag{42}$$

where Z is the charge number. The electron density, therefore, can be directly calculated

by combining Eqs 35, 41 and 42. As Fig. 2.26 demonstrates, the electron density, n, first

strongly rises with increasing temperature due to the onset of ionization. After

completely reaching the first ionization level the electron number density drops according

to the expansion of the gas with higher temperatures whenever the plasma pressure is

kept constant. The beginning higher order ionization cannot compensate this rarefaction,

and the maximum electron density of the plasma, therefore, occurs during the first

ionization.

The laser-plasma interaction not only depends on the number of free electrons that

define the plasma frequency, ω_p,

$$\omega_p = \left(\frac{e^2 \cdot n_e}{\varepsilon_0 m_e} \right)^{1/2} \quad , \tag{43}$$

but also on the energy transfer between electrons and ions and atoms, expressed in terms

of the electron collision frequency

$$\omega_e = \sum_g \left(\omega_{ea,g} + \sum_z \omega_{ei,Z,g} \right) \quad , \tag{44}$$

According to (Tannenbaum, 1973) the electron-atom collision frequency is given by

$$\omega_{ea,g} = \frac{8(2\pi)^{3/2}}{3\sqrt{m_e}} (k_b T_c)^{1/2} n_{a,g} D_{a,g}^2 \quad . \tag{45}$$
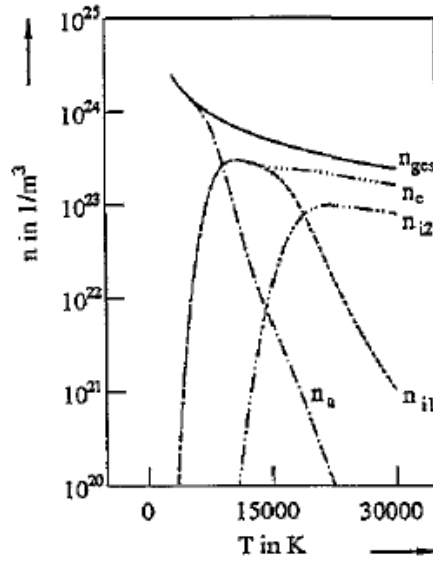
Fig. 2.26. Number densities of atoms, electrons, and ions in an iron plasma, p=1 bar
(Beck el al., 1995).

132

To calculate the collision frequency between electrons and ions for certain gas g, (Mitchener and Kruger, 1973), proposed the relation

$$\omega_{ei,g} = \frac{Z^2 e^2 n_{Z,g}}{3\varepsilon_0^2 \sqrt{m_e} (2\pi k_b T_e)^{3/2}} \ln \Lambda \quad , \tag{46}$$

using the Coulomb logarithm

$$\ln \Lambda = \ln\left(12 \frac{(\varepsilon_0 k_b T_e)^{3/2}}{e^3 \sqrt{n_e}} \right) \quad , \tag{47}$$

where m_e is the electron mass, and ε_0 is the elementary charge. Knowing the electron density and collision frequency, the optical properties of the plasma can be calculated by the dispersion relation given by Eq. 40. Resulting absorption coefficient and the real part of the complex refraction index are presented in Fig. 2.27. Related to the electron density, the absorption coefficient as well as the real refractive index exhibit maximal and minimal values at their first complete ionization.

a)   b)
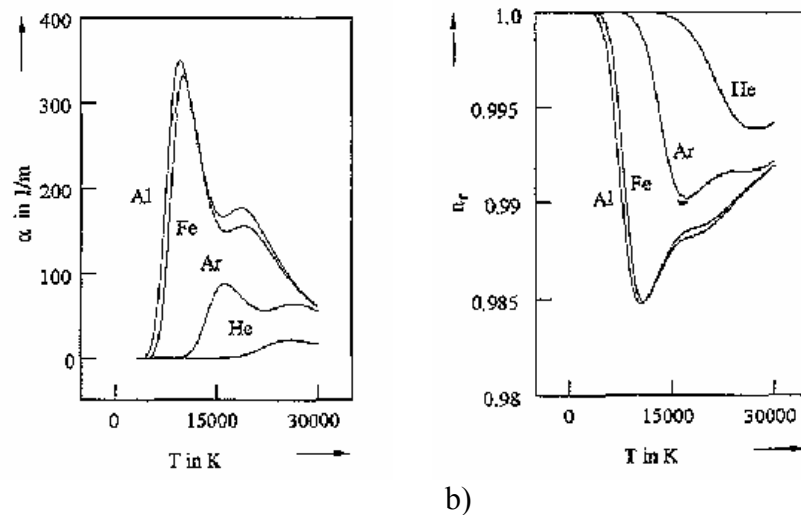
Fig. 2.27. Optical properties of various plasmas; $p=1$ bar as a function of temperature: absorption coefficient, b) the real refractive index (Beck el al., 1995).

133

To derive the absorption and refraction of the laser beam within the plasma
plume, temperature distribution and shielding gas content within the plume have to be
exactly known properties that are extremely difficult to obtain theoretically. In this
Dissertation, therefore, these properties are preset for calculation. They are
parametrically varied to demonstrate the possible effects of the plasma plume upon laser
focusing. The plasma plume is assumed to be elliptically shaped, Fig. 2.28, with a
Gaussian-like temperature distribution (Beck et al., 1995), according to

$$T(r,z) = T_{pt.max} \exp\left(2\left(\frac{r^2}{e_{pl}^2} + \frac{(z-r_{pl})^2}{z_{pl}^2}\right)\right) \quad , \tag{48}$$

where $T_{pl/max}$, is the maximum temperature in the center of the plasma plume, z is the
axial coordinate in direction of beam propagation, and r_{pl} is the half axis width of the
plasma plume.
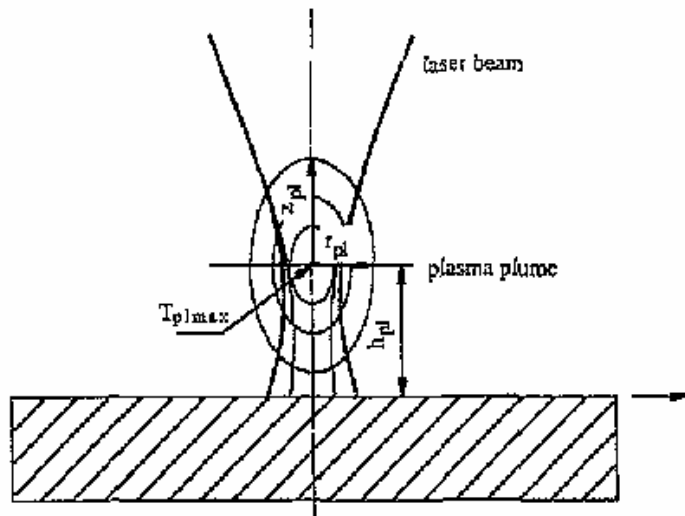
Fig. 2.28. A sketch of the plasma plume (Beck el al., 1995).

Plasma is in local thermodynamic equilibrium (LTE). LTE is the assumption that all particles have a Maxwellian velocity distribution and that collision processes dominate the rate equations such that Boltzmann statistics apply. To satisfy these conditions, electron densities of 10^{16} cm^{-3} are sufficient (Ready, 1971; Dowden et al., 1994). Since formation of the plasma plume is not the subject of this study, no attempt has been made to solve the plume formation mathematically. More details on this subject has been presented by Dowden et al., (1994). Instead, the objective of this Section is to demonstrate the effects of a plasma plume, experimentally observed for example by a video systems laser beam focusing and plasma formation.

It has to be pointed out, that demonstrated calculations and experimental results do not give exact numbers for the beam propagation and the focal diameter, Beck et al., 1995. The studies cover a wide range of situations, than the presented data demonstrate the magnitude of laser absorption and defocusing of the laser beam and their dependence on location, the shape and the temperature of the plasma as well as on the characteristics of the optics used.

In this Dissertation to demonstrate the effects of a plasma plume in the interaction of laser energy with matter, experiments were conducted using a fast CCD camera to monitor plasma. The high-speed video camera (characterized by a typical recording speed of 8000 frames/s) recorded spatial extent of the plasma plume. A representative picture from the camera recording plasma of the 304 stainless steel (SST) samples is displayed in Fig. 2.29.
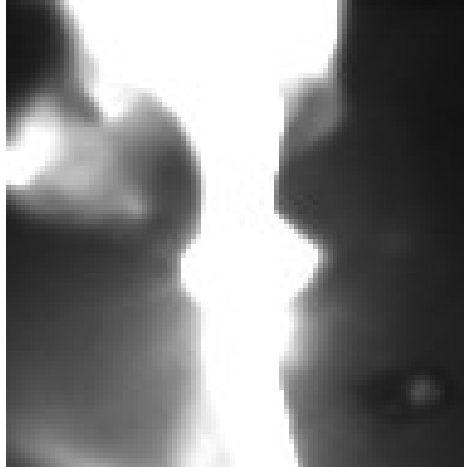
Fig. 2.29. Representative examples of plasma photograph under normal pressure conditions for a Nd:YAG laser power of 3.75 kW irradiating the 304 SST sample.

Temperature distribution within the plasma plume and its location and shape are, therefore, strictly pre-set for the calculation of the beam propagation. To derive the effects of the plasma plume systematically, properties of the plume were parametrically varied within the typical range given by the experimentalists Fig. 2.30. The shielding gas is assumed to be homogeneously distributed within the plume.
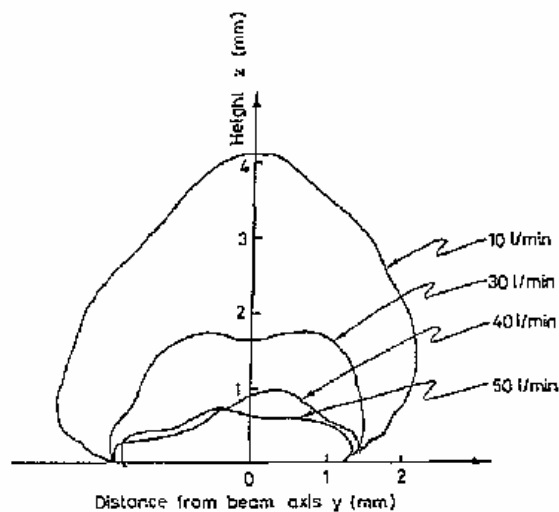
Fig. 2.30. Contours of the plasma plume taken by a CCD camera at various Ar-gas flow rates (Beck el al., 1995).

The effect of the plasma plume on the focal radius, h_{pl}, and subsequently on the

focus intensity is not only dependent on the plasma properties, but also on the *F*-number

of the focusing optics, as is demonstrated in Fig. 2.31. It becomes evident that the

smaller the *F*-number of the focusing optics the stronger the deterioration of refractive

effects of the laser-induced plasma is. Since the focusing radius produced by a small *F*-

number optics is very sensitive to plasma formation, using small *F*-number optics to

ensure high focal intensities presupposes an appropriate plasma control. The plasma lens

not only increases the beam radius but also changes location of the "effective focal

plane", which indicates position of the minimal beam radius of the focused beam. This

dislocation is demonstrated in Fig. 2.32. Whenever the metal vapor plasma is not thinned

by shielding gases, the dispersing effect of the plasma plume may exceed the focusing

effect of the lens. In this case, the plasma plume prevents further focusing of the beam,

and the position of the minimal beam radius is located within the plasma plume. The

effective focal position, therefore, is above the workpiece, indicated by a positive

displacement, Δz_f, in Fig. 2.32. As long as the dispersing effect of plasma is less than the

focusing effect of the lens, the effective focal plane is outside the plasma plume and

shifted in the direction of the beam propagation. Increasing the shielding gas content

within the plume reduces the dislocation of the focal plane. However, even a shielding

gas content of 60% He may lead to a dislocation of as much as 2 mm. For accurate

predictions of the hole profile the defocusing effect of the plasma has to be compensated

by the dislocation of the focal plane Δz_f.
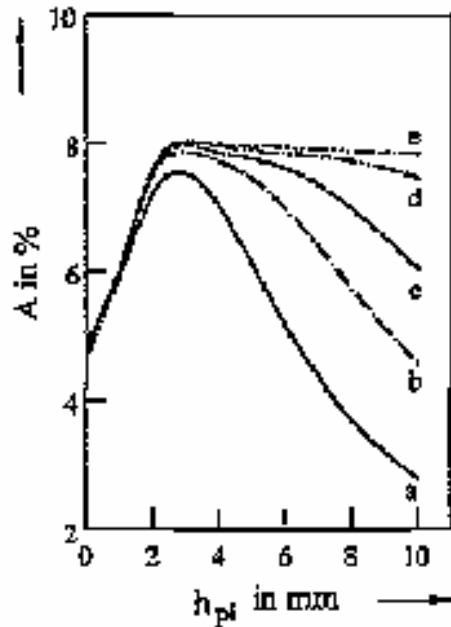
Fig. 2.31. The plasma-affected focusing radius relative to the undisturbed focusing radius and absorption within the plasma plume dependent on the F-number of the focusing optics and the position of the plasma plume: $p = 1$ bar, with focusing optics: (a) $F = 4$, (b) $F = 6$, (c) $F = 8$, (d) $F = 12$ and (e) $F = 20$ (Beck el al., 1995).
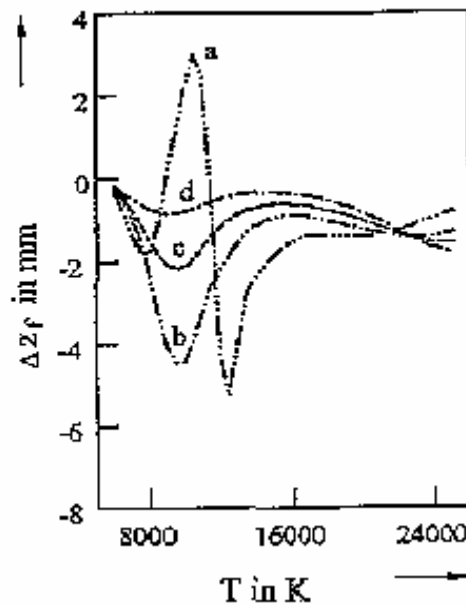
Fig. 2.32. Dislocation of the focal plane A,q and plasma-affected focusing radius relative to the undisturbed focusing radius in the effective focal plane dependent on plasma temperature and on the shielding gas content: $p = 1$ bar, $F = 7$, content of shielding He gas: (a) 0, (b) 40%, (c) 60%, and (d) 80% (Beck el al., 1995).

The effects of the plasma plume size and its distance from the surface are shown in Fig. 2.33. The results elucidate defocusing and absorption of the focused laser beam by a plasma plume leaving the workpiece indicating that whenever the plasma plume starts to detach from the surface defocusing increases (Beck el at., 1995). The intensity distribution is mainly changed by defocusing, especially for small plasma plumes. Even for a shielding gas content of 80% of He, the focusing radius can be enlarged by a factor of eight. In contrast to the severe defocusing, power absorption is moderate.
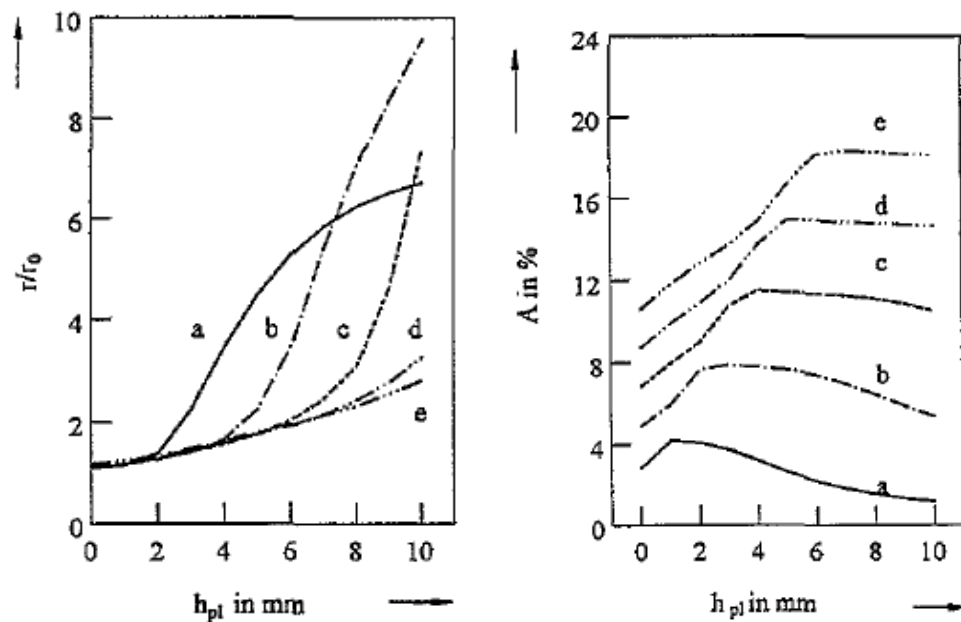
Fig. 2.33. The plasma-affected focusing radius relative to the undisturbed focusing radius and absorption within the plasma plume dependent on the size and position of the plume; p = 1 bar, T_{plmax} = 12,000 K, TEM$_{oo}$ mode, F = 7, with He content 80%. For: (a) z_{pl}=2 mm, r_{pl}=0.5 mm; (b) z_{pl}=4 mm, r_{pl}=1 mm; (c) z_{pl}=6 mm, r_{pl}=1.5 mm; (d) z_{pl}=8 mm, r_{pl}=2 mm; and (e) z_{pl}=10 mm, r_{pl}=2.5 mm (Beck el al., 1995).

The effect of plasma temperature and shielding gas content is shown in Fig. 2.34. For all shielding gas contents, dependence of the focus diameter on the plasma temperature is noticeable.
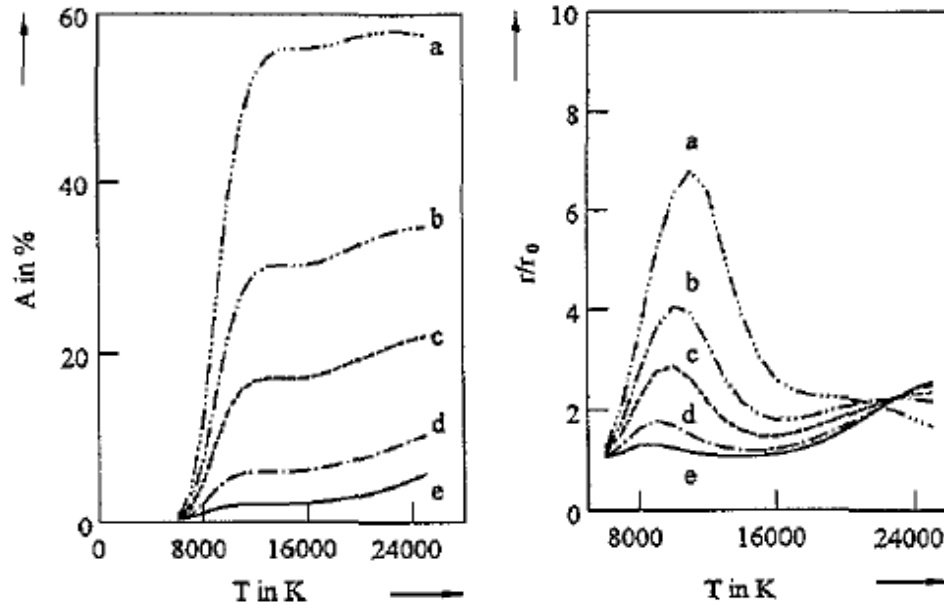
Fig. 2.34. The plasma-affected focusing radius relative to the undisturbed focusing radius and absorption within the plasma plume dependent on the size and position of the plume; p = 1 bar, T_{plmax}= 12,000 K, r_{pl}=0.5 mm, TEM$_{oo}$ mode, F = 7, with He content: (a) 0 (b) 40% (c) 60%; (d) 80%; and (e) 90% (Beck el al., 1995).

Defocusing is maximum at plasma temperatures of about 11,000 K at low He fraction. Since the electron densities drop with higher temperatures, defocusing again decreases for higher plasma temperatures up to the second ionization of the iron atoms, starting at about 20,000 K. Thinning the iron plasma by applying He as shielding gas limits enlargement of the focus radius. For 80% shielding gas content, the enlargement factor is less than two within a temperature range up to 22,000 K. In contrast to the defocusing, absorption is hardly affected by the plasma temperature (for plasma temperatures of more than 10,000 K, but is mainly dependent on the shielding gas content. As in the previous example, the assumption of a shielding gas content of about 90% leads to minor absorption of the laser beam less than *5%.*

140

Since the plasma-affected focusing diameter depends on this temperature, it obviously also fluctuates during processing. Whenever the plasma temperature varies within the temperature range 12,000-22,000 K, the focus diameter can temporarily change by a factor of two, even at a shielding gas content of 90% He. This might be one cause for process instabilities. To increase process stability, therefore, the temperature-dependence of the focusing diameter should be suppressed as much as possible. To avoid temperature-dependence of the focus diameter, the lensing effect of the plume must not be dependent on temperature; that is, the gradients of the refractive index in the radial direction have to remain constant within the plume.

Whereas pure gases lead to a focal spot size that is strongly dependent on plasma temperature, the optimized shielding gas mixture reduces this dependence. This ensures an almost complete decoupling of the intensity distribution in the focal plane from plasma temperature fluctuations. Like defocusing, the dislocation of the focal position also depends on the plasma temperature and can be reduced by utilizing an appropriate shielding gas mixture. For example, the plasma defocusing dislocates focal position from the surface of the workpiece to approximately 1 mm below and enlarges the effective focal radius by about 30%. Since the defocusing is almost constant within the temperature range 8,000 – 24,000 K, these effects can be taken into account during process optimization. The He:Ar shielding gas mixture is supposed to be favorable to obtain a stable micromachining process.

The expected microdrilled or weld depth when the focal radius is kept constant and the focal position is dislocated is illustrated in Fig. 2.35. The maximum welding

141

depth is attained for a focal position below the surface of the workpiece by about a

quarter of the total welding depth for iron and by about a seventh of the total welding

depth for aluminum. As the calculations indicate, optimizing the focal position is most

important when welding with laser powers close to the minimum laser power (Beck el at.,

1995). In this case, even small dislocations of the focal plane may interrupt the deep

welding process.
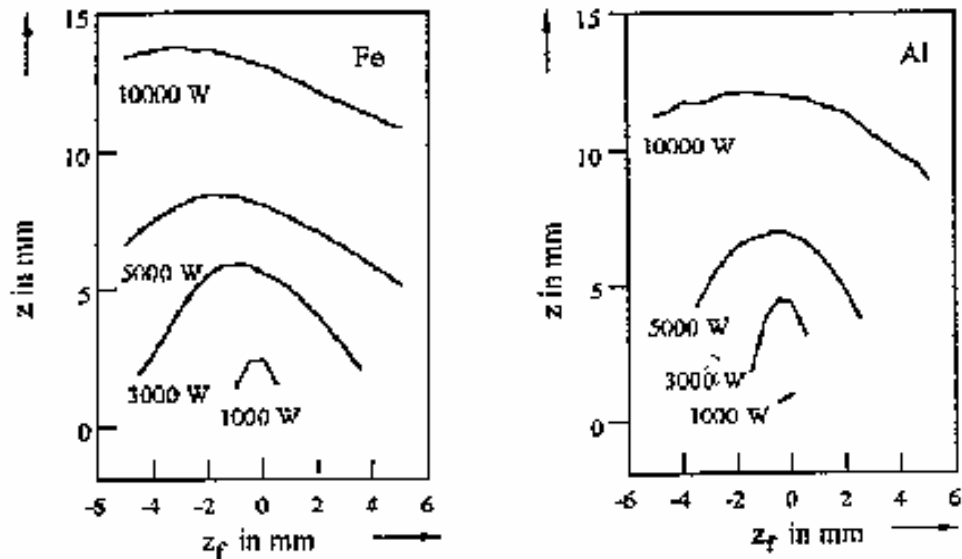
Fig. 2.35. Welding depth for iron and aluminum dependent on focal position and laser power; $\omega_o = 0.24$ mm, $u_o = 2$ m/min, CO_2 laser, $K = 0.2$ and $F = 7$ (Beck el al., 1995).

A plasma plume thinned by shielding gases is considered to be highly transparent.

Nevertheless, a considerable amount of refraction is present, enlarging the focus radius

and dislocating the focal plane. Even a small plume detaching from the surface may lead

to an increase in the focus radius that is sufficient to interrupt the micromachining

process. Plasma defocusing and not plasma absorption, therefore, is assumed to be the main cause of the so-called 'plasma shielding' observed in laser micromachining.

Additionally, defocusing by the plume depends on the plasma temperature. Since the plasma temperature is frequently modulated, the plasma-affected focus radius and position fluctuate as well. This leads to process instabilities which can partially be suppressed by appropriate shielding gases. Applying an appropriate shielding gas mixture further reduces the dependence of plasma defocusing on the plasma temperature and, therefore, further dampens the plasma-induced intensity fluctuations of the focused laser beam. A mixture of helium and argon in a ratio of 3: l is found to be favorable of enhancing process stability.

2.6.1. Plasma absorption considerations

Optical absorption by electrons depends on the electron density in the plasma. The electron density is critical, n_c, when the plasma frequency, ω_p, equals to the frequency of the incident light. When n_c is reached in the plasma, the laser radiation is completely absorbed before it strikes the target. Critical electron densities, n_{ec}, values for different laser wavelengths are listed in Table 4.

Table 4 Critical electron density for various laser wavelengths
(Boulmer-Leborgne et *al.*, 1993), n_{ec}=N$_{ec}$.

Laser type	Wavelength (μm)	Photon energy (eV)	N_{ec} (cm^{-3})
CO$_2$	10.6	0.12	10^{19}
Nd:YAG	1.06	1.2	10^{21}
Ruby	0.698	1.8	2.3×10^{21}
Excimer XeCl	0.308	4.08	1.2×10^{22}

The absorption and scattering of incident radiation by a weakly ionized plasma are determined by the electron density with the refractive index approximately given by

$$n = (1 - n_e n_c)^{\frac{1}{2}}, \tag{49}$$

where n_c is critical electron density defined as

$$n_c = \frac{m_e \varepsilon_0 \omega^2}{e^2} = 3.14 \times 10^{-10} \omega^2 \left(cm^{-3} \right) , \tag{50}$$

where ε_0 is the permittivity of free space, and ω is the angular frequency. For CO$_2$ laser radiation, $\omega = 1.78 \times 10^{14}$ rad/sec, and $n_c = 10^{19} cm^{-3}$. When $n_e < n_c$, the refractive index is real and radiation can propagate through the plasma; it is only when $n_e = n_c$ that radiation is prevented from entering the plasma.

Treusch (1986) described a strong dependence of absorption coefficient for inverse Bremsstrahlung as

$$\mu = \frac{v_c \omega_p^2}{c(\omega_p^2 + v_c^2)} , \tag{51}$$

where v_c is electron-atom/ion-phonon collision frequency, c speed of light, which decreases with increasing frequency, ω_p, resulting in lowering the threshold intensity with increasing wavelength.

The absorption and dissipation of incident laser radiation by the laser plasma can be obtained from the following time-dependent equations:

$$\frac{dn_e}{dt} = R_i - R_d - R_r \quad , \tag{52}$$

$$n_e \frac{d\bar{\varepsilon}}{dt} = \mu\, I - P_C - P_L \quad , \tag{53}$$

where, R_i, R_d, and R_r are the electron production, diffusion, and recombination rates, respectively; $\bar{\varepsilon}$ is the average electron energy, μ is the absorption coefficient for laser radiation, I is the laser intensity, P_c is the power loss from elastic collisions, and P_L is the power loss from inelastic collisions. Condition for rapid plasma heating is that the rate of energy input $\mu\, I$ exceeds the power loss due to elastic collisions. This requirement can be written as (Miyamoto and Arata, 1984).

$$\mu\, I = 2n_e \frac{m_e}{M} v\bar{\varepsilon} \quad , \tag{54}$$

where M is the mass of a neutral atom, and v is the collision frequency. The mean electron energy will be some fraction of E_i. With $\bar{\varepsilon} \approx 0.1 E_i$,

$$\mu\, I \sim \frac{n_e m_e}{5M} v E_i \quad . \tag{55}$$

Solana and Ocana, (1997), worked on constructing a full 3D weld keyhole geometry. In their calculations of ablation losses and evaporation effects they have

included energy-absorption mechanisms called Fresnel and inverse Bremsstrahlung. For proper evaluation of the collision energy attenuation in the plasma it was necessary for them to determine the dependence of absorption coefficient μ on the temperature inside the keyhole. An expression for absorption coefficient in plasma due to inverse Bremsstrahlung (Kaplan, 1994) is

$$\mu(T) = \frac{z^2 e^6 n_i n_e}{6\pi \xi_0^3 m_e^2 ch\omega^3 \left[1 - \left(\frac{\omega_0}{\omega}\right)^2\right]^{1/2}} \left(\frac{m_e}{2\pi kT}\right)^{1/2}$$
$$x\left[1 - \exp\left(-\frac{h\omega}{kT}\right)\right] 0.5\ln(1 + \Lambda^2) \quad ,$$

(56)

with

$$\Lambda = \frac{12\sqrt{2\pi}\varepsilon_0 m_e}{e^3 \omega_0}\left(\frac{kT_p}{m_e}\right)^{1/2}\frac{1}{Z}\left(\frac{Z}{1+Z}\right)^{1/2} \quad ,$$

(57)

where all variables were defined earlier.

The plasma is described as a function of temperature with equal density for electrons and ions, so the equation for pressure is

$$p = n_e kT\left(\frac{Z}{1+Z}\right) \quad ,$$

(58)

which together with Saha-Eggert equation provided that the plasma is at atmospheric pressure gives the value of the electronic density as a function of the temperature, which in turn is necessary to obtain an expression for the absorption coefficient dependent only on the temperature.

The inverse Bremsstrahlung absorption coefficient (assuming LTE conditions, Miyamoto, 1986) is

146

$$\mu\left(m^{-1}\right) = \frac{n_e n_i Z^2 e^6 2\pi}{6\sqrt{3} m \varepsilon_0{}^3 chw^3 m_e{}^2} \left[\frac{m_e}{2\pi k T_e}\right]^{\frac{1}{2}} \left[1 - \exp\left(-\frac{w}{kT_e}\right)\right]\overline{g} , \qquad (59)$$

where Z is the average ionic charge in the plasma, h is Planck's constant, c is the speed of light, and $\overline{g}$ is the quantum mechanical Gaunt factor, which typically is 1.3 to 1.6 for laser welding plasmas at 10.6 μm. For CO_2 or YAG laser radiation and plasma with $T_e \sim 8 \times 10^3\,^{\circ}\mathrm{K}$, $1 - \exp\left(-hw/kT_e\right) \sim hw/kT_e$, the Eq. 59 becomes

$$\mu\left(m^{-1}\right) = \frac{n_e n_i Z^2 e^6 \overline{g}}{6\sqrt{3} m \varepsilon_0{}^3 cw^2 (2\pi)^{\frac{1}{2}}} \left[\frac{1}{(m_e k T_e)^{\frac{3}{2}}}\right] . \qquad (60)$$

For weakly ionized plasma with Z=1, $\overline{g}$=1.5, m=1.0, and $w = 1.78 \times 10^{14}$ rad/sec, Eq. 60 simplifies to

$$\mu\left(m^{-1}\right) \sim \frac{3.3 \times 10^{-39} n_e{}^2}{T_e{}^{\frac{3}{2}}} , \qquad (61)$$

where n_e is given in meters^{-3} and T_e is given in K. Therefore, with $n_e = 10^{23}\,m^{-3}$ and $T_e = 6.2 \cdot 10^3\,K$, the initial absorption coefficient can be calculated to be $\mu_i = 70\,m^{-1}$.

There are two main effects resulting from a plasma which strongly interacts with the laser beam. The first is a reduction in light energy incident on the opaque target material. The second is the thermalization of the incident light energy with the associated effects on the pressure and density of the gas phase. In addition, the thermalized gas becomes a source for blackbody radiation, but this should be small compared to the energies of the incident laser radiation.

Solana et al. (1999), and Solana and Ocana (1997) show variation in the average

absorption coefficient with depth and the temperature. He observed correlation between

absorption and the power density of the laserbeam taking degree of ionization into

account. His results were in a good agreement with other researchers (Verwaerde et al.,

1995; Kaplan, 1994, Duley, 1999). The average absorption coefficient in the plasma

laser sources versus depth for a Gaussian beam is shown in Fig. 2.36.
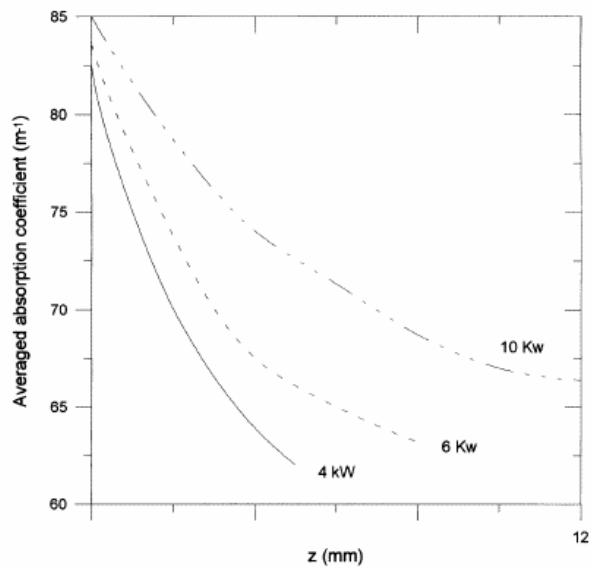
Fig. 2.36. The average absorption coefficient in the plasma laser sources versus depth of
a Gaussian beam, using focusing radius of 100 mm on 304 SST (Solana et al. 1999).

The laserbeam energy can be converted to heat energy, which is spread

throughout the entire cavity rather than being delivered just to the sample surface.

The absorption coefficient reaching maximum value relatively close to the

keyhole walls. The increasing temperature towards the center of the keyhole tends to

decrease the value of absorption coefficient, because the electron density is decreasing

there, so absorption coefficient is higher at the walls of the keyhole and lower in the

center of it and is a function of temperature.

With increasing depth in the keyhole the temperature gradient decreases and thus

the leading effect on the absorption coefficient as one moves towards the center of the

keyhole is not the electron density, but rather the effect of increasing ionization.

Absorption coefficient is decreasing with depth of the keyhole along the axis of the

sample.

During the Nd:YAG laser energy interaction with few samples the formation of a

plasma was examined. It was evident that for the energy density higher than 3×10^{10}

W/m^2, plasma is present and the surface absorption coefficient as well as the bulk

absorption coefficient is a function of temperature and results in depth of propagating

keyhole as stated before. Discussion on developing this function is shown in Section

4.3.1.

2.7. Analysis of the physical phenomena of laser micromachining

The mechanisms involved in laser micromachining, especially melt ejection

phenomena are rather complex and poorly understood. There are two important aspects

of laser interaction with materials not fully yet explained. The first is the laser-induced

reflectivity drop. The second, and probably the most important in micromachining, is the

quantitative connection between the absorbed laser energy and the extracted volume of

material during laser drilling.

The extent to which melt ejection occurs depends on both material properties and laser conditions. Expulsions of material during laser drilling were investigated in many publications; a summary of our literature review is shown in Chapter 1.

To construct a mathematical description corresponding to the presented physical model, shown in Fig. 2.1, the following assumptions were used: (a) the liquid is incompressible; (b) the thermo physical parameters of materials depend on temperature, (c) the melt layer is a thin boundary layer, and (d) the influence of surface tension and gravity on the melt flow are assumed to be insignificant compared to the effect of evaporation induced recoil pressure.

2.7.1. Material removal mechanism and energy transport in multiple phases

In laser micromachining process, heat transfer and fluid mechanics, convection as well as diffusion of the energy field should be considered. Thus the heat conduction equation should be replaced by the more general energy equation. Then, the heat transfer analysis and the fluid motion analysis of the process become coupled.

Combining the boundary conditions and initial conditions, a system of equations can be solved. In the programming, the non-linearity of the property are considered using either certain linearization approximations or using iterations.

A physical model of the melting front at the initial stage of drilling is shown in Fig. 2.37. The laser induced pressure gradient at the evaporation front pushed material radially outward, away from the axis of the drilling beam. The displaced material can

150

then either flow along the walls and out of the crater or, as observed with workpieces that deform during ablation, remains trapped within. Either way, as long as the displaced material does not obstruct the central part of the beam, the drilling velocity at the center of the drilled hole increases.
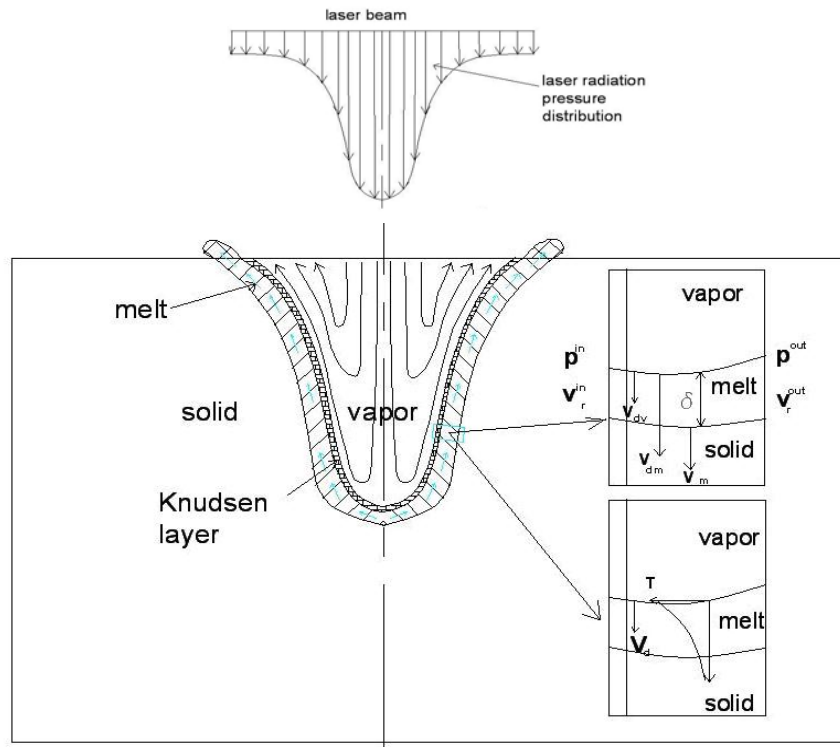
Fig. 2.37. Schematic of energy transport in multiple phases in laser drilling, the physical model of melt removal from the interaction zone, the cross section in the *x–z*, plane is shown.

Evaporation from the surface molten material causes melt surface shift into the material with velocity v_{dv}, which is directed normal to the melt surface. Temperature of the melt surface is different in different locations. Therefore, the evaporation rate and the related recoil pressure on the melt surface vary along the surface. In particular, the

values of pressure at the opposite sides of the computational finite element, p^{in} and p^{out}, are different. This pressure difference causes the melt flow, Fig. 2.37.

Because the melt flow accelerates or decelerates depending on the relative values of p^{in} and p^{out}, and the cross sections of the finite element volume at the flow entrance and exit are different, the quantities of melt entering and leaving the computational volume are not generally the same. Therefore, the melt thickness δ, Fig. 2.37, decreases or increases, resulting in the motion of the melt surface with velocity v_{dm}, which, like v_{dv}, is normal to the melt surface. Note that the evaporation component of the melt surface velocity, v_{dv}, is always directed into the sample, while the component of the melt surface velocity due to melt flow, v_{dm}, can be directed either into the sample or in the opposite direction. The resulting velocity of the melt surface, v_d, the "drilling" velocity, is the sum of the two components

$$v_d = v_{dm} + v_{dv} \quad . \tag{62}$$

The laser beam is absorbed in the near surface layer within a material thickness much smaller than the characteristic dimensions of the sample. Thus, the heat source can be approximated as a surface heat source. As discussed above, the surface of the melt moves into the sample. The heat source moves together with the surface. This causes melting of the additional solid metal, and the melting front propagates into the sample. Simultaneously, the melt flow transfers heat along the solid–liquid interface. Thus, both displacement of the heat source and the motion of the melt affect the temperature field.

Assuming incompressible liquid in the melt layer, independent thermo-physical properties of the temperature for the workpiece material, and surface heat source for the

laser power, the equations of conservation of momentum, and energy can be written as (Semak et al., 1999)

$$\text{div}\, V = 0 \quad , \tag{63}$$

$$\rho\left(\frac{\partial v}{\partial t} + V\,\text{grad} v\right) = -\text{grad}\, p + \mu_m\,\Delta V \quad , \tag{64}$$

$$\frac{\partial T}{\partial t} + V\text{grad} T = \frac{k}{c\cdot\rho}\nabla^2 T \quad , \tag{65}$$

where, V, ρ, c, T, and k are the velocity, density, specific heat, temperature, and thermal conductivity of solid or liquid material, μ_m is the melt viscosity, and p is pressure. The boundary condition at the liquid-vapor interface is defined in Eq. 163 and for the classic Stefan boundary condition is applied to the solid-liquid boundary (melting front $z=z_m$) is defined in Eq. 166.

The liquid pool temperature distribution is influenced by the surface tension gradient driven convection. It is known from recent theoretical and experimental research that when a liquid metal is heated by an intense laser beam, propagation of strong convection currents in the liquid pool, mainly driven by Marangoni force and to a much lesser extent by buoyancy force, is insufficient to eliminate the commonly present strong temperature gradient within the liquid. In laser processing of metals and alloys, the peak temperature reached at the surface is very high and exceeds the boiling point. For example, von Allmen determined molten pool temperatures in excess of boiling point for laser treatment of copper. Batanov et al. (1973) indicated that temperatures on the surface of a laser irradiated material can be higher than the boiling point. Paul and DebRoy; and Zacharia et al., (1999), have reported theoretically calculated temperatures

153

close to the boiling point for laser welding. Khan and DebRoy (1999) arrived at the same conclusion from an analysis of the experimentally determined values of relative vaporization rates of various alloying elements. Chan and Mazumder (1987), have also reported temperatures greater than the boiling point during laser irradiation of aluminum, titanium, and a superalloy. Theoretical calculations of the vaporization rates by Knight (1979) and Anisimov et al., (1971) are based on the premise that the liquid pool surface temperatures are higher than the boiling point. Thus, during laser irradiation, the equilibrium pressures at the pool surface are often higher than the atmospheric pressure and the excess pressure provides a driving force for liquid expulsion.

Several investigators have reported experimental results of metal expulsion during laser irradiation. Chun and Rose (1971) irradiated an aluminum target with 1 to 30 J laser pulses of duration 0.500 to 1.0 ms and observed that as much as 90% of the material lost was removed from the molten pool as liquid. During laser scribing of ceramics with ruby laser pulses, Wagner (1974) observed that a conical molten region was formed and all liquid was expelled.

As shown in Fig. 2.53, calculations may predict surface temperatures in excess of the material's boiling temperature, T_v; which is approximately 3,135 ºK for the iron. This is in contrast to most other models of laser welding and cutting or drilling, which assume that the melt surface temperature cannot exceed the boiling point. This assumption originates from belief that evaporation is a threshold process and that volumetric evaporation (boiling) can take place in the case of laser material interactions.

154

Another consequence of this belief is that propagation of the evaporation front can be simulated in terms of the 'problem of Stefan'. However, evaporation is not a threshold process. It can occur at any temperature exceeding absolute zero (Anisimov and Khokhlov, 1995). In addition, theoretical studies (Afanasiev and Krokhin, 1967) have shown that volumetric evaporation cannot take place during laser material interactions under typical industrial conditions; only surface evaporation can occur under these conditions. Thus, the surface temperature can significantly exceed the boiling point if the absorbed laser beam intensity is high. The velocity of the evaporation front is determined by exponential equation, Eq. 164 (Anisimov and Khokhlov, 1995), which is applicable at least for melt surface temperatures not exceeding the critical temperature. Therefore, due to the exponential dependence on the surface temperature, the approximation of evaporation front velocity in terms of the 'problem of Stefan' may results in significant errors.

2.7.1.1. Vaporization from irradiated surface

Model used in this Dissertation to obtain the temperature and pressure at liquid layer surface is an outgrowth of an earlier models presented by Anisimov et al. (1971) or Von Allmen (1976). It is assumed that the surface temperature $T_s = T_v$ and that surface properties are most influenced by the properties of vapor in the Knudsen layer, where particles leave the melted surface participate in enough collisions so Maxwellian type

distribution functions can be applied. The depth of this region is of the order of several mean free paths (sub-micron region).

Please bear in mind that our considerations are focused so far on the ablation processes that occur before melt starts to flow. The vaporization model suggested in this Dissertation includes two different mechanisms: surface and volume vaporization.

Under equilibrium conditions the rate of vaporization is equal to rate of condensation, i.e., the rate at which particles leave the surface of the liquid is equal to the rate at which particles collide with and stick to the surface. By computing the equilibrium rate at which gaseous particles collide with surface and correcting the fraction which sticks, it is possible to find the rate at which particles eject from the surface of the condensed phase as a function of temperature. The rate of collisions per area of particles with the melt is found by integrating the particle velocities over their Maxwellian velocity distribution. Evaluating the integral and using Hertz-Knudsen-Langmuir relation (Niedrig and Bostanjoglo, 1996) relation of rate of ablated atoms per area is

$$\dot{n}_e = \frac{P(T)}{\sqrt{2\pi M k_B T_s}} \quad , \tag{66}$$

where, $P(T)$ is saturated vapor pressure defined by Clausius-Claperon equation. Treating the vapor as an ideal gas, the equilibrium vapor pressure at melt surface, $P(T)$, can be related to the vaporization temperature by

$$P(T) = P_0 \exp\left(\frac{H_v}{R}\left(\frac{1}{T_{v,0}} - \frac{1}{T_v}\right)\right) \quad , \tag{67}$$

where R is universal gas constant, and P_0 is the ambient pressure associates with the reference vaporization temperature $T_{v,0}$.

Expression in Eq. 67 estimates the rate of vaporization for a single component material. If one deals with an alloy like 304 stainless steel, which is a multi-component material, Eq. 67 gives partial pressures separately for each component, and the total pressure would be the sum over all of the components.

The velocity v_{dvs} at which the surface of the condensed phase recedes due to loss of material by vaporization is related to molar evaporation flux by (Niedrig and Bostanjoglo, 1996)

$$\left(\frac{\partial \delta}{\partial t}\right)_s = v_{dvs} = -(1-\eta)2\dot{n}_e \frac{M}{\rho_m} \quad , \tag{68}$$

where η is the fraction of recondensing atoms and for most metal is assumed to be 18%,

The volume evaporation is assumed to occur by homogeneous nucleation (see Chapter 1). The formation of critical nuclei (of volumetric velocities) is given by (Niedrig and Bostanjoglo, 1996) as

$$\dot{n}_{en} = \frac{\rho_m}{M}\sqrt{\frac{2\sigma}{\sqrt{2\pi M}}} \exp\left(-\frac{H_v M}{k_B T_s} - \frac{16\pi\sigma^3}{3k_B T_s (p_b - p_e)^2}\right) \quad , \tag{69}$$

where H_v is the enthalpy of vaporization, and σ is the surface tension of the liquid-vapor interface, $p_e \approx P(T)/2$, p_b is are the external pressure exerted on the material by evaporating atoms and the pressure within the bubble. The number of atoms within a critical bubble is determine by

$$N_b = \frac{P_b \frac{4}{3} \pi r_b^3}{k_B T_s} \quad , \tag{70}$$

where r_b is the radius of critical bubble define by

$$r_b = \frac{2\sigma}{p_b - p_e} \delta\, v_{dv} N_b \quad . \tag{71}$$

The change of the layer thickness, δ, due to volume evaporation is proportional to the nucleation rate, the number of atoms, and the layer thickness, that is,

$$\left(\frac{\partial \delta}{\partial t}\right)_v = v_{dv\,v} = 2 \frac{M}{\rho} \delta\, v_{dv} N_b \quad . \tag{72}$$

The factor 2, in Eq. 72 is an estimated correction, which takes into account bursting of bubbles when micro debris and small droplets are expelled. Total change of the layer thickness is sum of two expressions given by Eq. 68 and Eq. 72.

2.7.1.2. Recoil forces

Absorption of the laser beam results in heating and melting of the solid metal, increases surface temperature, T_s, of the melt and produces recoil pressure and consequent ejection of the melt from the interaction zone. Melt ejection and evaporation result in a decrease in the melt thickness and melting of a new portion of the solid metal.

The main difficulty in the application of the melt ejection model to study the critical conditions for the initiation of liquid metal expulsion is that the retarding effect of

surface tension is not considered. Thus, a precondition for the application of the model is that the vapor recoil force must be significantly higher than the surface tension force.

Basu and DebRoy (1992) established that the peak temperature must exceed a critical temperature for liquid metal expulsion to occur. Furthermore, they demonstrated that the transition from melting to expulsion can be understood from the fundamental principles of transport phenomena. According to Basu and DebRoy (1992), value of the maximum weld pool surface temperature and just before the initiation of liquid metal expulsion can be determined from the following criterion: liquid expulsion takes place when the vapor recoil force overcomes the surface tension force of liquid metal at the periphery of keyhole pool. The recoil force, R, is calculated from the relation

$$R = 2\pi \int_{0}^{r_0} r\Delta P(r)dr \quad , \tag{73}$$

where r_0 is the radial distance at which the surface temperature is equal to the boiling point and $\Delta P(r)$ is the difference between the local equilibrium vapor pressure and the atmospheric pressure and is a function of radial distance from the beam axis. The calculated values of the surface tension force at the periphery of the weld pool, $2\pi r_0 \sigma$, where, σ is the surface tension at the melting point, and the recoil force for various values of T_0, for iron, are shown in Fig. 2.38. It is observed that the recoil force is a strong function of the peak temperature. The value of T_o for which the recoil and surface tension forces are equal is the critical temperature for liquid expulsion. Liquid expulsion from stainless steel can take place when the temperature at the center of the pool, T_o, reach a critical temperature, T_c, which is 3,380 °K,

159
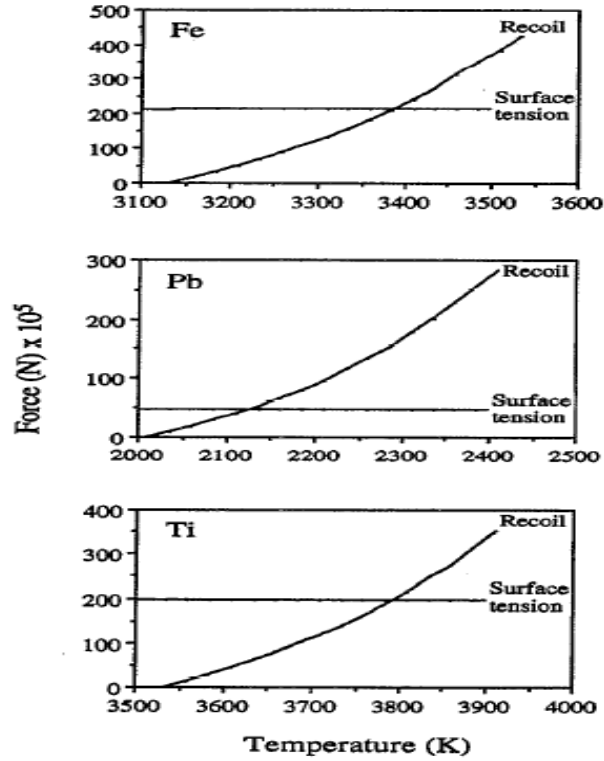
Fig. 2.38. The recoil force as a function of peak surface temperature
and the surface tension force at the melting point (Basu and DebRoy, 1992).

During laser irradiation, the rise and decay of the peak temperature at the surface

of a metal can be determined from (Basu and DebRoy, 1992) to be

$$T_0 - T_0^0 = 2I\sqrt{\frac{t}{\pi k \rho\, c_p}} \quad for \quad t \le t_p \quad , \tag{74}$$

$$T_0 - T_0^0 = 2I\sqrt{\frac{t}{\pi\, k\, \rho\, c_p}} - \sqrt{\frac{t - t_p}{\pi\, k\, \rho\, c_p}}\, for \quad t \ge t_p \quad . \tag{75}$$

where T_o and T_0^0 are the peak temperature at time t and just prior to irradiation

respectively, I is the local intensity of absorbed laser radiation, $k, \rho,$ and c_p are the thermal

conductivity, density, and specific heat of the metal, respectively. The temporal

temperature profile calculated from Eqs 74 and 75 neglects the effects of phase change,

160

variable material properties, and weld pool convective heat transport, but allows rough

estimation of the changing peak temperature on the surface. The temporal surface

temperature profiles for stainless steel irradiated by single pulses of length 0.5 and 1.0 ms

are presented in Fig. 2.39, (Basu and DebRoy, 1992). It is observed that for a pulse

length of 0.5 ms, the peak temperature reached is significantly lower than the minimum

peak temperature of 3380 K, required for liquid expulsion to occur. However, for a pulse

length of 1.0 ms the peak temperature exceeds the critical temperature. The results are

consistent with the experimental data. It should be noted that, although there is good

agreement between the predicted and the observed condition for expulsion, the equations

employed are not exact and the computed temperatures provide dependable trends, but

not rigorously computed temperature data.
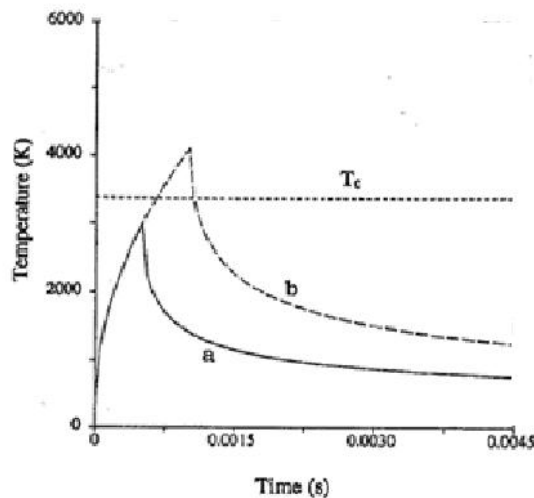
Fig. 2.39. Peak temperature vs time for a stainless steel sample irradiated by single
pulses of (a) 0.5 and (b) 1.0 ms durations (Basu and DebRoy, 1992).

Even for a small increase in temperature above the critical temperature for metal

expulsion, Fig. 2.40, the liquid experiences a large acceleration and is immediately

161

expelled. This conclusion is supported by the observation that after commencement of

the expulsion of liquid metal, no residual liquid metal is observed in the cavity. When

the peak temperature at the center of the pool exceeds the critical temperature, T_c, liquid

expulsion takes place. When molten metal is expelled from the weld pool, the laser beam

gets defocused resulting in a decrease in the heat flux. As a result, the peak temperature

may drop below the critical value and no further expulsion may take place. Thus, the

extent of melting at the time when the critical temperature is reached determines the

amount of liquid metal expelled.
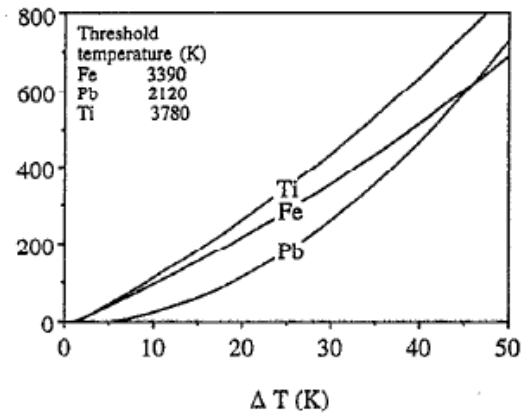
Fig. 2.40. Dimensionless acceleration of liquid metal as a function of the difference
between the peak surface temperature and the critical temperature
for expulsion, $\Delta T = T_s - T_c$ (Basu and DebRoy, 1992).

Application of the thin boundary layer assumption allows the pressure across the

molten layer to be approximated by the evaporation recoil pressure, p_r, applied to the

melt surface. The evaporation-induced recoil pressure generates melt flow with the

dominant direction being that in which the recoil-pressure gradient is the highest.

Assuming that a steady state has been reached and the distribution of the recoil pressure

along the short axis of the spot, x- or y-axis, is close to uniform, then the melt flow is a

162

one-dimensional flow and we can use Bernoulli's equation to relate the melt velocity v_m

at the edge of the laser spot to the value of the recoil pressure, p_r, (Semak and

Matsunawa, 1997)

$$p_r = \frac{\rho_m \cdot v_m^2}{2} \quad .$$

(76)

The recoil pressure is proportional to the saturated vapor pressure p_s, (Semak and

Matsunawa, 1997) which in turn depends on the melt's surface temperature T_s.

Application of the thin boundary layer assumption allows the pressure across the molten

layer to be approximated by the evaporation recoil pressure, p_r, applied to the melt

surface. Using the results presented in Anisimov et al., 1971, one can show that the

evaporation recoil pressure at the surface is related to the surface temperature, T_s,

according to the equation

$$p_r = A_{amb} B_0 T_s^{-\frac{1}{2}} \exp\left(\frac{-U}{T_s}\right) \quad ,$$

(77)

where, A_{amb} is an ambient pressure dependent coefficient, and B_0 is the evaporation

constant, and the parameter U is the energy of evaporation per atom defined as

$$U = \frac{M \cdot H_v}{N_a k_B} \quad ,$$

(78)

where: H_v is the latent heat of vaporization (per unit mass), k_B is Boltzmann's constant, M

is the atomic mass, and N_a is Avogadro's number. According to the calculations

performed by Anisimov and Khokhlov (1995), the coefficient A_{amb} depends on the

ambient pressure and its value varies from 0.55 for evaporation in vacuum to unity for the

case of evaporation under a high ambient pressure. Calculations (Anisimov and

Khokhlov, 1995) also have shown that, for practical values of the ambient pressure, the coefficient A_{amb} is close to its minimal value of 0.55.

The approximation of the thin boundary layer allows one to model the melt flow using quasi-one-dimensional equations in conservative form represented by a modification of the St. Venant equations for incompressible open-channel flow for the case of mass source (heating) due to melting and mass sink (cooling) due to evaporation

$$\frac{\partial(\delta)}{\partial t} + \frac{1}{r}\frac{\partial(r \cdot v_r \cdot \delta)}{\partial r} = -v_{dv} + v_m \quad , \tag{79}$$

$$\frac{\partial(v_r \delta)}{\partial t} + \frac{1}{r}\frac{\partial}{\partial r}\left[r\left(\delta \cdot v_r^2 + \frac{p\delta}{\rho}\right)\right] = \frac{p}{\rho}\left(\frac{1}{r}\frac{\partial \delta}{\partial r}\right) + \frac{\delta \cdot v_r^2}{r} - \left(v_{dv} - v_m\right)v_r - \frac{\mu_m}{\rho}\frac{v_r}{\delta} \quad , \tag{80}$$

where the r direction is along the melt surface, the z direction is normal to the melt surface, δ is the melt thickness, v_r is the radial melt flow velocity averaged over the melt layer thickness, and μ_m is the melt viscosity. The second term on the right-hand side of Eq. 80 represents deceleration/acceleration due to mass addition/loss determined by the combined effect of melting and evaporation. The third term on the right-hand side of Eq. 80 represents the effect of melt viscosity. Examining Eq. 79 one can easily see that the second term on the left-hand side and the first term on the right-hand side represent the components of melt surface velocity determined by melt ejection, v_{dm}, and melt evaporation, v_{dv}, respectively. Thus the velocity of the melt surface, or the 'drilling' velocity, v_d, is given by

$$v_d = \frac{1}{r}\frac{\partial(rv_r\delta)}{\partial r} - v_{dv} = -v_{dm} - v_{dv} \quad . \tag{81}$$

164

In formulating problem of interaction of laser beam with materials, one can assume radial symmetry, together with an incompressible molten substrate ejected from the irradiated spot as the surface reaches an elevated temperature. Taking into consideration the radial motion of the melt with an average velocity v_r determined by Eqs 79 and 80, and normal to the melt surface motion of the melt-vapor interface with velocity v_d determined by Eq. 81, one can write the heat transfer equations for the liquid and solid phases in the following form (Semak et al., 1999):

$$\frac{\partial T}{\partial t} + v_r \frac{\partial T}{\partial r} + v_d \frac{\partial T}{\partial z} = \frac{k_l}{\rho_l c_l}\left(\frac{\partial^2 T}{\partial r^2} + \frac{\partial^2 T}{\partial z^2} + \frac{1}{r}\frac{\partial T}{\partial r} \right) \quad , \tag{82}$$

$$\frac{\partial T}{\partial t} + v_d \frac{\partial T}{\partial z} = \frac{k_s}{\rho_s c_s}\left(\frac{\partial^2 T}{\partial r^2} + \frac{\partial^2 T}{\partial z^2} + \frac{1}{r}\frac{\partial T}{\partial r} \right) \quad , \tag{83}$$

where the subscripts "l" and "s" refer to the liquid and solid phases and ρ, c, T, and k and the density, specific heat, temperature and heat conductivity, respectively.

If the steady-state regime of evaporation and melt ejection is reached then both the melting front and the melt-vapor interface propagate inside the material along the z axis with constant "drilling" velocity v_d, for the material removal stage. In this case, following the conservation of mass, the melting rate of the solid metal equals the sum of the vaporization and melt ejection rates, (Semak and Matsunawa, 1997)

$$\frac{dm_s}{dt} = \frac{dm_m}{dt} + \frac{dm_v}{dt} \quad , \tag{84}$$

where m_s is the mass of metal melted, m_v is the mass of melted metal that was vaporized, m_m is the mass of melted metal that was ejected. The left-hand side of Eq. 84 is the melting rate of the solid and, the first and second terms on the right-hand side of the

equation represent the vaporization and melt ejection rates, respectively. Rewriting Eq. 84 for a hole diameter equivalent to the laser spot diameter of $2\omega_0$ gives

$$\pi \cdot \omega_0^2 \cdot \rho_s \cdot v_d = 2\pi \cdot \omega_0 \cdot \delta_m \cdot \rho_m \cdot v_m + 2\pi \cdot \omega_0 \cdot \rho_m \cdot v_{dv} \quad , \tag{85}$$

where, ρ_s and ρ_m are the densities of the solid and liquid phases, correspondingly, δ_m is the melt-layer thickness at the edge of the laser spot, v_m is the melt-ejection velocity along the short spot axis (the x axis) at the edge of the spot and v_{dv} is the evaporation front's velocity, directed along the z. Calculating the 'drilling' velocity, v_d, from Eq. 85 gives

$$v_d = 2\frac{\rho_m}{\rho_s}\frac{\delta_m}{\omega_0} \cdot v_m + \frac{\rho_m}{\rho_s} \cdot v_{dv} \quad . \tag{86}$$

After assumption that during steady-state front propagation with velocity v_d, the melt thickness is approximated as

$$\delta_m \approx \kappa_m / v_d \quad , \tag{87}$$

where, κ_m is the thermal diffusivity of the melt metal, then by substitution Eq. 87 into Eq. 86 and solving the quadratic equation and taking only the positive solution gives

$$v_d = \frac{1}{2}\left\{ \frac{\rho_m}{\rho_s} \cdot v_{dv} + \left[\left(\frac{\rho_m}{\rho_s} \cdot v_{dv} \right)^2 + 8\frac{\rho_m}{\rho_s}\frac{a_m}{\omega_0} \cdot v_m \right]^{0.5} \right\} \quad . \tag{88}$$

In analytical calculations, the value of the evaporation front velocity, v_{dv}, in Eq. 88 can be determined by the melt's surface temperature T_s (i. e., for iron the temperature distribution of melt surface is shown in Fig. 2.41) and is described by Eq. 164.
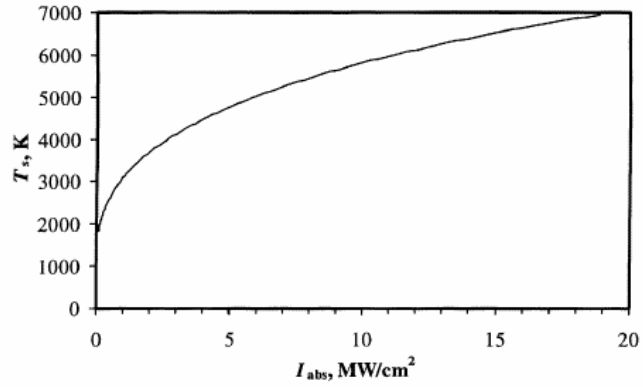
Fig. 2.41. The temperature dependence of the melt surface of iron on the absorbed laser intensity for a laser beam radius of $\omega = 1.9 \, x10^{-2}$ cm (Semak and Matsunawa, 1997).

In analytical calculations value of drilling velocity and melt ejection velocity can be estimated by taking values from the graphs shown in Fig. 2.42, and Fig. 2.43.
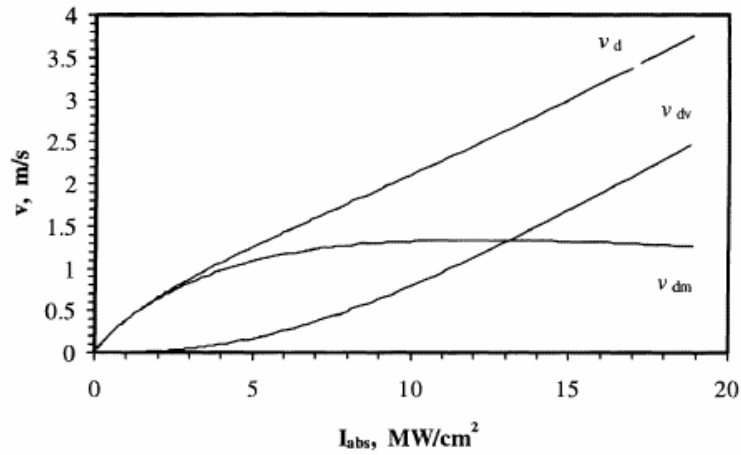
Fig. 2.42. Dependence of the drilling velocity v_d and its components, v_{dm} and v_{dv} on the absorbed laser intensity for the case of iron and a laser beam radius of $\omega = 1.9 \, x10^{-2}$ cm (Semak and Matsunawa, 1997).

167
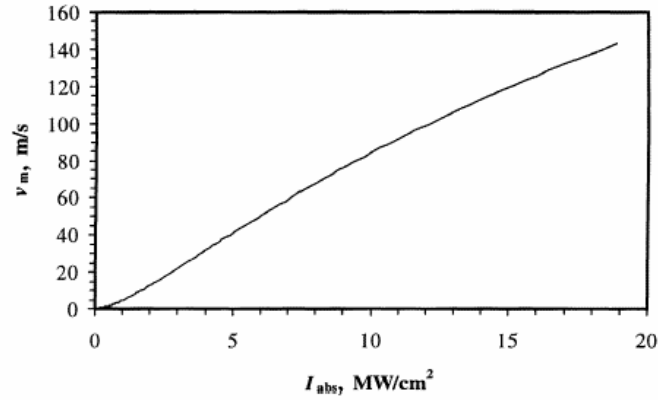
Fig. 2.43. The dependence of the melt velocity of iron on the absorbed laser intensity for a laser beam radius of $\omega = 1:9\, x10^{-2}$ cm (Semak and Matsunawa, 1997).

2.7.1.3. Energy balance in the molten layer and effect of assist gas pressure

The effect of the pressure induced on the melt surface when an assist gas jet is used during laser drilling is considered. It can be shown that for frictionless and adiabatic (isentropic) gas flow the total pressure along a streamline is constant and equals to the sum of the static and dynamic pressures (Fieret and Ward, 1986). The total pressure is often called the stagnation pressure since it is the static pressure of the gas if its velocity was isentropically reduced to zero. Since the hole bottom is assumed to be perpendicular to the gas axis, Fig. 2.44, and by assuming uniform assist gas pressure within the laser beam and zero outside the beam, the dynamic gas pressure can be neglected. At the nozzle exit the gas has accelerated up to the local speed of sound leading to the critical state due to adiabatic expansion of the

$$ p_c = \left(\frac{2}{\gamma + 1} \right)^{\gamma(\gamma - 1)} p_i \quad , \tag{89} $$

where the assist gas pressure at the nozzle exit, p_c, is determined by the assist gas pressure inside the nozzle, p_i. For diatomic gases such as O_2, the specific heat ratio, $\gamma = 1.4$. For simplicity the critical state is assumed to be found at the laser-drilled hole entrance, but with a reduced pressure due to the radial expansion of the gas outwards from the hole. Estimate of the reduced pressure is made by considering the geometrical areas of the gas flow entering the hole cavity and the gas flow that flows radially outwards as shown in Fig. 2.44 expressed as

$$A_{eff} = \pi\, \omega_0^2 \quad , \tag{90}$$
$$A_{\omega_0} = d_n \pi\, z_0 \quad , \tag{91}$$

where A_{eff} is the effective area of flow entering the hole defined by the laser beam radius, ω_0, since zero assist gas pressure outside the beam was assumed, $A_{\omega 0}$ is the cylindrical area where the radial loss of gas pressure flows as defined by the nozzle exit diameter, d_n and nozzle-workpiece distance, z_n. As a result of these two flows, the assist gas pressure, p_c, at the nozzle exit is reduced to p_{eff} as follows

$$p_{eff} = p_c \frac{A_{eff}}{A_{eff} + A_{\omega_0}} = f(p_i) \quad , \tag{92}$$

where, p_{eff} is the effective static gas pressure of the assist gas acting in the same direction as the recoil pressure on the melt surface, and $f(p_i)$ stands for the functional dependence on the inner gas pressure inside the nozzle. The pressure of the assist gas jet can be considered by adding the effective static gas pressure to the left-hand side of Eq. 92, yielding

$$p_r + p_{eff} = \frac{\rho_m v_m^2}{2} \quad . \tag{93}$$

Clearly, it can be seen from Eq. 93, that depending on the magnitude of p_{eff} the use of an assist gas jet will provide an additional momentum and will increase the melt eject velocity to allow faster melting of a new portion of the solid metal.

The following considers the energy balance in the molten layer exposed to the laser beam and O_2 assist gas when steady-state melt ejection from the interaction zone (i.e., hole bottom) is reached. In the coordinate system related to the melting front the solid is moving towards the melt front with velocity v_{dv}, melts and then the melt is partially ejected by the recoil pressure radially with velocity v_m and partially evaporated from the melt surface. The input power of the molten layer can be given as

$$P_l^{in} = I_{abs} \, \pi \, \omega_0^2 + P_{rp} \quad , \tag{94}$$

where I_{abs} is the absorbed laser intensity, and ω_0 is the laser beam radius (the area of the incident laser beam, A_l), and P_{rp} is the reactive power generated due to oxidation when an O_2 assist gas is employed.
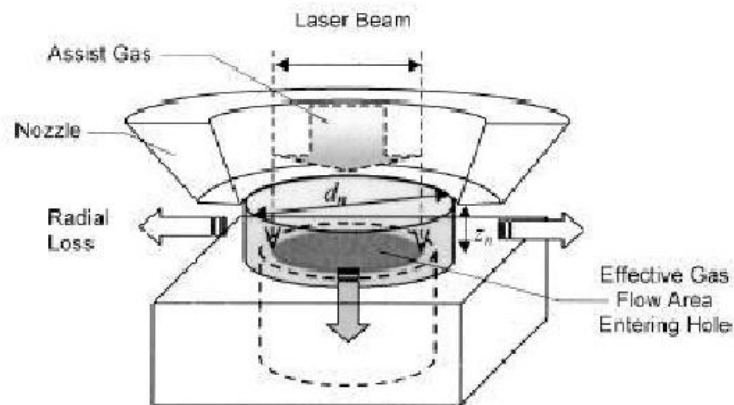
Fig. 2.44. Schematic of effective gas flow area entering hole defined by the laser beam diameter $2\omega_0$ and the cylindrical area of radial loss flow (Fieret and Ward, 1986).

2.7.1.4. Forced convection cooling by assist gas.

Many researchers have found that cooling by the assist or shroud gas can have a significant effect in laser materials processing, especially for low laser intensity processes such as high power diode laser removal of multilayer chlorinated rubber and diode laser welding of thermocouples. From work studying the laser cutting of metals, it was generally found that the cooling provided was reasonably small, except for very large flow rates. However, little work has been conducted to investigate the possible effects of assist gas cooling during laser drilling. As an approximation, the case of forced convection perpendicular to a plate has been considered as shown in Fig. 2.45. The heat transfer by forced convection between the melt surface at the hole bottom and the gas flowing perpendicular to the melt surface is simulated. The considered area is defined by the laser beam spot size, whereby the heat transfer between the hole walls and the assist gas is assumed negligible. This is a reasonable approximation since the main concern is to investigate the cooling rate of the melt surface, which directly affects the drilling velocity. First, the Reynolds number for the assist gas flow can be expressed as

$$\text{Re} = \frac{v_g 2\omega_0 \rho_g}{\mu} \quad , \tag{95}$$

where r_g is the assist gas density, n_g is flow velocity of the assist gas, μ is the dynamic viscosity of the gas and the width of the melt surface is approximated by the laser beam spot size $2\omega_0$. The convective cooling rate per unit area, Q_c, between the impinging assist gas and the melt surface is

$$Q_c = -h_c (T_s - T_i) \quad , \tag{96}$$

where T_s and T_i are the melt surface and assist gas temperatures respectively, h_c is the heat transfer coefficient, which can be determined from

$$h_c = \frac{k_g}{2\omega_0} C_c \, \mathrm{Re}^{n_c} \, \mathrm{Pr}^{1/3} \quad , \tag{97}$$

where k_g and Pr are the thermal conductivity and Prandt number of the assist gas respectively, C_c and n_c are the constants for forced convection perpendicular to the melt surface plate.
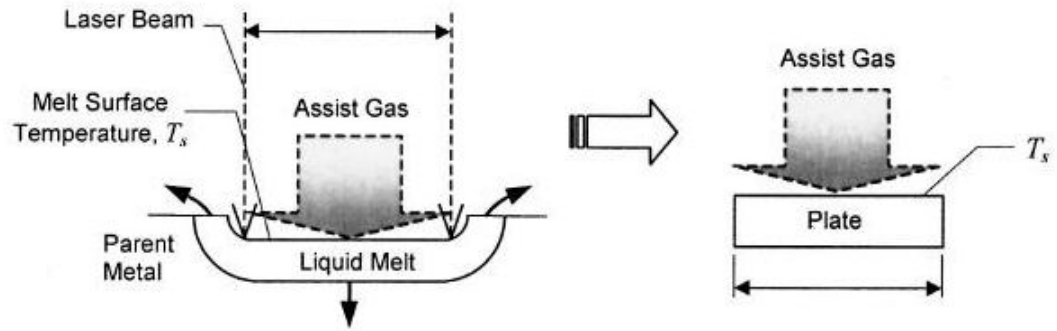
Fig. 2.45. Approximation of the forced convection cooling of the melt surface by the assist gas at the hole bottom (Semak et al, 1999).

Combining Eqs 95 to 97, the power lost due to cooling by the assist gas, $P_{cooling}$ within the melt surface area can be estimated to be

$$P_{cooling} = \frac{c_c k_g}{2} \left(\frac{2 v_g \omega_0 \rho_g}{\mu} \right)^{n_c} \mathrm{Pr}^{1/3} \, (T_s - T_i) \pi \omega_0^2 \quad , \tag{98}$$

It is important to mention that due to the complexity in the evaporation from surfaces, the above forced convection cooling analysis is treated as a first approximation. For example, if substantial evaporation is achieved a Knudsen layer may exist and the cooling effect may be affected (Semak et al, 1999).

An exothermic reaction is generated when the assist gas contains O_2, whereby the

O_2 would chemically react with the melt surface to generate an additional heat (Adams,

1970). Since O_2 assist gas is often used in most practical laser drilling processes, it is

therefore important to consider the contribution of the exothermic reaction in the model.

During the drilling process, the elements within the metal or alloy would be oxidized and

thus forming various oxide phases. In general, the total chemical equation for the

reaction between a metal, Me, and oxygen gas, O_2, to form an oxide Me_aO_b may be

written as

$$aMe+(b/2)O_2-> Me_aO_b .$$ (99)

Using X-ray diffraction (XRD), or wet chemical analyses, (Ivarson, et al., 1991), it is

possible to identify the principal oxide phases formed by analyzing the spatter or ejected

material. Consequently, in order to quantify additional thermal input, the heat generated

to transform each metal element to their relevant oxide phases, especially in alloys, needs

to be considered separately. Fundamentally, the rate of reaction is determined by the

drilling velocity or cutting speed, as it controls the rate at which the material is being cut

or drilled and thereby subjecting the melt to oxidation. Using the drilling velocity, v_d,

described in Eq. 86, the absolute reaction rate, R_{oe} (mol/s), for a particular metal element

in consideration is

$$R_{oe} = \frac{v_d \pi \omega_0^2 \rho_m}{M_{r,oe}} ,$$ (100)

where, $M_{r,oe}$ is the relative atomic mass of the metal element in consideration. The

numerator on the right-hand side of Eq. 100 is the rate of mass removal. Consequently,

the heat generated due to the oxidation of a particular element can be given as (Ivarson, et al., 1991)

$$P_{r,oe} = \frac{v_d \pi \omega_0^2 \rho_m}{M_{r,oe}} m_{oe} \Delta H_{ox} \quad , \tag{101}$$

where, m_{oe} is the estimated percentage mass of the element in consideration that is oxidized, ΔH_{ox} is the reaction heat of oxidation to form the particular oxide. For low carbon steel, the preferred oxidation is $Fe + 1/2 O_2 -> FeO$ and $\Delta H_{ox} = 158.75$ kJ/mol (Barin and Knacke, 1973). The total heat generated due to the oxidation of different elements for a particular metal or alloy in consideration can be described as follows

$$P_{rp} = \sum_{i=1}^{m_0} \frac{v_d \pi \omega_0^2 \rho_m}{M_{r,oei}} m_{oei} \Delta H_{oxi} \quad , \tag{102}$$

where, m_{oei} is the number of significant oxide phases that were formed for a particular metal or alloy.

The output power of the molten layer is composed of a conduction term, P_{cond}, a convection term, P_{conv}, a vaporization term, P_{vap}, a radiation term, P_{rad}, as well as the cooling term when an assist gas is used as follows:

$$P_l^{out} = P_{cond} + P_{conv} + P_{rad} + \cdot P_{cooling} \quad . \tag{103}$$

It has been shown that the radiation related energy transfer from the melt layer is relatively small and can be neglected (Semak and Matsunawa, 1997). The conduction term can be estimated from the sum of ''forward'' and ''radial'' components, i.e.,

$$P_{cond} \approx -k_s \nabla_{forward} T \pi \omega_0^2 - k_s \nabla_{radial} T \pi \cdot \omega_0^2 \quad , \tag{104}$$

where k_s is the thermal conductivity of the solid metal and the gradients of temperature are taken at the melt front along "forward" and perpendicularly "radial" to the motion of the retreating solid metal. The "forward" component can be given as

$$-k_s \nabla_{forward} T \, \pi \, w_0^2 = k_s \frac{T_m - T_0}{\kappa_s / v_d} \pi w_0^2 = \rho_s c_s (T_m - T_0) v_d \pi w_0^2 \quad , \tag{105}$$

where κ_s is the thermal diffusivity of the solid metal. The "radial" component can be estimated as (Semak and Matsunawa, 1997)

$$-k_s \nabla_{radial} T \, \pi \, \omega_0^2 \approx k_s \frac{T_m - T_0}{\left[\frac{\kappa_s}{v_d} \left(\omega_0 + \frac{\kappa_m}{v_d} \right) \right]^{1/2}} \pi \, \omega_0^2 \approx \frac{\rho_s c_s (T_m - T_0) v_d}{\left(\frac{\kappa_m}{\kappa_s} + \frac{v_d}{\kappa_s} \omega_0 \right)^{1/2}} \pi \, \omega_0^2 . \tag{106}$$

Since the "forward" component is used to pre-heat the solid metal, only the "radial" component is considered as losses of energy from the melt layer. Knowing the melt thickness, δ_m, the power spent for convection can thus be expressed as follows:

$$P_{conv} = 2\pi \, \pi \, \omega_0 \rho_m \left(c_m T^* + L_m \right) v_e \delta_m \approx 2\pi \, \omega_0 \rho_m \left(c_m T^* + L_m \right) \cdot \frac{v_e \kappa_m}{v_d} \quad , \tag{107}$$

where T^* is the average temperature in the melt layer, defined as

$$T^* = T_m + \alpha (T_s - T_m) \quad , \tag{108}$$

where T_m is the melting temperature, T_s is the surface temperature of the melt, and α is a constant smaller than unity. By taking into account of the vaporization front velocity, v_{dv}, the power used for vaporization is given as

$$P_{vap} = \rho_m v_{dv} H_v \, \pi \, \omega_0^2 \quad , \tag{109}$$

where the velocity of the evaporation front, v_{dv}, is determined by Eq. 164 and H_v is the latent heat of evaporation.

By combining Eqs. 94 to 109 and equating the absorbed laser intensity, I_{abs}, to the left-hand side of the Eq. 94 gives

$$I_{abs} = \left[2\rho_m \left(c_m T^* + H_m \right) \frac{v_m \kappa_m}{v_d w_0} + \rho_s c_s (T_m - T_0) v_d \right] +$$

$$- \sum_{i=1}^{m_0} \frac{v_d \pi \omega_0^2 \rho_m}{M_{r,oei}} m_{oei} \Delta H_{oxi} + \frac{c_c k_g}{2 w_0} \left(\frac{\omega_0 \rho_g v_g}{\mu} \right)^{n_c} \cdot \mathrm{Pr}^{1/3} (T_2 - T_1) + , \qquad (110)$$

$$+ \frac{\rho_s c_s (T_m - T_0) v_d}{\left(\frac{\kappa_m}{\kappa_s} + \frac{v_d}{\kappa_s} w_0 \right)^{1/2}} + \rho_m v_{dv} H_v$$

As can be seen from the forgoing considerations, drilling velocity and its components such as vaporization front velocity and recoil pressure, as well as the absorbed laser intensity and its fractions expended for heating, melting and, conduction and vaporization losses are expressed through Eqs 87, 88, 90, 91, 92, 106, 109. These equations implicitly depend on the thermophysical properties of the metal, the surface temperature of the melt as well as the geometrical properties of the laser beam. In addition, the possible effects of using O_2 assist gas have been considered. The momentum provided by the assist gas jet, which principally affects the melt eject velocity, v_m, is estimated through Eqs. 92 and 93. Using thermophysical properties collected in Table 5, the forced convection cooling by the assist gas on the melt surface can be estimated by Eq. 97 and related to the energy balance in Eq. 110. The additional energy generated due to the exothermic reaction is expressed in Eq. 102 and finally considered in the energy balance in Eq. 110.

176

Semak and Matsunawa (1997 reached similar conclusions defining absorbed laser energy. They also expressed the "drilling" velocity v_d and the melt ejection velocity v_m as a function of the surface temperature T_s of the melt using Eq. 110.

Table 5. Thermophysical properties of O_2 assist gas and gas nozzle parameters (Semak and Matsunawa, 1997).

O_2 Assist Gas Property	Value
Nozzle pressure, p_i (N/cm^2)	30
Gas flowrate, f_g (l/min)	40
Gas flow velocity, v_g (m/s)	377
Density of gas, ρ_g (10^{-3} g/cm^3)	1.3007
Dynamic viscosity of gas, μ (10^{-5} Ns/m^2)	2.01
Prantl number, Pr	0.73
Thermal conductivity, k_g (W/cm K)	2.59×10^{-4}
Temperature of assist gas, T_i (K)	300
Nozzle exit diameter, d_n (cm)	0.15
Nozzle-workpiece distance, z_n (cm)	0.22
Forced convection constant, C_c	0.228
Forced convection constant, n_c	0.731

Equation 110 gives an implicit dependence of the melting front velocity and its component, absorbed intensity, and the thermo-physical parameters of the workpiece as the function of the melting surface temperature. Therefore, by selecting a proper range of the melting surface temperature, the range of the recoil pressure and the melting front can be calculated.

2.7.2. Thermal energy balance concept

The energy balance within the interaction zone between the laser beam and workpiece is the key point in modeling laser material processing, especially for laser

machining on metals, where losses due to high reflectance and greater thermal conductivity are significant. The laser parameters have to be balanced in metal drilling to the material properties like absorptivity and thermal diffusivity. The drilling process is influenced by melt expulsion, absorption, and refraction of laser radiation in the expanding vapor plasma. A block diagram for various processes of material removal and their mutual influence for laser drilling is shown in Fig. 2.46.

The energy balance within the interaction zone between the laser beam and matter is the key point in modeling laser keyhole welding and cutting of metals. The error in estimating the relative values of various components in the balance equation can change not only the quantitative, but also the qualitative, character of the numerical results in, for example, calculation of the thermal field induced in the sample during laser treatment. Another important aspect, closely related to the energy balance problem, is the mechanism of the propagation of the beam-surface interface into a material. Its importance is determined by the fact that correct understanding of how the drilling, the welding, or cutting, front advances into the metal bulk will allow one to answer such vital questions as what is the expected penetration depth and where is the origin of instabilities affecting the quality of the process.
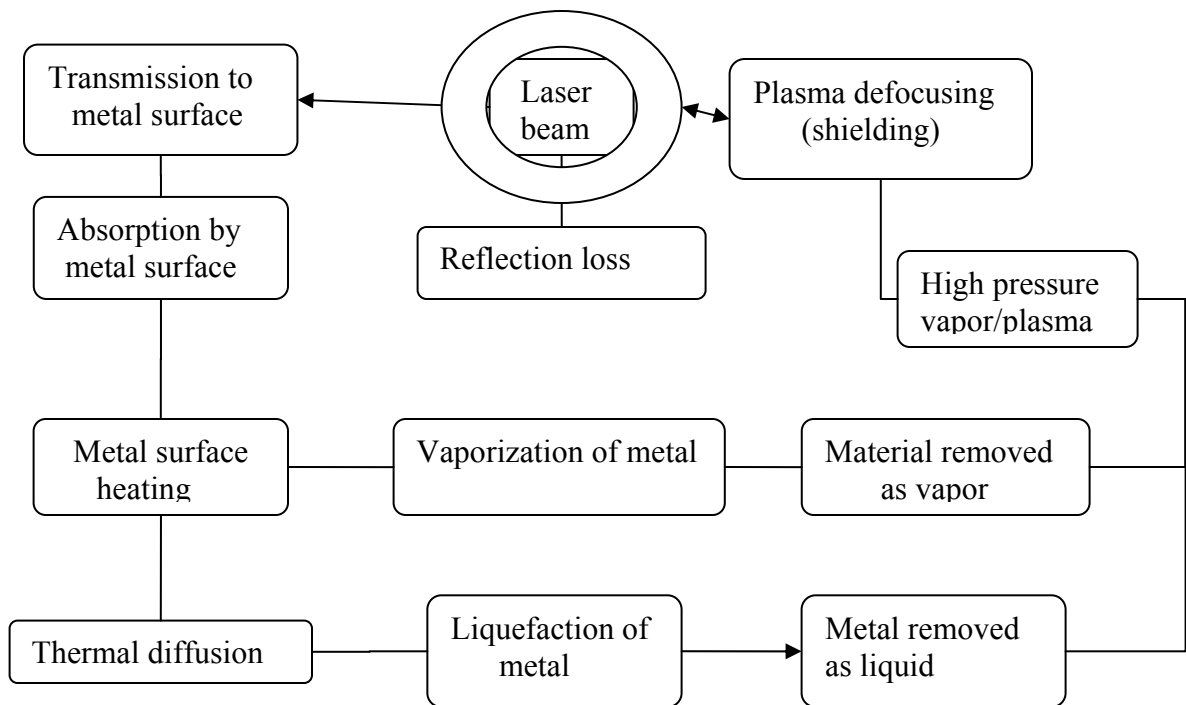
Fig. 2.46. Block diagram for the main processes of material removal and their mutual influences during laser drilling.

The thermal balance concept concentrates on coupling between incident laser radiation and reversible thermal response of a localized region on the metal. This process is best described as a constant pressure heat addition phenomenon, during which a material is being heated at constant pressure following a thermal response curve. During this phenomenon temperature vs. time relationship is characterized by four principal zones. The first zone represents the amount of constant pressure heat needed to bring the workpiece from room temperature of solid to molting temperature, T_m. The second zone represents the addition of heat needed to bring the workpiece completely from solid to molten phase. This is isothermal heat addition process called fusion. The third critical zone is a constant pressure heat addition, which brings the molten material up to its

179

boiling temperature, T_v. At the boiling point, the material undergoes another isothermal transformation, called vaporization. At this point the material reaches a gaseous, or vapor, state.

The total heat applied to bring the workpiece from room to vaporization temperature can be written as

$$Q_{total} = Mt \cdot c_p \cdot (T_m - T_a) + Mt \cdot H_f + Mt \cdot c_p \cdot (T_v - T_m) + Mt \cdot H_v \quad , \qquad (111)$$

where Mt is total mass of material in laser drilling zone (milligrams), c_p is specific heat of the material, H_f is latent heat of fusion, and H_v latent heat of vaporization.

2.7.2.1. Expulsion consideration

In laser microdrilling, material is removed as a mixture of melt and vapor. The proportions of which depend on material properties and laser beam intensity. Large amount of removed materials is advantageous from drilling efficiency point of view, but on the other hand can create more instability in the hole formation. The thicker the layer of melt, the less is defined the surface geometry, the more the hole geometry fluctuates.

The thickness of a layer molten during a laser pulse interaction with metals can be calculated and can be approximated as

$$\delta = 2\sqrt{\kappa \cdot t_p} \quad , \qquad (112)$$

where δ is molten layer thickness, κ is the thermal diffusivity, t_p is pulse duration (> 10 ps to be valid). Analyzing Eq. 112, the best way to increase drilling accuracy is by simply shortening the molten layer thickness by shortening the laser pulse time.

The molten material is ejected from the hole by the pressure gradient developed during the vaporization of the portion of the material. As a result more mass is removed compared to vaporization alone. The thermal balance model addresses expulsion concept directly in the heat transfer equations. Since the ejected material has to leave in molten form, our assessment accounts for all material ejected to leave when localized drilling zone reaches the molten state.

In order for melt displacement to occur, the evaporation recoil pressure must accelerate melt created anywhere in the fusion zone to a velocity sufficient for it to reach the edge of the melt pool during the portion of laser pulse remaining after the melting has occurred. Thus, an approximate criterion for the establishment of melt displacement can be formulated (Semak, el at., 2003)

$$t_{ej} = \frac{r_m}{v_m} \leq t_p - t_m \quad , \tag{113}$$

where t_{ej} is the time for melt displacement from the melt puddle, r_m is the melt puddle radius, v_m is the melt velocity averaged over the laser pulse duration, t_p, and t_m is the time to the initiation of surface melting.

Please note, that if condition in Eq. 113 is satisfied, then both keyhole welding and drilling can take place. The transition from welding to drilling requires application of another criterion, which describes whether surface tension at the melt edge is capable of retaining melt displaced from the beam irradiated area and forming a weld pool.

Considering the reflectivity and expulsion parameters the original thermal balance equation (given by Eq. 111) was modified to the first order approximation into

$$(1-R)Q_{total} = Mt \cdot c_p \cdot (T_m - T_a) + Mt \cdot H_f + (1 - M_{exp})Mt \cdot c_p \cdot (T_v - T_m) +$$
$$+ (1 - M_{exp})Mt \cdot H_v \quad , \qquad (114)$$

where, R is reflectivity and M_{exp} is expulsion fraction of material removed.

Boulmer-Leborgne et al. (1993) determined the mass of ablated materials, m, (Cu) for different irradiations and their results, Fig. 2.47, are in rather good accordance with the formula proposed by (Boulmer-Leborgne et al., 1993),

$$m = \frac{110 \cdot \Phi}{3 \cdot 10^{14}} \lambda^{-3/4} \quad , \qquad (115)$$

where Φ is the absorbed laser power density (W/cm^2). It is clear from Fig. 2.47, that short laser wavelengths favor the ablation process.

The average material removal rate in the laser drilling process can be obtained by the following fomula (Zhang and Faghri, 1999):

$$MR = \frac{2\pi\rho}{t_p} \int_0^\infty s_1(r, t_p)r dr \quad , \qquad (116)$$

will be compared with experimantal data and analysis, disscussed in the experimental part in Chapter 4.
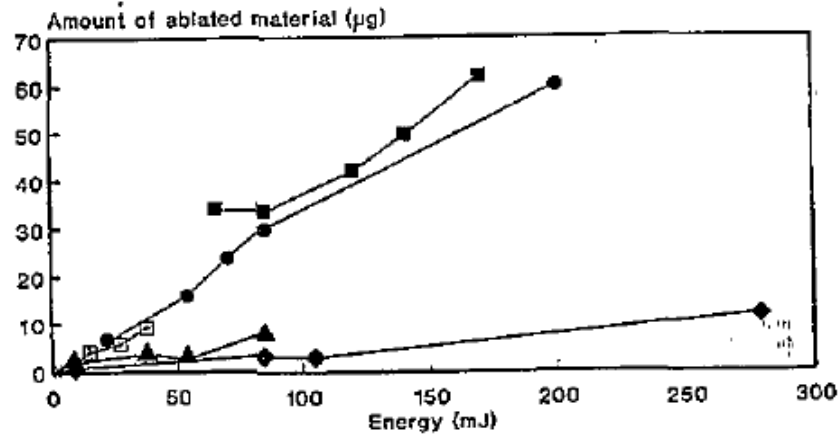
Fig. 2.47. Amount of ablated matter for different laser irradiations against absorbed laser energy (Boulmer-Leborgne et al., 1993), ¤ nitrogen, 337 nm; ● XeCI. 308 nm; □ Nd:YAG. 355" ▲ Nd:YAG, 532nm: ♦ Nd:YAG, 1064 nm; ■ ArF, 193 nm.

The comparison of calculated material removal rate, for the cases with and without conduction heat loss, and that of experimental data is shown in Fig. 2.48, (Zhang and Faghri, 1999). The experimental material removal rate was obtained by scaling micrographs of single shot drilled holes for pulse on time of 700 μs and radius of 0.254 mm at the Pratt and Whitney drilling facility (formarly) at North Haven, CT. It can be seen that the predicted materials removal rate with conduction heat loss is slightly lower than that without conduction heat loss, but the difference is less than 2%. This suggests that the overall effect of conduction heat loss on the material removal rates is not signicant. As can be seen from Fig. 2.48, the material removal rate predicted by the Zhang and Faghri's (1999) model is higher than that of experimental data for most cases. The possible cause of the over prediction may include uncertainty of absorptivity and possible partial laser beam blockage due to plasma, which is not taken into account in the

model. Considering these complicated phenomena, the agreement between calculated results and the experimental data is rather good.
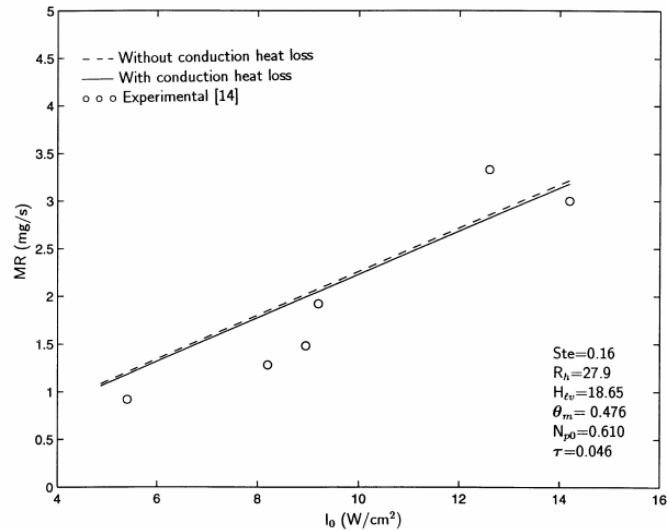
Fig. 2.48. Comparison of predicted and experimental material removal rate
(Zhang and Faghri, 1999).

Similar experiments were done by Voisey et al., (2000), and Veiko et al., (1980). More information on this subject and own experimental evidence in this field can be found in this Dissertation in the Section 4.3.2.

2.7.3. Threshold of laser micromachining

The metal surface is heated by the absorbed laser power up to the melting point and after a phase change finally to the vaporization temperature. The reflected radiation from the metal surface can influence the laser output via optical feedback. The threshold intensity, I_v, for material removal is determined by the losses due to surface reflection and

heat conduction into the material. The threshold is a function of beam radius, ω_0, at the metal surface, the processing time, t_p, the surface absorption coefficient, A, and the thermal diffusivity of the metal, κ. For a Gaussian intensity distribution the threshold intensity I_v is given by (Treusch and Herziger, 1986)

$$I_v = \frac{T_v k \sqrt{2\pi}}{A\omega_0 \, arctg\sqrt{8\kappa t_p / \omega_0^2}} \quad , \tag{117}$$

where T_v is the vaporization temperature, and k is thermal conductivity of the workpiece material.

A schematic representation of the dependences of melt displacement time and melting time as a function of pulse energy is shown in Fig. 2.49. Obviously, an increase in pulse energy results in a decrease of the displacement time, because, for a given pulse duration, a higher pulse energy corresponds to a higher beam intensity, a higher surface temperature, a higher evaporation recoil pressure and, consequently, a higher melt displacement velocity.
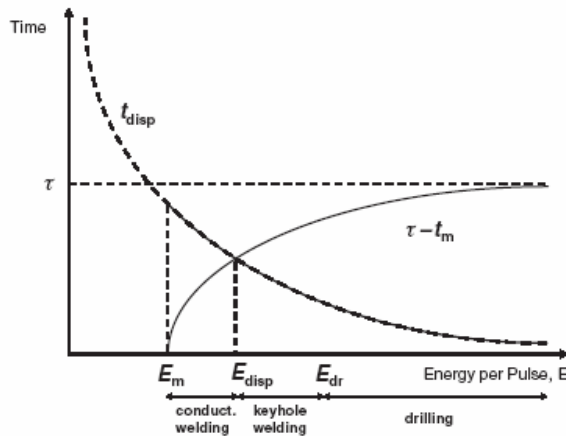
Fig. 2.49. Melt displacement time, t_{disp}, and portion of laser pulse remaining after beginning of surface melting, $\tau - t_m$, as a function of pulse energy (Semak el at., 2003).

Semak el at., (2003) concluded that the dependence of displacement time t_{disp} (presented in Fig. 2.49) versus pulse energies exists under the assumption that melt always exists on the surface. Of course, for energies lower than the melting threshold, E_m, the part of the curve representing displacement time has no physical meaning and is represented by a dashed line. For pulse energies greater than the melting threshold, the time when melt exists at the surface, $\tau - t_m$, increases. The melt existence time increases from zero when the pulse energy is equal to the threshold value E_m, and asymptotically approaches the pulse duration, τ. The displacement threshold E_{disp} indicates the laser pulse energy when the displacement time becomes equal to the melt existence time.

One can introduce a drilling threshold E_{dr}, corresponding to a condition when the velocity of melt displaced from the melt zone is high enough so that the dynamic pressure of the melt flow exceeds the (restraining) surface tension pressure at the melt pool edge. For pulse energies exceeding E_{dr}, drilling takes place. For pulse energies higher than the displacement threshold E_{disp} but less than the drilling threshold, E_{dr}, keyhole welding takes place. Lastly, for pulse energies between the melting threshold, E_m and the displacement threshold, E_{disp} so-called conduction limited welding takes place.

The position of the focal plane is known to have an effect on final shape of the hole as well as degree of penetration. As the laser focusing spot moves up and down, the laser material interaction area, z_F, varies according to expression, (Semak et al., 2003)

$$z_F = \omega_0 \left[1 + \left(\frac{\lambda_L z}{\pi \cdot \omega_0^2} \right)^2 \right]^{\frac{1}{2}} \quad , \tag{118}$$

where, λ_L is the laser light wavelength and ω_0 the laser beam radius at the beam waist. The incident power density is mainly determined by the focus-surface position, as is shown in Eq. 118. The optimal power density I_{mach} is identifying experimentally. In laser microdrilling using fiber optic cable, knowing the machining threshold is most critical for drilling to occur. Material is being drilled with a constant focal position, Eq. 118, and the removal stops when the depth z_{thresh} is obtained.

2.7.4. Consideration of the materials

In this Dissertation there were two vastly different materials considered: 304 stainless steel and single crystal silicon.

In the electronic industry, where components are often processed in a clean room environment, discharges of metal vapors are not acceptable. During laser microdrilling, especially during microwelding evaporation of alloying elements needs to be minimized. This is another reason to perform a qualitative understanding of evaporation materials (304 stainless steel) under consideration in laser processing.

Loss of alloying elements can result in significant changes in the microstructure and degradation of mechanical properties. He et al. (2003) and Moon et al. (2003) investigated the change in properties of aluminum alloy before and after welding using CO_2 laser with He gas shield. They found that the tensile properties of the welds were inferior to the base metal, mainly because of magnesium depletion, loss of strain hardened structure and porosity. They found that the hardness of weld metal was lower

than the base metal due to magnesium vaporization. The loss of hardness was contributed to a reduction in the solid strengthening effect of magnesium.

During laser micromachining, the main constituents of stainless steel vapor are iron, manganese, chromium, and nickel. In this Dissertation all properties of the material under investigation – 304 stainless steel was acquired either from manufacturer of the material or from the literature and are summarized in Table 6. Based on data obtained from steel's manufactures the 304 stainless steel samples had the following composition: 1.83wt%Mn, 18.1wt%Cr, 8.1wt%Ni, 0.39wt%Si, 0.04wt%C, 0.031wt% P, 0.002wt% S, 0.06wt% N and balance Fe.

In calculation of the laser micromachining commonly used material properties are: (for energy balance analysis) density, heat capacity, specific heat ratio, heat conductivity, heat diffusivity, latent heat, melting point, vaporization point; (for stress and momentum analysis): viscosity, modulus of elasticity, shears modulus, Poison's ratio, stress-strain constitutive relation. Typical basic material properties of stainless steel and single crystal silicon are summarized in the Table 6, Fig. 2.50, Fig. 2.51, and were used in calculations in this Dissertation.

Table 6. Properties of the materials used in this Dissertation (EMIS, 1988).

Nomenclature	Stainless steel 304	Single crystal silicon	Units
Density, ρ	$7.93 \cdot 10^3$	$2.33 \cdot 10^3$	$kg \cdot m^{-3}$
Latent heat of vaporization, H_v	$6.1 \cdot 10^6$	$5.97 \cdot 10^6$	J/kg
Latent heat of fusion, H_f	$2.73 \cdot 10^5$	$2.667 \cdot 10^5$	J/kg
Thermal conductivity k, at 23°C 500°C	16.2 21.4	14.1 43.0	$Wm^{-1}K^{-1}$ $Wm^{-1}K^{-1}$
Specific heat, c_p	0.50	0.70	$kJ \cdot kg^{-1}K^{-1}$
Melting temperature, T_m	1685	1683	°K
Vaporizing temperature, T_v	2910	2628	°K
Critical temperature, T_c	4074	5159	°K
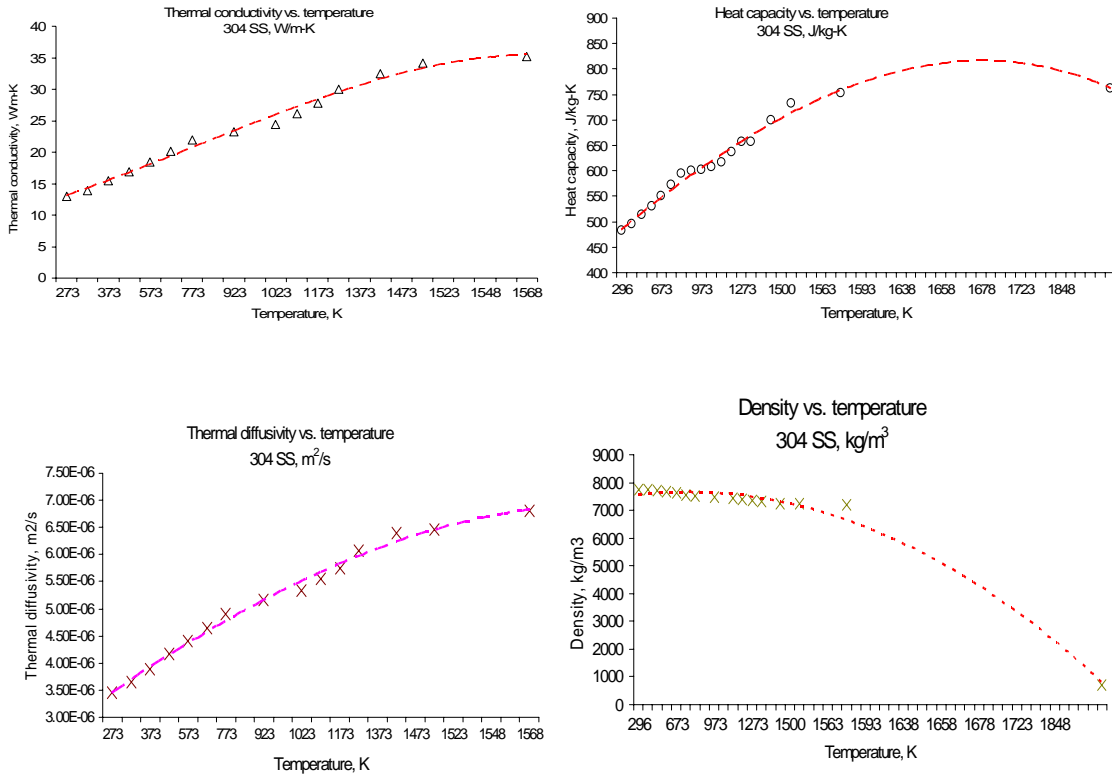
Fig. 2.50. Thermophysical properties of 304 stainless steel.
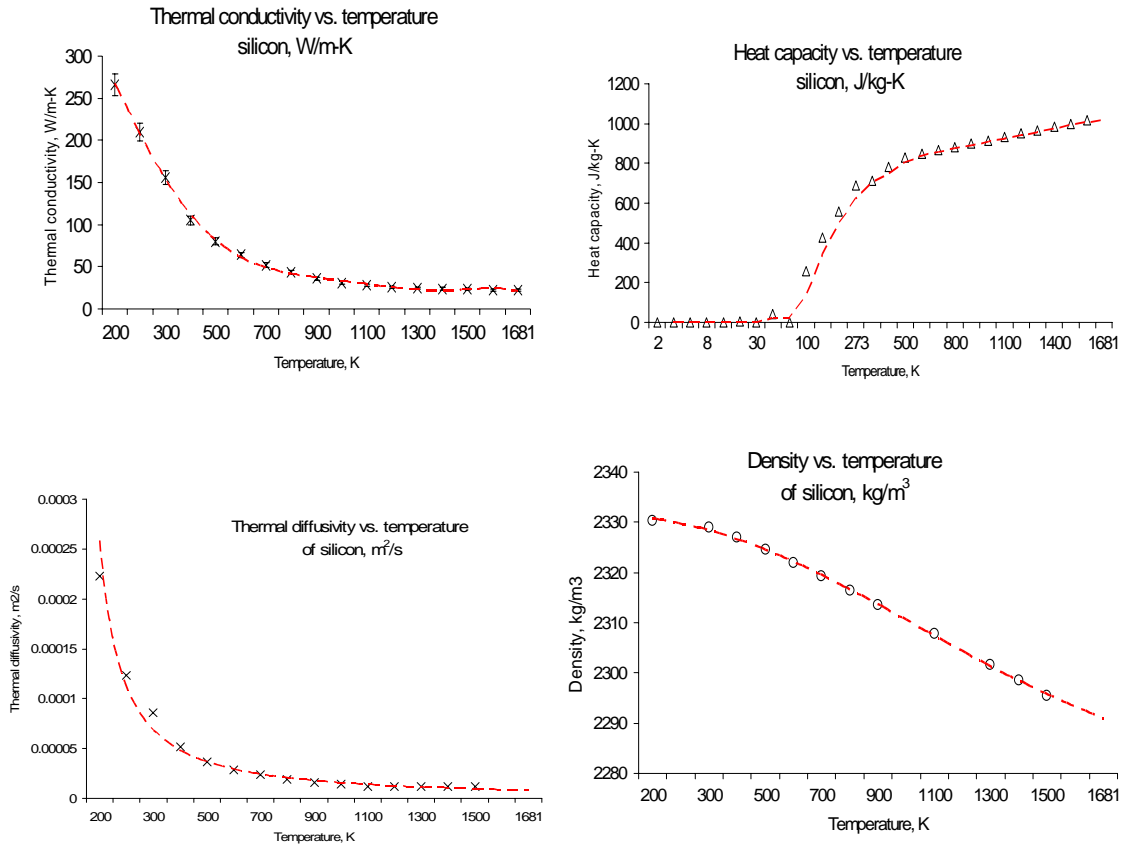
Fig. 2.51. Thermophysical properties of single crystal silicon (EMIS, 1988).

2.7.5. Mathematical formulation of the model

The mathematical model must be derived such that the parameters are easily handled. Once the model is verified by experiments, it can simulate the process and provide information such as heat-affected zone, transient temperature distribution, and cooling rates. Therefore, the model can reduce the experimentation by determining the effects of particular parameters beforehand.

This section presents the formulation of the general governing equation using the concept of the divergence of a transport intensity as the net accumulation rate of energy per unit volume of the medium under consideration. Prediction of thermal effects produced by laserbeam scanning the surface of an absorbing sample requires that three-dimensional heat transfer equation be solved subject to finite size conditions of a sample. The geometry considered in this Dissertation is illustrated in Fig. 2.52, which is finite in dimensions slab irradiated by a laserbeam impinging on its surface subject to convective and radiative losses.

Next, Section 2.7.6 considers the resulting boundary conditions.
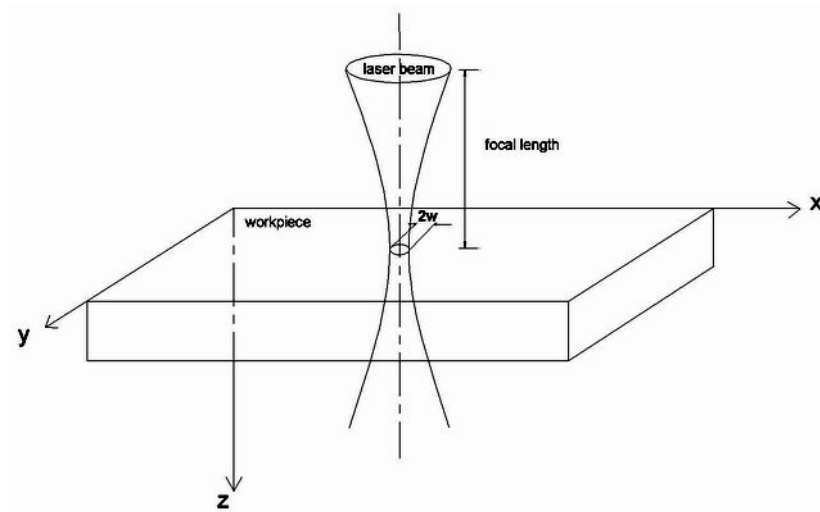
Fig. 2.52. Laserbeam impinging on a finite size sample.

Defining q_n as the magnitude of the heat flux in the n-direction (with n being x, y, z) one may introduce the vector sum, q, of the directional fluxes,

$$q = q_x \widehat{i} + q_y \widehat{j} + q_z \widehat{k} \quad,$$ (119)

where $(\widehat{i}, \widehat{j}, \widehat{k})$ are the unit vectors along each of the Cartesian coordinate directions.

191

Having defined a vector representation of the energy transport involved, one may write the expression for the net accumulation rate of thermal energy per unit volume as

$$\nabla \cdot q + Q = \frac{\partial u}{\partial t} \quad , \tag{120}$$

where Q is a volumetric term accounting for the internal generation of heat. The right hand side of Eq. 120 represents the total rate of change of the element's specific internal energy. Thus, Eq. 120 is a general statement of the first law of thermodynamics.

Using thermodynamic arguments, Eq. 120 can be expended further. If one considers sample under consideration to be a homogenous continuum composition, with more than one phase, than one can uniquely determine the state of any property of the continuum using two independent properties, specific energy and specific enthalpy, one can write (Nowak, 1990)

$$du_m = \left(\frac{\partial u_m}{\partial v} \right)_T dv + c_v dT \quad , \tag{121}$$

$$dh_m = \left(\frac{\partial h_m}{\partial p} \right)_T dp + c_p dT \quad , \tag{122}$$

where the specific heats at constant volume and pressure were defined, respectively, as

$$c_c = \left(\frac{\partial u}{\partial T} \right)_v \quad , \tag{123}$$

$$c_p = \left(\frac{\partial h}{\partial T} \right)_p \quad . \tag{124}$$

For solids and incompressible fluids the specific volume is assumed constant. If one also neglect pressure changes in the given process, Eqs 121 and 124 can be simplified to yield

$$du_m = c_v dT \quad , \tag{125}$$

$$dh_m = c_p dT \quad . \tag{126}$$

Recalling the definition of specific enthalpy,

$$h_m = u_m + pv \quad , \tag{127}$$

one can combine Eqs 124 and 121 to find that

$$c_p = c_v = c \quad , \text{ for } dv \approx dp \approx 0 \quad . \tag{128}$$

If pressure is allowed to vary, Eq. 127 still holds approximately for solids and incompressible fluids. Taking the relations in Eqs 125 and 127 and multiplying by the density of the medium results in expressions in terms relative to the unit volume as opposed to the unit mass. Using Eq. 127, these new volumetric terms can be expressed as

$$du = \rho \cdot c(T)dT \quad , \tag{129}$$

$$dh = \rho \cdot c(T)dT \quad , \tag{130}$$

and

$$h = u + \rho \cdot pv \quad . \tag{131}$$

Integrating both sides of Eq. 129 over proper variables and differentiating with respect to time yields

$$\frac{\partial u}{\partial t} = \rho \cdot \frac{\partial}{\partial t} \int_{T_0}^{T} c(T)dT \quad , \tag{132}$$

where T_0 is the temperature at the beginning and T is the temperature at the end of the infinitesimal time step, dt. For the particular very infinitesimal time interval dt one can assume a constant specific heat, than Eq. 132 simplifies to

$$\frac{\partial u}{\partial t} = \rho \cdot c \frac{\partial T}{\partial t} \quad , \tag{133}$$

since the initial temperature is constant with respect to time. Substituting Eq. 133 into Eq. 120 yields the heat diffusion equation

$$-\nabla q + Q = \rho \cdot c \frac{\partial T}{\partial t} \quad . \tag{134}$$

Solution of Eq. 134 for the time-dependent field, $T(x, y, z, t)$, requires the use of a constitutive equation relating the temperature to heat flow. For conductive heart transfer equation this relation is Fourier's law of conduction. It states that the heat flux in a direction n is proportional to the temperature gradient in that direction. Mathematically this is expressed as

$$q_n \widehat{n} = -k \cdot \frac{\partial T}{\partial n} \widehat{n} \quad , \tag{135}$$

where k is thermal conductivity and q_n is the heat flux in the n-direction. Negative sign is necessary to satisfy the second law of thermodynamics.

In the analysis of the Fourier heat conduction model, the heat flux through a given plane is considered as being a function of the spatial temperature gradient at that plane. This depends upon the assumption that the temperature gradient remains almost constant between two successive and closely spaced planes. However, the distance between these planes is finite, therefore, error occurs when high-order terms, which are neglected, become important at high power laser intensities. The heat flux through a given plane depends on the electron energy distribution through the material, therefore, the material cannot be considered as a homogeneous continuum when one is analyzing very short

pulses (shorter then a picosecond) at intermolecular level (distances less than 0.1 µm).

Substituting Eq. 135 into Eq. 134 yields

$$-\nabla \cdot (k\nabla T) + Q = \rho \cdot c \frac{\partial T}{\partial t} \quad , \tag{136}$$

which is the general form of the governing differential equation for isobaric thermal

conduction in a homogenous solid or incompressible fluid.

In laser micromachining, the internal energy generation, Q, is commonly thought

of as the rate of laser energy absorbed per unit volume in the irradiated medium. In case

of metals, this absorption occurs at beginning in a very thin layer at the surface of the

workpiece and, for many practical cases can be considered as a boundary condition to Eq.

136. This absorption process is calculated by Beer-Lambert's law, viz.

$$I(z) = \varepsilon \cdot I_0(0) \exp(-\mu \cdot z) \quad , \tag{137}$$

where $I(z)$ is the intensity of the incident radiation at a given distance, z, into the

absorbing medium from the irradiated surface, ε is the surface emissivity of the medium,

and μ is the absorption coefficient of the material, measure of the absorption of radiation

propagating through the medium. Using the terminology used in Eq. 120, differentiating

Eq. 153 with respect to the direction of propagation of the laser beam yields the

volumetric extraction rate of energy absorbed by the differential element. Since the

accumulation rate is negative of the extraction rate for a given volume, the necessary

volumetric term for use in Eq. 137, is given by

$$Q = -\frac{\partial I(z)}{\partial z} = \varepsilon \cdot \mu \cdot I_0(0) \exp(-\mu \cdot z) \quad . \tag{138}$$

Using the Drude-Zener theory (Yilbas, 1997), Eq. 138 leads to the following expression for $Q(x, y, z, t)$

$$Q(x, y, z, t) = A \cdot \exp(-\beta \cdot t) \cdot \mu \cdot I_0(x, y, 0, t) \exp(-\mu \cdot z) \quad , \tag{139}$$

where, A is the surface absorptivity, β is the pulse parameter, , and $I_0(x, y, 0, t)$ is laser radiation intensity at the material surface ($z = 0$).

In Eq. 139, absorption coefficient of the material μ measuring the absorption of radiation propagating through the medium is considered constant at this time, but based on a number of publications μ should be a function of temperature and axial position of the irradiated laser beam in respect to the material under consideration. At this time let us modify Eq. 139 to be

$$Q(x, y, z, t) = A \cdot \exp(-\beta \cdot t) \cdot \mu(T, z) \cdot I_0(x, y, 0, t) \exp(-\mu(T, z) \cdot z) \quad , \tag{140}$$

and function $\mu(T, z)$ will be defined later on in this Dissertation.

Incorporating Eq. 139 into Eq. 136, for laser pulse with a position-dependent intensity, for this form of pulse input, the Fourier differential Eq. 136 can be rewritten as

$$\rho \cdot c \frac{\partial T}{\partial t} = \nabla(k \nabla T) + Q \quad , \tag{141}$$

where ρ is the density of the material of the work piece, $c(T)$ is the temperature dependent specific heat of the material, $k(T)$ is the temperature dependent thermal conductivity, $T = T(x, y, z, t)$ is the resulting three-dimensional time dependent temperature distribution in the material, t is time, T_0 is the initial temperature, and x, y, z are the spatial Cartesian coordinates. $Q(x, y, z, t)$ is the rate at which heat is supplied to the solid per unit time per unit volume, depends on the laser pulse parameters and

physical and optical properties of material irradiated. Note that both A and μ are functions of temperature and the wavelength of the incident radiation.

Solid or liquid evaporates at any temperature greater then 0°K. The evaporation rates strongly depend on the surface temperature T_s. Equation 141 considers heat diffusion into material only through conduction. Based on experimental and theoretical evidence, evaporation takes place, so one has to consider moving elements of vapor and liquid inside the material during laser beam interaction.

Considering this fact, the general governing differential equation allowing a phase change process can be written as

$$\rho(T)\, c(T)\, \frac{\partial T}{\partial t} = \nabla(k\nabla T) + \rho(T)\, c(T)\, V_n(T)\, \nabla T + Q \quad , \tag{142}$$

where V_n is the normal component of the evaporation front or melted front velocity (recession velocity).

Let us define velocity, V_n. From literature (Tokarev, et al., 1995), the interface moves into the depth of the material at the speed defined as

$$V(T_s) = \frac{1-c}{\rho} \sqrt{\frac{M}{2\pi k_B T_s}}\, p_{sat}(T_s) \quad , \tag{143}$$

where c is recondensation factor which is usually taken as 0.18, and $p_{sat}(T_s)$ is saturated vapor pressure defined from Clapeyron-Clausius equation as

$$p_{sat}(T_s) = \varphi_0 \exp\left(-\frac{E_a}{k_B T_s}\right) \quad . \tag{144}$$

where φ_0 is preexponential factor, and E_a is an activation energy evaporation per atom.

Note that Eq. 143 is a pressure dependent function, which has to be calculated

simultaneously with temperature dependent velocity. Thus, let us derive a velocity as a

function of temperature and the latent heat of phase transition, which is also temperature

dependent.

The rate of change of latent heat with temperature can be expressed as (Yilbas et

al., 1996)

$$\frac{\partial H}{\partial T} = \frac{H}{T} + (c_{pv} - c_{pl}) - \frac{H}{v_v - v_l}\left[\left(\frac{\partial v_v}{\partial T}\right)_p - \left(\frac{\partial v_l}{\partial T}\right)_p\right] \quad , \tag{145}$$

where c_{pv} and c_{pl} are specific heats at constant pressure for vapor and liquid states,

respectively, and v_v and v_l are specific volumes for vapor and liquid states.

One has to realize that integration of the latent heat over the temperature ranging

from 0 to T_c is difficult, because we do not have enough information about values for the

latent heat especially at extreme value of the range under consideration. It is safe to

assume (Yilbas, 1996), that little inaccuracy is involved in taking the room temperature

latent heat as the latent heat at absolute zero, because, by knowing that

$v_v \langle\langle v_l$ and $\left(\frac{\partial v_v}{\partial T}\right)_p \rangle\rangle \left(\frac{\partial v_l}{\partial T}\right)_p$, i. e., the specific volume of gas, v_v is much grater than

the condensed liquid, v_l, and its rate of change with temperature at constant pressure is

correspondingly greater. Thus, Δc_p, is extremely small for temperature up to a room

temperature, T_a.

According to Maxwell's law the function of velocity distribution of molecules can

be defined as (Tabor, 1991)

$$f(V_n)dV_n = \sqrt{\frac{M}{2\pi\,k_B T_s}}\,\exp\left(\frac{MV_n^2}{2\pi\,k_B T_s}\right)dV_n \quad , \tag{146}$$

where V_n is the velocity in the direction normal to the surface, and the other parameters were defined earlier. Using vernacular terms, function $f(V_n)\mathrm{d}\,V_n$ is a ratio of number of atoms with velocity V_n to $V_n + dV_n$ per unit volume, to the total number of atoms per unit volume. Only those molecules whose velocity is greater than V_{min} obtained from equation given by (Tabor, 1991)

$$\frac{1}{2}MV_{min}^2 = H(T) \quad , \tag{147}$$

will escape from the retaining potential, where V_{min} lies in the z direction. If n is the number of atoms per unit volume then the number of atoms with velocities V_n to $V_n + dV_n$ per unit volume is $n\,f(V_n)dV_n$, and the number of atoms with these velocities passing a unit area per unit time is $n\,f(V_n)V_n\,dV_n$.

With the assumption made in Chapter 2.3, that all the atoms for which, $V_n \rangle V_{min}$, do not return to their equilibrium position are assumed to be evaporated. If N_G is the number of atoms evaporated per unit time per unit area, then

$$N_G = \int_{V_{min}}^{\infty}\left[n\,f(V_n)V_n\right]dV_n$$
$$= n\sqrt{\frac{M}{2\pi k_B T_s}}\int_{V_{min}}^{\infty}\left[\exp\left(\frac{MV_n^2}{2\pi k_B T_s}\right)V_n\right]dV_n \quad . \tag{148}$$

After integration and substitution of Eq. 147 into Eq. 148, we obtain

$$N_G = n \sqrt{\frac{M}{2\pi k_B T_s}} \exp\left(\frac{H(T)}{k_B T_s}\right) V_n \quad . \tag{149}$$

If atoms are equally spaced within the lattice a surface layer would consist of $n^{2/3}$ with an

evaporation time $n^{2/3} N_G$. The average velocity of the surface, V_n would be

$$V_n = \frac{1}{n^{1/3}} \frac{N_G}{n^{2/3}} \quad , \tag{150}$$

$$V_n = \sqrt{\frac{k_B T}{2\pi M}} \exp\left(-\frac{H(T)}{k_B T}\right) \quad . \tag{151}$$

Considering Eq. 151, the general governing differential equation defined in Eq.

152, with phase change processes could be written as

$$\rho(T)\, c(T)\, \frac{\partial T}{\partial t} = \nabla(k\nabla T) + \rho(T)\, c(T) \sqrt{\frac{k_B T}{2\pi M}} \exp\left(-\frac{H(T)}{k_B T}\right) \nabla T + Q \quad . \tag{152}$$

Note, that latent heat $H(T)$, in Eq. 142, based on some theoretical and experimental

evidence is temperature dependent and the final form of it is going to be described in

Section 3.2.6.3.

In order to solve Eq. 142, appropriate boundary conditions should be applied.

Section 2.7.6 is discussing formulation of the appropriate boundary conditions.

2.7.6. Boundary conditions

Boundary conditions are important part of a model. They influence the

programming and calculation results greatly. Specifying the suitable boundary

conditions is the basis for successful computation. Three kinds of boundary conditions

are typically encountered in heat conduction analysis. These are: i) given the boundary

temperature, T, ii) given the boundary heat flux, q, and iii) a boundary heat flux balance

relation. If the boundary temperature is given, there is no particular difficulty in

modeling, one needs only to specify the value of the boundary grids to the specified

temperature.

The magnitude of heat flux due to convection to the ambient from the sample

surface is expressed using Newtonian law of cooling

$$q_{conv} = h_c (T_s - T_{amb}) \quad , \tag{153}$$

where h_c, is convection heat transfer coefficient, T_s is the surface temperature, and T_{amb} is

the temperature of surrounding.

In order to determine h_c, the characteristic length L of the workpiece should be

$$L = \frac{Area}{Ob} \quad , \tag{154}$$

where, $Area$, is the area of the surface, and Ob is the perimeter of the workpiece. Then,

the Nusselt number for the horizontal plate is (Bejan, 1993)

$$N_u = 0.27 \cdot R_a^{0.25} , \tag{155}$$

where the Rayleigh number R_a is

$$R_a = \frac{g\beta}{\kappa\gamma} L^3 (T - T_{amb}) \quad . \tag{156}$$

In Eq. 156, g is the gravitational acceleration, β is the coefficient of volumetric thermal

expansion, κ is the thermal diffusivity, γ is the kinematic viscosity, and other

parameters are as defined for Eq. 153. The convective heat transfer coefficient h_c can be calculated as

$$h_c = N_u \frac{k_{air}}{L} \quad , \tag{157}$$

where k_{air} is the thermal conductivity of the air surrounding the workpiece. Radiation to the ambient is expressed using the relation

$$q_{rad} = \sigma \varepsilon (T_s^4 - T_{amb}^4) \quad , \tag{158}$$

where q_{rad} is the magnitude of radiation flux, ε is the emissivity of the material, and σ is the Stefan-Boltzmann constant. Note that convection is a linear function of temperature, whereas, radiation is a nonlinear, due to its dependence on the difference of the fourth powers of the surface and ambient temperature.

The magnitude of convection and conduction in the overall transport of heat can be evaluated from the value of the Peclet number, P_e, which is defined by

$$P_e = \frac{u \cdot c_p \cdot L_r}{k} \quad , \tag{159}$$

where, u is velocity, L_r is the characteristic length, taken as the pool radius at the top surface of the weld pool and the other parameters were defined earlier.

Heat transported by a combination of convection and conduction mechanism is observed in the weld pool in laser microwelding applications. When Peclet number is less than 1, the heat transport within the weld pool occurs primary by conduction. When Peclet number is much higher than 1, then the convective heat transport is the main mechanism of heat transfer in the material.

If one is using shielding gas in laser micromachining then heat transfer coefficient h_c required in Eq. 157, is calculated from Mazumder and Steel (1979) and Gordon and Cobonpue (1961) for case of a vertically impinging jet

$$h_c = 13 \, \mathrm{Re}^{0.3} \, \mathrm{Pr}^{0.35} \, k_g \frac{1}{B} \quad , \tag{160}$$

where B is the jet plate distance, Re is the Reynolds number at jet exit, Pr is the Prandt number for gas, and k_g is thermal conductivity of the gas.

Performing an energy balance on a boundary where both convection and radiation losses occur, one can relate the flux conducted to the interface to the convection and radiation losses by the expression

$$q_n = q_{conv} + q_{rad} \quad . \tag{161}$$

Substituting Eqs 135, 153, and 158 into 161 one obtains

$$-k\left(\frac{\partial T}{\partial n}\right)_s = h_c(T_s - T_\infty) + \sigma\varepsilon(T_s^4 - T_\infty^4) \quad , \tag{162}$$

where the term on the left-hand side of the Eq. 162 represents the magnitude of the heat conducted normal to the boundary surface. Equation 162 should be applied to all exposed boundary of the finite sample under consideration. Setting the right-hand side of Eq. 162 to zero accommodates insulated boundaries.

In laser microdrilling, Eq. 162 should be applied in the region of the newly vaporized material (hole area) and an appropriate heat transfer coefficient should be used. Since the question of modeling of the microdrilling phenomena is associated with creating the hole formation has not yet been solved, then to chose an appropriate heat

transfer coefficient is an educated guess and open to debate. More details on the hole

formation subject is described in Section 4.3.4.

Based on Chapter 2, in laser microdrilling phase transitions occur. For the case

when phase change transition takes place, the boundary condition at the liquid-vapor

interface is

$$-k\frac{\partial T}{\partial z}\bigg|_z + \rho\, v_{dv} H_v = (1-R)I_0 \quad , \tag{163}$$

where k is thermal conductivity of the solid or liquid phase, $\dfrac{\partial T}{\partial z}\bigg|_z$ is the temperature

gradient at the surface along the normal (z- axis), ρ is the density of the solid or liquid

phase, v_{dv} is the component of boundary velocity due to evaporation, R is the reflectivity

for the laser wavelength, and I_0 is the intensity of the laser beam at the surface.

For surface temperatures less than approximately half of the critical temperature, the

energy of evaporation per atom U can be assumed to be constant. Then the component of

the boundary velocity due to evaporation v_{dv} was defined by Eq. 151, and also defined in

similar fashion by Niedrig and Bostonjglo (1996)

$$v_{dv} = V_0 \exp\!\left(\frac{-U}{T_s}\right), \tag{164}$$

where V_0 is a coefficient of the order of magnitude of the sound velocity, T_s is the surface

temperature, and U is the energy of evaporation per atom defined as

$$U = \frac{M \cdot H_v}{N_a k_B} \quad , \tag{165}$$

where H_v is the latent heat of vaporization (per unit mass), k_B is Boltzmann's constant, M is the atomic mass, and N_a is Avogadro's number. Velocity V_n, defined in Eq. 151, is equal v_{dv}. In this Dissertation the latent heat of vaporization H_v, is going to be defined later as a function of temperature (only for higher temperatures) in Chapter 3.2.6.3.

The classic Stefan boundary condition is applied to the solid-liquid boundary (melting front $z=z_m$)

$$\rho H_f v_m = k_s \left. \frac{\partial T_s}{\partial z} \right|_{z=z_m} - k_l \left. \frac{\partial T_l}{\partial z} \right|_{z=z_m} , \tag{166}$$

where H_f is the latent heat of fusion, v_m is the melting front velocity, and subscripts "s" and "l" represent "solid" and "liquid", respectively. The Stephan boundary condition assumes an instant transition from solid to liquid at the melting temperature T_m and does not allow superheating at the melting front. The approximation is adequate for the slow velocities of melt front propagation typical of laser welding and drilling, where the melting kinetics can be disregarded.

To understand how the boundary conditions were defined, let us first comprehend material removal process together with energy transport in multiple phase transitions, which is going to be discus in the Section 2.7.1.

To establish effects of convective heat transfer coefficient due to evaporation recoil generated melt flow Semak et al. (1999) performed two simulations. In the first one recoil pressure and related melt flow were disregarded and in the second case recoil pressure and melt flow were accounted for. Those observations they supported by

calculating the melt surface temperatures at the axis of the laser beam for different values

of absorbed intensity I_0 presented in Fig. 2.53. When recoil pressure and melt flow were

included, the steady-state values of temperature were reached faster, and the maximum

temperature were lower and the cooling rates much higher, than for the case where recoil

pressure and flow were neglected. Analyzing, Fig. 2.53, one can calculate that ignoring

recoil pressure and associated convective heat transfer results in 1-5% error in

calculations of surface temperature in the center of the laser beam.
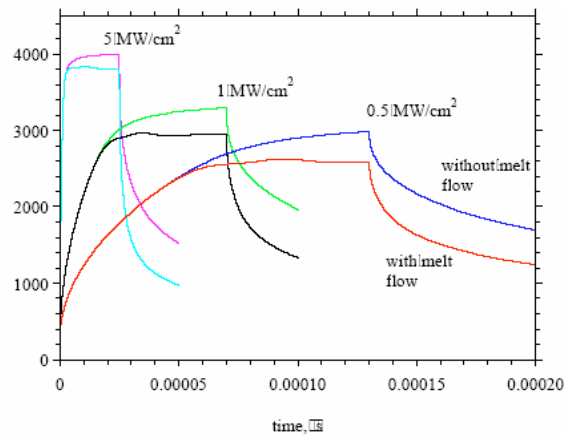
Fig. 2.53. Calculated temperature of iron surface at the beam axis for the cases without
(top curves) and with (bottom curves) melt flow, for the different maximum absorbed
intensity values and different laser pulse durations: 130 μs (0.5 MW cm^{-2}),
70 μs (1 MW cm^{-2}), and 25 μs (5 MW cm^{-2}) (Semak et al., 1999).

3. Solutions of the governing equation

This Chapter considers the solution of the general governing equation subject to

its related boundary conditions, by means of exact and numerical methods. This chapter

consists of a discussion of the approximate solution of the problem using mathematical

tools and is divided into four parts. First four sections Section 3.1.1, Section 3.1.2, Section 3.1.3, and Section 3.1.4 present an analytical method of the solution of the general governing equation using the Fourier theory. Section 3.1.5 is considering interaction of laser energy with materials using very short laser pulses and introduces electron-phonon theory approach to solve the heat transfer problem of the interaction of ultrashort pulses with the matter. Section 3.2 consists of a discussion of the approximate solution of the problem using the finite difference method (FDM) and finite element method (FEM), and presents the computer solutions developed in this Dissertation.

3.1. Analytical methods

There have been many analytical solution published for various special cases of the Fourier heat transfer equation. Section 3.1.1 illustrates analytical solution for heating case without phase change, by laser defined as a step function (constant heating). Next Section 3.1.2 considers analytical solution to the governing heat transfer equation for laser pulse with a time-dependent Gaussian pulse heating. Section 3.1.3 considers analytical solution of heat transfer equation with time dependent Gaussian laser pulse heating with convective boundary conditions. Section 3.1.4 describes heating analysis with time dependent pulse intensity and where evaporation is considered as the exclusive phenomenon taking place during the ablation process. Section 3.1.5 presents the heating analysis with pulsed laser heating process by considering both Fourier conduction and electron-phonon kinetic theory approaches.

3.1.1. Analytical solution of heat transfer equation with spatial dependent laser pulse heating

This Section presents analysis of the conduction heating process introduced for a practical Nd:YAG Gaussian laser pulse with a position-dependent intensity. An analytical solution to the problem is obtained with appropriate boundary conditions.

When the laser intensity is rather low, no phase transition occurs and the only effect of laser absorption is heating of the material. In metals the laser radiation is absorbed by "free electron", and the energy transfer in metals is also due to electron heat conduction. The temperature field is described by the standard Fourier heat conduction and for laser pulse with a position-dependent intensity, for this form of pulse input, the Fourier differential equation is described by Eq. 141. $Q(x,y,z,t)$ in this equation is defined by the Drude-Zener theory which leads to the following expression (Yilbas et al., 1996)

$$Q(x,y,z,t) = A \cdot \exp(-\beta \cdot t) \cdot \mu \cdot I_{\max}(x,y,t) \exp(-\mu \cdot z) \quad , \tag{167}$$

where, A is the surface absorptivity, β is the time pulse parameter, μ is the absorption coefficient of the material, and $I_0(x,y,t)$ is laser radiation intensity at the material surface ($z = 0$). According to Sparks (1975) μ is independent of temperature, while surface absorption coefficient of the material, $A = 1 - R$, where, R is the surface reflectivity, is linear function of the surface temperature

$$A = A_0 + A_1(T - T_0) \quad . \tag{168}$$

where A_0 is the surface absorptivity at room temperature, T_0, and for most of engineering materials, the absorption factor A_1 is almost unity for Nd:YAG laser wavelength. This

temperature dependence of surface absorptivity results from the fact that A is proportional

to the electron-phonon collision frequency which, in turn, is proportional to the crystal

lattice temperature.

For metals and certain applications, at temperatures above the Debye temperature,

it can be assumed that $k(T)$ and $c(T)$ do not change dramatically with temperature.

Therefore, assuming constant specific heat and thermal conductivity for a particular time

interval, Eq. 141 can be simplified to

$$k\left(\frac{\partial^2 T}{\partial z^2}\right) + \mu \cdot I_{max}(x,y,t)\exp(-\mu \cdot z) = \rho \cdot c \cdot \frac{\partial T}{\partial t} \quad , \tag{169}$$

In many practical cases the transverse dimensions of laser focusing spot are large

compared to the thickness of the heated layer, and heat conduction problem. Equation

169 can be considered one-dimensional and can be solved using standard methods,

Carslow and Jaeger (1969).

It is unnecessary to solve for the complete pulse since the complete solution may

be obtained by summation of the solutions for the individual parts of time exponential,

then equation is linear. Rearrangement of Eq. 169 gives

$$\frac{\partial^2 T}{\partial z^2} + \frac{\mu \cdot I_{max}}{k}\exp[-\mu \cdot z] = \frac{1}{\kappa} \cdot \frac{\partial T}{\partial t} \quad , \tag{170}$$

where thermal diffusivity, $\kappa = \dfrac{k}{\rho \cdot c}$, with boundary conditions

$$\left.\frac{\partial T}{\partial t}\right|_{x=0} = 0 \quad , \tag{171}$$

$$T(\infty, t) = 0 \quad , \tag{172}$$

$$T(z,0) = 0 \quad .$$
(173)

Laplace transform can be used to solve certain type of partial differential equations with two or more independent variables. To solve Eq. 170 let us show how to solve in detail differential equation using Laplace transformation of one dimensional heat equation

$$\frac{\partial^2 T}{\partial z^2} = \frac{1}{\kappa} \cdot \frac{\partial T}{\partial t} \quad .$$
(174)

The physical model of Eq. 174 is a semi-infinite slab of metal with a plane face on which the origin of the z-axis is located with the positive half of the axis directed into slab. This situation is illustrated in Fig. 3.1.

The approach will be to take Laplace transform of the dependent variable $T(z,t)$ in the heat equation with respect to the time t, as a result of which an ordinary differential equation with z as its independent variable will be obtained for the transformed variable that will then depend on both the Laplace transform variables s and z. After the ordinary differential equation has been solved for the transformed variable, the inverse Laplace transform ($£^{-1}$) will be used to recover the time variation, and so to arrive at the required solution as a function of z and t. Please note, that if the Laplace transform is applied to the independent variable t in the function of two variables $T(z, t)$, the variable z will behave like a constant. Consequently, the rules for transforming derivatives of functions of a single independent variable also apply to a function of two independent variables.
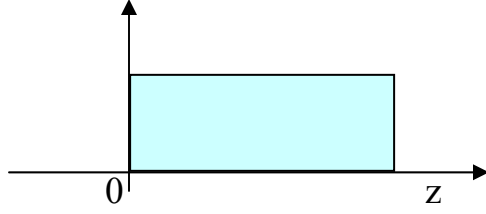
Fig. 3.1. Semi-infinite metal slab.

Using the notation $\overline{T}(z,s) = \pounds\left[T(z,t)\right]$ to denote the Laplace transform of $T(z\ t)$

with respect to the time.

The formula for the transform of derivative is

$$\pounds\left[\partial T(z,t)\right] = s\overline{T}(z,s) - T(z,0) \quad . \tag{175}$$

To proceed further we must now use the condition that at time $t=0$ the material of

the slab is at zero temperature, so $T(z,0)=0$, as a result of which

$$\pounds\left[\frac{\partial T(z,t)}{\partial t}\right] = s \cdot \overline{T}(z,s) \quad . \tag{176}$$

Next, since z is regarded as a constant, one has

$$\pounds\left[\frac{\partial^2 T(z,t)}{\partial z^2}\right] = \frac{\partial^2 T(z,s)}{\partial z^2} \quad . \tag{177}$$

Using Eq. 177 when taking the Laplace transform of the heat equation with

respect to t, and using the linearity property of the transform, one obtains

$$s \cdot \overline{T}(z,s) = \kappa \cdot \left[\frac{d^2\overline{T}(z,s)}{dz^2}\right] \quad , \tag{178}$$

where now one can use an ordinary derivative with respect to z, so z can be considered to

be the only independent variable. Therefore Eq. 178 can be rewritten as

$$\frac{d^2\overline{T}(z,s)}{dz^2} - \frac{s}{\kappa} \cdot \overline{T}(z,s) = 0 \quad , \tag{179}$$

211

Eq. 179 has the general solution of

$$\overline{T}(z,s) = C \exp\left[\sqrt{\frac{s}{\kappa}}z\right] + D \exp\left[-\sqrt{\frac{s}{\kappa}}z\right] \quad . \tag{180}$$

For $s \to +\infty$ $C = 0$ (temperature has to be finite for z > 0 and t > 0) so the Laplace transform of temperature is seen to be given by

$$\overline{T}(z,s) = D \exp\left[-\sqrt{\frac{s}{\kappa}}z\right] \quad . \tag{181}$$

To determine D we can use boundary condition on the plane face of the slab that requires $T(0,t)=T_0$ from which it follows that $\pounds\left[T(0,t)\right] = \frac{T_0}{s}$. Thus, the Laplace transform of the solution with respect to the time t is

$$\overline{T}(z,s) = \frac{T_0}{s} \exp\left[-\sqrt{\frac{s}{\kappa}} \cdot z\right] \quad . \tag{182}$$

To recover the time variation from Eq. 182, it is necessary to find inverse of Laplace function ($\pounds^{-1}$), i.e.,

$$\pounds^{-1}\left[\overline{T}(z,s)\right] = T(z,t) \quad . \tag{183}$$

Performing mathematical manipulations or using reference book with Laplace transforms functions, one can find, that

$$T(z,t) = T_0 \cdot erfc\left(\frac{z}{2\sqrt{\kappa \cdot t}}\right) \quad , \tag{184}$$

where, the error function, erf, is defined as

$$erf(z) = \frac{2}{\pi}\int_0^s e^{-u^2}\,du \quad , \tag{185}$$

and the complementary error function, *erfc,* is defined by Carslaw and Jaeger (1969), as

$$erfc(z) = 1 - erf(z) \; ,$$

(186)

where *z* is the independent variable, and *u* is the dummy variable.

Continuing the forgoing mathematical calculations, the Laplace transformation of Eq. 170 with respect to *t* and substitution of boundary condition Eq. 171 and yield

$$\frac{\partial^2 \overline{T}}{\partial z^2} - g^2 \overline{T} = \frac{-I_{max} \mu \cdot \exp[-\mu \cdot z]}{k \cdot s} \; ,$$

(187)

where $g^2 = \dfrac{s}{\kappa}$, and *s* the transform variable, with *T(z, s,)* which has a complimentary and particular solution

$$\overline{T} = C \exp(-gz) + D \exp(gz) - \frac{-I_{max} \mu \cdot \exp[-\mu \cdot z]}{k(s)(\mu^2 - g^2)} \; ,$$

(188)

where *C* and *D* are arbitrary constants. Substitution of boundary Eq. 172 and Eq. 173 into Eq. 188 gives the following constants:

$$D = 0 \text{ and } \qquad C = \frac{I_{max} \mu^2}{k \cdot g(s)(\mu^2 - g^2)} \; .$$

(189)

Therefore, the complex solution in the transform plane is

$$\overline{T} = \frac{-I_{max} \mu}{k(s)} \cdot \left[\frac{\mu \cdot \exp[-g \cdot z]}{g(g^2 - \mu^2)} - \frac{\cdot \exp[-\mu \cdot z]}{(g^2 - \mu^2)} \right] \; .$$

(190)

The problem now is to invert the solution of Eq. 190 which is a product of two *s*-functions. There are two ways to do this. The first is a convolution integral method and the second one is to entail expansion of the functions into partial fractions. Using the second method, the full solution obtained by inverse Laplace transformation of Eq. 190 is

$$T(z,t) = \frac{I_{max}\mu}{2k}\left\{ -\frac{4}{\mu}\sqrt{\frac{\kappa \cdot t}{\pi}} \cdot \exp\left(-\frac{z^2}{4\kappa \cdot t}\right) + \right.$$

$$-\left(\frac{1-\mu \cdot z}{\mu^2} - \frac{1+\mu \cdot z}{\mu^2}\right) \cdot erfc\left(\frac{z}{2\sqrt{\kappa \cdot t}}\right) +$$

$$-\frac{1}{\mu^2}\left[\exp(\kappa\mu^2 \cdot t - \mu \cdot z) \cdot erfc\left(\frac{z}{2\sqrt{\kappa \cdot t}} - \mu\sqrt{\kappa \cdot t}\right)\right] + \qquad (191)$$

$$-\frac{1}{\mu^2}\left[\exp(\kappa\mu^2 \cdot t + \mu \cdot z) \cdot erfc\left(\frac{z}{2\sqrt{\kappa \cdot t}} + \mu\sqrt{\kappa \cdot t}\right)\right]$$

$$\left. -\frac{2}{\mu^2}\exp(-\mu \cdot z)\left[1 - \exp(\kappa\mu^2 \cdot t)\right]\right\} \quad ,$$

where

$$erfc(z) = 1 - erf(z) = \frac{2}{\pi}\int_z^\infty e^{-u^2}du \quad , \text{ defined by Eqs 185and 186 and knowing that}$$

$$ierfc(z) = \int_z^\infty erfc\,\xi d\xi = \frac{1}{\sqrt{\tau}}\exp(-z^2) - z \cdot erfc(z) \quad , \qquad (192)$$

the final solution of Eq. 191 is

$$T(z,t) = \frac{2I_{max}}{k}\sqrt{\kappa \cdot t} \cdot ierfc\left(\frac{z}{2\sqrt{\kappa \cdot t}}\right)$$

$$-\frac{I_{max}}{k \cdot \mu} \cdot \exp(-\mu \cdot z) +$$

$$+\frac{I_{max}}{2k \cdot \mu}\exp\left[\kappa\mu^2 \cdot t - \mu \cdot z\right] \cdot erfc\left(\mu\sqrt{\kappa \cdot t} - \frac{z}{2\sqrt{\kappa \cdot t}}\right) + \qquad (193)$$

$$+\frac{I_{max}}{2k \cdot \mu}\exp\left[\kappa\mu^2 \cdot t + \mu \cdot z\right] \cdot erfc\left(\mu\sqrt{\kappa \cdot t} + \frac{z}{2\sqrt{\kappa \cdot t}}\right)$$

Equation 193 gives the temperature profile inside the material for a given laser beam

power intensity and is shown in Fig. 3.2.
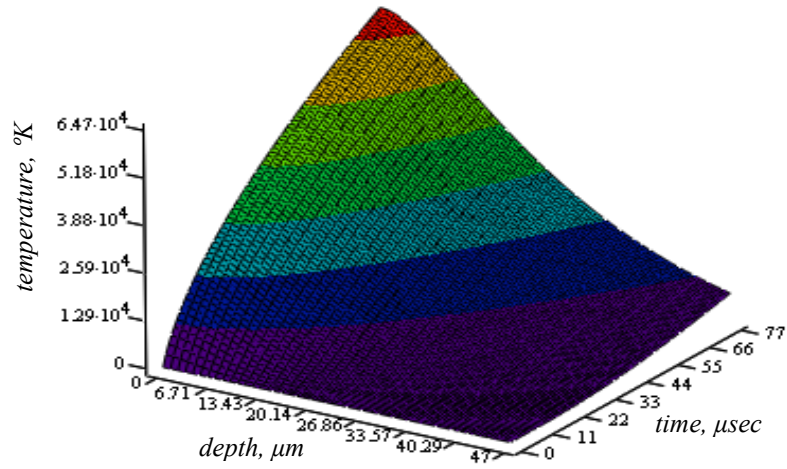
Fig. 3.2. Temperature distribution inside a material.

It should be noted that as the time tends to infinity in Eq. 193, i.e.,

$$\lim_{t \to \infty}[T(z,t)] = \infty \quad , \tag{194}$$

no steady state solution exists for the temperature distribution.

In the majority of calculations regarding the laser heating of solids surfaces, the temperature dependence of the surface reflectivity usually is neglected. If we set *A=0*, growth of the temperature at the surface in the center of laserbeam with time may be obtained by setting *z = 0* into Eq. 193, i.e.,

$$T(0,t) = \frac{I_{max}}{k \cdot \mu}\left[2\frac{\sqrt{\kappa\mu^2 \cdot t}}{\pi} + \exp(\kappa\mu^2 \cdot t)\cdot erfc(\mu\sqrt{\kappa \cdot t}) - 1\right] \quad , \tag{195}$$

Graphical representation of Eq. 195 is shown in Fig. 3.3.

215
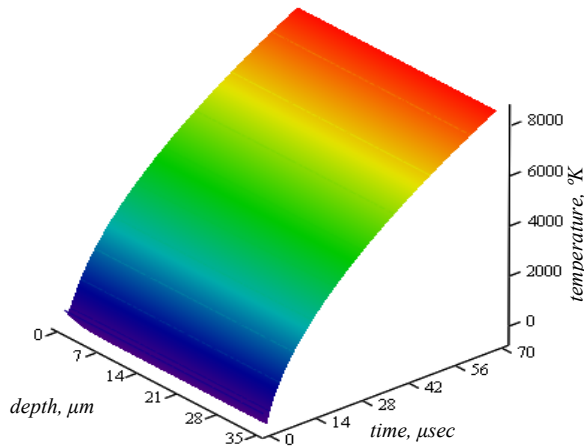
Fig. 3.3. Temperature distribution on the surface of the material.

Distribution in Fig. 3.3 represents the surface temperature of the workpiece during the laser interaction, and roughly one can estimate if there is going to be a drilling or melting on that surface. Writing in MathCAD parametric program as a function of thermal properties for different materials, (thermal conductivity of lead k=19.66, c=0.151; titanium, k=20.5, c=0.782, and 304 stainless steel k=41.84. c=0.418. Typical result of such a parametric study is illustrated in Fig. 3.4.

Using very complicated function, programming in MathCAD is not always easy. Thus, to obtained similar result, one can simply substitute values of thermo-physical parameters for solid first, then for liquid and by displaying them on two different graphs compare results. This method was used on Eq. 200, because equation is very complex.

216
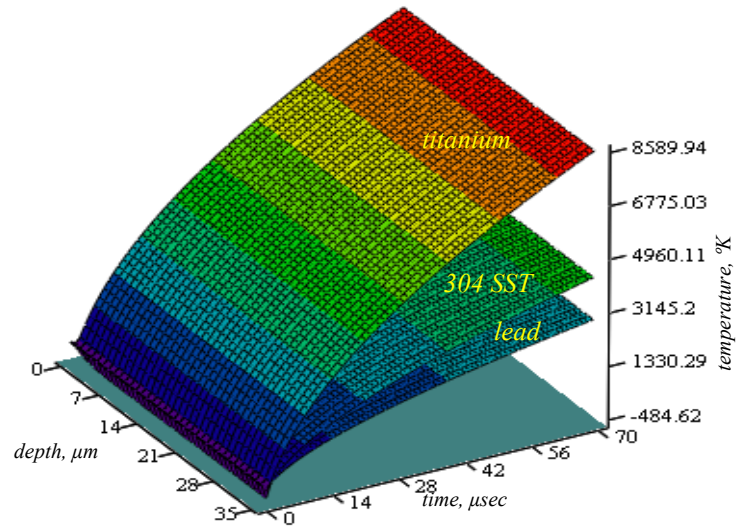
Fig. 3.4. Parametric study of thermal properties.

Examining further Eq. 193, assuming maximum absorption coefficient, let us say that μ goes to infinity, one obtains the following result

$$T(z,t) = \frac{2I_{max}}{k} \sqrt{\kappa \cdot t} \cdot ierfc\left(\frac{z}{2\sqrt{\kappa \cdot t}}\right) \quad .$$
(196)

Graphical representation of Eq. 196 is shown in Fig. 3.5
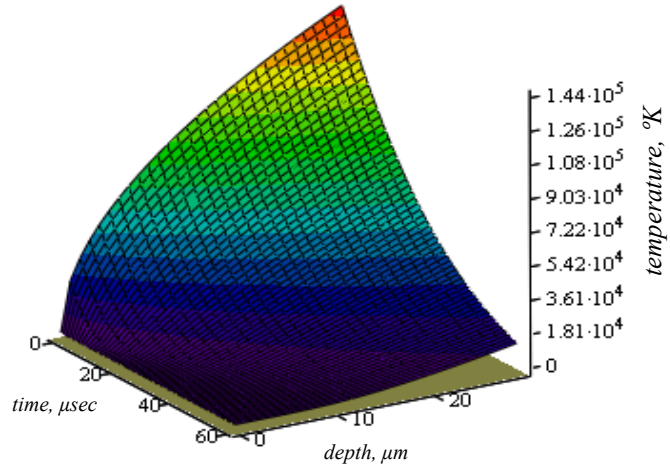
Fig. 3.5. Temperature distribution of the material with respect to time.

Differentiation of Eq. 193 with respect to z gives the temperature gradient inside the

material, i.e.,

$$
\begin{aligned}
\frac{d}{dz}T(z,t) = {} & \frac{I_{max}}{k}\exp(-\mu \cdot z) - \frac{I_{max}}{k}\,erfc\!\left(\frac{z}{2\sqrt{\kappa \cdot t}}\right) + \\
& - \frac{I_{max}}{2k}\exp(\kappa\mu^2 \cdot t - \mu \cdot z)\cdot erfc\!\left(\mu\sqrt{\kappa \cdot t} - \frac{z}{2\sqrt{\kappa \cdot t}}\right) + \\
& + \frac{I_{max}}{2k}\exp(\kappa\mu^2 \cdot t + \mu \cdot z)\cdot erfc\!\left(\mu\sqrt{\kappa \cdot t} + \frac{z}{2\sqrt{\kappa \cdot t}}\right) \quad .
\end{aligned}
\tag{197}
$$

It is evident that $dT(z,\,t)/dz$, Fig. 3.6, will only be zero at the surface, i.e.,

maximum temperature will occur at the surface.

218
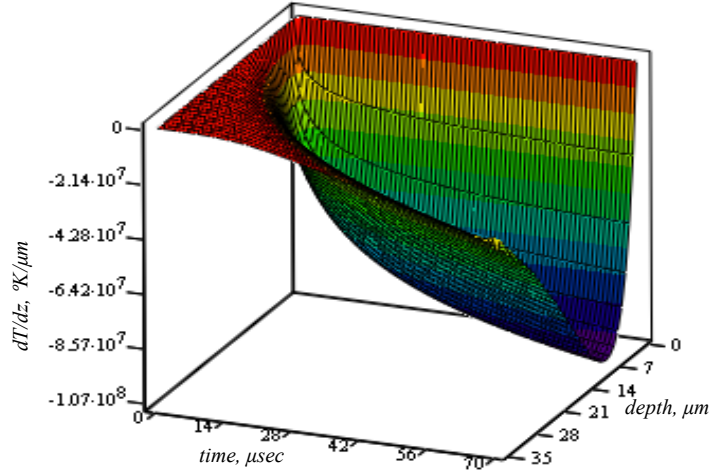
Fig. 3.6. Temperature gradient distribution inside the material with respect to time.

The variation of dT/dz with distance z i.e., (depth, expressed in μm) as a function of tree different time instances is shown in Fig. 3.7. As illustrated in Fig. 3.7 the slope of the curves decreases reaching the minimum and then increases to attain almost zero as the temperature profile becomes almost asymptotic with z. In this case, the behavior of dT/dx with z may be divided into three regions, which are indicated in Fig. 3.7. In the first region, the heat gain due to laser irradiation dominates the conduction losses; i.e., the internal energy increase is considerably high as compared to conduction losses. In the second region, the slope has a $z =$ minimum value; in this case, the energy gain due to incident laser beam balances the conduction losses, i.e., the internal energy of the material remains almost constant. In this case, the distance z corresponding to this point may be defined as the equilibrium distance $(z)_{eq,,}$ (Fig. 3.8), and dT/dz becomes $(dT/dz)_{min}$. In the third region, the slope increases to reach almost zero. In this region, conduction

219

losses are dominant and the energy gain due to the external field is insignificant, i.e., the internal energy decreases as the distance increases.
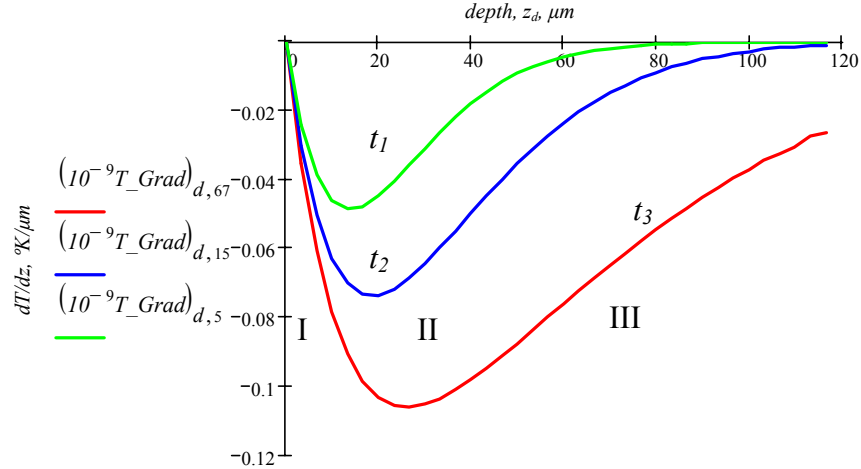
Fig. 3.7. Temperature gradient distribution inside the material for different times.

Variation of the equilibrium distance shown in Fig. 3.8, can be dimensionlized by

$$(z\,\mu)_{eq} = C(\kappa\,\mu^2 t)_q^m \quad , \tag{198}$$

and is expected, that increase in heating time increases the dimensionless equilibrium distance, which in turn increases the dimensionless equilibrium temperature, which can be defined as

$$\left(\frac{T(z,t)}{I_{max}/k\,\mu}\right)_{eq} = C(z\,\mu)_{eq}^m \quad . \tag{199}$$

where C is the constant and m is the power. In other words the equilibrium temperature is defined as the temperature where dT/dz is minimum.
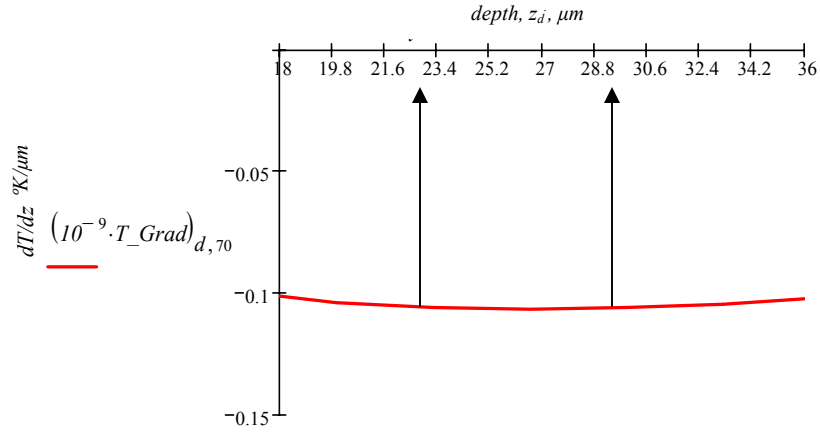
Fig. 3.8. Equlibrium distance.

Based on research done by Yilbas and Sami, (1997), the relationship between equilibrium temperature and equilibrium distance on the logarithmic scale is linear for all materials and pulse lengths.

If the pulse length is approximately 10^{-9}s the analysis of the heat transfer process using the Fourier equation becomes invalid. In this case the heating process would be non-equilibrium.

In semi-infinite medium as shown in Fig. 3.1, at $T=0$ with no heat flow at $t=0$ and with the heat source defined in Eq. 137, solution to this same problem is

$$
\begin{aligned}
T(z,t) = {} & \frac{2I_{max}}{\mu\,k}\sqrt{\kappa\cdot t}\cdot ierfc\!\left(\frac{z}{2\sqrt{\kappa\cdot t}}\right) \\
& - \frac{I_{max}}{k\cdot\mu^2}\cdot\exp(-\mu\cdot z)+ \\
& + \frac{I_{max}}{2k\cdot\mu^2}\exp\!\left[\kappa\mu^2\cdot t-\mu\cdot z\right]\cdot erfc\!\left(\mu\sqrt{\kappa\cdot t}-\frac{z}{2\sqrt{\kappa\cdot t}}\right)+ \\
& + \frac{I_{max}}{2k\cdot\mu^2}\exp\!\left[\kappa\mu^2\cdot t+\mu\cdot z\right]\cdot erfc\!\left(\mu\sqrt{\kappa\cdot t}+\frac{z}{2\sqrt{\kappa\cdot t}}\right)
\end{aligned}
\qquad (200)
$$

and is illustrated in Fig. 3.9. Solution in Eq. 200, is identical to Sparks's (1976) solution for finite thickness slab $l >> \delta$.

Let us consider variation of the temperature distribution with respect to the difference from the material properties variations with temperature. Analytically one can determine that based on extreme material properties for maximum and minimum values of thermal properties, known from the literature. Thermal conductivity varies between 14.9 and 16.2, for ambient temperature, T_a, and 32 for vaporization temperature, T_v, heat capacity c_p varies from 500 to 824, and density ρ varies from 7,870 to 8,000 g/m^3. Discrepancies related to the thermo physical properties of the material could be determined by substituting the lowest and the highest values to solution given by Eq. 200.

Examining graphs in Fig. 3.9 and Fig. 3.10, one can conclude that neglecting temperature dependencies of the material may invoke an estimated error roughly about 50%.
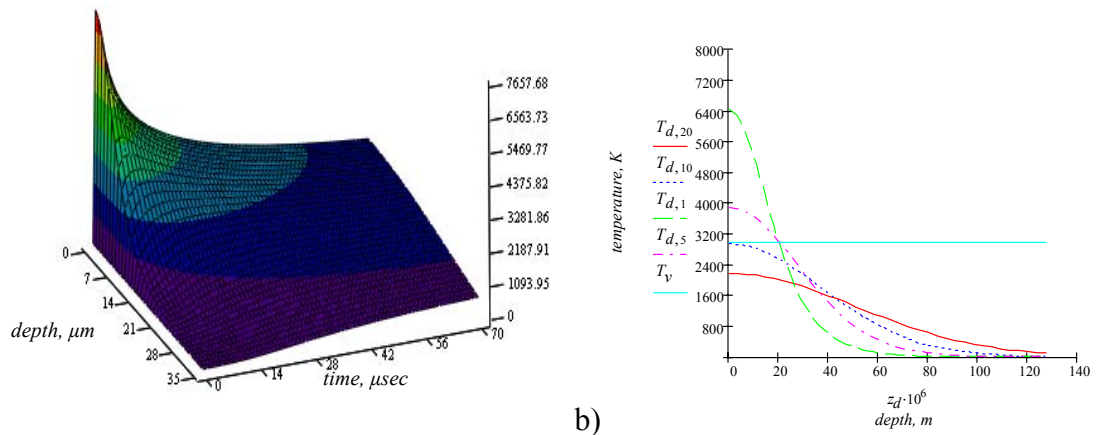
Fig. 3.9. Temperature distrubution of laser irradiated material with the lowest values of thermo-physical parameters, a) temperature as a function of depth and time, b) tempearutre or melting of the material with depth calculated using Eq. .
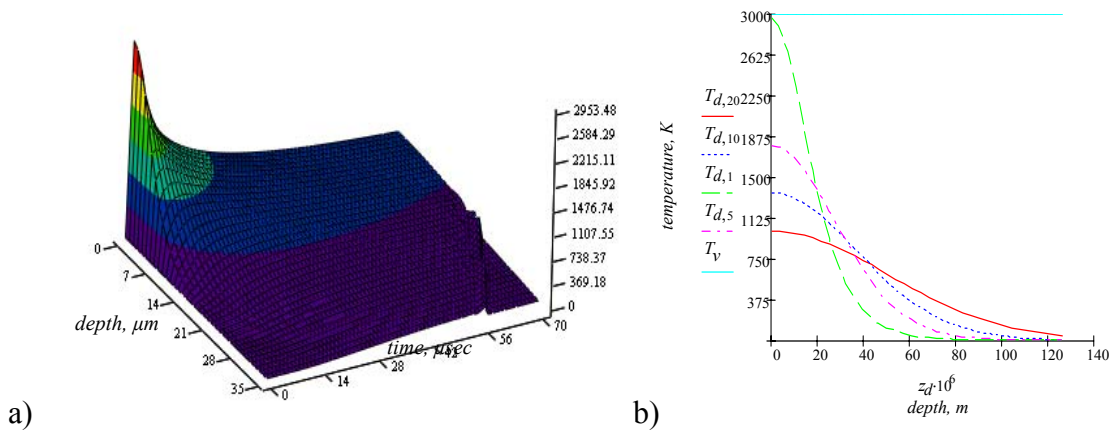
Fig. 3.10. Temperature distrubution of laser irradiated material with the highest values of thermo-physical parameters, a) temperature as a function of depth and time, b) temperature or melting of the material with depth.

Based on Anisimov and Khokhlov (1995) rate of cooling after the end of the pulse can be estimated by Eq. 201 and graphically represented as in Fig. 3.11.

$$VimpC(z,t) = \frac{2AI_{max}}{k} \begin{bmatrix} \sqrt{\frac{\kappa}{t1_t}} \cdot ierfc\left(\frac{z}{2\sqrt{\kappa \cdot t}}\right) + \\ + \frac{z\ erfc\left(\frac{z}{2\sqrt{\kappa \cdot t}}\right)}{2\ t1_t} - \\ + \sqrt{\frac{\kappa}{t1_t - t_p}} \cdot ierfc\left(\mu\sqrt{\kappa \cdot t} - \frac{z}{2\sqrt{\kappa \cdot t}}\right) + \\ - \frac{z}{2(t1_t - t_p)} \cdot erfc\left(\mu\sqrt{\kappa \cdot t} + \frac{z}{2\sqrt{\kappa \cdot t}}\right) \end{bmatrix}. \qquad (201)$$
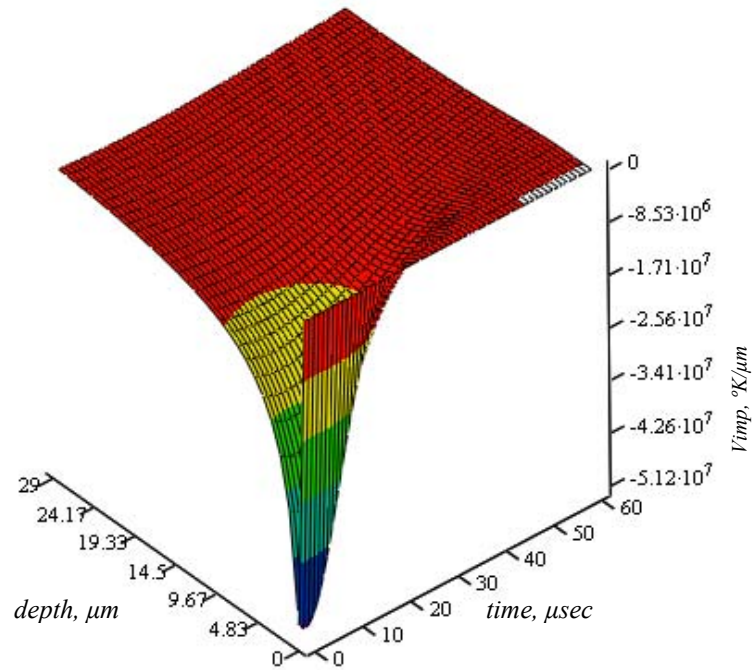
Fig. 3.11. Rate of cooling of the workpiece after the end of laser pulse.

3.1.2. Analytical solution of heat transfer equation with time dependent Gaussian laser pulse heating

This Section presents time-unsteady analysis of the conduction limited heating process introduced for a practical Nd:YAG laser pulse with a time-dependent intensity. An analytical solution to the problem is obtained with appropriate boundary conditions.

The output from a pulsed Nd:YAG laser is described by approximating the form of the true output by the subtraction of two exponential functions. This analytical form is given by

$$I_0 = I_{max} \cdot \left[\exp(-\beta \cdot t) - \exp(-\gamma \cdot t) \right] \quad . \tag{202}$$

For metals and certain applications, at temperatures above the Debye temperature, it can be assumed that $k(T)$ and $c(T)$ do not change with temperature. Therefore, assuming constant specific heat and thermal conductivity for a particular time interval, Eq. 141 can be simplified to

$$k \left(\frac{\partial^2 T}{\partial z^2} \right) + \exp\left[-(\beta \cdot t + \gamma \cdot t) \right] \cdot \mu \cdot I_{max}(x,y,t) \exp(-\mu \cdot z) = \rho \cdot c \cdot \frac{\partial T}{\partial t} \quad . \tag{203}$$

It is unnecessary to solve for the complete pulse, since the complete solution may be obtained by summation of the solutions for the individual parts of time exponential, then equation is linear. Rearrangement of Eq. 203 gives

$$\frac{\partial^2 T}{\partial z^2} + \frac{\mu \cdot I_{max}}{k} \exp(-\mu z) \exp\left[-(\beta \cdot t) - \exp(\mu \cdot z) \right] = \frac{1}{\kappa} \cdot \frac{\partial T}{\partial t} \quad , \tag{204}$$

with boundary conditions

$$\left. \frac{\partial T}{\partial t} \right|_{x=0} = 0 \quad , \tag{205}$$

$$T(\infty, t) = 0 \quad, \tag{206}$$

$$T(z,0) = 0 \quad. \tag{207}$$

Laplace transformation of Eq. 204 with respect to t and substitution of boundary condition from Eq. 206 gives

$$\frac{\partial^2 \overline{T}}{\partial \cdot z^2} - g^2 \overline{T} = \frac{- I_{max} \mu \cdot \exp[-\mu \cdot z]}{k(s + \beta)} \quad, \tag{208}$$

with $T = (z, s)$, $g^2 = \dfrac{s}{\kappa}$, and s the transform variable, which has a complimentary and particular solution:

$$\overline{T} = A \exp(-gz) + B \exp(gz) - \frac{- I_{max} \mu \cdot \exp[-\mu \cdot z]}{k(s + \beta)(\mu^2 - g^2)} \quad, \tag{209}$$

where A and B are arbitrary constants. Substitution of boundary Eqs 205 into Eq. 207 gives these constants as, $B = 0$,

and $\quad A = \dfrac{I_{max} \mu^2}{k \cdot g(p + \beta)(\mu^2 - g^2)}$, therefore, the complex solution in the transform plane is

$$\overline{T} = \frac{- I_{max} \mu}{k(p + \beta)} \cdot \left[\frac{\mu \cdot \exp[-g \cdot z]}{g(g^2 - \mu^2)} - \frac{\cdot \exp[-\mu \cdot z]}{(g^2 - \mu^2)} \right] \quad. \tag{210}$$

The problem now is to invert this solution, which is a product of two p-functions. There are two ways to do this. The first is a convolution integral method and the second method is simpler, entailing expansion of the functions into partial fractions. Using the second method the full solution, obtained by inverse Laplace transformation of Eq. 210 is

$$T(z,t) = \frac{I_{max}\mu}{2k} \cdot \frac{\kappa}{(\beta + \kappa \cdot \mu^2)}$$

$$\left\{ i\mu\sqrt{\frac{\alpha}{\beta}}\exp(-\beta \cdot t)\left[\exp\left(iz\sqrt{\frac{\beta}{\kappa}}\right)erfc\left(\frac{z}{2\sqrt{\kappa \cdot t}} + i\sqrt{\beta \cdot t}\right)\right] + \right.$$

$$- \left[\exp\left(-iz\frac{\sqrt{\beta}}{\kappa}\right)erfc\left(\frac{z}{2\sqrt{\kappa \cdot t}} - i\sqrt{\beta \cdot t}\right)\right] +$$

$$+ \exp(\alpha\mu^2 t)\left(\exp(\mu \cdot z) \cdot erfc\left(\frac{z}{2\sqrt{\kappa \cdot t}} + \mu\sqrt{\kappa \cdot t}\right)\right) +$$

$$- \left[\exp(-\mu \cdot z)erfc\left(\frac{z}{2\sqrt{\kappa \cdot t}} - \mu\sqrt{\alpha \cdot t}\right)\right] +$$

$$\left. + 2\exp(-\mu \cdot z)\left(\exp(\kappa\mu^2 \cdot t) - \exp(-\beta \cdot t)\right) \right\}$$

(211)

Using the relationship *erfc(-z) = 2-erfc(z)* gives the solution

$$T(z,t) = \frac{I_{max}\mu}{2k} \cdot \frac{\kappa}{(\beta + \kappa \cdot \mu^2)}$$

$$\left\{ i\mu\sqrt{\frac{\kappa}{\beta}}\exp(-\beta \cdot t)\left[\begin{array}{c} \left[\exp\left(iz\sqrt{\frac{\beta}{\kappa}}\right)erfc\left(\frac{z}{2\sqrt{\kappa \cdot t}} + i\sqrt{\beta \cdot t}\right)\right] \\ -\left[\exp\left(-iz\sqrt{\frac{\beta}{\kappa}}\right)erfc\left(\frac{z}{2\sqrt{\kappa \cdot t}} - i\sqrt{\beta \cdot t}\right)\right] \end{array} \right] + \right.$$

$$\left. + \exp(\alpha\mu^2 t)\left[\begin{array}{c} \left(\exp(\mu \cdot z) \cdot erfc\left(\frac{z}{2\sqrt{\kappa \cdot t}} + \mu\sqrt{\kappa \cdot t}\right)\right) \\ -\exp(-\mu \cdot z)erfc\left(\mu\sqrt{\kappa \cdot t} - \frac{z}{2\sqrt{\kappa \cdot t}}\right) + \\ -2\exp[-(\beta \cdot t + \mu \cdot z)] \end{array} \right] \right\},$$

(212)

The temperature distribution calculated in Eq. 212, is illustrated in Fig. 3.12.

Fig. 3.12. a) Temperature distribution inside the material (*z*-axis) with respect to time: b) temperature vs. depth of the workpiece, at few different time form the beginnig of the pulse, with the highest values of thermo-physical parameters calculated using Eq. 212.

Fig. 3.13. a) Temperature distribution inside the material (*z*-axis) with respect to time: b) temperature vs. depth of the workpiece, at few different time form the beginnig of the pulse, with the lowest values of thermo-physical parameters calculated using Eq. 212.

The time at which the maximum value of the pulse occurs can be obtained by

differentiating Eq. 202 with respect to *t,* for the pulse. Mathematically speaking, one has

to find t, in the condition that the first derivative of this function should be equal to zero, which gives the condition for the maximum time, t_{max}

$$t_{max} = \frac{\ln\left(\frac{\gamma}{\beta}\right)}{\gamma - \beta} \quad , \tag{213}$$

or

$$\sqrt{\beta t_{max}} = \sqrt{\frac{\ln\left(\frac{\gamma}{\beta}\right)}{\frac{\gamma}{\beta} - 1}} \quad . \tag{214}$$

Insertion of Eq. 214 into Eq. 212 gives the maximum temperature when the maximum pulse occurs. Solving Eqs 212 and 214 gives the condition that the maximum temperature may coincides with the maximum pulse amplitude, i.e., at this point

$$\sqrt{\beta t_{max}} = 1.282 \text{, and } \sqrt{\gamma / \beta} = 1.596 \quad .$$

The time at which the maximum temperature occurs is a function of pulse parameters, provided that the pulse rise times are much greater than the equilibrium time $C / \kappa \mu^2$, described in Section 3.1.1. The surface temperature depends on absorption depth in the initial stages of the pulse and ability to absorb the laser depends on the shape of the pulse Yilbas et al., 1996.

The knowledge of pulse parameters β and γ allows at least theoretically, to adjust the pulse for maximum desired effect based on deductions from the physics of lasing system.

229

3.1.3. Analytical solution of heat transfer equation with time dependent Gaussian laser pulse heating with convective boundary conditions

This Section presents time-unsteady analysis of the conduction limited heating process introduced for a practical Nd-YAG laser pulse with a time-dependent intensity. An analytical solution to the problem is obtained with appropriate boundary conditions.

The output from a pulsed Nd-YAG laser is described by approximating the form of the true output by the subtraction of two exponential functions. This analytical form is given by

$$I = AI_{max} \cdot \left[\exp(-\beta \cdot t) - \exp(-\gamma \cdot t)\right] \quad . \tag{215}$$

For metals and certain applications, at temperatures above the Debye temperature, it can be assumed that $k(T)$ and $c(T)$ do not change with temperature. Therefore, assuming constant specific heat and thermal conductivity for a particular time interval, Eq. 141 can be simplified to

$$\rho \cdot c \cdot \frac{\partial T}{\partial t} = k \left(\frac{\partial^2 T}{\partial z^2} \right) + \exp\left[-(\beta\, t)\right] - \exp\left[-\gamma t\right] A\,\mu\,I_{max}(x,y,t)\exp(-\mu \cdot z) \quad .\tag{216}$$

It is unnecessary to solve for the complete pulse, since the complete solution may be obtained by summation of the solutions for the individual parts of time exponential, then equation is linear. Rearrangement of Eq. 216 gives

$$\frac{\partial^2 T}{\partial z^2} + A\frac{\mu \cdot I_{max}}{k}\exp\left[-\beta \cdot t\right] - \exp\left[-\gamma \cdot t\right]\exp\left[\mu \cdot z\right] = \frac{1}{\kappa} \cdot \frac{\partial T}{\partial t} \quad , \tag{217}$$

with boundary conditions

$$\left.\frac{\partial T}{\partial t}\right|_{x=0} = \frac{h}{k}(T(0,t) - T_0) \quad , \tag{218}$$

230

$$T(\infty,t) = 0 \quad,$$ (219)

$$T(z,0) = 0 \quad.$$ (220)

Complete solution can be obtained by subtraction of solutions for the individual parts of the time exponential pulse. It should be noted that for the solution of a complete pulse, the ambient temperature is considered as zero (T_0=0). Hence, the heat transfer for the half-pulse becomes

$$\frac{\partial^2 T}{\partial z^2} + A\frac{\mu \cdot I_{max}}{k} \exp[-(\beta \cdot t + \mu \cdot z)] = \frac{1}{\kappa} \cdot \frac{\partial T}{\partial t} \quad.$$ (221)

The solution of Eq. 221 can be obtained through the Laplace transformation method, with respect to t

$$\frac{\partial^2 \overline{T}}{\partial \cdot z^2} + \frac{AI_{max}\mu \cdot \exp[-\mu \cdot z]}{k(p+\beta)} = \frac{1}{\kappa}[p\overline{T} - T(z,0)] \quad,$$ (222)

with $\overline{T} =(z, p)$, and $T(z,0)$=0, where, p the transform variable, which has a complimentary and particular solution.

The full solution, obtained by inverse Laplace transformation of Eq. 222 is

$$T(z,t) = a_{10} + \left[\begin{array}{c} i\mu\sqrt{\dfrac{\kappa}{\beta}}\exp(-\beta\cdot t)\left[\begin{array}{c} l_1\exp\!\left(iz\sqrt{\dfrac{\beta}{\kappa}}\right)erfc\!\left(\dfrac{z}{2\sqrt{\kappa\cdot t}}+i\sqrt{\beta\cdot t}\right)+ \\[2mm] l_2\exp\!\left(-iz\sqrt{\dfrac{\beta}{\kappa}}\right)erfc\!\left(\dfrac{z}{2\sqrt{\kappa\cdot t}}-i\sqrt{\beta\cdot t}\right)\end{array}\right]+ \\[8mm] +\mu\sqrt{\kappa}\exp(\alpha\mu^2 t)\left[\begin{array}{c} l_3\exp(-\mu z)erfc\!\left(\dfrac{z}{2\sqrt{\kappa\cdot t}}-\mu\sqrt{\beta\cdot t}\right)+ \\[2mm] -l_4\exp(\mu z)erfc\!\left(\dfrac{z}{2\sqrt{\kappa\cdot t}}+\mu\sqrt{\beta\cdot t}\right)\end{array}\right]+ \\[8mm] -w_1 l_5\exp(w_1\dfrac{z}{\sqrt{\kappa}})\exp(w_1^2 t)erfc\!\left(\dfrac{z}{2\sqrt{\kappa\cdot t}}+w_1\sqrt{t}\right)\end{array}\right]+$$

$$+\left[\begin{array}{c} \dfrac{a_{20}}{\beta+\kappa\mu^2}\exp(\alpha\mu^2 t)-\exp(-\beta\cdot t)\exp(-\mu\cdot z)+ \\[6mm] -\dfrac{a_{30}}{w_1}\left(\begin{array}{c} -\exp(w_1\dfrac{z}{\sqrt{\kappa}})\exp(w_1^2 t)erfc\!\left(\dfrac{z}{2\sqrt{\kappa\cdot t}}+w_1\sqrt{t}\right)+ \\[4mm] erfc\!\left(\dfrac{z}{2\sqrt{\kappa\cdot t}}\right)\end{array}\right)\end{array}\right], \qquad (223)$$

where

$$a_{10} = \frac{-\mu\cdot I_{max}\kappa\,(h+k\,\mu)}{k^2}, \qquad (224)$$

$$a_{20} = \frac{I_{max}\kappa\,\mu}{k}, \qquad (225)$$

$$a_{30} = \frac{\sqrt{\kappa}\,h}{k}T_0, \qquad (226)$$

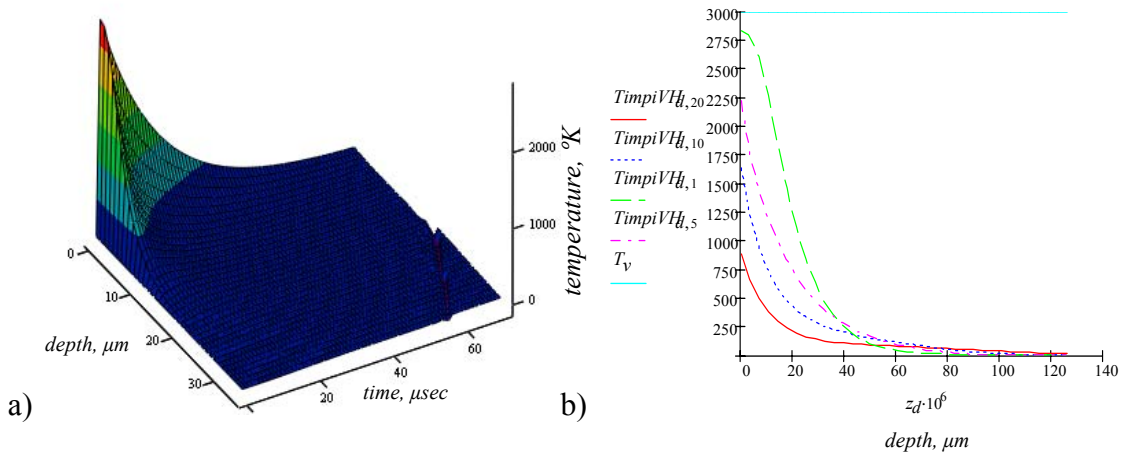The temperature distribution calculated in Eq. 223 is illustrated in Fig. 3.14.
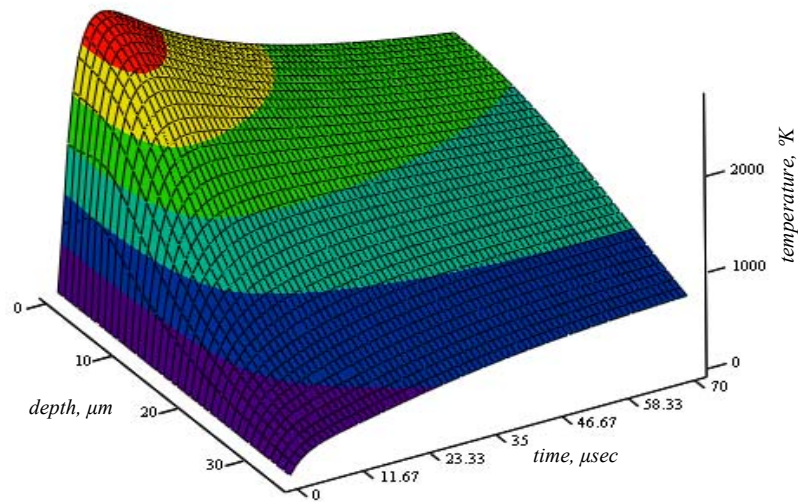
Fig. 3.14. a) Temperature distribution inside the material (z-axis) with respect to time:
b) temperature vs. depth of the workpiece, at few different time form the beginnig of the
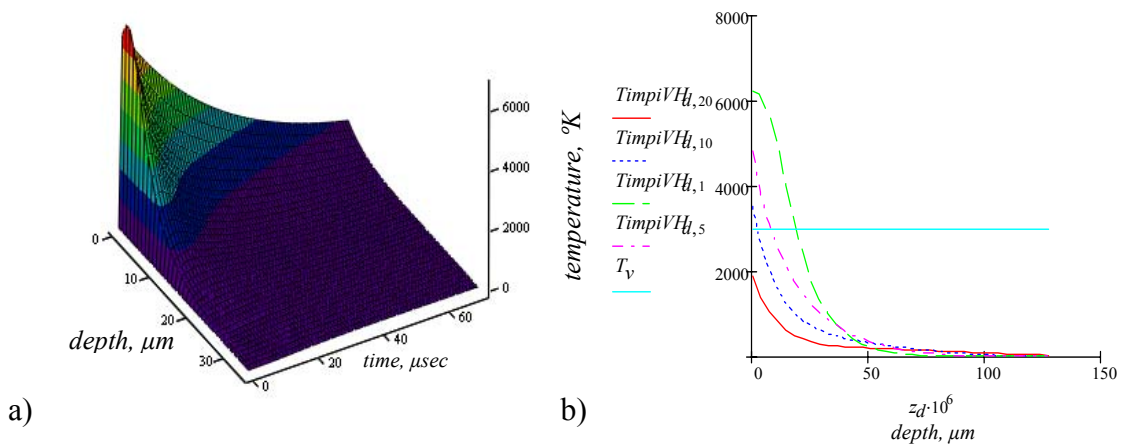pulse, with the highest values of thermo-physical parameters calculated using Eq. 223.
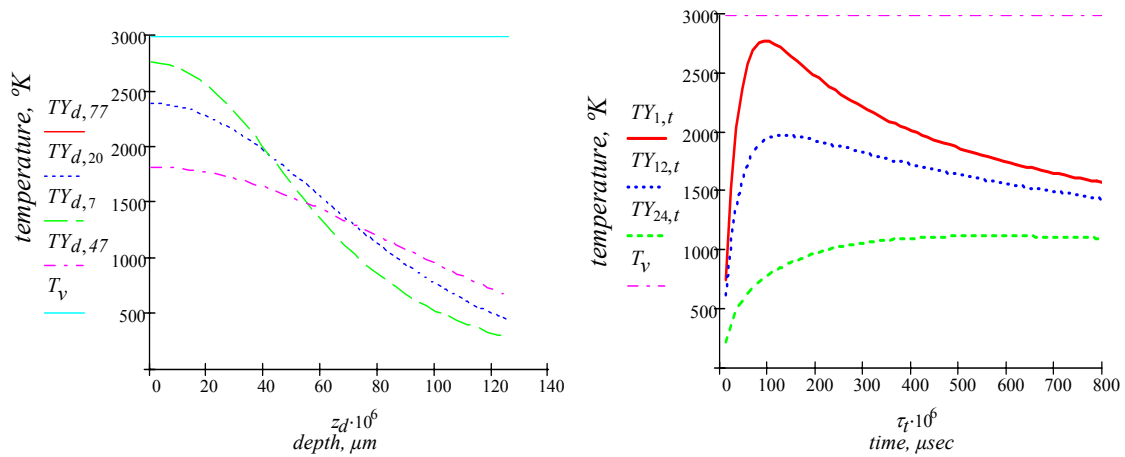
Fig. 3.15. a) Temperature distribution inside the material (z-axis) for few different times;
b) transient distrubution of the workpiece, at few different depths, with the highest
values of thermo-physical parameters calculated using Eq. 223.

233
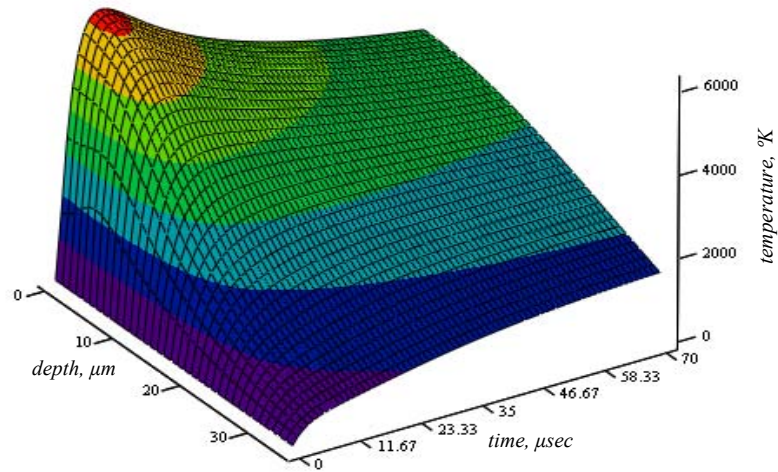
Fig. 3.16. Temperature distribution inside the material (*z*-axis) with respect to time, with the lowest values of thermo-physical parameters calculated using Eq. 223.
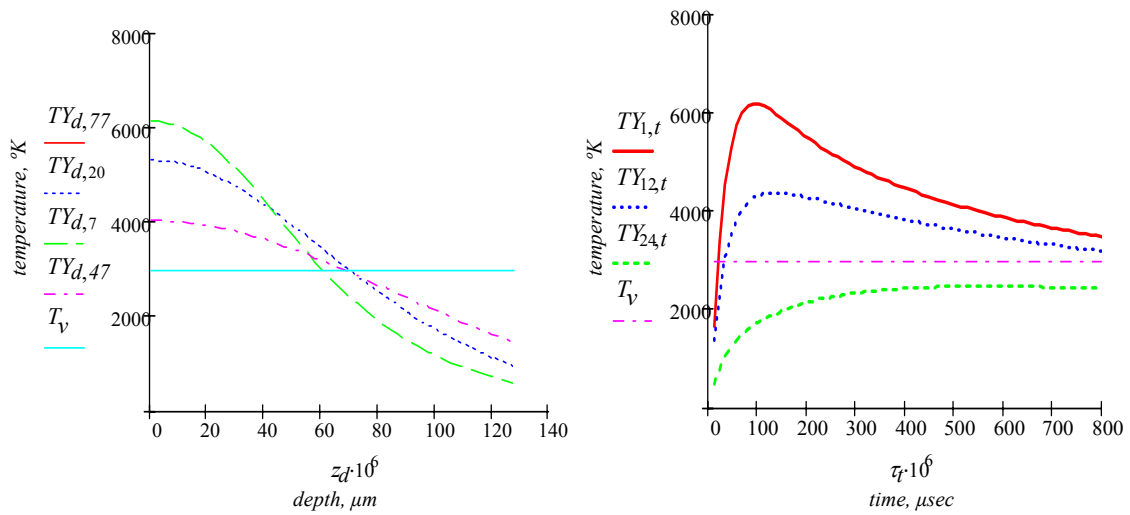
Fig. 3.17. a) Temperature distribution inside the material (*z*-axis) for few different times; b) transient distrubution of the workpiece, at few different depths, with the lowest values of thermo-physical parameters calculated using Eq. 223.

3.1.4. Analytical solution of governing heat transfer equation, considering transfer evaporative case

This Section presents analysis of the heating process. In the heating analysis, evaporation is considered as the exclusive phenomenon taking place during the ablation process. Based on forgoing discussion, melting without vaporization can be produced only in very narrow range of laser parameters. Usually both phase transitions (melting and vaporization) occurs almost simultaneously in standard laser applications. Note, that the latent heat of vaporization is larger then that of fusion by the factor of 20-50 times. Thus, evaporation plays the most important part in the energy balance.

To simplify our discussion we will assume that the vaporization occurs in vacuum and the vapor does not absorb the laser energy. When the vapor does not absorb the laser light, the process in the condensed and gaseous phases can be considered separately. An analytical solution to the problem is obtained with appropriate boundary conditions. In this case, plasma formation, liquid expulsion, and nucleate boiling are omitted.

Solid or liquid evaporates at any temperature greater then 0°K. The evaporation rates strongly depend on the temperature, T. This dependence can be written in the form

$$V_n = V_0 \exp\left(-\frac{U}{T}\right) ,$$
(227)

where V_n is the normal component of the evaporation front velocity, and

$$U = \frac{MH_v}{N_a k_B} ,$$
(228)

and H_v is the latent heat of vaporization (per unit mass)., k_B is Boltzmann's constant, M is the atomic mass, and V_0 is a constant whose value is of the order of the speed of sound in

the condensed phase. The Fourier differential equations allowing a phase change process can be written as

$$\rho(T)\frac{\partial}{\partial t}\int_{T_0}^{T}c(T)dT = \frac{\partial}{\partial x}\left[k(T)\frac{\partial T}{\partial x}\right] + \frac{\partial}{\partial y}\left[k(T)\frac{\partial T}{\partial y}\right] + \frac{\partial}{\partial z}\left[k(T)\frac{\partial T}{\partial z}\right] + $$
$$+ \rho(T)\cdot c(T)\cdot V\frac{\partial T}{\partial z} + Q \tag{229}$$

where $\rho(T)$ is the density of the material of the workpiece, $c(T)$ is the temperature dependent specific heat of the material, $k(T)$ is the temperature dependent thermal conductivity, V is the recession velocity, and $T = T(x, y, z, t)$ is the resulting three-dimensional time dependent temperature distribution in the material, t is time, T_0 is the initial temperature, and x, y, z are the spatial Cartesian coordinates.

$Q(x, y, z, t)$ is the rate at which heat is supplied to the solid per unit time per unit volume, depends on the laser pulse parameters and optical properties of material irradiated and defined by Eq. 167.

Sparks (1975) defined absorption coefficient of the material as a linear function of the surface temperature in Eq. 166. For practical reason the absorption factor A we assume as unity. This temperature dependence of A results from the fact that A is proportional to the electron-phonon collision frequency which, in turn, is proportional to the crystal lattice temperature.

The recession velocity of the surface can be formulated from energy balance at the free surface of irradiated workpiece. In this case the energy flux at the free surface can be written as

$$I_0 = \rho(T) \, V[cT_s + H_v] \quad , \tag{230}$$

where, $I_0 = I_{max}(1 - R) \quad$, $\tag{231}$

and T_s is the surface temperature and H_v is the latent heat of vaporization and R is surface

reflectivity. Rearrangement of Eq. 230 yields

$$V = \frac{I_0}{\rho(T) \cdot [c(T)T_s + H_v]} \quad . \tag{232}$$

For metals and certain applications, at temperatures above the Debye temperature, it can

be assumed that $k(T)$, $\rho(T)$ and $c(T)$ do not change dramatically with temperature.

Therefore, assuming constant specific heat and thermal conductivity for a particular time

interval, Eq. 229 can be simplified to

$$\rho \cdot c \cdot \frac{\partial T}{\partial t} = k\left(\frac{\partial^2 T}{\partial z^2}\right) + \rho \cdot c \cdot V \frac{\partial T}{\partial z} + \\ + I_{max}(x, y, t)(1 - R)\exp(-\beta \cdot t) \cdot \mu \cdot \exp(-\mu \cdot z) \quad . \tag{233}$$

It should be noted that peak power intensity, I_{max} does not vary with time. Since the

surface temperature is time dependant, the recession velocity varies with time. This

result is non-linear form of Eq. 233, which cannot be solved analytically by Laplace

transformation method. For a known surface temperature there is a unique value for

recession velocity, so an iterative method can be applied here to solve Eq. 233

analytically. In our case keeping the recession velocity constant in Eq. 232 enables us to

determine the surface temperature analytically and after obtaining the surface temperature

the recession velocity can be calculated using Eq. 232. This procedure can be repeated so

long as the surface temperature and recession velocity converge to correct results.

Rearrangement of Eq. 233 gives

$$\frac{\partial^2 T}{\partial z^2} + \frac{V}{\kappa}\frac{\partial T}{\partial z} + \frac{\mu \cdot I_0}{k}\exp(-\beta \cdot t)\exp(-\mu \cdot z) = \frac{1}{\kappa} \cdot \frac{\partial T}{\partial t} \quad , \tag{234}$$

where thermal diffusivity $\kappa = \dfrac{k}{\rho \cdot c}$, with boundary conditions

$$\left.\begin{array}{l} \dfrac{\partial T}{\partial t}\bigg|_{x=0} = \dfrac{\rho \cdot V \cdot L}{k} \\[2mm] T(\infty, t) = 0 \\[1mm] T(z,0) = 0 \end{array}\right\} \quad . \tag{235}$$

We can apply the Laplace transform, defined as

$$u(z, p) = \int_0^\infty T(z,t)e^{-pt}dt \quad . \tag{236}$$

Laplace transformation of Eq. 234 with respect to t and substitution of boundary condition from Eq. 235 gives

$$\frac{\partial^2 \overline{T}}{\partial z^2} + \frac{V}{\kappa}\frac{\partial \overline{T}}{\partial z} - \frac{p}{\kappa}\overline{T} = \frac{-I_0\mu \cdot \exp[-\mu \cdot z]}{k \cdot (p + \beta)} \quad , \tag{237}$$

with $T= (z, p)$, and p the transform variable, which has a complimentary (homogenous) and particular solution

$$\overline{T} = \overline{T}_h + \overline{T}_p \quad . \tag{238}$$

The characteristic equation for the homogenous solution can be written as

$$\varsigma^2 + \frac{V}{\kappa}\varsigma - \frac{p}{\kappa} = 0 \quad , \tag{239}$$

which leads

$$\varsigma_{1,2} = -\frac{V}{2\kappa} \pm \frac{\sqrt{V^2 + 4p\kappa}}{2\kappa} \quad . \tag{240}$$

The homogeneous solution from Eq. 239 yields

$$\overline{T}_h = c_1 e^{\varsigma_1 z} + c_2 e^{\varsigma_2 z} \quad , \tag{241}$$

or

$$\overline{T}_h = e^{-\frac{Vz}{2\kappa}} \left[c_1 e^{-\frac{\sqrt{V^2+4p\kappa}}{2\kappa}z} + c_2 e^{\frac{\sqrt{V^2+4p\kappa}}{2\kappa}z} \right] \quad . \tag{242}$$

For the particular solution, one can propose exponential solution

$$\overline{T}_p = A_0 e^{-\delta z} \quad . \tag{243}$$

Substitution of T_p given by Eq. 243 into Eq. 233 results in

$$A_0 \delta^2 e^{-\delta z} - \frac{V}{\kappa} A_0 \delta \ e^{-\delta z} - \frac{p}{\kappa} A_0 \delta \ e^{-\delta z} = H_0 e^{-\delta z} \quad , \tag{244}$$

where, $H_0 = I_0 \dfrac{1}{(p+\beta)} \dfrac{\delta}{k} \quad , \tag{245}$

$$A_0 = -\frac{H_0 \kappa}{p + V\delta - \kappa\delta^2} \quad , \tag{246}$$

and substituting Eqs 246 into Eq. 243 and Eq. 242 into Eq. 238, we obtain

$$\overline{T} = e^{-\frac{Vz}{2\kappa}} \left[c_1 e^{-\frac{\sqrt{V^2+4p\kappa}}{2\kappa}z} + c_2 e^{\frac{\sqrt{V^2+4p\kappa}}{2\kappa}z} \right] - \frac{H_0 \kappa}{p + V\delta - \kappa\delta^2} \quad . \tag{247}$$

Defining

$$V_1 = V\delta - \kappa\delta^2 \quad , \tag{248}$$

substituting Eq. 248 and using boundary Eq. 235, then $c_2=0$, therefore,

$$\overline{T} = c_1 e^{-\frac{1}{2\kappa}[V+\sqrt{V^2+4p\kappa}]z} + \frac{I_1 \delta\kappa}{k} \frac{e^{-\delta z}}{(p+\beta)(p+V_1)} \quad . \tag{249}$$

We can calculate c_1 by using boundary condition and defining

$$\varpi_1 = \frac{I_0 \delta \kappa}{k} \quad , \tag{250}$$

$$\frac{\partial \overline{T}}{\partial z} = \left\{ -\frac{1}{2\kappa}[V + \sqrt{V^2 + 4p\kappa}]c_1 e^{-\frac{1}{2\kappa}[V + \sqrt{V^2 + 4p\kappa}]z} - \frac{\delta \varpi_1 \kappa \cdot e^{-\delta z}}{(p+\beta)(p+V_1)} \right\}_{z=0}$$

$$= \frac{\rho \cdot VL}{kp} \quad , \tag{251}$$

from Eq. 251, c_1 is

$$c_1 = -\frac{2\delta \cdot \varpi_1 \cdot \kappa}{(p+\beta)(p+V_1)(V + \sqrt{V^2 + 4p\kappa})} - \frac{2\kappa \dfrac{\rho \cdot VL}{k}}{p(V + \sqrt{V^2 + 4p\kappa})} \quad , \tag{252}$$

Hence,

$$\overline{T} = \frac{2\kappa \cdot \delta \cdot \varpi_1 e^{-\frac{1}{2\kappa}[V + \sqrt{V^2 + 4p\kappa}]z}}{(p+\beta)(p+V_1)(V + \sqrt{V^2 + 4p\kappa})} + \frac{\varpi_1 e^{-\delta z}}{(p+\beta)(p+V_1)} + \overline{T}_{mm} \quad , \tag{253}$$

where

$$\overline{T}_{mm} = -\frac{2\kappa \cdot \rho \cdot VL \cdot e^{-\frac{1}{2\kappa}[V + \sqrt{V^2 + 4p\kappa}]z}}{k \cdot p(V + \sqrt{V^2 + 4p\kappa})} \quad . \tag{254}$$

For the purpose of easier handling calculations for the future, let us define: H_1, H_2, and H_3 to be

$$H_1 = \frac{e^{-\frac{1}{2\kappa}[V + \sqrt{V^2 + 4p\kappa}]z}}{(p+\beta)(p+V_1)(V + \sqrt{V^2 + 4p\kappa})} \quad , \tag{255}$$

$$H_2 = \frac{1}{(p+\beta)(p+V_1)} = \frac{1}{V_1 - \beta}\left[\frac{1}{p+\beta} - \frac{1}{p+V_1}\right] \quad , \tag{256}$$

$$H_3 = \frac{e^{-\frac{1}{2\cdot\kappa}[V+\sqrt{V^2+4\,p\kappa}]z}}{p(V+\sqrt{V^2+4\,p\kappa})} \quad . \tag{257}$$

Consequently,

$$\overline{T}(z,t) = \pounds^{-1}\overline{\overline{T}} \quad , \tag{258}$$

$$\overline{T}(z,t) = -2\kappa\cdot\mu\cdot\varpi_1\,\pounds^{-1}H_1 + \varpi_1 e^{-\mu\cdot z}\,\pounds^{-1}H_2 - 2\kappa\frac{\rho\cdot VL}{k}\,\pounds^{-1}H_3 \quad . \tag{259}$$

To obtain the inverse transformation of functions $\pounds^{-1}H_1$ and $\pounds^{-1}H_3$, let us introduce

$$s = V^2 + 4\kappa\cdot\rho \qquad or \qquad ds = 4\cdot\kappa\cdot dp \quad and \quad p = \frac{1}{4\cdot\kappa}(s-V^2) \tag{260}$$

therefore, $\pounds^{-1}H_1 = \dfrac{1}{2\pi\cdot i}\displaystyle\int_{c-i\infty}^{c+i\infty} e^{tp}H_1(p)dp$ \hfill (261)

or

$$\pounds^{-1}H_1 = \frac{1}{4\kappa}e^{-\left(\frac{Vz}{2\kappa}+\frac{V^2}{4\kappa}\right)}\frac{1}{2\pi\cdot i}\int_{\overline{c}-\infty}^{\overline{c}+\infty}\frac{e^{-\left(\frac{Vz}{2\kappa}+\frac{V^2}{4\kappa}\right)}}{\left(\dfrac{s}{4\kappa}-\dfrac{V^2}{4\kappa}+\beta\right)\left(\dfrac{s}{4\kappa}-\dfrac{V^2}{4\kappa}+V_1\right)(V+\sqrt{s})}\,ds \quad , \tag{262}$$

where $\overline{c} = 4\kappa\cdot c + V_2$ \quad . \hfill (263)

We can use one more transformation by letting

$$\vartheta = \frac{1}{4\kappa} \quad or \quad ds = 4\kappa\cdot d\vartheta \tag{264}$$

after lengthy algebra, we obtain

$$\pounds^{-1}H_1 = e^{-\left(\frac{Vz}{2\kappa}+\frac{V^2}{4\kappa}\right)}\frac{1}{2\pi\cdot i}\int_{\overline{c}-\infty}^{\overline{c}+\infty}\frac{4\cdot\kappa\cdot e^{-\left(\frac{z\sqrt{p}}{\sqrt{\kappa}}\right)}\cdot e^{\vartheta\cdot t}}{\left(\vartheta-\dfrac{V^2}{4\kappa}+\beta\right)\left(\vartheta-\dfrac{V^2}{4\kappa}+V_1\right)(V+2\sqrt{\kappa}\sqrt{\vartheta})}\,d\vartheta \quad , \tag{265}$$

where $\hat{c} = \bar{c}/4\kappa$. (266)

hence, $\pounds^{-1} H_1 = 4 \cdot \kappa \cdot e^{-\frac{V}{2\kappa}\left(z+t\frac{V}{2}\right)} \cdot \pounds^{-1} H_4$, (267)

where $H_4 = \dfrac{e^{-\left(\frac{z\sqrt{p}}{\sqrt{\kappa}}\right)}}{\left(p - \dfrac{V^2}{4\kappa} + \beta\right)\left(p - \dfrac{V^2}{4\kappa} + V_1\right)(V + 2\sqrt{\kappa}\sqrt{p})}$. (268)

Similarly, $\pounds^{-1} H_3$ can be obtained, i.e.,

$$\pounds^{-1} H_3 = 4 \cdot \kappa \cdot e^{-\frac{V}{2\kappa}\left(z+t\frac{V}{2}\right)} \cdot \pounds^{-1} H_7 \quad,$$ (269)

where $H_7 = \dfrac{e^{-\left(\frac{z\sqrt{p}}{\sqrt{\kappa}}\right)}}{\left(\sqrt{\kappa}\sqrt{p} - V^2\right)\left(2\sqrt{\kappa}\sqrt{p} + V\right)^2}$, (270)

or $H_7 = \dfrac{1}{8\kappa\sqrt{\kappa}} \dfrac{e^{-\left(\frac{z\sqrt{p}}{\sqrt{\kappa}}\right)}}{\left(\sqrt{p} - \xi\right)\left(\sqrt{p} + \xi^2\right)}$, (271)

where

$$\xi = \frac{V}{2\sqrt{\kappa}} \quad .$$ (272)

Introducing partial fractions and rearrangement yields

$$H_7 = \frac{1}{8V^2\sqrt{\kappa}}\left[\frac{e^{-\left(\frac{z\sqrt{p}}{\sqrt{\kappa}}\right)}}{\left(\sqrt{p} - \xi\right)} - \frac{e^{-\left(\frac{z\sqrt{p}}{\sqrt{\kappa}}\right)}}{\left(\sqrt{p} + \xi\right)} - \frac{e^{-\left(\frac{z\sqrt{p}}{\sqrt{\kappa}}\right)}}{\sqrt{\kappa}\left(\sqrt{p} + \xi\right)^2}\right] \quad .$$ (273)

It is noted from the Laplace inversion that

$$\pounds^{-1} \frac{e^{-k\sqrt{p}}}{a + \sqrt{p}} = \frac{1}{\sqrt{\pi \cdot t}} e^{-\frac{k^2}{2t}} - a e^{ak} e^{a^2 t} erfc\left(a\sqrt{t} + \frac{k}{2\sqrt{t}}\right) \quad,$$ (274)

242

where complimentary error function is defined as

$$erfc(z) = 1 - erf(z) \quad , \tag{275}$$

and

$$erfc(z) = 1 - erf(z) = \frac{2}{\pi} \int_z^\infty e^{-u^2} du \quad . \tag{276}$$

Therefore,

$$\pounds^{-1} \frac{e^{-\frac{z}{\sqrt{\kappa}}\sqrt{p}}}{\sqrt{p}-\xi} = \frac{1}{\sqrt{\pi \cdot t}} e^{-\frac{z^2}{2\kappa t}} + \frac{V}{2\sqrt{\kappa}} e^{-\frac{Vz}{2\kappa}} e^{\frac{V^2}{4\kappa}t} erfc\left(\frac{z}{2\sqrt{\kappa \cdot t}} - \frac{V}{2\sqrt{\kappa}}\sqrt{t} \right) \quad , \tag{277}$$

$$\pounds^{-1} \frac{e^{-\frac{z}{\sqrt{\kappa}}\sqrt{p}}}{\sqrt{p}+\xi} = \frac{1}{\sqrt{\pi \cdot t}} e^{-\frac{z^2}{2\kappa t}} - \frac{V}{2\sqrt{\kappa}} e^{\frac{Vz}{2\kappa}} e^{\frac{V^2}{4\kappa}t} erfc\left(\frac{z}{2\sqrt{\kappa \cdot t}} + \frac{V}{2\sqrt{\kappa}}\sqrt{t} \right) \quad . \tag{278}$$

Letting $\sqrt{p}+\xi = \sqrt{s}$ and using the definition of inverse Laplace integral

$$\pounds^{-1} \frac{e^{-\left(\frac{z}{\sqrt{\kappa}}\sqrt{p}\right)}}{\left(\sqrt{p}+\xi\right)^2} \quad \text{becomes}$$

$$\pounds^{-1} \frac{e^{-\frac{z}{\sqrt{\kappa}}\sqrt{p}}}{\left(\sqrt{p}+\xi\right)^2} = e^{\frac{Vz}{2\kappa}} e^{\frac{V^2}{4\kappa}t} erfc\left(\frac{z\sqrt{t}}{2\sqrt{\kappa \cdot}} + \frac{z}{2\sqrt{\kappa t}} \right)\left(1 + \frac{Vz}{2\kappa} + \frac{V^2 t}{2\kappa} \right) - \frac{V\sqrt{t}}{2\sqrt{\pi \kappa \cdot}} e^{-\frac{z^2}{4\kappa \cdot t}}, \tag{279}$$

using Eqs 277, 278, 279, and after simplifications, the Laplace inversion of H_3 becomes

$$\pounds^{-1} H_3 = \frac{1}{16\kappa V}\left[e^{\frac{Vz}{\kappa}} erfc\left(\frac{z-Vt}{2\sqrt{\kappa \cdot t}} \right) - \left(1 + \frac{Vz}{\kappa} + \frac{V^2 t}{\kappa} \right) erfc\left(\frac{z+Vt}{2\sqrt{\kappa \cdot t}} \right) \right] +$$
$$+ \frac{\sqrt{t}}{8\kappa\sqrt{\pi\kappa}} e^{-\frac{(z+Vtz)^2}{4\kappa \cdot t}} \tag{280}$$

Let $w_2^2 = \frac{V^2}{4\kappa}$, $k_1 = \frac{z}{\sqrt{\kappa}}$, $w_3^2 = \frac{V^2}{4\kappa} - V_1$, $w_4 = \frac{V}{2\sqrt{\kappa}}$, $\tag{281}$

then H_4 becomes

$$H_4 = \frac{1}{\left(\sqrt{p}^2 - w_2^2\right)\left(\sqrt{p}^2 - w_3^2\right)\left(\sqrt{p} + w_4\right)} \frac{1}{2\sqrt{\kappa}} e^{-\left(k_1\sqrt{p}\right)} \quad , \tag{282}$$

and, after using partial fraction expansion, H_5 becomes

$$H_4 = \left[\begin{array}{c} \dfrac{D_1}{\left(\sqrt{p} - w_2\right)} + \dfrac{D_2}{\left(\sqrt{p} + w_2\right)}\dfrac{D_3}{\left(\sqrt{p} - w_3\right)}\dfrac{D_4}{\left(\sqrt{p} + w_3\right)} \\[3mm] + \dfrac{D_5}{\left(\sqrt{p} + w_4\right)} \end{array}\right] \frac{1}{2\sqrt{\kappa}} e^{-\left(k_1\sqrt{p}\right)} \quad , \tag{283}$$

where, $D_1 = \dfrac{1}{2w_2\left(w_2^2 - w_3^2\right)\left(w_2 + w_4\right)}$, $\tag{284}$

$$D_2 = \frac{1}{2w_2\left(w_2^2 - w_3^2\right)\left(-w_2 + w_4\right)} \quad , \tag{285}$$

$$D_3 = \frac{1}{2w_3\left(w_3^2 - w_2^2\right)\left(w_3 + w_4\right)} \quad , \tag{286}$$

$$D_4 = \frac{1}{2w_3\left(w_3^2 - w_2^2\right)\left(-w_3 + w_4\right)} \quad , \tag{287}$$

$$D_5 = \frac{1}{\left(w_4^2 - w_2^2\right)\left(w_4^2 + w_3^2\right)} \quad . \tag{288}$$

After substituting Eqs 284-288 into Eq. 283, $\pounds^{-1}H_4$ can be rewritten as

$$
£^{-1} H_4 = \frac{1}{2\sqrt{\kappa}} \left\{
\begin{aligned}
& D_1 \left[\left(\frac{1}{\sqrt{\pi \cdot t}} \right) e^{-\frac{k_1^2}{4t}} + w_2 e^{-w_2 k_1} e^{w_2^2 t_1} erfc\left(-w_2 \sqrt{t} + \frac{k_1}{2\sqrt{t}} \right) \right] \\
& + D_2 \left[\left(\frac{1}{\sqrt{\pi \cdot t}} \right) e^{-\frac{k_1^2}{4t}} - w_2 e^{-w_2 k_1} e^{w_2^2 t_1} erfc\left(w_2 \sqrt{t} + \frac{k_1}{2\sqrt{t}} \right) \right] \\
& + D_3 \left[\left(\frac{1}{\sqrt{\pi \cdot t}} \right) e^{-\frac{k_1^2}{4t}} + w_3 e^{-w_3 k_1} e^{w_3^2 t_1} erfc\left(-w_3 \sqrt{t} + \frac{k_1}{2\sqrt{t}} \right) \right] \\
& + D_4 \left[\left(\frac{1}{\sqrt{\pi \cdot t}} \right) e^{-\frac{k_1^2}{4t}} - w_3 e^{w_3 k_1} e^{w_3^2 t_1} erfc\left(w_3 \sqrt{t} + \frac{k_1}{2\sqrt{t}} \right) \right] \\
& + D_5 \left[\left(\frac{1}{\sqrt{\pi \cdot t}} \right) e^{-\frac{k_1^2}{4t}} - w_4 e^{w_4 k_1} e^{-w_4^2 t_1} erfc\left(w_4 \sqrt{t} + \frac{k_1}{2\sqrt{t}} \right) \right]
\end{aligned}
\right\} . \qquad (289)
$$

However, it is known from Eq. 258, that $T(x,t)$ can be written as

$$
\overline{T}(z,t) = £^{-1}\overline{T} = -2\kappa \cdot \mu \cdot \varpi_1 e^{-\frac{V}{2\cdot\kappa}[z+\frac{V}{2}t]} £^{-1} H_4 + \varpi_1 e^{-\mu \cdot z} £^{-1} H_2 - 8\kappa^2 \frac{\rho V L}{k} £^{-1} H_3 \quad (290)
$$

note that

$$
£^{-1} H_2 = \frac{1}{V_1 - \beta}(e^{-\beta \cdot t} - e^{-V_1 \cdot t}) \qquad (291)
$$

Substituting Eqs 280, 289, 291, into Eq. 290, we get

$$T(z,t) = \frac{\kappa \cdot \mu \cdot \varpi_1}{\sqrt{\kappa}} e^{-\frac{V}{2 \cdot \kappa}(z+\frac{V}{2}t)} \left\{ \begin{array}{l} \frac{1}{\sqrt{\pi \cdot t}} e^{-\frac{k_1^2}{4t}} [D_1 + D_2 + D_3 + D_4 + D_5] \\[2ex] D_1 \left[w_2 e^{-w_2 k_1} e^{w_2^2 t_1} erfc\left(-w_2 \sqrt{t} + \frac{k_1}{2\sqrt{t}} \right) \right] \\[2ex] + D_2 \left[-w_2 e^{-w_2 k_1} e^{w_2^2 t_1} erfc\left(w_2 \sqrt{t} + \frac{k_1}{2\sqrt{t}} \right) \right] \\[2ex] + D_3 \left[w_3 e^{-w_3 k_1} e^{w_3^2 t_1} erfc\left(-w_3 \sqrt{t} + \frac{k_1}{2\sqrt{t}} \right) \right] \\[2ex] + D_4 \left[-w_3 e^{w_3 k_1} e^{w_3^2 t_1} erfc\left(w_3 \sqrt{t} + \frac{k_1}{2\sqrt{t}} \right) \right] \\[2ex] + D_5 \left[-w_4 e^{w_4 k_1} e^{-w_4^2 t_1} erfc\left(w_4 \sqrt{t} + \frac{k_1}{2\sqrt{t}} \right) \right] \\[2ex] + \frac{\varpi_1}{V_1 - \beta} e^{-\mu \cdot z} [e^{-\beta \cdot t} - e^{-V_1 \cdot t}] \end{array} \right\}$$

$$- \frac{\alpha \cdot \kappa \cdot L}{2k} e^{-\frac{Vz}{\kappa}} erfc\left(\frac{z - Vt}{2\sqrt{\kappa \cdot t}} \right)$$

$$- \left[\left(1 + \frac{Vz}{\kappa} + \frac{V^2 t}{\kappa} \right) erfc\left(\frac{z + Vt}{2\sqrt{\kappa \cdot t}} \right) \right]$$

$$- \frac{\rho \cdot V \cdot L}{k} \frac{\sqrt{\kappa \cdot t}}{\sqrt{\pi}} e^{-\frac{(z+Vt)^2}{4\kappa \cdot t}}$$

(292)

Knowing that $D_1 + D_2 + D_3 + D_3 + D_5 = 0$, Eq. 292 becomes

$$T(z,t) = \sqrt{\kappa} \cdot \mu \cdot \varpi_1 e^{-\frac{V}{2\cdot\kappa}\left(z+\frac{V}{2}t\right)}$$

$$\left\{ \frac{e^{w_2^2 t}}{2\left(w_2^2-w_3^2\right)} \left[e^{-w_2 k_1} \frac{erfc\left(-w_2\sqrt{t}+\frac{k_1}{2\sqrt{t}}\right)}{w_2+w_4} + e^{w_2 k_1} \frac{erfc\left(w_2\sqrt{t}+\frac{k_1}{2\sqrt{t}}\right)}{w_4-w_2} \right] \right.$$

$$+ \frac{e^{w_3^2 t}}{2\left(w_3^2-w_2^2\right)} \left[e^{-w_3 k_1} \frac{erfc\left(-w_3\sqrt{t}+\frac{k_1}{2\sqrt{t}}\right)}{w_3+w_4} + e^{w_3 k_1} \frac{erfc\left(w_3\sqrt{t}+\frac{k_1}{2\sqrt{t}}\right)}{w_4-w_3} \right]$$

$$\left. - D_5 w_4 e^{w_4^2 t} e^{w_4^2 k_1} erfc\left(w_4\sqrt{t}+\frac{k_1}{2\sqrt{t}}\right) \right\}$$

$$+ \frac{\varpi_1}{V_1-\beta} e^{-\mu\cdot z} [e^{-\beta\cdot t} - e^{-V_1\cdot t}] - \frac{\alpha\cdot\kappa\cdot L}{2k} e^{-\frac{Vz}{\kappa}} erfc\left(\frac{z-Vt}{2\sqrt{\kappa\cdot t}}\right) \qquad . \text{(293)}$$

$$- \left[\left(1+\frac{Vz}{\kappa}+\frac{V^2 t}{\kappa}\right) erfc\left(\frac{z+Vt}{2\sqrt{\kappa\cdot t}}\right) \right] - \frac{\rho\cdot V\cdot L}{k} \frac{\sqrt{\kappa\cdot t}}{\sqrt{\pi}} e^{-\frac{(z+Vt)^2}{4\kappa\cdot t}}$$

In order to generate graphical representation of Eq. 293, let us define the

following variables, which will be later used in MathCAD program:

$$i = 0..N.........z_i = \frac{h_t i}{N} \quad , \tag{294}$$

$$j = 1...L.........t_j = \frac{\tau_i j}{L} \quad , \tag{295}$$

$$\tau_j = \kappa\, \mu^2\, t , \tag{296}$$

$$V^0 = \frac{V}{\kappa\,\mu} \qquad\qquad \text{or} \qquad\qquad V^0 = 1 + \frac{V_1}{\kappa\mu^2} \;, \qquad\qquad (297)$$

$$\beta^0 = \frac{1}{\kappa\mu^2}\beta \;\;, \qquad\qquad (298)$$

$$w_2 = \frac{V^0}{4\kappa} - \beta^0 \;, \qquad\qquad (299)$$

$$w_3 = \left(\frac{V^0 - 2}{2}\right)\kappa\mu^2 \;\;, \qquad\qquad (300)$$

$$w_4 = \frac{V^0}{2}\sqrt{\kappa\mu} \;\;, \qquad\qquad (301)$$

$$D_5 = \frac{1}{\beta^O\left(V^0 - 1\right)\left(\kappa\mu^2\right)^2} \quad \text{or} \qquad D_5 = \frac{1}{\beta\,V_1} \;\;. \qquad\qquad (302)$$

One can use MathCad program to perform calculations, so our function $T(x,t)$ can be formulated as $T_{i,j}$ and substituting above parameters we can obtain

$$T_{i,j}(z,t) = \frac{-I_{max}}{k\,\mu}\exp\left[\frac{-V^{0^2}}{2}\left(z_d + \frac{-V^0}{2}\tau_t\right)\right]$$

$$x\left\{\frac{\exp\left[\frac{V^{0^2}}{4}-\left(V^0-1\right)\right]t_j}{\left[V^0-(1+\beta^0)\right]}\right\}$$

$$\left[\frac{\exp\left[\left[\frac{V^{0^2}}{4}-\left(V^0-1\right)\right]t_j\right]}{\left[V^0-\left(1+\beta^0\right)\right]}\left[\exp\left[-\left(\sqrt{\frac{V^0}{4}}-\beta\right)\right]z_i\frac{1-erf\left[-\sqrt{\left(\frac{V^{0^2}}{4}-\beta^0\right)}\right]t_j+}{\sqrt{V^{0^2}-\beta^0}+V^0}+\frac{z_i}{2\sqrt{t_j}}\right.\right.$$

$$\left.+\exp\left[\left(\sqrt{\frac{V^{0^2}}{4}}-\beta^0\right)z_i\right]\frac{1-erf\left[\sqrt{\left(\frac{V^{0^2}}{4}-\beta^0\right)}t_j\right]+\frac{z_i}{2\sqrt{t_j}}}{\left(V^0-\sqrt{V^{0^2}-\beta^0}\right)}\right]$$

$$+\frac{\exp\left[\left[\frac{V^{0^2}}{4}-\left(V^0-1\right)\right]t_j\right]}{\left[\beta^0-\left(V^0-1\right)\right]}\left[\exp\left[-\sqrt{\frac{V^{0^2}}{4}-\left(V^0-1\right)}\right]\frac{1-erf\left[-\sqrt{\left[\frac{V^{0^2}}{4}-\left(V^0-1\right)\right]t_j+\frac{z_i}{2\sqrt{t_j}}}\right]}{\sqrt{V^{0^2}-4\left(V^0-1\right)}+V^0}\right.$$

$$\left.+\exp\left[\sqrt{\frac{V^{0^2}}{4}-\left(V^0-1\right)}\right]\frac{1-erf\left[\sqrt{\left[\frac{V^{0^2}}{4}-\left(V^0-1\right)\right]t_j+\frac{z_i}{2\sqrt{t_j}}}\right]}{-\sqrt{V^{0^2}-4\left(V^0-1\right)}+V^0}\right.$$

$$\left.+\frac{-1}{2\beta^0\left(V^0-1\right)}\exp\left[\frac{V^{0^2}}{4}t_j\right]\exp\left[\frac{V^0}{2}\left(z_i\right)\right]\left(1-erf\left(\frac{V^0}{2}t_j+\frac{z_i}{2\sqrt{t_j}}\right)\right)\right]$$

$$+-\frac{-kpl}{2k}\left[e^{-V^0z_i}\left(1-erf\left(\frac{z_i-V^0t_j}{2\sqrt{t_j}}\right)\right)-\left(1+V^0z_1+V^{0^2}t_j\right)\left(1-erf\left(\frac{z_i+V^0t_j}{2\sqrt{t_j}}\right)\right)\right.$$

$$\left.+\frac{2V^0t_j}{\sqrt{\pi}}\exp\left[-\left(\frac{V^{0^2}}{4\tau_j}-\frac{V^0z_i}{2}+\frac{V^{0^2}t_j}{4}\right)\right]\right]$$

$$\left.+\left[\frac{I_{max}}{k\mu}\frac{1}{\left(V^0-1\right)-\beta^0}e^{-z_i}\left[\exp\left[e^{-\beta^0t_j}-e^{-\left(V^0-1\right)t_j}\right]\right]\right]\right]$$

(303)

249

$$E_{1_{I,J}} = \sqrt{\left(\frac{V^{O^2}}{4} - \beta^0\right)t_j + \frac{z_i}{2\sqrt{t_j}}}, \tag{304}$$

$$E_{2_{i,j}} = \sqrt{\left[\frac{V^0}{4} - \left(V^0 - 1\right)\right]t_j + \frac{z_i}{2\sqrt{t_j}}}, \tag{305}$$

$$E_{3_{i,j}} = \sqrt{V^{0^2} - 4\left(V^0 - 1\right)}, \tag{306}$$

$$E_{4_{I,J}} = e^{-\left[\sqrt{\frac{V^{O^2}}{4} - \left(V^0 - 1\right)}\right]z_1}, \tag{307}$$

$$E_{5_{i,j}} = e^{-\left(\sqrt{\frac{V^{0^2}}{4} - \beta^0}\right)z_I}, \tag{308}$$

$$E_{6_{I,J}} = \frac{V^0}{2}t_j + \frac{z_i}{2\sqrt{t_j}}, \tag{309}$$

$$E_{7_{i,j}} = \frac{z_i + V^0 t_j}{2\sqrt{t_j}}, \tag{310}$$

$$E_{8_{i,j}} = \frac{V^{0^2}}{4} - \left(V^0 - 1\right), \tag{311}$$

$$T(z,t) = \frac{-I_{max}}{k\,\mu} \exp\left[\frac{-V^{0^2}}{2}\left(z_d + \frac{-V^{0}}{2}\tau_t\right)\right] \times$$

$$\times \left\{ \begin{array}{l} \dfrac{\exp\left(E_{8_{d,t}}\right)\tau_t}{\left[V^{0} - (1+\beta^{0})\right]}\left[E_{5_{d,t}}\dfrac{1 - erf\left(-\mathrm{Re}\left(E_{1_{d,t}}\right)\right)}{\sqrt{V^{0^2} - \beta^{0}} + V^{0}} + E_{5_{d,t}}\dfrac{1 - erf\left(-\mathrm{Re}\left(E_{1_{d,t}}\right)\right)}{\left(V^{0} - \sqrt{V^{0^2} - \beta^{0}}\right)}\right] \\[3ex] + \dfrac{e^{E_{8_{d,t}}\tau_t}}{\left[\beta^{0} - \left(V^{0} - 1\right)\right]}\left(E_{4_{d,t}}\dfrac{1 - erf\left(-E_{2_{d,t}}\right)}{E_{3_{d,t}} + V^{0}} + E_{4_{d,t}}\dfrac{1 - erf\left(-E_{2_{d,t}}\right)}{-E_{3_{d,t}} + V^{0}}\right) + \\[3ex] + \dfrac{-1}{2\beta^{0}\left(V^{0} - 1\right)}\exp\left[\dfrac{V^{0^2}}{4}\tau_t\right]\exp\left[\dfrac{V^{0}}{2}z_d\right]\left(1 - erf\left(E_{6_{d,t}}\right)\right) \\[3ex] + -\dfrac{\kappa\rho L}{2k}\left[\begin{array}{l} e^{-V^{0}z_d}\left(1 - erf\left(\dfrac{z_d - V^{0}\tau_t}{2\sqrt{\tau_t}}\right)\right) - \\[2ex] \left(1 + V^{0}z_d + V^{0^2}\tau_t\right)\left(1 - erf\left(E_{7_{d,t}}\right)\right)\end{array}\right] \\[4ex] + \dfrac{2V^{0}\tau_T}{\sqrt{\pi}}\exp\left[-\left(\dfrac{V^{0^2}}{4\tau_t} - \dfrac{V^{0}z_d}{2} + \dfrac{V^{0^2}\tau_t}{4}\right)\right] \\[3ex] + \left[\dfrac{I_0}{k\mu}\dfrac{1}{\left(V^{0} - 1\right) - \beta^{0}}\exp\left[-z_d\left[e^{-\beta^{0}\tau_t} - e^{-\left(V^{0-1}\right)\tau_t}\right]\right]\right] \end{array}\right\} .$$

(

312)

Temperature distribution with respect to depth of the workpiece and time is graphically

shown in Fig. 3.18, where recession velocity of vaporization surface was estimated to be

about 33 m/s.
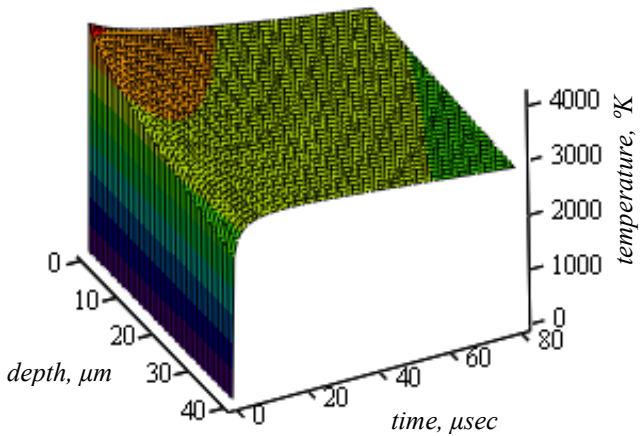
Fig. 3.18. Temperature distribution of the workpiece with consideration of transfer evaporative case calculated using Eq. 312.

A closed form solution illustrated in Fig. 3.18, is limited to the surface ablation only and does not considering the plasma formation and liquid expulsion from irradiated workpiece.

The temperature gradient attains relatively lower values in the surface vicinity of the substrate material than that corresponding to some depth below the surface. In this case, internal energy gain in this region due to absorption of a laser beam energy becomes more important as compared to diffusional heat transfer from the surface vicinity to the bulk of the substrate material due to temperature gradient. As the heating period progresses, the point of minimum temperature gradient moves towards the solid bulk of the substrate material.

In the region beyond the point of minimum temperature gradient, the diffusional energy transport plays an important role inside the substrate material.

252

The large change in the power intensity occurs with increasing $\beta°$; however, the

magnitude of temperatures in the surface region does not alter considerably. This is

because of the rate of evaporation, which increases with increasing power intensity.

Consequently, the convective boundary condition at the surface suppresses the

temperature rise in the surface vicinity at high power intensities.

3.1.5. Analytical solution of heat transfer equation with kinetic theory approach

This Section examines pulsed laser heating process by considering both Fourier

conduction and electron-phonon kinetic theory approaches. A 1D kinetic theory

approach is presented. More specifically, this Section is focused on development of

equations governing an interaction of a Gaussian laser beam with materials, where

analytical solution of these equations based on both the Fourier heat conduction theory

and kinetic theory approach using a Laplace integral transformed method is utilized. A

comparison of the analytical solution of the Fourier theory and closed form solution of

the kinetic theory approach is introduced in the next Section of this Dissertation. The

temperature distribution for the heated material predicted from the kinetic theory are

compared with the Fourier theory findings.

Most theoretical work relating to laser beam interaction with materials is based on

the solution of the classical heat conduction equation derived from Fourier theory. It has

been shown that the Fourier theory of heat conduction is not fully applicable to short

pulsed laser heating due to the assumptions made in the theory. These assumptions

include: matter is assumed as continuous and homogeneous, and that the heat flux across any plane is a function of only the temperature gradient at that plane. The first assumption is not valid for distances less than interatomic spacing and the second is only true if all the energy crossing the isothermal plane is accounted for.

Conduction in metals occurs due to subsequent collisions between excited electrons and lattice site atoms. The electron motion in the substrate is random, which means that electrons move from the surface to the bulk as well as from the bulk to the surface. Moreover, the amount of energy transferred to lattice site atoms depends on the electron energy distribution in a particular region. Harrington (1967) showed, based on kinetic theory considerations, that electrons within five times of the electron mean free path contribute 98.5% of the total energy transported provided that $\partial T/\partial z$ is constant over this distance. Consequently, attempting to generate the Fourier equation, the application of $q=-k\partial T/\partial z$ is limited to planes in excess of ten times the electron mean free path apart. In addition, the absorption depth of the metals is of the order of ten electron mean free paths; therefore, the gradient $\partial T/\partial z$ is not uniform over the spatial increment ($\Delta z \geq 10\lambda$, λ being the electron mean free path). In this case, the higher order gradients ($\partial^3 T/\partial z^3$), which are neglected in the Fourier heating model, become important and the validity of the Fourier heating model comes into question. Therefore, it becomes necessary to examine the laser-induced conduction heating on a microscopic scale.

The applicability of the Fourier equation in laser heating is limited to the cases in which low power laser intensities are employed (Yilbas, et al., 2000). This is due to the following facts:

1. In the analysis of the Fourier heat conduction model, the heat flux through a given plane is considered as being a function of the spatial temperature gradient at that plane. This depends upon the assumption that the temperature gradient remains almost constant between two successive and closely spaced planes. The distance between these planes is finite, therefore, error occurs when high-order terms, which are neglected, become important at high power laser intensities.

2. The heat flux through a given plane depends on the electron energy distribution through the material, therefore, the material cannot be considered as a homogeneous continuum.

Consequently, a new model may be required to be developed for heating mechanism, which is appropriate to high power laser heating process. A model considering a kinetic theory approach describing the transport of energy by electrons within the electron mean free path may be suitable in this case. The basis of this model was introduced by Yilbas (2001) for one-dimensional heating. It was shown that the predictions made from the new model agree well with the experimental findings. He adopted the electron motion in metals to formulate the laser pulse heating process. The heating process was established based on a kinetic energy transfer mechanism, which occurred during the collisions between excited electrons and lattice site atoms. In this case, the excess electron energy was transferred to lattice site atoms resulting in increased amplitude of lattice site vibrations during the collision process.

In this Section, comparisons of the electron kinetic theory approach are made with Fourier theory models for a pulse laser heating process. The temperature field due to

255

each model is predicted for step intensity as well as exponentially decaying intensity pulses. The study is extended to include the analytical solution to the electron kinetic theory approach for Gaussian intensity pulses. Electron kinetic theory approach is based on electron and phonon movements.

3.1.5.1. Electron-phonon analytical solution

The kinetic theory approach essentially deals with the kinetic energy transfer mechanism that occurs when electrons and lattice atoms with different energies interact. In order to simplify the phenomenon, some useful assumptions are made. These include omission of thermionic emission, attainment of steady space charge, and mean free path of molecules being independent of temperature. A net flow of electrons occurs in the substrate by the presence of an electron source at infinity, and the electron gives fraction of its excess energy to the lattice site atoms during an electron–phonon collision and this fraction is assumed to be constant throughout the successive collisions.

When the electron absorbs the incident laser energy, some excess energy of the electron is transferred to the lattice site atoms during electron–phonon collision process. This energy manifests itself as an increase in the amplitude of the atomic vibration (phonon). As a result, neighboring atoms in the lattice are forced away to new equilibrium positions and absorb some of this extra energy in the process. A stage may be reached where eventually the lattice site atoms in the localized region around the original collision site are all in equilibrium and have increased their vibrational energies.

It is this energy mechanism, which defines the conduction process in the solid substrate when subjected to a laser heating pulse.

The amount of energy which electrons from section *I* transfer to lattice site atoms in the same section, Fig. 3.19, can be calculated as follows. The number of electrons leaving section *I*, is: $N_z \cdot A_z \cdot \overline{V_z} \cdot dt$, where $A_z = dx \cdot dy$, and N_z is the number density of electrons which transfer energy to *dz* from *dζ*, and $\overline{V_z}$ is the average electron velocity entering the control volume in the *z*-axis across area A_z at time *dt*.
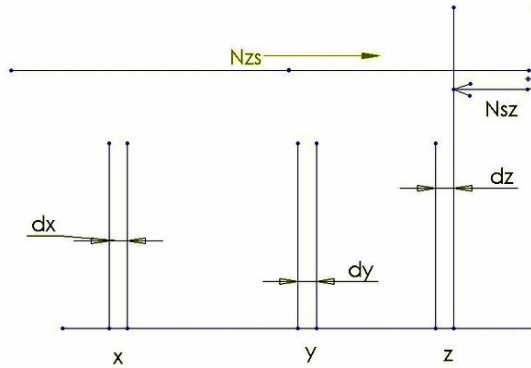
Fig. 3.19. Electron movement at the metal surface vicinity, (*z=0* is the surface).

The energy of *N* atoms in one direction due to lattice vibration is: $E = N \cdot k_B \cdot T$, which can be described as the phonon energy. The number of collisions, which takes place between electrons and phonons through the material, can be assessed by the total collision probability of electrons. Probability of electron traveling a distance *z*, where, *z<<2λ,* (*λ* being the mean free path), without making a collision is $\exp\left(-\dfrac{z}{\lambda}\right)$, the probability of an electron having just collided in *dz* is $\dfrac{dz}{\lambda}$.

In general, thermal conductivity is usually defined with respect to steady heat transfer through homogenous medium in a random process. Thus, the thermal conductivity in one direction can be defined as

$$k = \frac{N \overline{V}_z k_B \lambda}{6} \quad .$$

(313)

It has been shown that for the temperatures higher than the Debye temperature, thermal conductivity can be assumed constant. The number of the electrons which have just collided in section I is: $N_{\zeta z} \cdot A_z \cdot \overline{V}_z \frac{d\zeta}{\lambda} \cdot dt$. Therefore, the number of electrons, which have just collided in $d\zeta$ during dt is:

$$N_{z\zeta} \cdot A_z \cdot \overline{V}_z \int_{-\infty}^{\infty} \exp\left(-\frac{|z-\zeta|}{\lambda}\right) \frac{d\zeta}{\lambda} \cdot \frac{dz}{\lambda} \quad ,$$

(314)

and which then travel to section II before colliding in $dz,$ where $\int_{-\infty}^{\infty} \exp\left(-\frac{|z-\zeta|}{\lambda}\right) \frac{d\zeta}{\lambda} \frac{dz}{\lambda}$ is the total electrons-lattice site atoms collision probability as described in (Yilbas, 2001). The negative sign of the integral is due to a mirror image introduced at a surface. This mirror image represents reflected electrons from the free surface. The net transfer of energy during the electron-phonon collision through the entire body can be written as

$$\Delta E_{z,t} = \int_{-\infty}^{\infty} \exp\left(-\frac{|z-\zeta|}{\lambda}\right) \frac{dz}{\lambda} \cdot \frac{d\zeta}{\lambda} f \cdot \left[E_{\zeta,t} - E_{z,t}\right] \quad ,$$

(315)

where $E_{\zeta,t}$ and $E_{z,t}$ are energy of electrons and energy of phonons at a considered region respectively, in the z-axis and parameter f is a fraction of electron energy. It is suggested that the rate of transfer of energy between the electrons and the molecules will be determined only by the difference in temperature of the electrons and the lattice

vibrations. If the temperature of the lattice site atoms in *dz* is *Φ(z,t)* and the temperature

of the electrons when they arrive at *dz* is *Θ(ζ,t)*, then the energy transfer to the lattice site

atoms in *dz* from collisions with electrons in which the electrons give up a fraction ``*f*'' of

their excess energy is

$$N_{\zeta z} \cdot A_z \cdot \overline{V}_z \cdot dt \cdot \frac{d\zeta}{\lambda} \frac{dz}{\lambda} \exp\left(-\frac{|z-\zeta|}{\lambda}\right) f \cdot k_B [\Theta(\zeta,t) - \Phi(z,t)]$$ Summing the

contributions from all such sections to obtain the energy in section *II* gives

$$\Delta E_{z,t} = A_z dz \cdot dt \cdot \int_{-\infty}^{\infty} \frac{N_{\zeta z} \overline{V}}{\lambda} \frac{f}{\lambda} \frac{k_B}{\lambda} \exp\left(-\frac{|z-\zeta|}{\lambda}\right) [\Theta(\zeta,t) - \Phi(z,t)] d\zeta \quad . \tag{316}$$

During electron-phonon collision, some fraction *f* of the electron excess energy is

transferred to the phonon. For any inelastic collision, the conservation of energy in any

section may be written as

Electron energy entering the section =

electron energy living the section + (317)

+ energy transfer to phonons in the section

This gives

$$f = \frac{electron\ energy\ in - electron\ energy\ out}{excess\ electron\ energy\ in}$$

$$f = \frac{(E_{el})_{in} - (E_{el})_{out}}{(E_{el})_{in} - E_{phonon}} \quad . \tag{318}$$

providing that $0 \le f \le 1$ from the energy conservation, where $(E_{el})_{excess} = (E_{el})_{in} - E_{phonon}$,

and E_{phonon}= mean energy of phonon. The effective *f* value over a region sufficiently

large to allow many collisions approaches unity and this corresponds to the attainment of

thermal equilibrium. In the case of a single collision, f depends only upon the masses of the colliding particles, according to

$$f = \frac{2M \cdot m}{(M + m)^2} \quad , \tag{319}$$

where M and m are the masses of an atom and an electron, respectively. Substituting appropriate values shows, that the f value is of the order of 10^{-4}. The most energetic phonon is only 0.01 eV, assuming $c_s = 10^5$ cm/s (velocity of sound in the solid), but electrons near the Fermi level have energies of several eV; hence, when such electrons are scattered, only a small fraction of their energy can be given during an electron-phonon collision. In the present analysis, f is equal to 10^{-4} and assumed as a constant over successive collisions. The change of irradiance of the laser beam passing through a homogenous medium (metal), as a function of distance is given by $dI_z / dz = -\mu \cdot I_z(z)$, where μ is the absorption coefficient. The negative sign indicates the reduction in beam irradiance due to absorption as μ is a positive quantity. The absorption of the incident laser bam takes place in z-axis. Integrating defined dI_z / dz , the intensity of the incident beam at any plane z inside the substrate is: $I_z = I_0 \exp(-\mu \cdot z)$, where I_0 is the peak intensity of incident irradiance. The limit for a small section Δz wide at z, the energy absorbed is

$$\frac{dI_z}{dz} = \frac{d}{dz}\left(\mu \cdot I_0 \exp(-\mu \cdot z)\right) \quad \text{, or } I_z = -I_0 \frac{d}{dz}\left|f(z)\right| \quad,$$

or $I_z = -I_0 f'(z)$, (320)

where $f'(z)$ is the absorption function. Since the mirror image situation is considered, Fig. 3.19, for electron movement at the surface, the laser beam will be absorbed in a manner described by: $-f'(z) = \frac{d}{dz}\left|\exp(-\mu \cdot |z|)\right|$, for all z. Using Eq. 320 for intensity of the laser beam, the rate of applied external energy at dz during the time interval dt can be given as

$$\Delta E_{z,t}\big|_{abs} = I_0 \cdot \mu \cdot e^{-\mu \cdot z} A \cdot dt \cdot dz \quad,$$ (321)

the total energy increase in the material at dz during time dt is

$$N \cdot A(E_{z,t+dt} - E_{z,t})dz = \Delta E_{z,t} + E_{z,t}\big|_{abs} \quad.$$ (322)

The total amount of energy, which is absorbed in an element $\partial\xi$, area A in time dt is: $-I_0 \cdot A\, dt \cdot d\xi \cdot f'(\xi)$, since all the beam energy is absorbed in the z direction. One must allow for the possibility that electron densities may vary throughout the material and, in particular, the number traveling from $d\zeta$ to dz may not be the same as that from dz to $d\zeta$. Therefore, the proportion of energy which is absorbed by the electrons which travel from $d\zeta$ to dz in dt is: $-I_0 \cdot A\, dt \cdot d\xi \cdot f'(\xi) \cdot \dfrac{N_{\zeta z}}{N_{\zeta z} + N_{z\zeta}}$.

The average energy absorbed by one electron in $d\xi$ in a time dt is: $-I_0 \cdot \dfrac{f'(\xi) \cdot d\xi}{\left(N_{\zeta z} + N_{z\zeta}\right)\overline{V}}$,

and the total amount absorbed by this electron from dz to $d\zeta$ is: $\displaystyle\int_z^\zeta I_0 \cdot \dfrac{f'(\xi) \cdot d\xi}{\left(N_{\zeta z} + N_{z\zeta}\right)\overline{V}}$.

The final temperature of the electrons in dz after the collision process can be readily found from the conservation of energy, i.e.,

Total electron energy after collision = total electron energy in during dt – change of lattice site energy .

The assumption that all directions of travel are equally probable gives: $N_{\zeta z} = N_{\cdot z \zeta} = \dfrac{N}{6}$

where N is the number of free electrons per unit volume. Therefore,

$$\frac{\partial}{\partial t}(\rho \cdot c \cdot \Phi(z,t)) = \int_{-\infty}^{\infty} \frac{f\,k}{\lambda^3} \exp\left(-\frac{|z-\zeta|}{\lambda}\right) \Theta(\zeta,t)d\zeta -$$

$$-\int_{-\infty}^{\infty} \frac{f\,k}{\lambda^3} \exp\left(-\frac{|z-\zeta|}{\lambda}\right) \Phi(z,t)d\zeta \qquad (323)$$

$$+\int_{-\infty}^{\infty} \frac{I_{\cdot 0}f}{\lambda^2} \exp\left(-\frac{|z-\zeta|}{\lambda}\right) \int_{z}^{\zeta} f'(z)d\xi d\zeta \quad ,$$

and

$$\int_{-\infty}^{\infty} \frac{k}{\lambda^3} \exp\left(-\frac{|z-\zeta|}{\lambda}\right) \left(\Theta(\zeta,t)d\zeta - f\,\Phi(z,t)d\zeta\right) =$$

$$\int_{-\infty}^{\infty} \frac{k}{\lambda^3} \exp\left(-\frac{|z-\zeta|}{\lambda}\right)(1-f)\,\Theta(\zeta,t)d\zeta \qquad (324)$$

$$+\int_{-\infty}^{\infty} (1-f)\exp\left(-\frac{|z-\zeta|}{\lambda}\right) \int_{z}^{\zeta} f'(z)d\xi d\zeta \quad .$$

Equations 323 and 324 are of interest to laser machining. The method of solution to be used in the following analysis is the transformation of the simultaneous differential-integral Eqs 323 and 324 using the Fourier integral transformation, with respect to z. The resulting ordinary differential equations may then be handled much more conveniently. The Fourier transformation of a function $f(z)$ is defined (Yilbas, 2001) by

$$F[f(z)] = \int_{-\infty}^{\infty} \exp(-i\omega \cdot z) f(z) dz = F(\omega) \tag{325}$$

and the Fourier inversion is given as

$$f(z) = \frac{1}{2\pi} \int_{-\infty}^{\infty} F(\omega)(\exp(-i\omega \cdot z) d\omega) = F(\omega) \quad . \tag{326}$$

The Fourier transformation of the convolution integral $\int_{-\infty}^{\infty} f(\xi) g(z - \zeta) d\zeta$ is the

product of the transforms $f(\omega) \cdot \overline{g}(\omega)$ and the transform of function $\exp\left(-\frac{|z|}{\lambda}\right)$ is

$\frac{2\lambda}{1 + \omega^2 \lambda^2}$. Applying Fourier transformation to Eqs 323 and 324 yields

$$(f + \omega^2 \lambda^2) \frac{\partial}{\partial t}(\rho \cdot c \cdot \Phi) = -\omega^2 k f \overline{\Theta} + I_0 \delta f \frac{2\delta}{\delta^2 + \omega^2} \quad . \tag{327}$$

The multiplication in the transform domain by $(i\omega)^2$ corresponds to a second-

order differential in the real plane. Hence, the inversion of Eq. 327 gives

$$\left(f - \frac{\lambda^2 \mu^2}{\partial z^2}\right) \rho \cdot c \cdot \frac{\partial \Phi}{\partial t} = kf \frac{\partial^2 \Phi}{\partial z^2} + I_0 \mu f \exp(-\mu|z|) \quad . \tag{328}$$

If the term $\left(\frac{\lambda^2 \mu^2}{f \cdot \partial z^2}\right) \rho \cdot c \cdot \frac{\partial \Phi}{\partial t}$ is neglected for all f values, Eq. 328 becomes

$$\rho \cdot c \cdot \frac{\partial \Phi}{\partial t} = k \frac{\partial^2 \Phi}{\partial z^2} + I_0 \mu \exp(-\mu|z|) \quad , \tag{329}$$

which is the same as a Fourier heat conduction equation, shown as Eq. 170. It is apparent

that the electron kinetic theory equations for the heat conduction process are much more

general than the Fourier equation. The new model of the conduction process is valid in

regions close to the surface where an absorption process takes place and therefore, the

263

temperature profiles, which are obtained in these regions, can be expected to be valid.

One further advantage of this new approach is that the problem is completely specified,

together with spatial boundary conditions, by the final equations, and that these equations

can be solved using the method of Fourier transformation.

The solution of Eq. 327 in the transform plane for the Gaussian intensity pulse is

$$\Phi(z,t) = \frac{AI_0\mu}{\rho \cdot c} \left[\frac{1}{\beta(1-\mu^2\lambda^2)+\kappa\mu^2} \right] \left\{ \begin{array}{l} i\mu\sqrt{\dfrac{\kappa-\beta\lambda}{\beta}}\exp\left[-\dfrac{\beta\kappa t}{\kappa-\beta\lambda^2}\right]\exp\left[i|z|\sqrt{\dfrac{\beta}{\kappa-\beta\lambda^2}}\right] \\[1em] erfc\left[\dfrac{|z|}{2\sqrt{\kappa t}}+i\sqrt{\dfrac{\beta\kappa t}{\kappa-\beta\lambda^2}}\right] \\[1em] -\exp\left[i|z|\sqrt{\dfrac{\beta}{\kappa-\beta\lambda^2}}\right]erfc\left[\dfrac{|z|}{2\sqrt{\kappa t}}-i\sqrt{\dfrac{\beta\kappa t}{\kappa-\beta\lambda^2}}\right]+ \\[1em] \exp(\kappa\mu^2 t+\mu|z|)erfc\left[\mu\sqrt{\kappa t}+\dfrac{|z|}{2\sqrt{\kappa t}}\right]+ \\[1em] -\exp(\kappa\mu^2 t-\mu|z|)erfc\left[\mu\sqrt{\kappa t}-\dfrac{|z|}{2\sqrt{\kappa t}}\right] \\[1em] -2\exp\left[-\dfrac{\beta\kappa t}{\kappa-\beta\lambda^2}+\mu|z|\right] \end{array} \right\}\lambda^2 \quad (330)$$

and gives the closed form result of the electron kinetic theory approach, which

graphically is shown in Fig. 3.20.
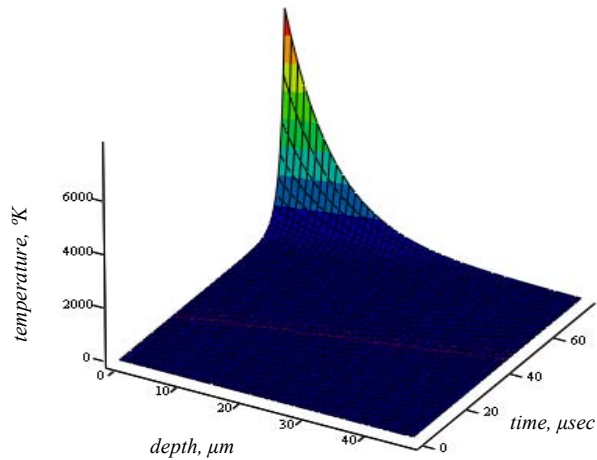
Fig. 3.20. Temperature, closed form solution of the electron kinetic theory approach, with respect to depth of the sample and time.

3.1.5.2. Comparison of Fourier and kinetic theory

Comparison of analytical results of the Fourier relation given by Eq. 212, and kinetic theory equation, Eq. 330, shows that the two are identical when the following two conditions are meet: $\mu^2 \lambda^2 \langle\langle 1$ and $\kappa \rangle\rangle \beta \lambda^2$. For most materials, μ and λ are of the same order of magnitude. Since μ is of the order of 10^{-5} and λ is of the order of 10^{-8}, then $\beta \rangle\rangle 10^{11}$. This scenario corresponds to laser micromachining for laser pulses with picosecond rise times. Generally, $\beta \rangle\rangle \dfrac{\kappa}{\lambda^2}$ and Eq. 330 reduces to exactly the analytical solution obtained from the Fourier theory for the exponential pulse, provided that $1 >> \mu^2 \lambda^2$. When "β" approaches zero, the pulse solution reduces to that for a constant intensity analytical solution of Fourier heating, Eq. 212. The comparison of the temperature gradient $\partial \Phi / \partial z$ predicted from the Fourier and electron kinetic theories

265

with the distance in the *z*-axis for two pulse lengths is shown in Fig. 3.21. The

temperature gradients predicted from both theories are similar for the long pulse length

$t_{pulse} = 6x10^{-10} s$. In general, the temperature gradient decreases sharply in the surface

vicinity to reach its minimum.
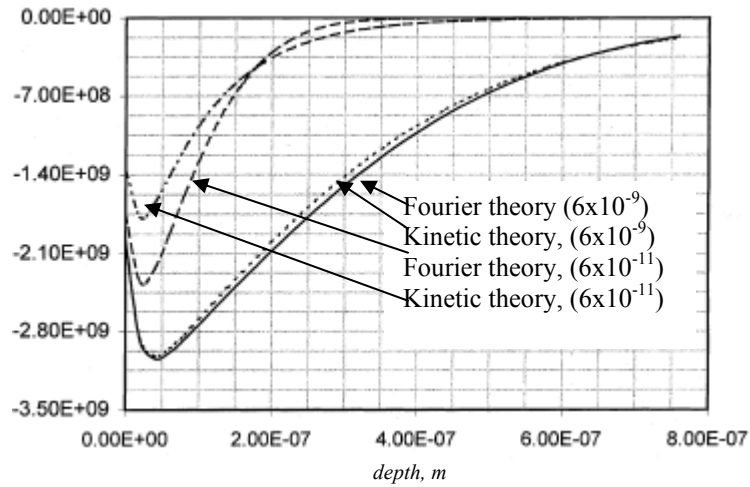
Fig. 3.21. *dT/dz* predicted from the Fourier and kinetic theory, along the *z*-axis for two
pulse lengths: *6·10⁻⁹*s and *6·10⁻¹¹*s (Yilbas, 2001).

As the distance from the point of minimum increases further inside the substrate,

$\partial\Phi / \partial z$ increases gradually. The sharp decrease of $\partial\Phi / \partial z$ in the surface vicinity is due to

the rapid increase of the temperature in this region. In this case, the energy absorbed by

the electrons in the surface vicinity is converted into the internal energy gain of the

substrate through collision process. This gives rise to a sharp increase of the lattice site

temperature. The energy balance attains among the absorbed energy, internal energy

gain, and the conduction process at the point of minimum $\partial\Phi / \partial z$. As the distance

increases beyond the point of minimum, the gradual increase in $\partial\Phi / \partial z$ reveals that the

conduction effect due to phonon relaxation dominates. However, as the pulse length

266

reduces, less than $t_{pulse} \langle\ 6x10^{-11} s$, the temperature gradients predicted from both theories differ considerably. The temperature gradient predicted from the Fourier theory reduces significantly as compared to its counterpart predicted from electron kinetic theory. The difference in $\partial\Phi/\partial z$ predicted from both theories is due to the temperature response of the material for a short laser heating pulse as indicated earlier.

In summary, one can deduct a following conclusions: Temperature profiles predicted from Fourier heating model with kinetic theory approach for 1-dimensional model were compared in this study. In general, temperature profiles for 1-dimensional Fourier heating case and kinetic theory approach are very similar. Although the Fourier heating model fails to predict correct temperatures for the short pulse heating case. The equilibrium time exists for a given material, the balance occurs between the internal energy gain due to laser irradiation and the conduction losses. The analytical solution of the electron kinetic theory approach obtained for the exponentially decaying pulse reduces to a step input intensity solution when β approaches zero. Moreover, the closed form solution of the electron kinetic theory for the step input intensity approaches the Fourier solution when $\mu^2 \dfrac{\lambda^2}{f} \langle\langle 1$. The electron kinetic theory results deviate considerably from the Fourier theory results when $\beta >> 10^{11}$.

The difference in temperature profiles occurs because of the fact that the electrons in the surface vicinity absorb the incident laser energy and the excited electrons do not make sufficient collisions with the lattice site atoms to transfer their excess energy in the surface region. Thus, lattice site temperature in this region becomes lower than the

electron temperature as evident from Fig. 3.21, in which the electron temperature

distribution inside the substrate is shown. Therefore, the Fourier theory fails to predict

the temperature rise in the surface vicinity accurately for heating time of $t_{pulse} \langle \ 6x10^{-11}s$.

3.2. Finite difference methods

In this Section, the solution of governing equation is accomplished using an

explicit finite difference approximation and the corresponding boundary conditions. The

representative results for computational investigations are presented and discussed. To

solve general governing equation, Eq. 141, finite difference method (FDM) was used, and

the approximations to model the governing equation were based on forward-difference in

time and central-difference in space.

3.2.1.   Finite difference formulae

Defining function u whose value u_i is known at a number of discrete points, the

approximation of the first derivative $u_i{}'$ at point i one can define as

$$u_i{}' = \frac{u_{i+1} - u_i}{\delta} \ ,$$
(331)

where δ is the interval separating the two values of function u. The expression from Eq.

331 is known as a forward-difference approximation of the derivative of u at point i. The

central-difference formula can be expressed as

$$u_i' = \frac{u_{i+1} - u_{i-1}}{2\delta} \quad , \tag{332}$$

The error resulting from a central difference is smaller than from a forward, or backward difference. Consequently it is beneficial to use central difference method for the calculations whenever possible.

The second derivative of u at point i can be considered as derivative of derivative of u at this same point i, or

$$u_i'' = \frac{u_{i-1} + u_{i+1} - 2u_i}{\delta^2} \quad , \tag{333}$$

which is considered the central-difference formula for u_i''.

Examination of the governing equation shows that the heat conduction equation requires evaluation of the first-order derivative with respect to time and the second-order derivatives with respect to each of the coordinate directions x, y, and z. The time derivative is commonly evaluated using a forward difference, and each of the spatial derivatives is expressed using the central difference expression. Summarized, a three-dimensional model under consideration requires creating a three-dimensional grid of points at which corresponding solution values are determined. This grid is often referred as a mesh and the individual points of the mesh as nodes.

3.2.2. Explicit formulation of governing equation

In order to calculate the temperature from the governing equation using FDM we must express the temperature at node (i, j, k) at time $t+dt$ explicitly in terms of the

temperatures of the surrounding nodes at time t. This approach is called an explicit formulation, which allows one to simplify march through the finite difference mesh and solve for the temperature at succeeding time step, provided the initial temperature of the entire grid is known. Sometimes one can call it a forward-difference formulation since the time derivative is expressed using a forward difference.

The other basic technique involves solving the temperatures in the nodal mesh at time t in terms of nodal temperature at time $t+dt$ is called an implicit formulation, since the temperature at any given node is not explicitly stated in the resulting equation, but a set of linear equations involving the entire nodal mesh is considered.

Both of the above methods have their advantages and disadvantages. It was shown that selection of small increments in the node spacing requires the use of a small time step to insure a convergent solution. The implicit method, on the other hand, does not have any such stability requirements relating the node spacing and the time step.
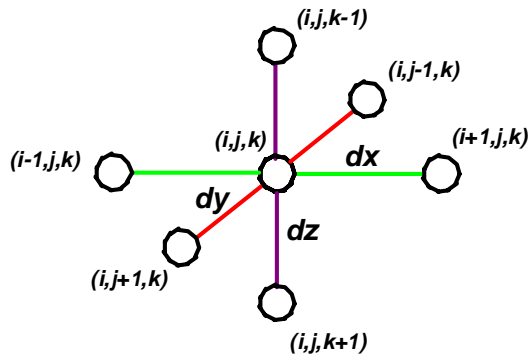

Fig. 3.22. General three-dimensional finite difference grid.

Consequently much larger time increment can be used to solve a given task, but with difficulties connected with the solution of the simultaneous equations resulting from

the formulation. The solution approach selected for this Dissertation was the explicit method.

In order to simplify further developments, it will be useful to expend the governing equation, Eq. 142, in conventional notation

$$\rho(T)\frac{\partial}{\partial t}\int_{T_0}^{T}c(T)dT = \frac{\partial}{\partial x}\left[k(T)\frac{\partial T}{\partial x}\right] + \frac{\partial}{\partial y}\left[k(T)\frac{\partial T}{\partial y}\right] + \frac{\partial}{\partial z}\left[k(T)\frac{\partial T}{\partial z}\right] +$$
$$+ \rho(T)\,c(T)\,V\,\frac{\partial T}{\partial z} + Q \quad ,$$

(334)

which applies for any interior point of the internal nodes in the sample and all terms of the equation were defined earlier. Analyzing Eq. 334, one can notice that the first three terms on the right hand side of the equation are the volumetric accumulation rates of energy due to the variation of the thermal conductivity due to variation of three-dimensional temperature field. Note that those terms depend on both the magnitude of the thermal gradient and the temperature dependence of the thermal conductivity. The forth term of Eq. 334 expressing energy lost on melting expulsion of melted and vaporized material, where V is drilling velocity of vaporized front of vapor, normal to Knudsen layer. The last term of the right hand side of Eq. 334 is the Cartesian analog of the volumetric accumulation rate due to the equivalent internal generation of energy. The sum of those terms equals the net volumetric accumulation rate of energy, which is written on the left-hand side of Eq. 334.

Substitution of Eqs 332 and 333, into Eq. 334 yields

$$
\Delta T_{i,j,k} = \frac{\Delta t}{\rho c} \left\{ k_{i,j,k}^t \left[\frac{T_{i-1,j,k}^t + T_{i+1,j,k}^t - 2T_{i,j,k}^t}{(\Delta x)^2} + \frac{T_{i,j-1,k}^t + T_{i,j+1,k}^t - 2T_{i,j,k}^t}{(\Delta y)^2} \right. \right.
$$

$$
\left. + \frac{T_{i,j,k-1}^t + T_{i,j,k+1}^t - 2T_{i,j,k}^t}{(\Delta z)^2} \right] +
$$

$$
+ \left[\frac{\left(k_{i+1,j,k}^t - k_{i-1,j,k}^t\right)\left(T_{i+1,j,k}^t - T_{i-1,j,k}^t\right)}{4(\Delta x)^2} + \right.
$$

$$
+ \frac{\left(k_{i,j+1,k}^t - k_{i,j-1,k}^t\right)\left(T_{i,j+1,k}^t - T_{i,j-1,k}^t\right)}{4(\Delta y)^2} +
$$

$$
\left. \left. + \frac{\left(k_{i,j,k+1}^t - k_{i,j,k-1}^t\right)\left(T_{i,j,k+1}^t - T_{i,j,k-1}^t\right)}{4(\Delta z)^2} \right] + V_z \frac{T_{i,j,k+1}^t - T_{i,j,k-1}^t}{2\Delta z} + Q \right\} \quad , \tag{335}
$$

where $\Delta T_{i,j,k} = T_{i,j,k}^{t+\Delta t} - T_{i,j,k}^t$, $\tag{336}$

The nomenclature in above equations was defined earlier, Fig. 3.22. Please note that the specific heat and density are dependent from the temperature. One way to account for that is to evaluate $c = c(T^t{}_{i,j,k})$ or $\rho = \rho\, (T^t{}_{i,j,k})$.

For further analysis, it is convenient to rewrite Eq. 335 into a general form as

$$
\Delta T_{i,j,k} = \frac{\Delta t}{\rho\, c}\left(\zeta_{i,j,k} - \phi_{i,j,k} T_{i,j,k}^t\right) \quad , \tag{337}
$$

where the parameters $\zeta_{i,j,k}$, and $\varphi_{i,j,k}$ are defined respectively, as

$$\varsigma_{i,j,k} = k_{i,j,k}^t \left[\frac{T_{i-1,j,k}^t + T_{i+1,j,k}^t - 2T_{i,j,k}^t}{(\Delta x)^2} + \frac{T_{i,j-1,k}^t + T_{i,j+1,k}^t - 2T_{i,j,k}^t}{(\Delta y)^2} + \right.$$

$$+ \frac{T_{i,j,k-1}^t + T_{i,j,k+1}^t - 2T_{i,j,k}^t}{(\Delta z)^2} \left. \right] +$$

$$+ \left[\frac{\left(k_{i+1,j,k}^t - k_{i-1,j,k}^t \right)\left(T_{i+1,j,k}^t - T_{i-1,j,k}^t \right)}{4(\Delta x)^2} + \right. \tag{338}$$

$$+ \frac{\left(k_{i,j+1,k}^t - k_{i,j-1,k}^t \right)\left(T_{i,j+1,k}^t - T_{i,j-1,k}^t \right)}{4(\Delta y)^2} +$$

$$\left. + \frac{\left(k_{i,j,k+1}^t - k_{i,j,k-1}^t \right)\left(T_{i,j,k+1}^t - T_{i,j,k-1}^t \right)}{4(\Delta z)^2} \right] + V_z \frac{T_{i,j,k+1}^t - T_{i,j,k-1}^t}{2(\Delta z)} \quad ,$$

and

$$\phi_{i,j,k} = 2k^t{}_{i,j,k} \left(\frac{1}{(\Delta x)^2} + \frac{1}{(\Delta y)^2} + \frac{1}{(\Delta z)^2} \right) \quad . \tag{339}$$

3.2.3. Stability of explicit solutions

The explicit formulation of governing equation as written in Eq. 337 is only conditionally stable, as was stated earlier. The stability depends on the relationship between material properties, the time increment Δt and the spatial increments dx, dy, and dz. For stability analysis, one can rewrite Eq. 337 as

$$\Delta T_{i,j,k} = \frac{\Delta t\, \phi_{i,j,k}}{\rho\, c} \left(\frac{\varsigma_{i,j,k}}{\phi_{i,j,k}} - T_{i,j,k}^t \right) \quad . \tag{340}$$

For steady-state temperature, $T_{i,j,k}^{ss}$ at node *(i,j,k)* Eq. 340 convergence to zero if

$$T_{i,j,k}^{SS} = \frac{\zeta_{i,j,k}}{\phi_{i,j,k}} \quad . \tag{341}$$

Substituting Eq. 341 into Eq. 337 one obtains a relationship, which mathematically can be illustrated as

$$\Delta T_{i,j,k} = \frac{\phi_{i,j,k} \Delta t}{\rho\, c} \left(T_{i,j,k}^{SS} - T_{i,j,k}^{t} \right) \quad . \tag{342}$$

Analysis of Eq. 342 reveals that sufficient condition for convergence of Eq. 337 to the steady state temperature is

$$0 \le \frac{\Delta t\, \phi_{i,j,k}}{\rho\, c} \le 1 \quad . \tag{343}$$

The stability criterion presented in Eq. 342 does relate the time interval Δt, to the given material properties and to geometrical coefficient $\phi_{i,j,k}$. Procedure for writing the transient equation for a given type of node, solving for the steady-state temperature and then substituting back into the original equation is general and should be repeated for every type of node element present in the model under consideration. Subsequent sections present more comprehensive information of this procedure for the computer model developed for this Dissertation.

3.2.4. Model geometry

To facilitate solution by FDM, the workpiece must be subdivided into an array of nodes, in Fig. 3.23. The model geometry of the problem is shown in Fig. 3.23

Nowakowski (1990). The origin of the Cartesian coordinate system is located at the top, far left corner of the sample. Associated with each node is a volume element. Note that the elements corresponding to the surface, edge, and corner nodes are smaller than a typical interior element. This is due to the fact that nodes corresponding to these elements are placed on the boundaries defining the workpiece. Note also that the center of the irradiating laser beam is placed in the center of the top surface of the workpiece. Each face of the model can have unique heat transfer coefficients. That possibility enables one to consider various boundary conditions. For example, one can model an insulated boundary by setting the heat transfer coefficient to zero along the proper face. Analyzing the geometrical positions of nodal points with respect to unique heat transfer coefficients on each side of the sample one can distinguish four typical nodal elements in order to describe the processes of heat transfer. These typical nodal elements are internal nodes, wall nodes, edge nodes, and corner nodes, Fig. 3.24.

LASERBEAM

hzl

hyl

hxl

X

hxr

Y

Z

hyr

hzr
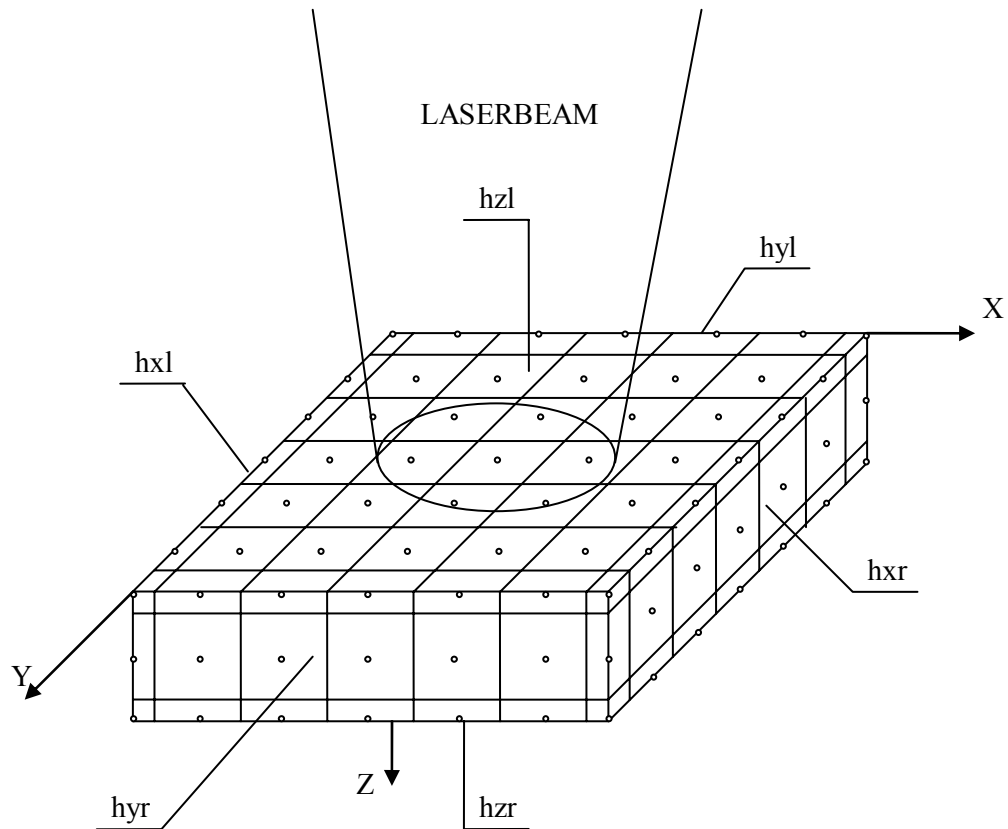
hxl – sum of convection and radiation coefficients on the workpiece surface with surface normal pointing in the negative *x*-direction,

hxr – sum of convection and radiation coefficients on the workpiece surface with surface normal pointing in the positive *x*-direction,

hyl – sum of convection and radiation coefficients on the workpiece surface with surface normal pointing in the negative *y*-direction,

hyr – sum of convection and radiation coefficients on the workpiece surface with surface normal pointing in the positive *y*-direction,

hzl – sum of convection and radiation coefficients on the workpiece surface with surface normal pointing in the negative *z*-direction,

hzr – sum of convection and radiation coefficients on the workpiece surface with surface normal pointing in the positive *z*-direction,

Fig. 3.23. Three-dimensional finite difference subdivision of a workpiece.

3.2.5. General element equation

Examination of the model geometry illustrated in Fig. 3.23 indicates that the inclusion of finite model dimensions introduces variations on the general discretization mesh. As shown, these variations produce volume elements corresponding to interior, wall, edge, and corner nodes. Note that in addition to changing boundary conditions for each element, the definition of interior, wall, edge, and corner nodes placed on the region boundaries leads to elements of varying sizes.

In this Dissertation, finite difference equations, relating to the typical nodes, shown in Fig. 3.24 were developed. In the first step to developing a general node equation, consider first the solution of general equation with a constant thermal conductivity; the effects of variable thermal conductivity will be implemented into the analysis later. Development of the finite difference model for that case of constant thermo physical parameters was previously developed (Nowakowski, 1990).
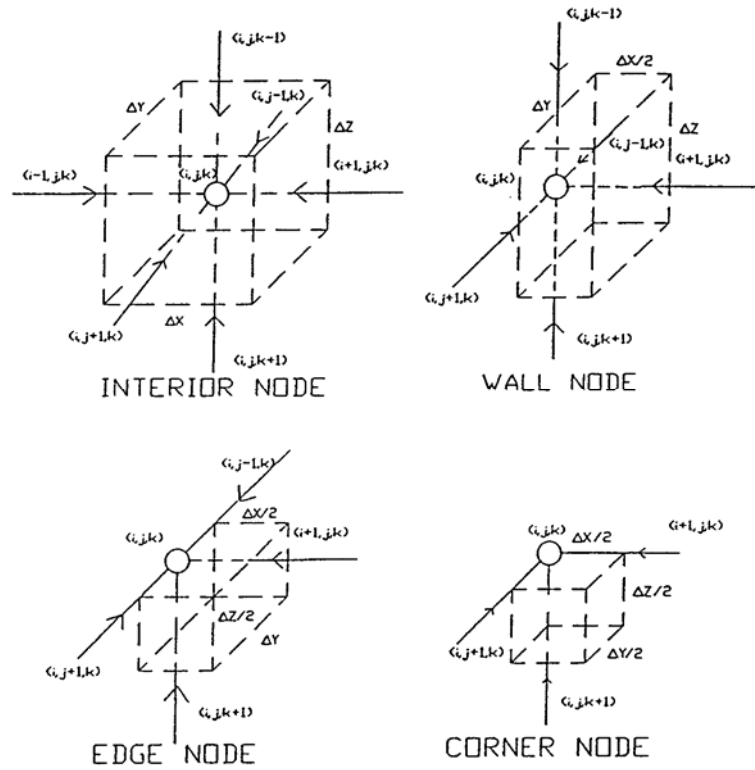
Fig. 3.24. The four typical nodal elements of a workpiece.

Equations 335 through 337 were developed by the simple explicit FDM. Because this method is conditionally stable, in order to guarantee the convergence of the solution a further stability analysis for this FDM model is required (Nowakowski, 1990). At present time, for this discussion only the results are important.

3.2.5.1. Generalized element

Equations developed by Nowakowski (1990) can be modified and combined into one general formulation. Such a general element has the advantage of being easily

278

modified to account for various boundary conditions which occur when 3D modification
of the node mesh is incorporated in the process of hole formation.

Recalling our discussion in Section 3.2.2, one can notice, that the governing heat
transfer equation and its linear boundary conditions are all expressed in terms of thermal
gradients at each node defined by physical coordinates x, y, z. Each node can be thought
of as consisting of two terms: 1st term containing information on the heat transfer
mechanisms present at the node, 2nd term describing its neighboring nodes. Those two
terms have been already defined in Eqs 338 and 339.

In order to facilitate this discussion let us first start with a consideration of an
interior node, equation with constant thermal conductivity. In this case Eq. 337 can be
rewritten into a form of Eq. 337, i.e.,

$$\Delta T_{i,j,k} = \frac{\Delta t}{\rho\, c}\left(\varsigma_{i,j,k} - \phi_{i,j,k} T^{t}_{i,j,k}\right) \quad , \tag{344}$$

$$\varsigma_{i,j,k} = k_{i,j,k}\left[\frac{T^{t}_{i-1,j,k} + T^{t}_{i+1,j,k}}{(\Delta x)^2} + \frac{T^{t}_{i,j-1,k} + T^{t}_{i,j+1,k}}{(\Delta y)^2} + \frac{T^{t}_{i,j,k-1} + T^{t}_{i,j,k+1}}{(\Delta z)^2}\right] +$$
$$+ V_z\, \frac{T^{t}_{i,j,k+1} - T^{t}_{i,j,k-1}}{2(\Delta z)} \quad , \tag{345}$$

$$\phi_{i,j,k} = 2k_{i,j,k}\left(\frac{1}{(\Delta x)^2} + \frac{1}{(\Delta y)^2} + \frac{1}{(\Delta z)^2}\right) \quad . \tag{346}$$

In a similar manner equations for other types of nodes can be written in the form of Eq.
337. For each case, a new pair of coefficients must be defined.

For the case of a typical wall node, Fig. 3.24 , the coefficients are

$$\varsigma_{0,j,k} = k_{i,j,k}^{t} \left[\frac{2T_{i,j,k}^{t}}{(\Delta x)^{2}} + \frac{T_{0,j-1,k}^{t} + T_{0,j+1,k}^{t}}{(\Delta y)^{2}} + \frac{T_{0,j,k-1}^{t} + T_{0,j,k+1}^{t}}{(\Delta z)^{2}} \right] +$$
$$+ \frac{2h_{xl}}{(\Delta x)} T_{a} + V_{z} \frac{T_{i,j,k+1}^{t} - T_{i,j,k-1}^{t}}{2(\Delta z)} \quad , \tag{347}$$

and

$$\phi_{0,j,k} = 2 \left\{ k_{i,j,k} \left(\frac{1}{(\Delta x)^{2}} + \frac{1}{(\Delta y)^{2}} + \frac{1}{(\Delta z)^{2}} \right) + \frac{h_{xl}}{\Delta x} \right\} \quad . \tag{348}$$

For typical edge node, the coefficients are

$$\varsigma_{0,j,0} = k_{i,j,k}^{t} \left[\frac{2T_{i,j,k}^{t}}{(\Delta x)^{2}} + \frac{T_{0,-1,0}^{t} + T_{0,1,0}^{t}}{(\Delta y)^{2}} + \frac{2T_{0,0,1}^{t}}{(\Delta z)^{2}} \right] +$$
$$+ 2 \left(\frac{h_{xl}}{\Delta x} + \frac{h_{zl}}{\Delta z} \right) T_{a} + V_{z} \frac{T_{0,0,1}^{t}}{\Delta z} \quad , \tag{349}$$

$$\phi_{0,j,k} = 2 \left\{ k_{i,j,k} \left(\frac{1}{(\Delta x)^{2}} + \frac{1}{(\Delta y)^{2}} + \frac{1}{(\Delta z)^{2}} \right) + \frac{h_{xl}}{\Delta x} + \frac{h_{zl}}{\Delta z} \right\} \quad . \tag{350}$$

For the corner node, one obtains

$$\varsigma_{0,j,0} = k_{i,j,k}^{t} \left[\frac{2T_{1,0,0}^{t}}{(\Delta x)^{2}} + \frac{T_{0,1,0}^{t}}{(\Delta y)^{2}} + \frac{T_{0,0,1}^{t}}{(\Delta z)^{2}} \right] + V_{z} \frac{T_{0,0,1}^{t}}{2\Delta z} + \left(\frac{h_{xl}}{\Delta x} + \frac{h_{yl}}{\Delta y} + \frac{h_{zl}}{\Delta z} \right) T_{a} \quad , \tag{351}$$

$$\phi_{0,j,k} = 2 \left\{ k_{i,j,k} \left(\frac{1}{(\Delta x)^{2}} + \frac{1}{(\Delta y)^{2}} + \frac{1}{(\Delta z)^{2}} \right) + \frac{h_{xl}}{\Delta x} + \frac{h_{yl}}{\Delta y} + \frac{h_{zl}}{\Delta z} \right\} \quad . \tag{352}$$

In Eqs 344 to 352, T_{a} is the ambient temperature while h_{x}, h_{y}, and h_{z}, are heat transfer coefficients on the sample faces normal to the x, y, and z directions, respectively. Subscripts l and r used in representation of the heat transfer coefficients refer to the sample's surface with surface normal pointing in the negative (or left) and positive (or

right) direction of the coordinate axes, respectively. Note, that the radiation losses and thermal conductivity temperature dependence is not yet taken into account.

Considering possible forms of heat transfer that can occur across the boundaries of a typical element one can formulate a general equation on the basis of energy balance on those elements, that is,

$$\rho c \frac{T'_{i,j,k} - T_{i,j,k}}{\Delta t} \left[\frac{\Delta x}{S^x_{i,j,k}} \cdot \frac{\Delta y}{S^y_{i,j,k}} \cdot \frac{\Delta z}{S^z_{i,j,k}} \right] = \sum_1^6 Q_{cond} - \sum_1^6 Q_{conv} - \sum_1^6 Q_{rad} \qquad . \tag{353}$$

Proceeding further one can obtain

$$\rho c \frac{T'_{i,j,k} - T_{i,j,k}}{\Delta t} \left[\frac{\Delta x}{S^x_{i,j,k}} \cdot \frac{\Delta y}{S^y_{i,j,k}} \cdot \frac{\Delta z}{S^z_{i,j,k}} \right] =$$

$$Q^{xl}_{cond} + Q^{xr}_{cond} + Q^{yl}_{cond} + Q^{yr}_{cond} + Q^{zl}_{cond} + Q^{zr}_{cond} +$$

$$- Q^{xl}_{conv} - Q^{xl}_{conv} - Q^{xl}_{conv} - Q^{xl}_{conv} - Q^{xl}_{conv} - Q^{xl}_{conv} + \tag{354}$$

$$- Q^{xl}_{rad} - Q^{xr}_{rad} - Q^{yl}_{rad} - Q^{yr}_{rad} - Q^{zl}_{rad} - Q^{zr}_{rad} \qquad .$$

.

where $S^x_{i,j,k}, S^y_{i,j,k}, S^z_{i,j,k}$, are scaling factors describing the length of the element in the x, y, and z directions, respectively, while Q^{xl}_{cond}, Q^{xl}_{conv}, Q^{xl}_{rad}, Q^{xl}_{rad}, Q^{xl}_{rad}, Q^{xl}_{rad}, Q^{xl}_{rad}, Q^{xl}_{rad}, Q^{xl}_{rad}, refer to the heat transfer due to conduction, convection, and radiation to the ambient regions in the x, y, and z directions respectively.

To take full advantage of the computer algorithm one can make use of Boolean expressions corresponding to each possible mode of heat transfer at every node represented by subscripts i, j, and k and its neighbors, the coefficients needed to evaluate Eq. 354 can be expressed as

$$\varsigma_{i,j,k} = \varsigma^x_{i,j,k} + \varsigma^y_{i,j,k} + \varsigma^z_{i,j,k} + S^Q_{i,j,k} \cdot Q_{i,j,k} \qquad , \tag{355}$$

and

$$\phi_{i,j,k} = \varsigma^{x}_{i,j,k} + \varsigma^{y}_{i,j,k} + \varsigma^{z}_{i,j,k} \quad . \tag{356}$$

where

$$\varsigma^{x}_{i,j,k} = S^{x}_{i,j,k} \left\{ \left[S^{kxl}_{i,j,k} \cdot \frac{k}{(\Delta x)^2} + S^{hxl}_{i,j,k} \cdot \frac{h_h}{\Delta x} \right] T_{i-1,j,k} + \right.$$

$$+ \left[S^{kxl}_{i,j,k} \cdot \frac{k_{i,j,k} \cdot}{(\Delta x)^2} + S^{hxl}_{i,j,k} \cdot \frac{h_h \cdot}{\Delta x} \right] T_{i+1,j,k} + \tag{357}$$

$$\left. + \left[S^{hxl}_{i,j,k} \cdot \frac{h_{xl} \cdot}{\Delta x} + S^{hxr}_{i,j,k} \cdot \frac{h_{xr} \cdot}{\Delta x} \right] T_a \right\} \quad ,$$

and

$$\phi^{x}_{i,j,k} = \phi^{x}_{i,j,k} \left\{ \left[S^{kxl}_{i,j,k} + S^{xr}_{i,j,k} \right] \frac{k}{(\Delta x)^2} + \left[S^{axl}_{i,j,k} \cdot \frac{h_{xl} \cdot}{\Delta x} + S^{axr}_{i,j,k} \cdot \frac{h_{xr} \cdot}{\Delta x} \right] + \right.$$

$$\left. + \left[S^{hxl}_{i,j,k} + S^{hxr}_{i,j,k} \right] \frac{h_h \cdot}{\Delta x} \right\} \quad . \tag{358}$$

It should be noted that Eqs 357 and 358 are for the *x*-direction only. For *y*- and *z*-directions one can write similar expressions using superscript *y* for *y*-direction, and *z* for *z*-direction.

Note that those coefficients are the Boolean expressions which modify the general node formula to the specific node under consideration.

In the case where thermal conductivity is not constant with the temperature, general expression for coefficient $\varsigma_{i,j,k}$ and $\phi_{i,j,k}$ are

$$\varsigma_{i,j,k}^{x} = S_{i,j,k}^{x}\left\{\left[\frac{S_{i,j,k}^{kxl}\cdot(k_{i-1,j,k}-k_{i,j,k})+S_{i,j,k}^{kxl}\cdot S_{i,j,k}^{kxr}(k_{i,j,k}-k_{i+1,j,k})}{\left\{\Delta x\left[S_{i,j,k}^{kxl}+S_{i,j,k}^{kxr}\right]\right\}^{2}}+\right.\right.$$

$$+S_{i,j,k}^{kxl}\cdot\frac{k_{i,j,k}\cdot}{(\Delta x)^{2}}+S_{i,j,k}^{hxl}\cdot\frac{h_{h}}{\Delta x}\left]T_{i,j,k}+\right.$$

$$+\left[\frac{S_{i,j,k}^{kxr}\cdot(k_{i+1,j,k}-k_{i,j,k})+S_{i,j,k}^{kxl}\cdot S_{i,j,k}^{kxr}(k_{i,j,k}-k_{i-1,j,k})}{\Delta x}+\right.$$ (359)

$$+S_{i,j,k}^{kxr}\cdot\frac{k_{i,j,k}\cdot}{(\Delta x)^{2}}+S_{i,j,k}^{hxr}\cdot\frac{h_{h}\cdot}{\Delta x}\left]T_{i+1,j,k}+\right.$$

$$+\left.\left[\frac{S_{i,j,k}^{kxl}\cdot(k_{i-1,j,k}-k_{i,j,k})+S_{i,j,k}^{kxl}\cdot S_{i,j,k}^{kxr}(k_{i,j,k}-k_{i+1,j,k})}{\Delta x}\right]\right\},$$

and

$$\phi_{i,j,k}^{x} = S_{i,j,k}^{x}\left\{\left[\frac{S_{i,j,k}^{kxl}\cdot(k_{i-1,j,k}-k_{i,j,k})+S_{i,j,k}^{kxr}\cdot(k_{i+1,j,k}-k_{i,j,k})}{\left(\Delta x\left[S_{i,j,k}^{kxl}+S_{i,j,k}^{kxr}\right]\right)^{2}}+\right.\right.$$

$$+\left[\frac{S_{i,j,k}^{kxr}\cdot(k_{i+1,j,k}-k_{i,j,k})+S_{i,j,k}^{kxl}\cdot S_{i,j,k}^{kxr}(2k_{i,j,k}-k_{i-1,j,k}-k_{i+1,j,k})}{\left(\Delta x\left[S_{i,j,k}^{kxl}+S_{i,j,k}^{kxr}\right]\right)^{2}}+\right.$$ (360)

$$+\left[S_{i,j,k}^{kxl}+S_{i,j,k}^{hxr}\right]\frac{k_{i,j,k}\cdot}{(\Delta x)^{2}}+$$

$$+\left.\left[\frac{\left(S_{i,j,k}^{kxl}+S_{i,j,k}^{kxl}\right)\cdot h_{h}+S_{i,j,k}^{hxl}\cdot h_{xl}+S_{i,j,k}^{hxr}h_{xr}}{\Delta x}\right]\right\}.$$

Following the forgoing procedure, equations similar to Eqs 359 and 360 can be written for y-and z-directions.

The inclusion of radiation terms into expressions for the coefficients $\varsigma_{i,j,k}$ and $\phi_{i,j,k}$ is fairly straightforward when linearized the radiation boundary conditions with the definition of temperature-dependent, effective radiation heat transfer coefficient, $h_{i,j,k}^{R}$ such that

283

$$h_{i,j,k}^{R} = \sigma \cdot \varepsilon \cdot \left(T_{i,j,k}\right)^{3} \quad . \tag{361}$$

The resulting modifications to Eqs 359 and 360 are

$$\varsigma_{i,j,k}^{\sum x} = \varsigma_{i,j,k}^{x} + \left[S_{i,j,k}^{Rxl} + S_{i,j,k}^{Rxr}\right] \cdot S_{i,j,k}^{x} \frac{\sigma \cdot \varepsilon \, T_{a}^{4}}{\Delta x} \quad , \tag{362}$$

and

$$\phi_{i,j,k}^{\sum x} = \phi_{i,j,k}^{x} + \left[S_{i,j,k}^{Rxl} + S_{i,j,k}^{Rxr}\right] \cdot S_{i,j,k}^{x} \frac{h_{i,j,k}^{R}}{\Delta x} \quad , \tag{363}$$

respectively. Equations 362 and 363 can be derived for the *y*- and *z*-directions, and the final form of modified parameters are defined as

$$\varsigma_{i,j,k}^{\sum} = \varsigma_{i,j,k}^{\sum x} + \varsigma_{i,j,k}^{\sum y} + \varsigma_{i,j,k}^{\sum z} + S_{i,j,k}^{Q} \cdot Q_{i,j,k} \quad , \tag{364}$$

and

$$\phi_{i,j,k}^{\sum} = \phi_{i,j,k}^{\sum x} + \phi_{i,j,k}^{\sum y} + \phi_{i,j,k}^{\sum z} \quad , \tag{365}$$

where Boolean expression has zero value for all nodes of the mesh, except those irradiated directly by the laserbeam. Substitution of Eqs 364 and 365 into Eq. 344 yields the final difference formulation of general governing equation subject to the specific boundary conditions.

The final form of Eqs 364 and 365 was used in this Dissertation to develop computer program to study interaction of the laserbeam with matter. The computer program outline is given in the flow diagram shown in Fig. 3.30. The effectiveness of this solution was subject to parameters defining operating characteristics of the laser system. Those characteristics were measured and calculated during the course of this Dissertation.

3.2.6. Computer program considerations

Search for an adequate commercially available software to simulate laser beam interaction with matter failed. The main reason was that to effectively model interaction of laserbeam with materials the laser beam's characteristics must be measured and then linked directly to the computer algorithm.

Solution of the general governing equation (Eq. 142) was obtained using computer software developed in this Dissertation. The solution procedure adopted in this Dissertation was an explicit finite difference formulation (finite forward in time and central difference in space) of Eq. 142, and its corresponding boundary conditions, described in Section 2.7.6.

The effectiveness of this solution was subject to parameters defining operating characteristics of the laser beam, such as: energy per pulse, pulse duration, and laser beam diameter, temporal and spatial laserbeam characteristic. These characteristics were measured during the course of this Dissertation.

Solution of Eq. 142 will be discussed in the subsequent sections of this Dissertation. The resulting set of finite difference equation were solved using the algorithm outlined in Fig. 3.30. Borland Turbo Pascal software was used to write computer code, listed in Appendix A.

Geometry of the workpiece utilized in the experiments (10 mm by 25 mm by 0.762 mm) and because of the fact, that significant temperature gradient under the laser beam irradiance, exist only at a small laser beam spot, then the workpiece with the dimensions of 1.3 mm by 1.3 mm by 0.762 mm was used in the FDM computation (Han,

1999). The user first needs to choose the input data file, which contains the material thermal and physical properties, the interface would calculate and output the maximum time step in order to achieve convergence, more details on this subject in Section 3.2.3.

The software used to diagnose the laser beam distribution and interface programs for 3D stages were written in Quick Basic, Section 4.2.

Data analysis like temperature distribution across the sample was done using MathCad, Grapher, and Surfer software. All data input and output formats were developed using ASCI formats, as listed in Appendix A.

3.2.6.1. Phase transition and hole formation

In micromachining applications heating of the sample undergoes various phase transformations (described earlier) like solid to liquid, liquid to vapor, and vapor to plasma phases. Computer programs developed consider all of the phase transformations. The procedure is very general and may be used for most of materials (not only metals) and includes some of the mass expulsion phenomena. The hole development in the workpiece changes the sample geometry and must, therefore, be tracked throughout the solution procedures. The process for phase transitions is straightforward. As the computer program algorithm marches through the finite difference grid at a given time step, the previous temperature at node (i,j,k) is compared to the temperature for initiation of a given phase transition. If the node temperature falls within a prescribed tolerance, the given phase transformation occurs. The phase change is modeled as an isothermal

process in which the energy required for transition is equal to the latent heat of the particular transition (melting or vaporization). The temperature of that particular node is held at the transition temperature, potentially for multiple iterations, until it has accumulated the amount of energy equal to the latent heat of the transition.

The temperature of that particular node is held at the transition temperature, potentially for multiple iterations, until it has accumulated the amount of energy equal to the latent heat of the transition. In other words the change in element internal energy is expressed as a change in enthalpy of that element, or mathematically this process is implemented by modifying Eq. 344 as

$$h_{i,j,k}^{t+\Delta t} = h_{i,j,k}^{t} + \frac{\Delta t}{\rho} \left(\zeta_{i,j,k} - \phi_{i,j,k} T_{i,j,k}^{t} \right) \quad , \tag{366}$$

In Eq. 366, $h_{i,j,k}^{t}$ is the value of nodal enthalpy at time t, and the second term on the right hand side of the equation is the incremental change in nodal enthalpy occurring as a result of the energy transfer during the present iteration of the solution. Isothermal nature of the phase change at node (i,j,k) is guaranteed by evaluating Eq. 366 in place of Eq. 336 and by setting

$$T_{i,j,k}^{t+\Delta t} = T_{i,j,k}^{t} \quad . \tag{367}$$

This procedure is followed until the variable $h_{i,j,k}^{t}$ is equal to the latent heat of the given transition. At that time, the temperature at node (i,j,k) is allowed to vary by evaluating Eqs 336 and Eq. 344 for subsequent iterations in time at node (i,j,k) until the next transition.

At the end of evaporation transition, the node is considered to be annihilated or at the certain laser energy density is going to change into plasma and to constitute in any case a region corresponding to a hole. The hole creation in the workpiece changes the material geometry and must, therefore, be tracked throughout the solution procedure. For semitransparent materials, for example, the possibility of subsurface hole formation must also be considered.

The effect of hole formation on the problem geometry is illustrated schematically in Fig. 3.25. Examination of this illustration reveals few key problems one has to face with and they have to be considered in development of the solution model.
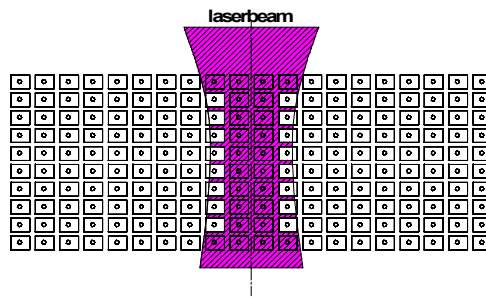

Fig. 3.25. Hole formation.

The essential modeling issue is related to the question of the effects of material removal on beam attenuation and how to model the heat transfer along the side and bottom of the hole (i.e., Marangoni effect and Knudsen layer). Computer code was written (as a part of this Dissertation) in modular and universal way and can support any value of surface convection coefficient, including a temperature dependent function, Appendix A. The approach taken in this dissertation is the following.

Under normal conditions the heat is absorbed first in a very thin Knudsen layer. When that layer become liquid it is still being heated until it reaches the critical

temperature, which was calculated to be about 1.4 times the boiling temperature. Then the liquid metal exhibits dielectric behavior and becomes transparent to the laserbeam. That implies that there cannot be any laser absorption at this point in the superheated layer. All of the absorption is concentrated then on very small region below where the temperature is just below the critical temperature. Material is removed at the top of the dielectric layer by evaporation. At the sidewalls material is forced away by the plasma pressure on the liquid while at the end of the pulse, when the pressure suddenly drops, material is removed by the boiling of superheated liquid.

In this Dissertation a coefficient of heat transfer between the nodes in the hole and the hole wall has been considered. The temperature of the hole's wall was to be $T_{i,j,k}^{wall}$ and of the node in the vaporized region T_h. The resulting heat loss across the hole boundary can be expressed by modifying Eq. 142, i.e.,

$$q_{i,j,k}^{h} = -h_h(T_{i,j,k}^{wall} - T_h) \quad , \tag{368}$$

where h_h is the wall heat transfer coefficient defined by

$$h_h = h_{ch} + h_{rh} \quad . \tag{369}$$

In Eq. 369, h_{ch} and h_{rh} is convective and radiative heat transfer coefficient, respectively.

If shield gas is used or any other nozzle for assisting gas in micromachining application then convective heat transfer coefficient, h_{ch} was determined by Gordon and Cobonque (1961)

$$h_{ch} = 13 \, \text{Re}^{0.5} \, \text{Pr}^{0.33} \frac{k_{gas}}{B} \quad . \tag{370}$$

where, B is the jet plate distance, Re is the Reynolds number at jet exit, Pr is the Prandt number for gas, and k is the thermal conductivity of gas.

The radiative heat transfer coefficient h_{rh} was determine from its definition

$$q^r_{i,j,k} = -h_{rh} A(T^{wall}_{i,j,k} - T_h) \quad , \tag{371}$$

and the Stefan-Boltzmann, Eq. 159, from which derives

$$h_{rh} = \sigma \cdot A(T^{wall\,2}_{i,j,k} + T_h^{\,2})(T^{wall}_{i,j,k} + T_h) \quad . \tag{372}$$

The melting phase change process was achieved by calculating $T^{wall}_{i,j,k}$ for wall surface grid points and if it exceeded the boiling point of the material, then that grid point was deemed to be transparent and the incident power fell on the grid point below it, after suffering some absorption and so on through the entire substrate while the transparent grid points kept their high temperature. In real conditions that would be the case, because in the vaporization zone during laser interaction time the hole is filled with hot vapor and plasma.

3.2.6.2. Absorption coefficient considerations

First issue is the effect of material removal on the attenuation of the laserbeam at point below the hole. Examining Eq. 139 one sees that the equivalent internal power generation due to the laserbeam is reduced exponentially with the distance the beam propagates within the material. As a result, Eq. 139 can be modified to

$$Q(x,y,z,t) = A \cdot \exp(-\mu \cdot t)\mu \cdot I_0(x,y,0,t)$$
$$\exp\left\{-[\mu_s \cdot k + (\mu_v - \mu_s)wsp_{i,j,k}^t]\Delta z\right\} \quad , \tag{373}$$

where $wsp_{i,j,k}^t$ is a record of the number of vaporized nodes above the node (i,j,k) at time t. This is important for the laserbeam decreasing the amount of attenuation material through which the beam must pass in order to reach the node (i,j,k). Selection for the values for absorption coefficients, μ, μ_s and μ_v is dependent from the material properties of the irradiated surface.

To obtain an accurate theoretical value for the absorption coefficient seems to be rather difficult task because not only the inverse Bremsstrahlung effects and Fresnel absorption on the walls of the hole are present, but also interaction with some of the liquid droplets detached from the liquid layer of the drill hole occurs. These droplets would actually block some of the incident radiation by absorbing the incident energy or partially reflect it back. The actual value depends on the liquid density and viscosity, as well as on the input laser beam intensity. Its value can be inferred for different material and thickness.

The first step considered in this Dissertation was linear model, which could be viewed as very realistic providing that the predicted results correlate well with observed results. Analyzing Eq. 373 and the fact that if the power entering the melted zone undergoes exponential decay, according to Beer-Lambert law one can carry out the following analysis.

The range of reasonable values for absorption coefficient was calculated by considering the fact that a material (304 stainless steel) has a typical surface reflectivity at

1.064 mm radiation of 60%, the remaining 40% of incident power from the laser is sufficient to initiate a melt of material, at which point the melt behaves as a black body and absorbs 100% of the power. Absorption takes place in the plasma field due to high electron density of the hot vapor (~6,200 deg K). Based on experimental data from the literature, Mazumder and Steen (1980) that the laser penetration at 1,300 W into steel achieves a depth of 2.3 mm virtually independent over speed range 5-25 mm/s. At 1,500 W, depth was 2.5 mm, and at 1,700 W depth of 2.72 mm. To calculate that only an absorption coefficient of 670 m^{-1} is less than 40% of the power available at the maximum penetration depth, i.e., less than the power required to initiate the melting. Thus, for the 304 stainless steel sample (material thickness equals 0.762 mm) first consideration in this Dissertation was that the initial μ was chosen to be 670 m^{-1} (0.67 mm^{-1}) a value corresponding with that used by others researchers. The precise value depends on the liquid density and viscosity, as well as on the input laserbeam intensity. Its value can be inferred for different material and thickness.

In order to pursue a simpler way of caring out the overall calculations of absorption coefficients for liquid and vapor, the average Fresnel absorption was fitted into exponential curve, so that Fresnel and Bremsstrahlung mechanisms were to be described approximately (Niedrig and Bostanjoglo, 1996). It was found that integrated absorption coefficient, once it has average inside the hole in the range 200- 1000 m^{-1}, depending on the process parameters. If a linear approach was assumed, values of absorption coefficients were in the following ranges: for solid phase, μ_s=67,000m^{-1}, for liquid, μ_l =4050 m^{-1}, and for the vapor phase, μ_v = 202 m^{-1}. The implementation of a

linear absorption coefficient reduces the computation time while keeps an acceptable agreement with experiment data, but did not created realistic hole profiles, when the computer program was running and results were compared to experimental data.

Absorption coefficients mentioned above were very different, depending on a specific application.

Niedrig and Bostanjoglo (1996) interpolated the extinction coefficient using power function

$$\mu[T] = 17.7\left(1 - \frac{T}{T_v}\right)^{2.2}.$$ (374)

It can be seen from Fig. 3.26 (Shen and Zhang, 2001) that the effect of the temperature-dependent absorbtance is greatest at the surface and then decreases with depth.
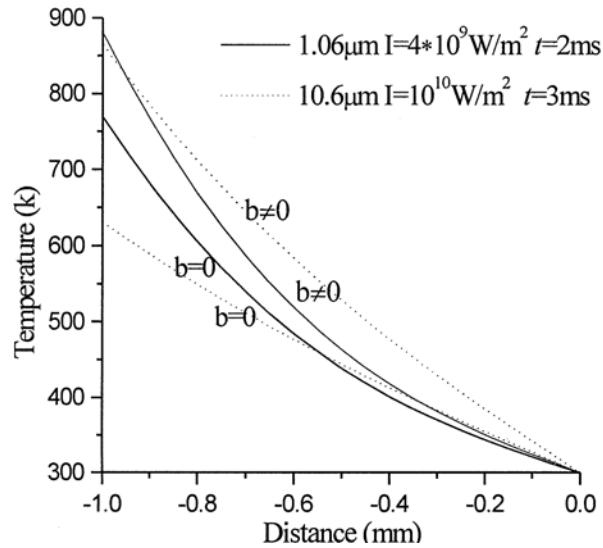
Fig. 3.26. Temperature distribution in an aluminum plate.

Based on Eq. 374 absorption of the radiation penetrating the workpiece was considered to be dependent of temperature and based on Fig. 3.26, is dependent on depth and lateral position of the laserbeam. Implementation of a constant absorption coefficient would reduces the computation time, but will not make realistic hole profiles. Based on the findings in literature and trial and error, in our FDM computer program absorption coefficient was chosen as function of temperature and position (radial and axial), $\mu[x,y,z,T(x,y,z)]$, as

$$\mu[x, y, z, T(x, y, z)] = \mu(z) \cdot \left(1 - \frac{T(x, y, z, t)}{T_c}\right)^2 , \tag{375}$$

where

$$\mu(z) = \mu_{final} + \frac{\mu_{initial}}{k+2} \exp\left(-\frac{k}{2}\right) , \tag{376}$$

and critical temperature T_c which is calculated to be about 1.4 times the boiling temperature. The account was also taken for the temperature variation within the plasma filled keyhole, and was assumed to be in the range between vaporization temperature, T_v, and critical temperature, T_c, and at the top surface plasma temperature, T_p, to be about 2 times T_v. Equation 376 was established based on the fact that the energy deposition law follows a quasi-inverse exponential dependence, which means that for high absorption coefficient much more energy is deposited at the near entrance of the hole than at its bottom. Absorption coefficient defined in Eq. 376 is similar to equation for surface tension (Niedrig and Bostanjoglo, 1996) and is based on the fact that absorption of the laser energy is higher at the walls of the keyhole cavity than in the center, which

corresponds to the higher temperature in the center of the laser beam than at the edge of the beam (the higher temperature the lower the absorption coefficient).

Summarizing, the absorption of the radiation penetrating the sample was considered to be not only dependent on depth and lateral position of the laser beam, but also on temperature of the material under consideration. In the central portion of the laser beam the temperature is higher then at the wall at a keyhole and the absorption at the walls seems to be higher then in the center of the beam. The temperature variation within the plasma filled keyhole was assumed to be in the range between vaporization temperature T_v and critical temperature T_c to be 1.4 times vapor temperature T_v. The model proposed in this Dissertation could be viewed as very realistic providing that the calculated results correlate well with the observed results.

The next difficulty arising in modeling of laser interaction with matter is simulating the effects of the high pressure resulting from subsurface vaporization or the plasma formation. Certain simplification on the problem formulation was deemed an appropriate trade-off for the present time, thus the assumption of constant pressure (i.e., ambient pressure) model was adopted in the Dissertation.

After performing preliminary experiments and some calculations of amount of material removed during microdrilling a linear function was adopted in the computer code which determines ratio of amount of removed material (vaporized and ejected) to the total material of the holes.

3.2.6.3. Enthalpy consideration

Frequently enthalpy of vaporization is assumed to be constant. The enthalpy strongly influences the vapor pressure, which can be evaluated from the Clausius-Clapeyron relationship given by Eq. 67.

Describing evaporation transition, the liquid surface layer formed while the laser pulse moves into the material at the rate determined by the quantity of vapor expelled. As the temperature of the liquid molecules increases, the additional energy needed to free molecules from the binding forces decreases. The latent heat of vaporization, therefore, decreases with the temperature until the critical temperature is reached. The latent heat of vaporization can be written in terms of the surface temperature as (Yilbas el at., 1996; Niedrig and Bostanjoglo, 1996)

$$H_v[T(x,y,z,t)] = H_{v0}\left(1-\left(\frac{T(x,y,z,t)}{T_c}\right)^2\right)^{1/2} , \tag{377}$$

where H_{v0} is the latent heat vaporization at absolute zero. Newly defined parameter can be introduced now in the component of the boundary velocity due to evaporation v_{dv} defined by Eq. 164,

$$V_n = \sqrt{\frac{k_B T_s}{2\pi M}} \exp\left(-\frac{H_v}{k_B T_s}\right) , \tag{378}$$

and being a function of temperature now, can be defined as

$$v_{dv} = \sqrt{\frac{k_B T_s}{2\pi M}} \exp\left(\frac{-H_{v0}\sqrt{1-\left(\frac{T(x,y,z,t)}{T_c}\right)^2}}{k_B T_s}\right), \tag{379}$$

3.2.7. FEM - TAS solutions

To verify own analytical solution and also to compare them to own numerical solutions described in Section 3.2.8, we employed Thermal Analysis Software (TAS), which is a well known in industry, thermal finite modeling software written by Harvard Thermal Inc. (Rosato, 2004). TAS is a finite element program. Finite element modeling is a process of linking the mathematical equations and solving them simultaneously to give a solution to the problem under consideration. Formulation and interaction of laser energy with 3D slab of material started from building 3D model, as shown in Fig. 3.27, by dividing it into some 400,000 tetrahedral elements. Next step was to apply boundary conditions, thermo physical properties, and finally apply the heat source. Program is very generic and there is always more than one way of programming in TAS. The way we defined the heat source, was as follows: we defined a transient surface heat load to the cylinders we built for the purpose of parametrically changing the size and heat load conditions. In other words, the heat source varied spatially and temporally and geometrically in form of circles applied to the top surface.
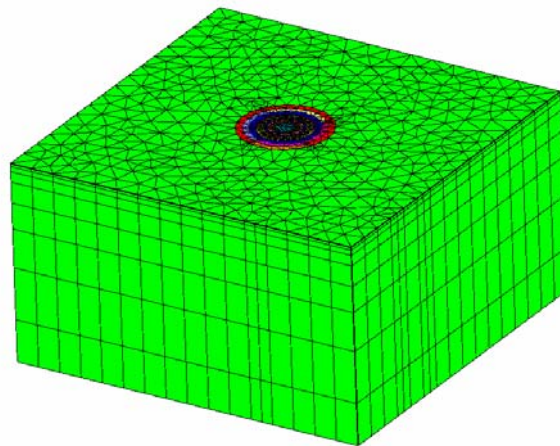
Fig. 3.27. 3D model for TAS calculations used in this Dissertation.

TAS contains possibility of using temperature dependent thermo physical properties, as well as a new ablative module to solve ablating problems. We incorporated into TAS temperature dependent properties defined earlier in Section 2.7.4.

Typical solution output of the temperature distribution across the plane perpendicular to top surface of model in z-direction is shown in Fig. 3.28, and at the top of the workpiece is shown in Fig. 3.29. Program is very powerful and useful for parametric study of different temperature depended thermo-physical parameters, and laser beam spatial and temporal variations, but does not consider any of the phase changes of the material under large heat load. That is a reason why in order to successfully predict the profile of the drilled hole own program was written.

° C
4934.14
4780.73
4627.32
4473.91
4320.50
4167.09
4013.68
3860.27
3706.85
3553.44
3400.03
3246.62
3093.21
2939.80
2786.39
2632.98
2479.57
2326.16
2172.75
2019.34
1865.93
1712.52
1559.11
1405.70
1252.29
1098.87
945.46
792.05
638.64
485.23
331.82
178.41
25.00
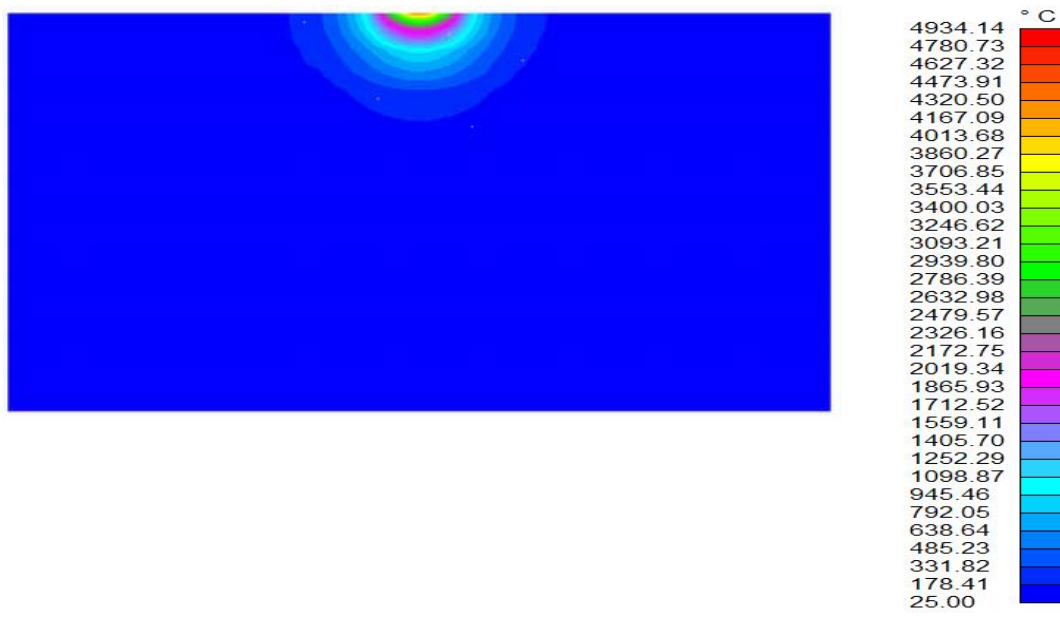
Fig. 3.28. Temperature distribution of a typical cross-section of the workpiece, in z-direction using TAS.
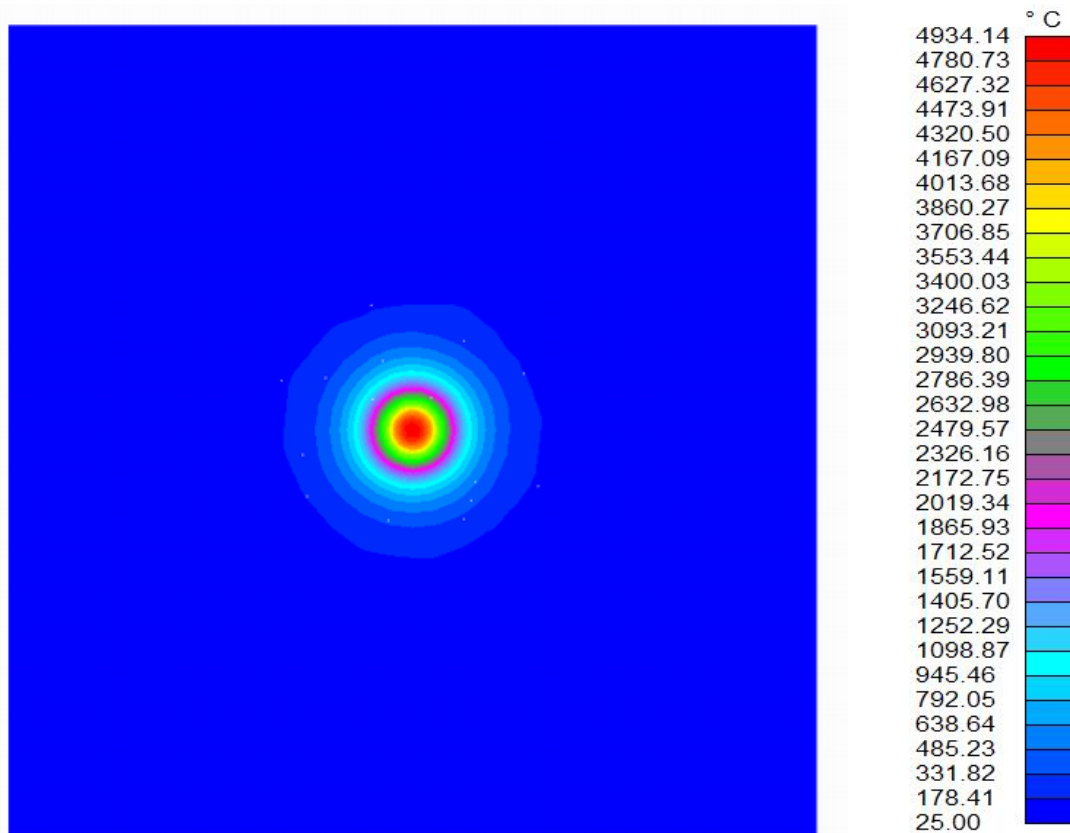
Fig. 3.29. Temperature distribution of a typical cross-section of the workpiece, in *x-y-*
direction using TAS (top surface).

3.2.8. FDM solutions

Using Borland Turbo Pascal, MathCAD, Quick Basic, Surfer and Grapher

programs, the finite difference algorithm, Fig. 3.30, was implemented. At beginning of

the program the user first needs to choose the input data file – material data, the interface

would calculate and output the time step in order to achieve convergence (stability

criteria), as described in Section 3.2.3.

Begin

Sample geometry
Thermal properties
Physical properties
Computation setup

User input

Calculate properties

Error checking
Establish stability criteria

Create FDM grid

Repeat to max count/time

Yes

Node inside

No

Select power distribution

Uniform power distribution

Gaussian power distribution

Triangular power distribution

Calculated Power

Measured power distribution

Update properties
Check for the phase change

Evaluate node temperature:
Tt = T+ΔT

Temperature 2D cross-sections

Temperature 3D illustration-surface

T = Tt

End

Fig. 3.30. Flow chart for the FDM process.

300

Then, the user can accept that time step or input another time step, which is less than the calculated maximum time step, also input number of iterations to skip the data output to display in the file output, in order to save some disk space. In addition, there are several more option to choose from to consider experimentally measured laserbeam characteristic, Gaussian beam distribution, square or triangular laserbeam distribution. The other options to choose from are few different temporal characteristics of the laser pulse, square, triangular, or measured. Then the program will compute the overall temperature profiles, and output the temperature, convection and radiation heat loss of any nodes on the sample and melting isotherms into files. A 3D graphic of the temperature distribution of any node at the sample can be obtained by linking data output files directly to MathCAD programs, which was written for the purpose of illustrating and interpreting the results of laser material interaction. Typical profile of the microdrilled holes (using a color palette isotherms) are shown in Fig. 3.31, Fig. 3.32, and Fig. 3.33. That way one can obtain a temperature distribution at any cross-section of the sample at any time from the beginning of the pulse and after when the laserbeam ceased to exist. In addition two other programs were used: MathCAD and Grapher to demonstrate the surface temperature distribution at any surface perpendicular to impinging laserbeam at any time from the beginning of the laserbeam interaction, example of which is illustrated in Fig. 3.32 and Fig. 3.33.
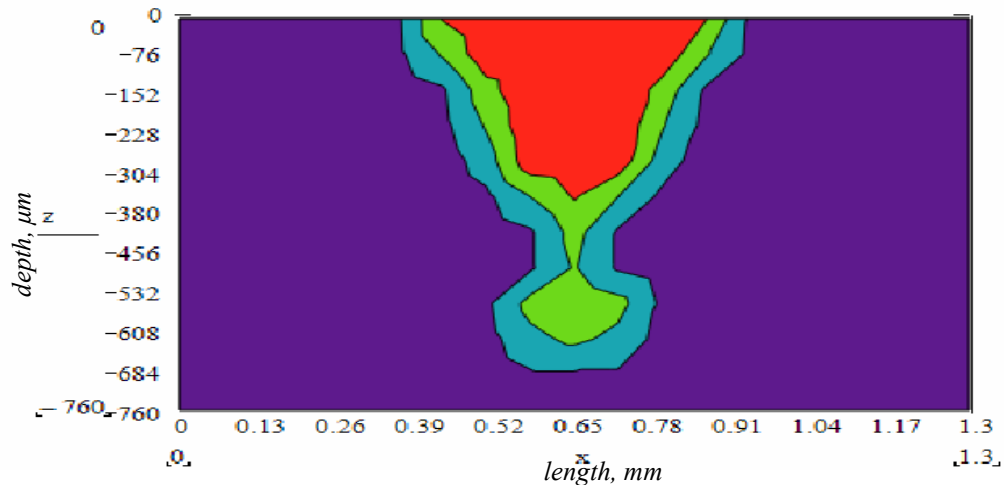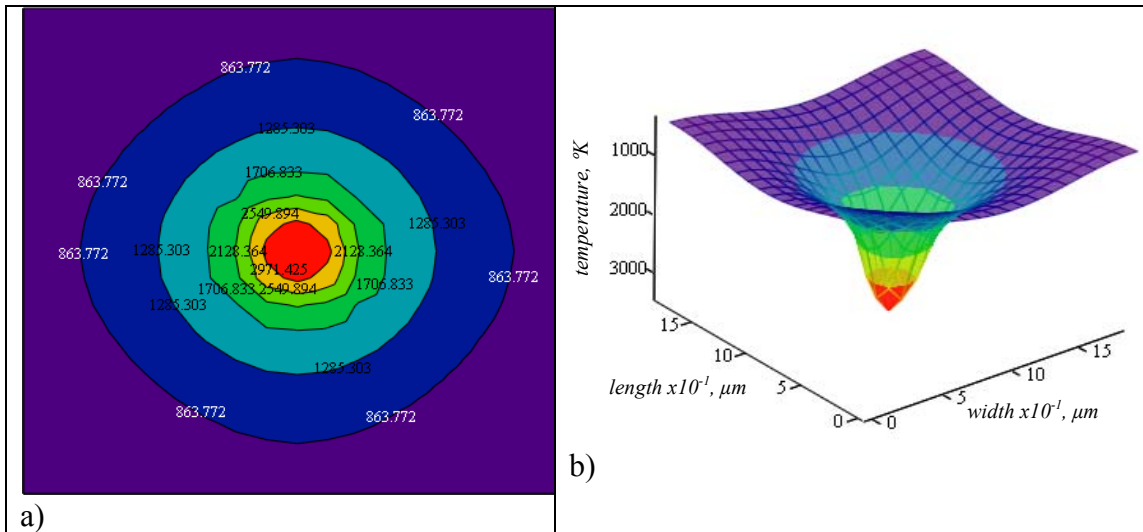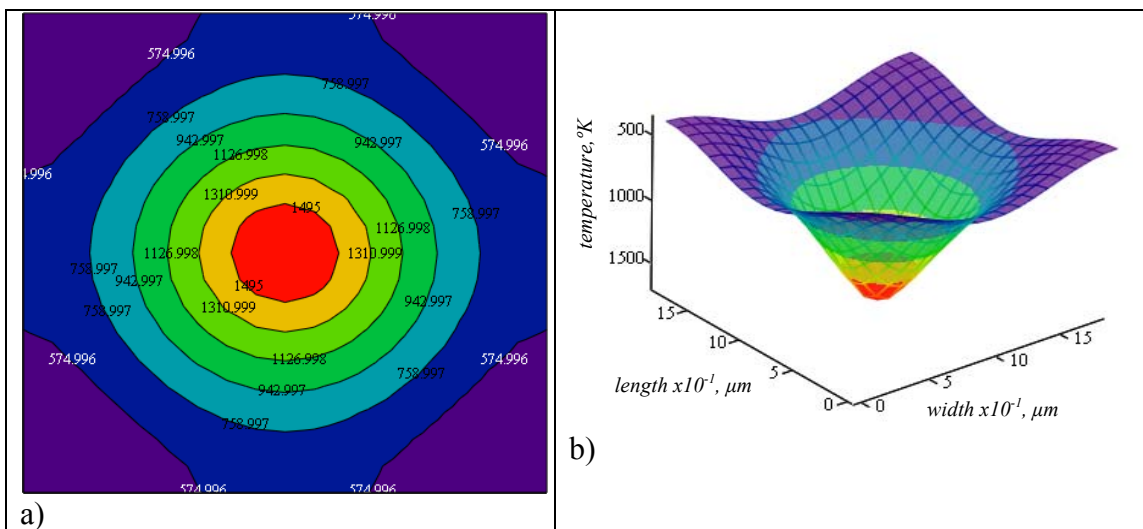
Fig. 3.31. Example of a 2D temperature distribution around the hole cross section profile could be obtained from the computer program at any time during or after the end of the laser pulse of the workpiece in the axial cross section plane of the laser beam.

Computer program is using the workpiece's temperature dependent parameters, which were found in the literature, but program needs also the other important input parameters temporal and spatial laserbeam characteristics. Those parameters were not available in the literature. They were not available from laser manufactures, either. The use of assumed parameters that approximate characteristics of laserbeam leads to erroneous results, especially for determining the hole profile characteristics. Therefore, to effectively model interaction of laserbeam with materials, the laser beam's characteristics must be measured and then linked directly to the computer algorithm, Section 4.2.

Fig. 3.32. Example of temperature distribution around the hole profile could be obtained from the computer program at any time during or after the end of the laser pulse of the workpiece: a) 2D and b) 3D surface temperature distribution taken from the bottom of the workpiece.

Fig. 3.33. Example of temperature distribution around the hole profile could be obtained from the computer program at any time during or after the end of the laser pulse of the workpiece: a) 2D and b) 3D surface temperature distribution taken from the middle of the workpiece.

4. Experimental investigations

The purpose of this chapter is to present and discuss some representative results of the experimental work on interaction of pulsed laserbeam with stainless steel and single crystal silicon samples. Experimental section started from Chapter 4.1 in which the laser system (including fiber optic attachment) used in experiments throughout preparation of this dissertation is described. Temporal, spatial, stability and other characteristics of the laser system used in this Dissertation are presented in Section 4.2. Representative results of laser microdrilling on materials are presented and discussed in Section 4.3 for the effect of laser parameters on the microdrilling results.

Correlations between computational and experimental investigations for laser material processing are included in Section 5, follows with Section 6 which contains summary of observations done in this Dissertation and some recommendations for the future, finished with conclusions and future work in Sections 7 and 8.

4.1. Nd:YAG laser system

For experimental study for this Dissertation a Nd:YAG class 4 pulsed laser, model KLS 126, manufactured by Lasag Industrial Lasers Corporation was used, Fig. 4.1. The maximum values, which should never be exceeded are: laser is rated at a maximum average output power of 200 W, with a single pulse capability up to 130 J, and voltage up to 370 V and wavelength $\lambda = 1.064$ μm. The pulse duration is variable between 0.1 to 10 ms, (Lasag, 1997).

The output energy was measured with a built-in power measurement unit. Pulse energy represents the energy coming out directly from the resonator and is calculated by integration over the pulse length and displayed on a LCD display. The Lasag's Nd:YAG laser system is also equipped with He:Ne laser class 2 continuous wave laser for alignment purposes. Its maximum output is 0.5 mW.

Fig. 4.1. Laser system used in this study.

When Nd:YAG laserbeam will focused to a small spot then one can drill, cut, melt, and burn through any materials. This interaction of laser energy with various materials is a subject of this Dissertation.

One of the unique feature of Nd:YAG laser systems is that they are flexible and fiber cable can be attached to them in order to transmit the laser beam to a workpiece.

4.1.1. Fiber optic attachment

Fiber optic (FO) can be long, thin strand of very pure glass about the diameter of a human hair and used to transmit light signals over long distances. A single optical fiber has the following parts: core (thin glass center of the fiber where the light travels), cladding (outer optical material surrounding the core that reflects the light back into the core), and buffer coating (plastic coating that protects the fiber from damage and moisture), Fig. 4.2a, and Fig. 4.2b.

a)   b)
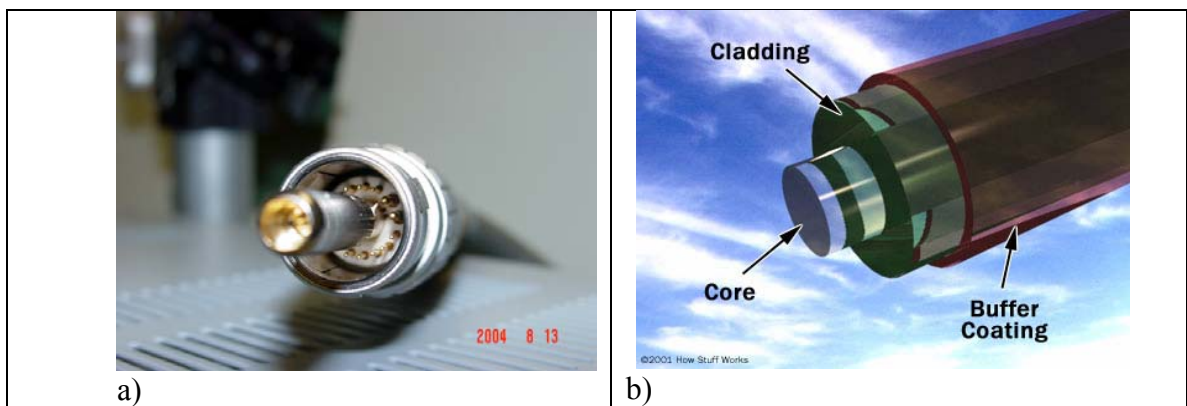
Fig. 4.2. Fiber optic connector: a) photograph, b) schematic.

The light in a fiber-optic cable travels through the core by constantly bouncing from the cladding (mirror-lined walls), a principle called total internal reflection. Because the cladding does not absorb any light from the core, the light wave can travel great distances. However, some of the light signal degrades within the fiber, mostly due to impurities in the glass. The extent that the signal degrades depends on the purity of the glass and the wavelength of the transmitted light (for example, 850 nm = 60 to 75 percent/km; 1,300 nm = 50 to 60 percent/km; 1,550 nm is greater than 50 percent/km).

When light passes from a medium with one index of refraction (n_1) to another medium with a lower index of refraction (n_2), it bends or refracts away from an imaginary line perpendicular to the surface (normal line). As the angle of the beam through n_1 becomes greater with respect to the normal line, the refracted light through n_2 bends further away from the line. At one particular angle known as the critical angle, the refracted light will not go into n_2, but instead will travel along the surface between the two media (*sin [critical angle] = n_2/n_1* where n_1 and n_2 are the indices of refraction [n_1 is less than n_2]). If the beam through n_1 is greater than the critical angle, then the refracted beam will be reflected entirely back into n_1, which is known as the total internal reflection, illustrated in Fig. 4.3, even though n_2 may be transparent. In physics, the critical angle is described with respect to the normal line. In fiber optics, the critical angle is described with respect to the parallel axis running down the middle of the fiber.
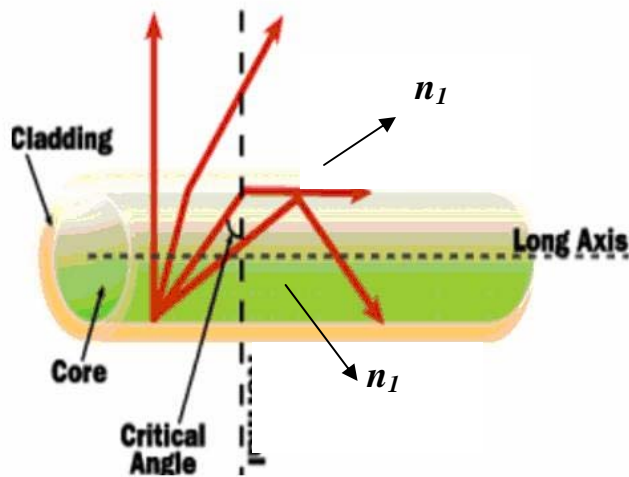
Fig. 4.3. Total internal reflection in an optical fiber.

The core layer of the fiber has a larger refractive index than the outer cladding layer, ideally 100% of the incident laser energy is reflected up and down and is trapped inside the core under two assumptions. First, the laser incident on the fiber above a critical angle to allow total internal reflection, otherwise part of the light is reflected and part is transmitted, which means lower efficiency, which is not desirable. Another assumption is that the core doesn't absorb any energy as light is transmitting through it. Unfortunately all materials absorb a portion of light energy or attenuate the light as light propagates through. Modern optical fiber has an energy loss as small as 4dB/km.

Considering absorption one must keep in mind that the absorption of a material is strongly related to the wavelength. For practical fibers, the core material has low absorption for the 1.06 micron Nd:YAG laser, but the absorption is much higher at 10.6 micron (CO_2 laser) or at UV wavelength. Higher absorption means higher percentage of the laser light being transformed into thermal energy. This is the reason why only Nd:YAG laser is supplied with the ability of beam delivery with fibers. Laser beam delivery through fibers first found application in telecommunications, which only use very small energy levels. In telecommunication, the major concern is whether information can be transmitted without distortion and at high speed. In laser machining, however, the major concern is that whether sufficient high power can transmitted to the workpiece with high beam quality.

Since laser material processing requires very high irradiance, up to 10^{10} W/cm^2 at up to 15 kilowatts (kW) of average power, the coupling of high power lasers into

308

multimode fibers becomes an important issue. To get high beam quality from the output

of the fiber, however, single-mode fibers could be the solution.

The single mode fiber optic cable is constructed with a central core that carries the

laser, a cladding region that acts as a mirror to the laser such that all the light remains in

the core, and an outer metal jacket to protect from light leakage. The core diameter of the

fiber can vary in diameter according to the required spot size needs and input laser power.

In terms of focused spot size the core diameter directly affects the final focus spot size,

and therefore the peak power density. For example a 300 micron core fiber has half the

focused spot size of a 600 micron core fiber, and so has four times the peak power

density. However, the 600 micron fiber, shown in Fig. 4.4, has no power limitations

whereas the 300 micron fiber does. The selection of fiber is application related.
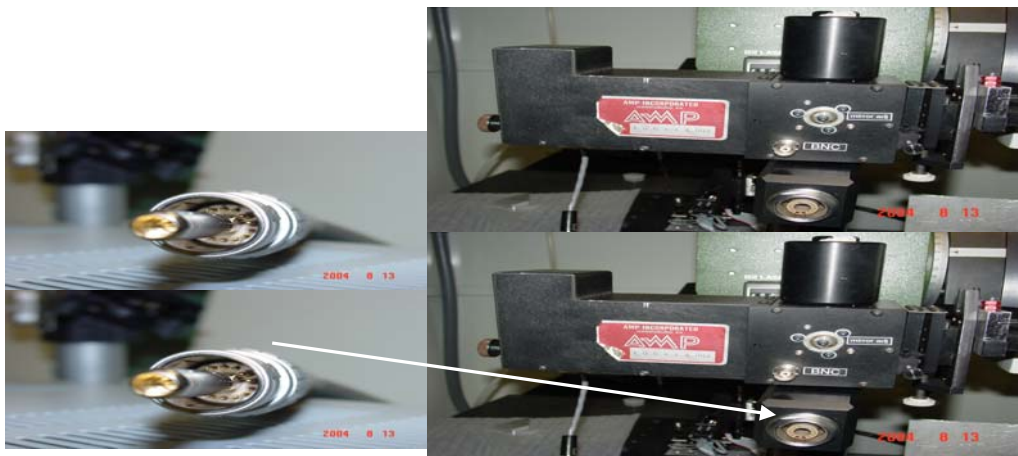
Fig. 4.4. 600 μm end of the FO cable (left picture) will be connected to the focusing
head, as illustrated on the right picture with the arrow.

High precision material removal is needed in all micro-machining applications.

Excimer lasers are widely used for this purpose. Excimer process is generally ablative,

and relies on the short laser wavelength. Although highly precise, it allows only a limited depth of material (1-10 microns) to be removed per pulse. Nd:YAG processing is generally thermal and allows removal depths of a couple of hundreds of microns with a single pulse. When a high beam quality is used, this process can provide sufficient precision and feature size for many applications. Nd:YAG laser machining system is more flexible than excimer lasers. An additional benefit of the Nd:YAG system is that light can be delivered to the workpiece through optical fibers. It is often easier and less expensive to process the workpiece by delivery laser beam through the fiber and focusing optics across it, rather than moving either the workpiece or the laser itself.
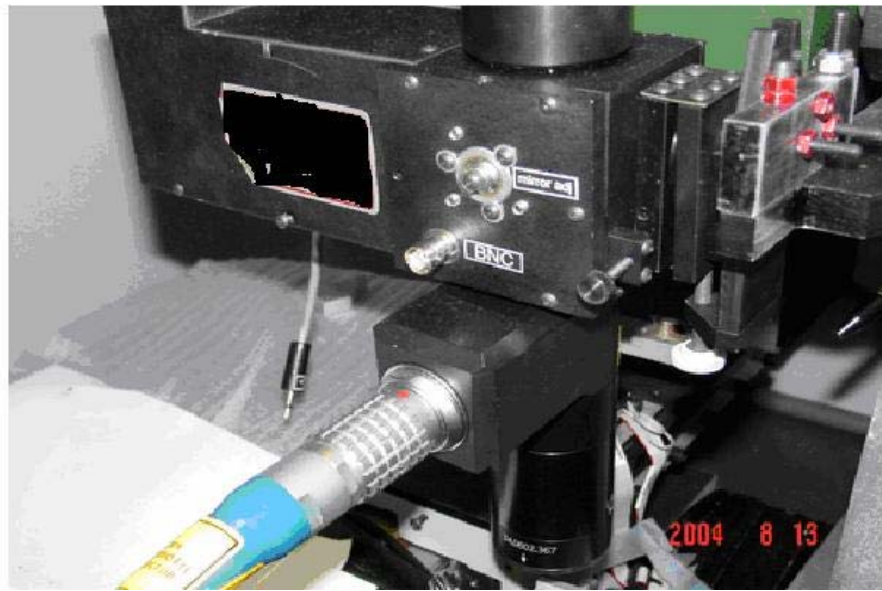
Fig. 4.5. 600 μm end of the FO cable connected to FO head.

Numerical Aperture (NA) for fiber optics, measures the difference between the core refractive index (n_1) and the cladding refractive index (n_2):

$$NA = \sqrt{n_1^2 - n_2^2} \quad .$$

<div align="right">(380)</div>

Coupling light from an industrial Nd:YAG system, shown in Fig. 4.4 and Fig. 4.5, into a single-mode fiber poses practical problems. Only part of the laser energy is coupled into the core of the fiber, the remainder of the laser energy is coupled into the fiber cladding, which can lead to thermal damage at the point where the cladding modes are removed. In any practical situation, the cladding of a glass optical fiber is covered by a protective buffer layer. Even for $M^2=1$, only 70% of laser energy is coupled into the core. If a reflective material, such as a metal coating, is placed in optical contact with the fiber cladding, it will absorb a small percentage of the cladding light on each reflection. To maximize the amount of energy to be coupled to FO cable, alignment of FO cable to the internal laser optics, se Fig. 4.6, is very important, and should be verified often.
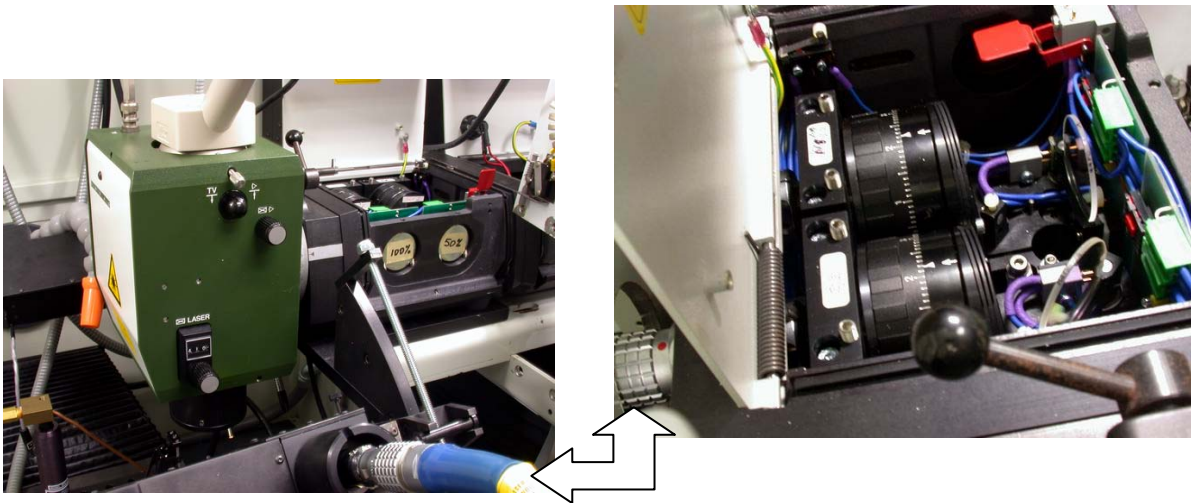
Fig. 4.6. FO laser beam delivery subsystem to two FO cables for laser micromachining.

4.1.2. Fiber optic optical consideration

A shorter fiber optic cable produces little modification to the input laserbeam. On the other hand long and large in diameter fibers, cause the output to be independent of the input distribution. Based on experience and literature (Hunter et al., 1996), the fiber has significantly altered the laserbeam profile and masks many properties of the source laser. The focused beam profile is, subject to aberrations and magnification effects of the impinging lens, the profile on the fiber output face. The length of the fiber was not long enough to allow the formation of the top-hat profile expected for a long step-index fiber. Instead, a pointed top profile was generated.

Smaller size fibers produce less degradation of beam quality. The worst case beam quality from fiber optic cable can be estimated using the conventional definition of M^2. This definition is based on a Gaussian beam and the 86% energy enclosure beam waist is used and considering the angle of divergence one can obtain the following

$$M^2 = 0.86 \cdot r_{fiber} \cdot \arcsin(NA) \frac{\pi}{\lambda} \quad , \tag{381}$$

where r_{fiber} is the fiber radius, NA is the numerical aperture of the fiber. Geometrically, the size of the image of the fiber face is given by

$$r_b = m \cdot r_{fiber} + r_{blur} \quad . \tag{382}$$

where m is the absolute value of the magnification of the imaging system, and r_{blur} is the blur introduced because of diffraction effects or aberrations in the optical system and maximum aberration can be estimated to be $r_{blur} = 0.5 \cdot m \cdot r_{fiber}$.

Clearly, smaller fibers are preferred in order to get the best beam quality. However, the laser itself imposes some constrains. The laserbeam focused spot size has to be smaller than the fiber core to avoid heat effects and allow for the mechanical tolerances of the fiber optic connectors. The minimum fiber optic diameter , d, to be selected as a function of M^2 and NA is given by Hunter et al. (1996)

$$d = M^2 K \frac{2ab}{c} \frac{\lambda}{\pi \tan(\arcsin(NA))} \quad , \tag{383}$$

where K is the aberration of the fiber optics and λ is wavelength, a is spot size if the collimated beam exiting the laser, b is the focused beam size of the lease beam on the fiber face and c is the desired fiber fill factor. If a and b are 1.5 and c is 0.8 at the wavelength of 1064 nm, $NA=0.2$ and $M^2K=70$ the minimum fiber diameter would be 650 µm.

The primary reason for damaging the high power FO connectors is heating in the connectors. If the fiber's input and output optics are properly designed, most of the connector heating comes from spurious reflections or refractions at the fiber end faces. The primary causes are the refractive index discontinuity at the fiber surface (Fresnel losses) and scattering from the surface imperfections. The Fresnel losses can be minimized by applying antireflection coatings on the fiber and optimizing the surface quality.

The importance of the choices made in a laser beam delivery system can be seen by analyzing the power levels required for microdrilling or welding with irradiance

threshold. The laser beam power required to exceed the threshold irradiance can be computed by

$$P = 0.86 \frac{\pi \cdot I_t}{T} \left(\frac{\omega}{F}\right)^2 \quad , \tag{384}$$

where I_t is the threshold irradiance, ω is the focused 86% energy enclosure radius, T is the power transmission and F is a factor that depends on the characteristic of the fiber. For step index fibers $F=1$, but for gradient-index fibers is greater than one. In conclusion, reducing size of ω reduces the total laser power required, and that can be done by using a smaller core diameter fiber, using gradient-index fiber or shorter focal length lenses.

4.2. Characterization of the laser beam

Characterization of the laser beam consists of measurements of average laser power, energy per pulse, peak power per pulse, and irradiance distribution of the laser beam as a function of position across the beam (spatial distribution) and time from the initiation of the output (temporal distribution). In practice, one also needs to measure the beam spot size along the optical path *z-axis* and calculate the other beam parameters like: depth of focus and beam divergence. In microdrilling applications very important parameter is the transverse mode of the laser beam, which is going to be discussed in this section also. In addition, temporal stability of the laser pulse should be also checked, which is described at the end of this section.

4.2.1. Average power and energy measurements of laser beam

Determination of the average laser power and the average energy per pulse was measured with Coherent Labmaster Power Detector Model LM 200, Fig. 4.7, and with internally built energy meter. Experimental setup for this procedure is illustrated in Fig. 4.11. The entire beam was focused onto the designated target in the power meter to insure that the full energy of the beam was delivered to the meter.

For the stable laser system one may consider that the total energy measured by the power meter is equally delivered by each pulse and, consequently,

$$\Delta E_{pulse} = \frac{\Delta E_{total}}{n_{pulse}} = \frac{P\Delta t_{total}}{n_{pulse}} \quad , \tag{385}$$

where ΔE_{pulse} is the average energy delivered per pulse, ΔE_{total} is the total change in energy of the meter during the experimental period , n_{pulse} is the number of pulses incorporated into experiment, P is the average laser power, and t_{pulse} is the total time of the power meter measurement.

The Lasag's Nd-YAG laser system is a mid-power system capable of delivering a maximum average power of 130W and a maximum energy per pulse of about 150 J,. both for 4 msec pulse duration. These values agree well with manufacturer's provided data.
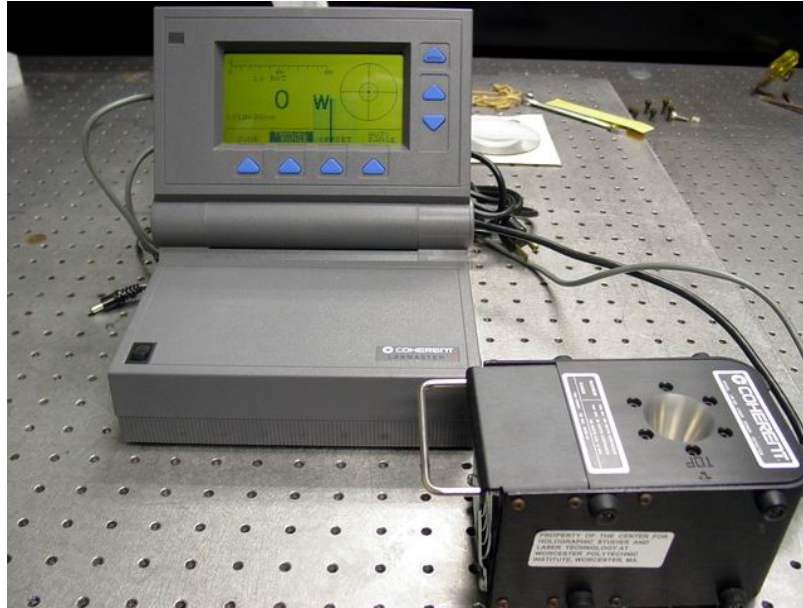
Fig. 4.7. Coherent Labmaster Power Detector Model LM 200.

4.2.2. Measurements of temporal distribution

In the literature (Boulmer-Leborgne, et al., 1993) the temperature calculations are usually made with rectangular laser pulse shapes. Evolution of the temperature of a target surface irradiated by a rectangular pulse is shown in Fig. 4.8. The vaporization threshold occurs as soon as $T_s > T_{vap}$. (T_s, is the surface temperature, T_{vap}, the vaporization temperature of the target). With other lasers the integral must be evaluated using the exact temporal shape of the laser pulse. Using different pulse shapes, different irradiated surface temperature evolutions are determined, resulting in different laser beam-target interaction effects. Two different pulse shapes modulated by varying the active gas mixture concentration in the laser can be obtained using a TEA-CO_2 laser are illustrated in Fig. 4.9 (Boulmer-Leborgne, et al., 1993). Evolution of the temperature of a titanium target surface, T_s, irradiated by those two different pulses A and B are shown in

316

Fig. 4.10. The vaporization threshold occurs as soon as $T_s > T_{vap}$ (T_{vap} is the vaporization temperature of the target). It can be observed that the pulse shape (B) results in a longer surface heating time induced by its long tail. Thus the vaporized material quantity is larger with this pulse shape than with the short one (A), but the vaporization threshold occurs later. The quantity of vaporized mass depends on the laser wavelength and on the laser energy absorbed by the sample.
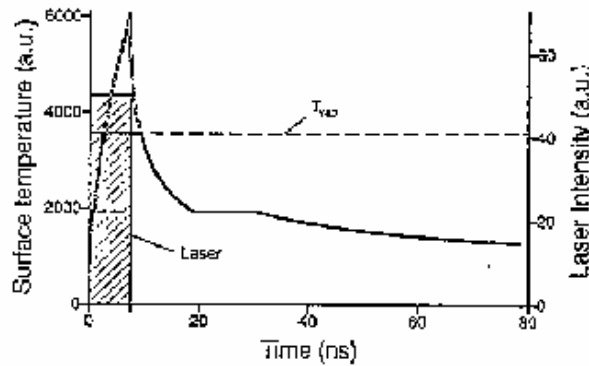
Fig. 4.8. Evolution of the temperature of a target by a rectangular pulse (Boulmer-Leborgne, et al., 1993).
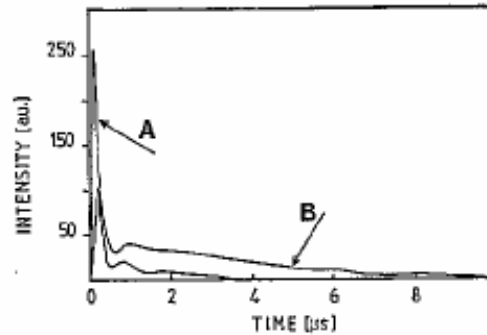
Fig. 4.9. Different pulse shapes from TEA-CO2 laser: A and B relate to two different gas mixture concentrations in the laser (Boulmer-Leborgne, et al., 1993).
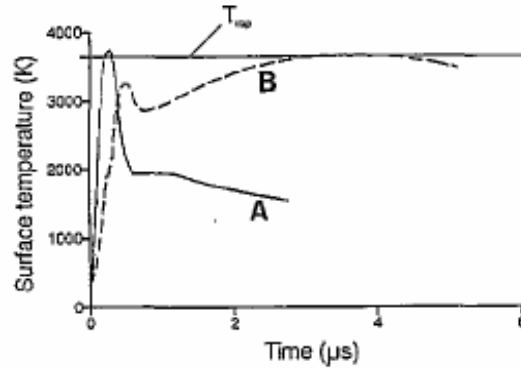
Fig. 4.10. Surface temperature evolution resulting from TEA-CO$_2$ laser pulses for Ti target: A and B relate to two different gas mixture concentrations in the laser (Boulmer-Leborgne, et al., 1993).

Laser beam characteristic of our laser systems were not available from the manufacturer and had to be measured during this study. These measurements were made using a photo-diode that was placed as is shown in Fig. 4.11. Calibration of the diode output to produce absolute power measurements for a given pulse was accomplished by relating the diode measurements to measurements of the energy per pulse. Normalizing the power curve relative to the maximum total beam power P_{max}, recorded for a given pulse and time τ relative to the pulse length t_p, one can write

$$P(\tau) = P_{max} \cdot p(\tau) \quad , \tag{386}$$

where $\quad \tau = t/t_p ,$ (387)

$$P_{max} = \frac{\Delta E_{pulse}}{t_p \int_0^1 p(\tau)d\tau} \quad , \tag{388}$$

where $p(\tau)$ is the normalized beam power as a function of normalized time into the pulse, and ΔE_{pulse} is average energy delivered per pulse.

318
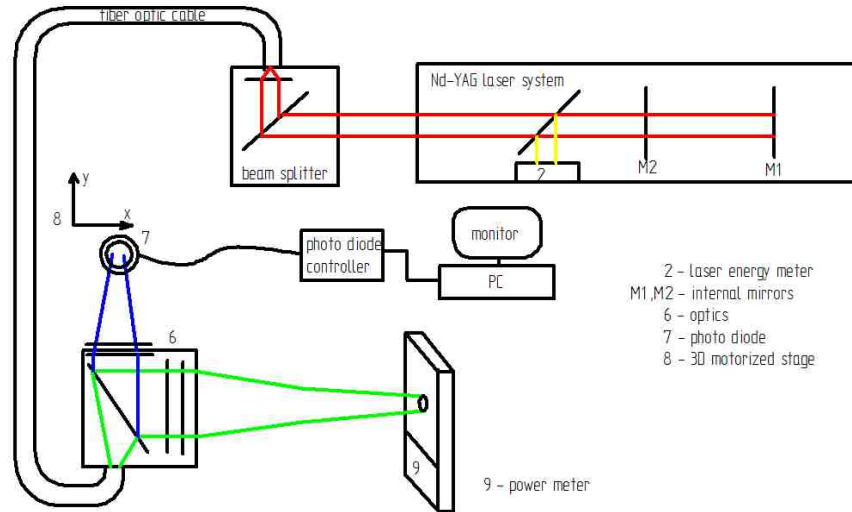
Fig. 4.11. Setup for measurement of the temporal laser beam characteristics.

The relative power curve can be approximated by a least-squares error polynomial and evaluation of integral of Eq. 388 can be accomplished numerically by applying Simpson's rule directly to the numerical data or by integration of the least-squares error polynomial

$$p(\tau) = \sum_{i=0}^{n} a_i \tau^i \quad , \tag{389}$$

where a_i are the coefficients of the least-squares fit and n is the order of the least-squares fit polynomial. Substituting Eq. 389 into Eq. 388 and performing the indicated integration yields

$$P(\tau) = \frac{\Delta E_{pulse} \sum\limits_{i=0}^{n} a_i \tau^i}{t_p \sum\limits_{i=0}^{n} \frac{a_i}{i+1}} \quad ,$$

(390)
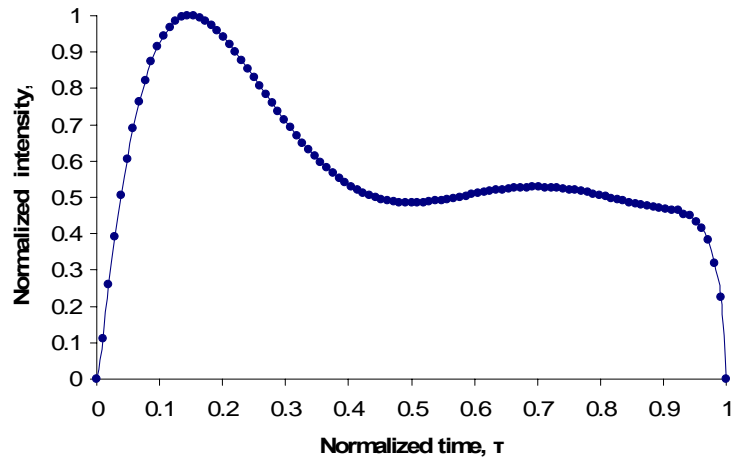
Fig. 4.12. Typical measured normalized temporal characteristics of the Nd-YAG laser beam, which shows normalized laser beam intensity $p(\tau)$ vs. normalized time τ.

Fig. 4.13 shows more examples of measured temporal characteristic of Nd:YAG laser beam (Nowakowski, 1990).
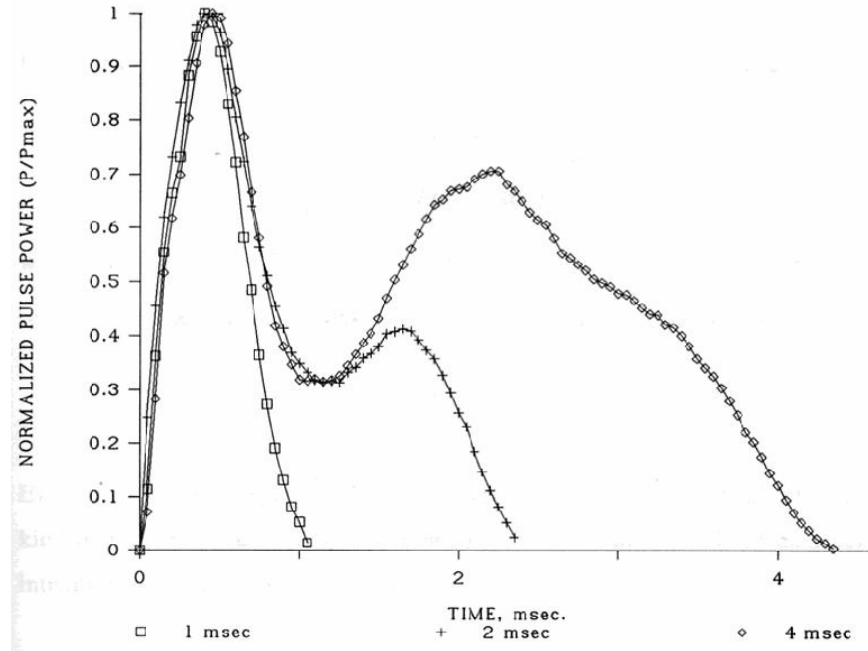
Fig. 4.13. Temporal laser beam characteristics for different pulse lenghts.

4.2.3. Measurements of spatial irradiance distribution

The incident laser beam has a spatial intensity distribution, which in drilling is usually a Gaussian distribution produced by a laser operating in TEM_{00} mode (M^2). To measure spatial characteristic of the laser beam, beam intensity profiler (BeamView[®] Analyzer system) was used (thanks to Dr Marinis of Draper Laboratories) was available. A typical Gaussian distribution was measured on the Argon laser, Fig. 4.14. To measure our Nd:YAG laser beam with this device we encountered a couple of problems. First, a beam intensity profiler is rather large piece of equipment and due to space limitations inside the enclosure box of the Nd:YAG laser system (laser beam is impinging vertically on the workpiece as seen on Fig. 4.25) and the second, that for infrared wavelengths a

321

special filters were required.   Because of those reasons our own laser beam intensity
measurement system was build and used in the course of this Dissertation.   Typical
measurement setup of such a system is shown in Fig. 4.15.
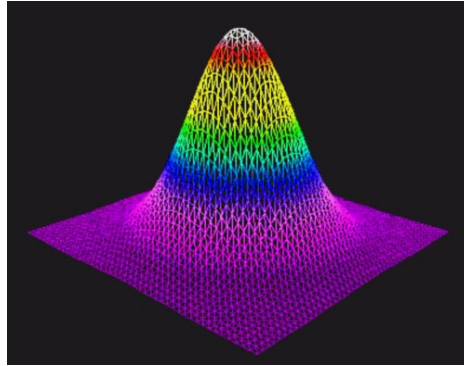
Fig. 4.14. Gaussian spatial laser beam distribution measured by
beam intensity profiler.

Most important part of the system for measuring spatial bema distribution was
Newport's photo detector, model 818-F-SL with picowatts digital optical power meter,
Model 1830-C, Fig. 4.16, which is essentially this same as that used in temporal beam
characteristic, except one modification. Originally the beam splitter was used, but in the
case of measuring spatial beam intensity, we can not afford a risk of any distortion
coming from additional optics in the system. Distortion could be due to the asymmetric
spot formed as a result of reflection of an imperfectly collimated beam at the inclined
beam splitter.

Since the goal of this spatial beam characteristic measurements was to determine
intensity of the beam in the plane of that diode, than distortion of the beam cross-section
could not be tolerated. Positioning of the detector in the path of the beam, required use of

322

aperture and protecting filters against potentially high incident flux. Consequently a few neutral density filters were added to attenuate the incident beam.
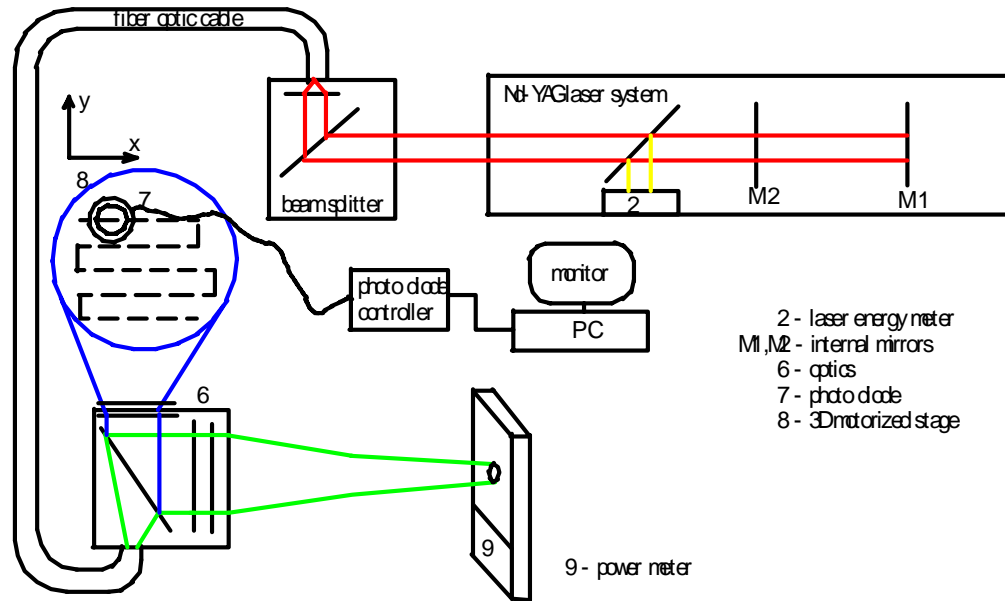
Fig. 4.15. Setup for measurement of the spatial laser beam characteristics.

In addition, to eliminate unwanted background radiation, which might add to a noise in the readings, an interference filter passing only a narrow band of wavelengths of interest (1064 nm) was added in front of the detector, which in turn attenuated the original beam even more. The resulting total attenuation of the laser signal incident onto the photodiode was on the order of 10^{-11}. This value of attenuation is not an exaggeration considering the fact that we are dealing with intensity of the beam in the order of 10^{12} W/m^2.

The detector was fixtured on a 3D micro computer controlled micro-stage with position accuracy of about 0.3 μm. The *x-y* positioner enabled scanning of the laser beam in lateral direction of beam propagation using raster type of scanning.

Fig. 4.16. Digital optical power meter used for experiments.

Data (intensity) were collected at each point of scanning range (1 inch by 1 inch). The interfacing software for this experiment, as well other diode measurements described were written in Quick Basic, during this study, specifically for this task. In addition to collecting raw data from the photo diode, another program was written to present the data in 2D or 3D graphical display, using the least square approximation technique, to obtain the irradiance distribution as a function of both time and position (*x*-*y*). Fig. 4.17 shows a typical result for stable quasi-Gaussian output of the laser.
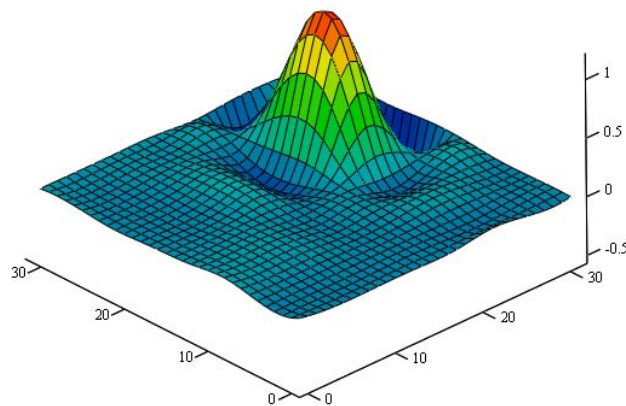
Fig. 4.17. Spatial laser beam distribution measured at close proximity of the focal plane positon.

Please take a note of the fact, that Fig. 4.17 represents results of a time-varying spatial distribution of the laser beam irradiance, i.e., that could be different for different times during temporal variation of the laser pulse. At this time for purpose of this analysis, it was assumed that the relative irradiance of the laser beam is constant. Single typical function was used to describe the relative relation between spatial and temporal variation of the beam. Knowledge of a time history of the total laser beam power, described in Section 4.2.2, and the present measurement information will be enough to determine absolute values of a spatial irradiance function at any given time during course of the laser pulse.

Defining irradiance as the rate of energy flow per unit area, one may integrate over the irradiated area to arrive at the total rate of energy flow across the given surface. The laser power, $P(\tau)$ as a function of normalized time into pulse, can be expressed as:

$$P(\tau) = \int_A I(x, y, z, t)dA \quad ,$$
(391)

where, $I(x,y,z,\tau)$ is irradiance at a point specified by coordinates x and y at a given time τ. Expressing the irradiance as a product of time-dependent function $I_0(\tau)$ and position-dependent function $I_R(x, y)$

$$P(\tau) = I_0(\tau) \int_A I_R(x, y)dA \quad ,$$
(392)

where
$$I(x, y, \tau) = I_0(\tau) I_R(x, y) \quad .$$
(393)

The focused beam radius w is specified as the distance between the center of the beam and a point where the intensity is reduced from its maximum value at the bean

center by a factor of e^2. To facilitate for non-circular cross-sections, this $1/e^2$ radius will depend on the direction under consideration. The beam radius along the x-axis R_x can be set to w. Defining dimensionless parameters ξ and ψ to express the position coordinates x and y, and the eccentricity e_{cc} of the laser spot in terms of w yields

$$\xi = x / R_x = x / w \quad , \tag{394}$$

$$\psi = y / R_y = \frac{y}{e_{cc} w} \quad , \tag{395}$$

$$e_{cc} = R_y / R_x \quad . \tag{396}$$

Adopting this convention and using element of differential area

$$dA = e_{cc} \cdot w^2 d\xi d\psi \quad , \tag{397}$$

one can rewrite Eq. 392 as

$$P(\tau) = e_{cc.} \cdot w^2 I_0(\tau) \int_{-1}^{1} \int_{-1}^{1} I'(\xi, \psi) d\xi d\psi \quad . \tag{398}$$

Solution of Eq. 398 for $I_0(\tau)$ yields

$$I_0(\tau) = \frac{P(\tau)}{e_{cc.} \cdot w^2 \int_{-1}^{1} \int_{-1}^{1} I_R(\xi, \psi) d\xi d\psi} \quad , \tag{399}$$

which is the maximum value of the spatial irradiance distribution at time τ. Substituting Eq. 399 into Eq. 393 results in the absolute time-varying spatial irradiance distribution across the laser beam, i.e.,

$$I(\xi, \psi, \tau) = \frac{\Delta E_{pulse} \cdot I_R(\xi, \psi) \sum_{i=0}^{n} a_i \tau^i}{e_{cc} \cdot w^2 \cdot t_p I_A \sum_{i=0}^{n} \frac{a_i}{i+1}} \quad , \tag{400}$$

where

$$I_A = \int_{-1}^{1} \int_{-1}^{1} I_R(\xi,\psi)\,d\xi\,d\psi \tag{401}$$

is numerical approximation for the area integral showed in Eq. 400.

Lambert's law for the energy delivered to the material in laser micro machining is absorbed in the surface region according to Eq. 144. Combined laserbeam characteristic spatial and temporal characteristics and utilizing Eq. 400 and Eq. 144 and introducing the exponential decay yielding at a distance z below the irradiated surface

$$I(\xi,\psi,z,\tau) = \frac{\Delta E_{pulse} \cdot I_R(\xi,\psi)\sum_{i=0}^{n} a_i \tau^i}{e_{cc} \cdot \omega(z)^2 \cdot t_p\, I_A \sum_{i=0}^{n} \dfrac{a_i}{i+1}}\, e^{-\mu \cdot z} \quad, \tag{402}$$

where μ is the exponential absorption coefficient for the given material.

Approximation of the radius of the laserbeam at any distance z from the origin of the sample under consideration is given by (Nowak, 1990)

$$\omega(z) = \theta\left|z - z_f\right| + \omega_0 \quad, \tag{403}$$

where θ is the half-angle laser divergence, and ω_0 is radius of laser beam at the focal distance or at the waist of the beam, z_f the location of the focal plane.

Better results using different relationship for the radius of the laser beam at any distance (Zhao and DebRoy, 2003) defined as

$$\omega(z) = \omega_0 \left[1 + \left(\frac{z \pm z_f}{2 \cdot \omega_0 \, F / D_o} \right)^2 \right]^{\frac{1}{2}} \quad , \tag{404}$$

was used in the Dissertation, where F is the focal length of the last focusing optical lens on the path of the laser beam just before hit the workpiece and D_0 is diameter of that laser beam on this lens. Substitution of Eq. 404 into Eq. 402 yields

$$I(\xi,\psi,z,\tau) = \frac{\Delta E_{pulse} \cdot I_R(\xi,\psi) \sum\limits_{i=0}^{n} a_i \tau^i}{e_{cc}\omega_0^{\,2} \left[1 + \left(\dfrac{z \pm z_f}{2 \cdot \omega_0 \, F / D_o} \right)^2 \right] t_p \, I_A \sum\limits_{i=0}^{n} \dfrac{b_i}{i+1}} \, e^{-\mu \cdot z} \quad . \tag{405}$$

The power density at any point (x,y,z), the position coordinates defined in terms of the laserbeam dimension at a distance z below the irradiated surface ($z=0$), at time τ, and using terms defined in Section 3.2.6.2, the net volumetric accumulation rate of energy due to the laserbeam is expressed as

$$Q(\xi,\psi,z,\tau) = \frac{A \cdot \mu \cdot \Delta E_{pulse} \cdot I_R(\xi,\psi) \sum\limits_{i=0}^{n} a_i \tau^i}{e_{cc}\omega_0^{\,2} \left[1 + \left(\dfrac{z \pm z_f}{2 \cdot \omega_0 \, F / D_o} \right)^2 \right] \cdot t_p \, I_A \sum\limits_{i=0}^{n} \dfrac{a_i}{i+1}} \, e^{-\mu \cdot z} \quad . \tag{406}$$

Equation 406 is almost the final expression, which is going to be used in the computer algorithm calculations described in Section 3.2.6.2, with the exception of defining the absorptivity coefficient, which remains to be performed.

Examining Fig. 4.17 more closely, one can notice that the bottom of irradiance distribution is not smooth, there are some disturbance of intensity (small waves). In order to verify this we had to switch to higher gain of measuring range in the amplifier used,

because for higher gain nose to signal ratio was too high. By using higher gain and

zooming in the area of interest, and collecting data, we plotted them in Fig. 4.18.
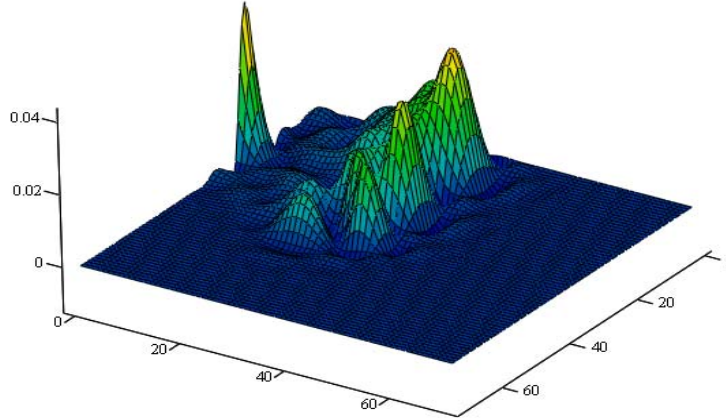
Fig. 4.18. Spatial laser beam distribution measured at the higher gain of the amplifier at
peripheries of the laser beam.

Analyzing both functions of the spatial laser beam distribution presented in Fig.

4.18 and Fig. 4.17, we can overlap them together and obtain a full image of the laser

beam. Using mathematical analysis of the shape of a spatial laser beam distribution and

with help of MathCAD, a mathematical approximation of the measured spatial laser

beam distribution can be defined mathematically as

$$fz(\xi,\psi) = 0.51\cos(\sqrt{3(1.5\xi)^2 + 3(1.5\psi)^2}\ e^{-\gamma} + 0.5 \quad , \tag{407}$$

where

$$\gamma(\xi,\psi) = 0.5(0.7\xi)^2 + 0.5(0.7\psi)^2 \quad , \tag{408}$$

which is graphically represented in Fig. 4.19.

329
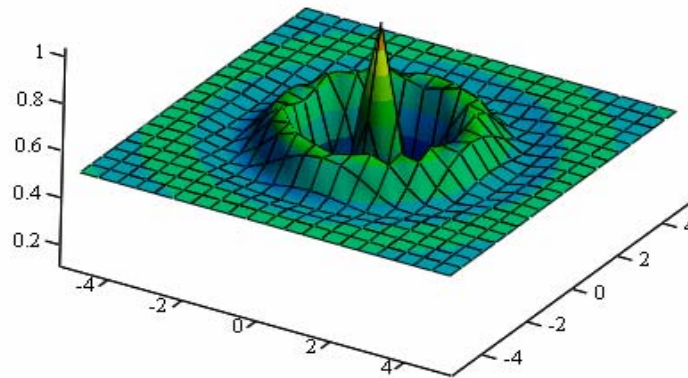
Fig. 4.19. Mathematical spatial laser beam representation of a beam focused at 0.042 mm above focal plane position (lbwp).

Please note that plot in Fig. 4.19 is normalized to maximum irradiance occurring within the cross-section of the laser beam.

4.2.4. Transverse mode of laser beam

One of the most important parameters in laser microdrilling, of especially dielectric materials, is the transverse mode of the laser beam. Nd:YAG class 4 pulsed laser, model KLS 126, manufactured by Lasag Industrial Lasers Corporation used in this Dissertation is producing a nearly TEM_{00} mode with use of an aperture (approximately 6 mm in diameter).

As illustrated in Fig. 4.20, use of the mode electing apertures within the laser cavity significantly alters output of the laser.

The significance of changing the diameter of the laser beam before the focusing lens is manifested in the divergence of that beam, which irradiates the workpiece.

Divergence, Φ, of the laser beam of radius ω_{lens}, measured at the lens focused to a spot of radius ω_0, by a lens of focal length F, is defined

$$\Phi = \frac{\omega_{lens} - \omega_0}{F} \approx \frac{\omega_{lens}}{F} \quad , \tag{409}$$

since in most applications $\omega_{lens} << \omega_0$. Examining Eq. 409, a decrease in diameter of the unfocused laser beam by a factor of n, results in a reduction of the beam divergence by the same factor n. Since the divergence of the beam governs the diameters of the laser beam's cross section along the axis of propagation, the taper of a laser-drilled hole depends on the divergence of the irradiated laser beam. As was mentioned previously, dependence of the hole taper on laser beam divergence is governed, in part, by the thermo physical properties of the workpiece. Considering one of them, thermal conductivity, one should observe a stronger correlation between laser beam divergence and hole taper in dielectric materials, such as silicon, than in a good conductor, such as stainless steel.
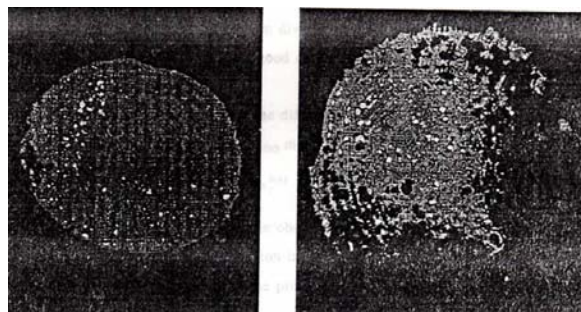
Fig. 4.20. Typical burn patterns created byNd:YAG laser a) with and b) without aperture in laser cavity (Nowakowski, 1990).
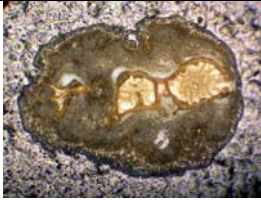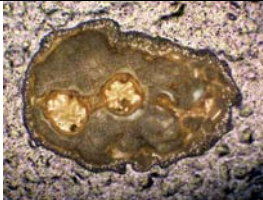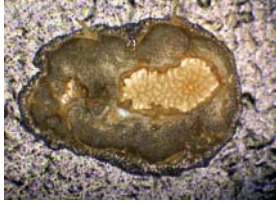
Additionally, it should be observed that the diffraction-limited spot size of a focused laser is most closely approximated by a TEM_{00} mode laser and is given by
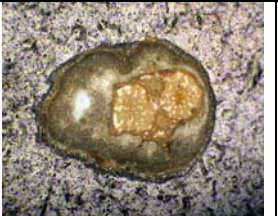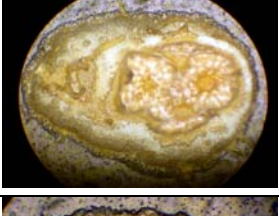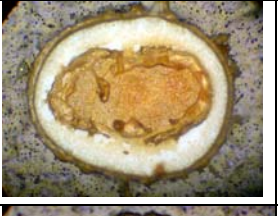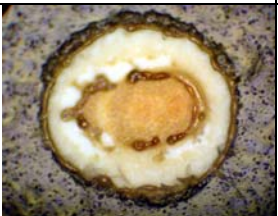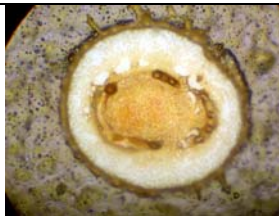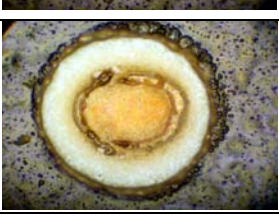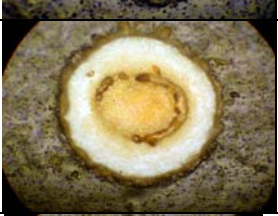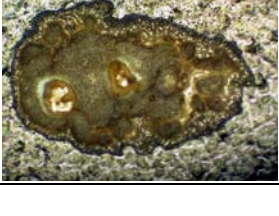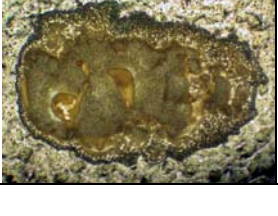
$$\omega_{lens}^{diff} = \frac{\lambda\, F}{\pi\, \omega_{lens}} \quad . \tag{410}$$

Inspection of Eqs 409 and 410, and observation that by installing an aperture within the resonator cavity leads to reduction in the diameter of the laser beam, indicates that the nearly TEM_{00} mode should be the preferred mode of laser operation in microdrilling.

Studying some preliminary results of drilled holes we have noticed that the hole shape is not round like supposed to look for the Gaussian type of the laser beam. There were some disturbances around hole, and the hole was not round. Then I learned that drilled hole was by mistake processed not the beam minimum focal spot. That knowledge triggered the new series of tests performed by scanning the beam in *z*-direction, i.e., axially with the beam, are summarized in Table 7.

Table 7. Typical burn patterns produced by laser: a) paper was above the laser's beam waist, and b) paper was below laser's beam waist.

	Distance from z=0	Above waist, POSITIVE value	Above waist, POSITIVE value	Below waist-NEGATIVE value
Min 12,28	739.2	N/A		
11,13, 27	646.8			

10,14, 26	554.4			
9, 15, 25	462			
8, 16, 24	369.6			
7, 17, 23	277.2			
6, 18, 22	184.8			
5, 19 ,21	92.4			
20	0			
Max 29,30	-831.6			

Taking an average diameter of burned spots showed in Table 7, a function of laser beam

burned spot diameter with respect to focal position was built and illustrated in Fig. 4.21.
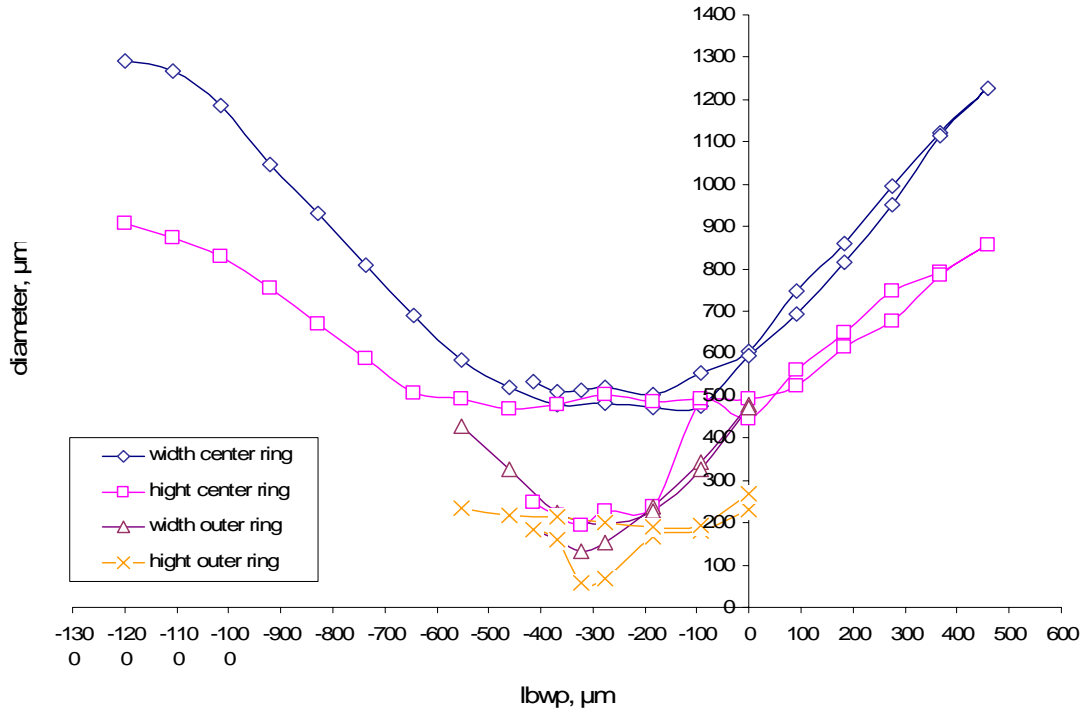
Fig. 4.21. Analyzing the spatial beam distribution using black burn paper and as a result
determining minimum beam waist position.

The burned patterns showed in Table 7 are 2D representation of a spatial laser

beam characteristic. In order to compare it to 3D spatial laser beam characteristic raster

scan of a laser beam was performed again (Fig. 4.11) at this same particular focal

position of the beam and comparison is presented in Fig. 4.22, which is 3D graphical

representation of 2D burn paper next to the graph.

a)   b)
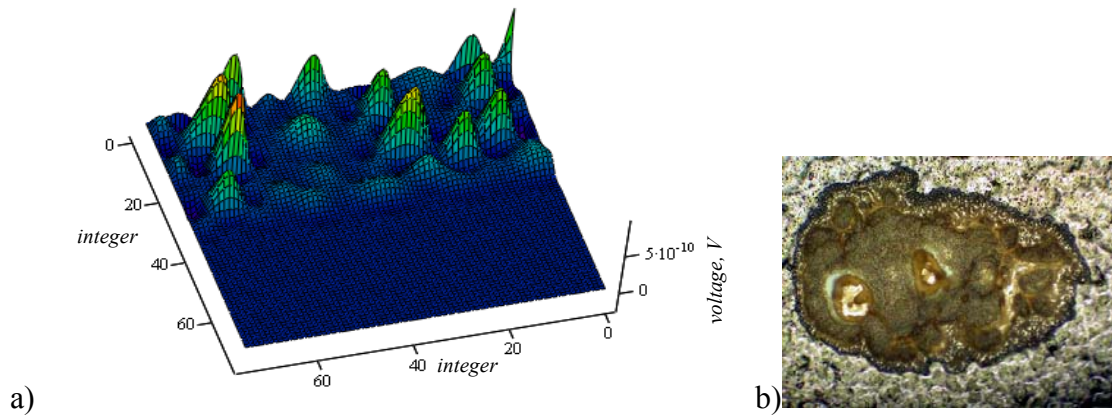
Fig. 4.22. 3D and 2D laser beam representation of a spatial laser beam distribution: a) obtaned by scaning the beam with the photo detector, b) black paper burn of this same beam at this same focal location of the focusing lens (about 831.6 μm).

4.2.5. Stability of laser beam distribution

For the purpose of controlling the process results and for the knowledge of the repeatability it is necessary to determine stability of the laser output. For the laser operating in multimode, such a measure of laser stability would not be practical due to the random nature of laser output. Since the majority of work performed in this Dissertation was done using one pulse, Gaussian type of laser, the investigation of laser stability was conducted in an approximate fashion by considering variation of the peak value of the average beam irradiance as a function of a series of single pulses fired by the laser in a sequential manner.

The setup for measurement of the laser stability was identical to the setup for determination of temporal laser beam distribution, Fig. 4.11. Results shown in Fig. 4.23, indicate that the laser system is very stable. At the beginning, after the laser system was

turn on, some small fluctuations were observed for the first few pulses. In order to set

some standard for measurements of laser's performance for this Dissertation, it was

decided to consider the output of the laser after initial warm up of the system, and after

few trial pulses, next pulse was considered as typical and considered stable. Function

illustrated in Fig. 4.23 is a function of laser irradiance versus voltage applied to the flash

lamp. As illustrated, the maximum variation of the first two peak pulse irradiance of the

beam was no greater than 5% of the maximum-recorded value.
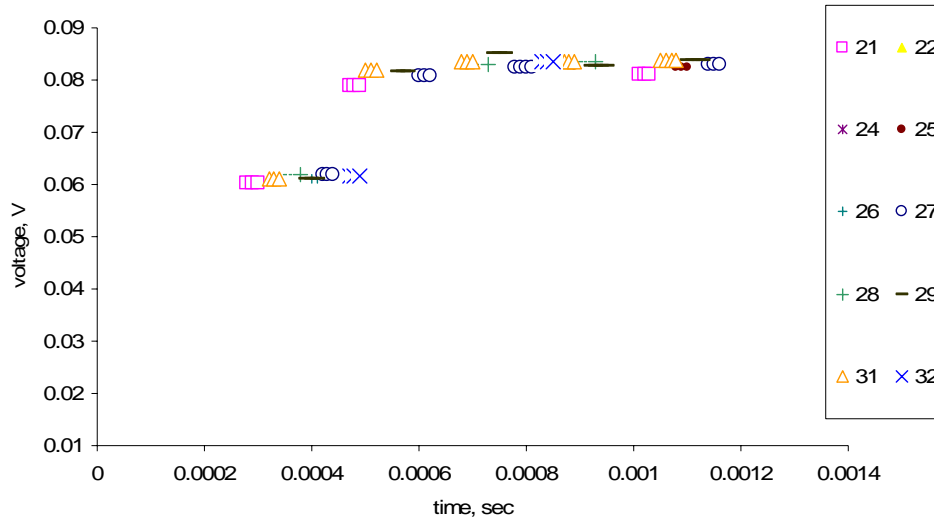
Fig. 4.23. Stablity of the Nd:YAG laser beam.

4.3. Experimental investigations of laser microdrilling

This part of experimental portion of this Dissertation deals with a study of

important parameters in the control of laser microdrilling process. In laser microdrilling,

the basic quantities like the drilling rate, the amount of vaporized material, the hole

diameter, or heat affected zone, can be directly measured very accurately, but the difficult part is to describe the laser beam interaction inside the hole and the hole profile.

Laser microdrilling is already an established method for production of high precision features like via formation, especially in microelectronics industry (Han and Pryputniewicz, 2003a, 2003b). Although holes have been made in this Dissertation, e.g., Fig. 4.24, they are not "perfect". To improve quality of the laser micromachined holes, the following issues should be addressed and resolved:

1. Recast layers causing cracks;

2. Taper of the drilled hole may be too large;

3. The shape of the hole is not satisfactory;

4. High aspect ratio is difficult to reach;

5. Coatings around the hole tend to chip off;

6. Redeposition around the hole needs post processing.
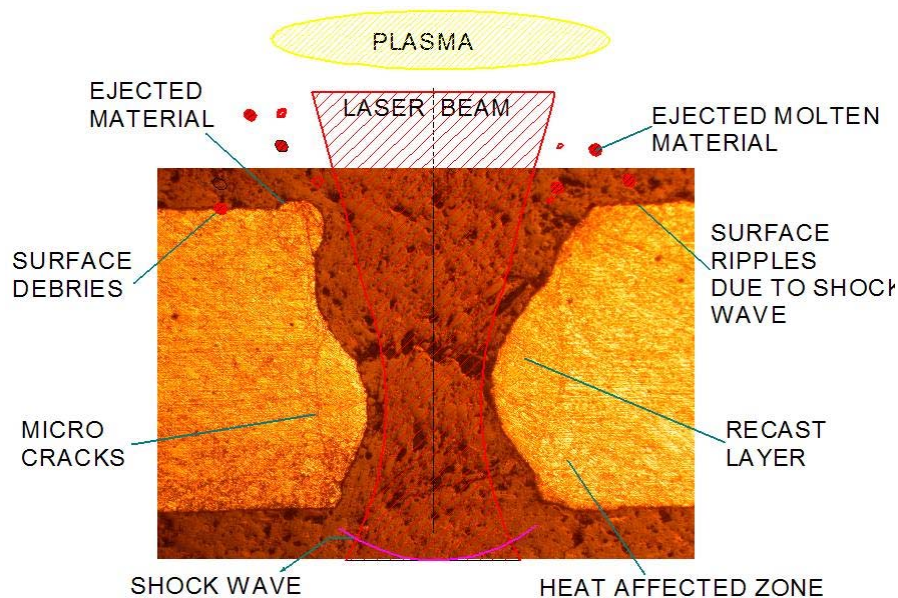
Fig. 4.24. Schematic of laser drilled hole profile.

337

In general, laser drilling is governed by energy balance between the irradiated laser energy and the conduction heat into the workpiece, the energy losses to the environment, and energy required for phase changes in the workpiece.

Experiments were conducted as a part of this Dissertation in the CHSLT laboratories at the room temperature without any shielding gas with the Nd:YAG laser system, Fig. 4.1, to validate effects of these characteristics. Particular attention was directed to the case of drilling two different material 304 stainless steel and singles crystal silicon. Thickness of the first material was about 0.762 mm, and the second one, silicon about 0.300 mm. The setup used for microdrilling process of samples is illustrated in Fig. 4.25, which also shows the samples were held horizontally in the fixture attached to 3D *x-y-z* positioning table with positioning accuracy 0.0003 mm. The resulting samples of laser drilled holes consisted of a series of rows of holes in each workpiece considered.

Parameters that were adjusted during performing the microdrilling operations included lens focal length, position of the laser beam focal point, laser energy, laser pulse width, and frequency of the laser beam per hole. Results of those experiments and a discussion of their correlation with exact and approximate solutions are presented in Chapter 5.
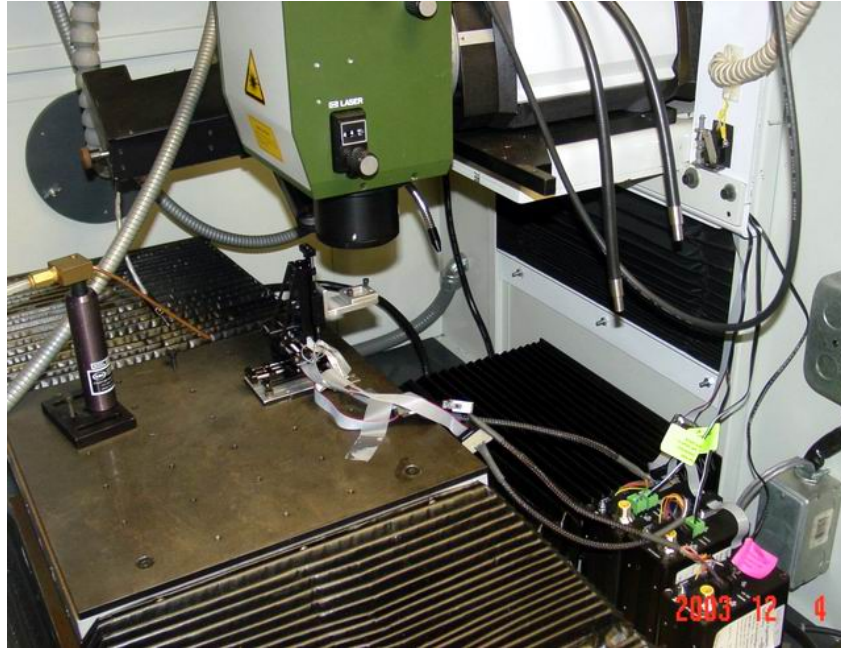
Fig. 4.25. Laser setup for microdrilling.

4.3.1. Coupling of laser energy with the target material

The laser beam intensity absorption and redistribution inside the hole can be measured only indirectly as part of many interacting phenomena such as: fluid motion, hole instabilities, plasma formation, and multiple reflections on the hole wall. It has been proven as a part of research for this Dissertation that laser beam characteristics (spatial and temporal intensity distribution) as well as the variation of material properties influence shape of the hole.

When laser beam strikes on the target material, part of the energy is reflected and part of it is absorbed. The absorbed energy heats up the target materials. This absorption and reflection have a resonant feature due to the microstructures of materials. When laser

beam acts on the material, laser energy is first absorbed by free electrons. The absorbed

energy propagates through the electron subsystem and then is transferred to the lattice. In

this way laser energy is transferred to the ambient target material. This process has a

resonant feature because materials show different absorptions to lasers with different

wavelengths (Han, 1999). This dependence of absorption on wavelength is determined

by the microstructure and EM properties of the material. When the laser intensity is

rather low, no phase transition occurs and the only effect of laser absorption is heating of

the material. In metals the laser radiation is absorbed by "free electrons", and the energy

transfer in metals is also due to electron heat conduction.

In many practical cases, the Drude-Zener theory provides description of optical

properties of material whose optical absorption is mainly due to free electrons

(Nowakowski and Pryputniewicz, 2004). Solid and liquid metals are typical examples of

such materials. In case of machining applications of a partially absorbing medium

Lambert law can be applied. Utilizing Eq. 406 and introducing the exponential decay

yielding at a distance z below the irradiated surface, we obtain

$$Q(\xi,\psi,z,\tau) = \frac{A \cdot \mu \cdot \Delta E_{pulse} \cdot I_R(\xi,\psi) \sum_{i=0}^{n} a_i \tau^i}{e_{cc} \omega_0^{\ 2} \left[1 + \left(\frac{z \pm z_f}{2 \cdot \omega_0 \ F/D_o} \right)^2 \right] \cdot t_p \ I_A \sum_{i=0}^{n} \frac{a_i}{i+1}} e^{-\mu \cdot z} \quad , \qquad (411)$$

where μ is the exponential absorption coefficient for the given material (Nowakowski et

al., 2005) is defined by Eq. 375. Combining Eq. 411 with Eq. 375 the final definition of

the absorbed laser energy by the material is

$$Q(\xi,\psi,z,\tau) = \cfrac{\left[A\,\mu_{final} + \dfrac{\mu_{initial}}{k+2}\exp\left(-\dfrac{k}{2}\right)\right]\left(1-\dfrac{T(x,y,z,t)}{T_c}\right)^2 \Delta E_{pulse} \cdot I_R(\xi,\psi)\sum\limits_{i=0}^{n} a_i\tau^i}{e_{cc}\,\omega_0^2\left[1+\left(\dfrac{z\pm z_f}{2\cdot\omega_0\ F/D_o}\right)^2\right]\cdot t_p\ I_A\sum\limits_{i=0}^{n}\dfrac{a_j}{i+1}} \times$$

$$\times\ \exp\left[\left(-\mu_{final}+\dfrac{\mu_{initial}}{k+2}\exp\left(-\dfrac{k}{2}\right)\right)\left(1-\dfrac{T(x,y,z,t)}{T_c}\right)^2 z\right], \qquad (412)$$

4.3.2. Material removal tests

In laser microdrilling, material is removed as a mixture of melt and vapor, Fig. 4.24. The proportions between the melt and the vapor depend on material properties and laser beam intensity. Large amount of removed materials is advantageous from drilling efficiency point of view, but on the other hand can create more instability in the hole formation. The thicker the layer of melt, the less is defined the surface geometry, the more the hole geometry fluctuates. The thickness of a layer molten during a laser pulse interaction with metals is approximated by Eq. 143, where δ is molten layer thickness, and t_p is pulse duration (>10ps to be valid). Analyzing Eq. 143 the best way to increase drilling accuracy is by simply shortening the molten layer thickness by shortening the laser pulse time.

The molten material is ejected from the hole by the pressure gradient developed during the vaporization of the portion of the material. As a result, more mass is removed compared to vaporization alone. The thermal balance model addresses this concept directly in the heat transfer equations. Since the ejected material has to leave in molten

form, our assessments account for all material ejected to leave when localized drilling zone reaches the fully molten state.

Experiments were conducted as a part of research for this Dissertation in the CHSLT laboratories at the room temperature without any shielding gas. The targets were 0.762 mm thick stainless steel plates mounted perpendicular to laser beam direction. For drilling process of above materials Nd:YAG laser was used, Fig. 4.1. Laser wavelength is 1064 nm, pulse duration was varied from 0.1 to 2.5 ms. Different energy levels were used to explore the optimum conditions for Nd:YAG laser drilling (Han et al., 2004).

With the thermal balance analytically assessed, actual material removal tests were performed. These tests considered interaction of 1064 nm wavelength energy with samples of 304 stainless steel. The laser parameters and optical transmission equipment is shown schematically in Fig. 4.26. Expulsion considerations were also of principal interest to the model. In efforts to gather information on the amount of material removed, an expulsion collection scheme was put together. This plan was to measure and weight all samples before and after the laser drilling was perfumed, consolidated a large portion of the material removed in the molten state into the glass tubes and allowed us to directly measure it. Presence of metal vapor and tiny metal droplets on the wall of the glass tube are shown in Fig. 4.27. Several droplets can be seen on this macrograph. Clearly, mass loss is contributed by vaporization of alloying elements and the ejection of metal droplets. Comparing amount of vaporized and ejected material, and examining the whole volume of the drilled hole in the sample we noticed that the volume increased with the increase of energy delivered to the sample. Drilling tests on 304 stainless steel have

342

followed linear correlation between material removal and input pulse energy as illustrated in Fig. 4.28. With this as a basis, a thermal model with physical and optical material characteristics and with measured laser beam spatial and temporal characteristics was build.
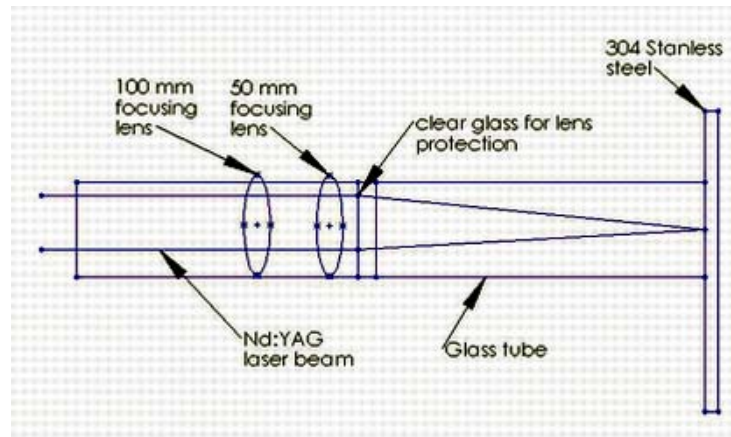
Fig. 4.26. Laboratory setup used during laser drilling of 304 stainless steel samples.

Due to limitations in the collection scheme, it will be difficult to support the trend of expelled material decreasing linearly with increasing pulse energy due to the fact that this were just preliminary tests and there are more tests required to fully illustrate the occurring phenomenon. In the scheme of the test of measuring at the entrance, exit, and mean diameters of the drilled holes, one can calculate average volume of the holes and mass of that material and compare results with numerical and experimental data.
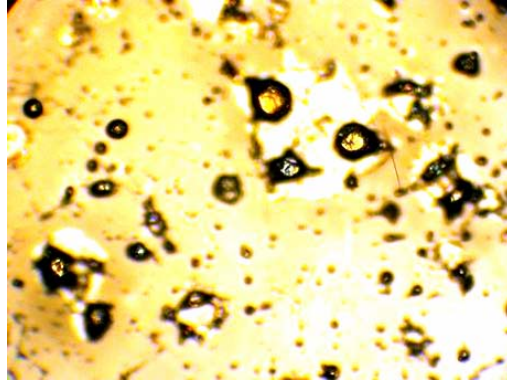
Fig. 4.27. Particles of 304 stainless steel ejected from the drilled hole, where open glass
tube placed co-axial with the laser beam during microdrilling process.
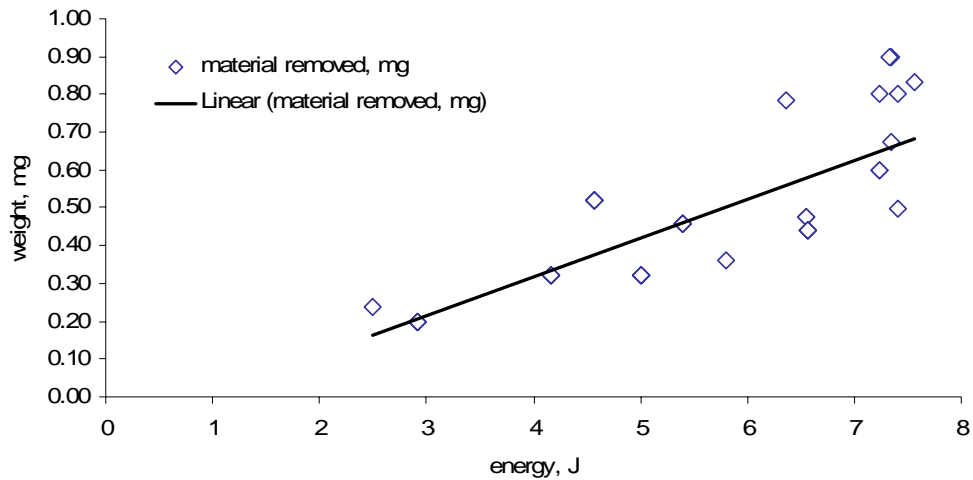
Fig. 4.28. Material removed during laser drilling of 304 stainless steel samples.

Considering the reflectivity and expulsion parameters the original thermal balance
equation was modified. The first order approximation used in this analysis transformed
Eq. 111 into

$$(1-R)Q_{total} = Mt \cdot c_p \cdot (T_m - T_a) + Mt \cdot H_f +$$
$$+ (1 - M_{exp})Mt \cdot c_p \cdot (T_v - T_m) + (1 - M_{exp})Mt \cdot H_v \quad , \tag{413}$$

where R is the reflectivity and M_{exp} is the expulsion fraction of material removed. With a
thermal balance analytically assessed actual material removal tests were performed.

344

A control-volume based on the computational approach was developed to solve the governing relation given by Eq. 142. Using the enthalpy method to deal with the phase change problem, while solving Eq. 142, a 3D model and a computer program was built to simulate the drilling process.

In the calculations of the temperature profiles in the material several conditions have to be taken into account: (i) the surface is moving due to evaporation of material, (ii) the heat of fusion creates a moving boundary, (Stefan problem), (iii) the liquid material loses its metallic properties above the critical temperature. Then the liquid metal exhibits dielectric behavior and becomes transparent. At the critical temperature (about 1.4 times T_v) material absorptivity approaches zero, which implies that there cannot be any laser absorption in the superheated layer; all of the absorption is concentrated in a small region where the temperature is just below the critical temperature T_c. Material is removed at the top of the dielectric layer by evaporation. At the sidewalls material is forced away by the plasma pressure on the liquid while at the end of the pulse, when the pressure suddenly drops, material is removed by the boiling of superheated liquid.

4.3.3. Investigation of laser microdrilling using high speed filming

In Section 2.6, plasma formation was described and in Section 2.7.1.3 we defined theoretically velocity of liquid ejection as well as the velocity of vaporization. Although data are available and quoted in Fig. 2.42 and Fig. 2.43, but to verify those data and to

345

study more thoroughly laser microdrilling process a high speed CCD camera was employed, Fig. 4.29.

A question is in which state the material is removed mainly. In Section 4.3.2, where we calculated how much of the removed material from the hole was being removed by vaporization vs. how much of it was being expelled in form of a liquid. Hopefully experiments with fast rate photography method, will shine on us some more light into the "dark tunnel" which is expulsion of a molten material problem during laser microdrilling.

A Pixelling 6.6 MByte CCD camera, Fig. 4.29a, with maximum frame rates of 18,000 frames per second was used for preliminary study of measurements of expulsion velocity and to study plasma formation. The camera was installed, Fig. 4.29b, orthogonally to the laser beam, which was impinging vertically on the workpiece. The drilling events were captured using the highest frame rate of 18,000 fps with known dimensions of viewing area. The target was illuminated with He:Ne laser beam for ease of targeting the small area of interest on the workpiece. The laser pulse length, coming through attached fiber optic cable, varied between 0.8 to 10 ms, with focusing spot of 0.300 mm. Workpiece material used was 304 stainless steel with thickness of about 0.762 mm.

Fig. 4.29. CCD camera used in the experiments.

The laser microdrilling process can be described in the following stages: a) the material is being removed as a mixture of melt and vapor in conical shape fashion, Fig. 4.30a, and Fig. 4.30b, driven by the vapor pressure inside the hole, than the plasma is being formed, then in the next stage random droplets of melted material are being seen, leaving the hole. The last stage occurs at the end of the pulse, when the pressure suddenly drops and massive evaporation takes place.
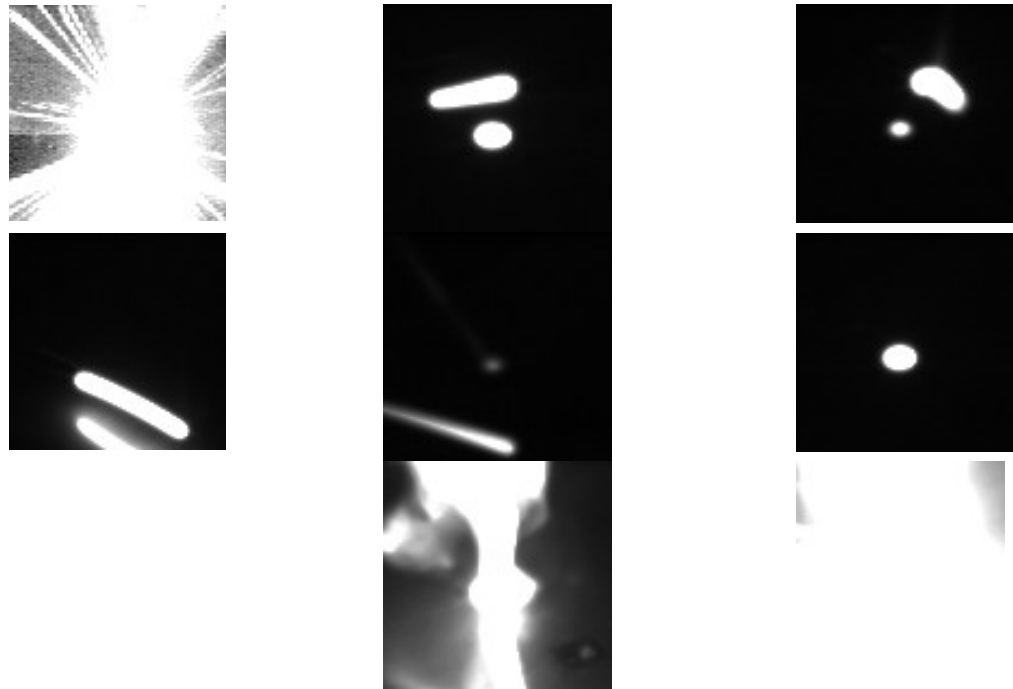
a)
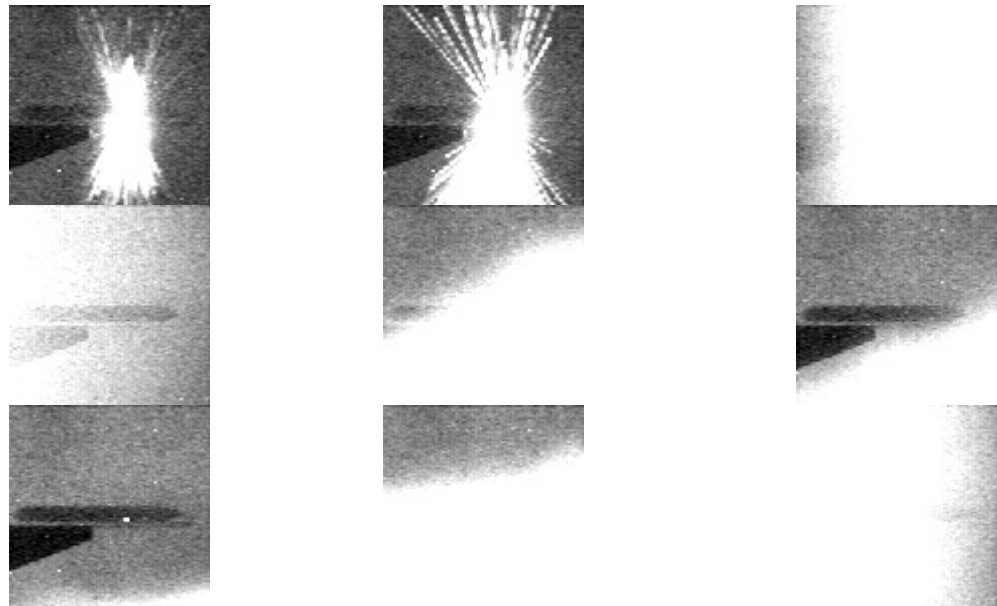
b)

Fig. 4.30. Sequential frames from filming of laser microdrilling process: vaporization and liquid ejection process, plasma formation, random particles ejection and vaporization, spontaneous vaporization at the end of the pulse for two different pulses:
a) $t_p=3.5$ ms, b) $t_p=4.5$ ms.

The velocity of the melt within the conical sheet was estimated from the high speed filming to be in the range 20-35 m/s. The single droplets were moving at a slower rate, estimated to be in range 5-17 m/s.

4.3.4. Experimental examples of the laser microdrilling

One of the goals of this work is to identify the primary cause of hole geometry variations by understanding of the effects of laser parameters and the melt ejection process on hole repeatability.

Picture of a typical laser hole drilled in 304 stainless steel, Fig. 4.31, shows effects of strong fluid motion. Recast layers of the holes are clearly seen in Fig. 4.31b and Fig. 4.32b. For lower intensities (just above the drilling threshold) heat conduction and reflection losses are dominant. For higher intensities, effects such as beam defocusing in the vapor cloud or even induced air-breakdown severely degrade the drilling efficiency and reproducibility of the drilling process.

Typical laser drilled holes in silicon single crystal material is shown in Fig. 4.33. All tests were performed with interaction of a single laser pulse duration. The goal was to determine relationship between delivered laser energy to the sample and amount removed from it (by direct weight measurement and hole geometry approximations).
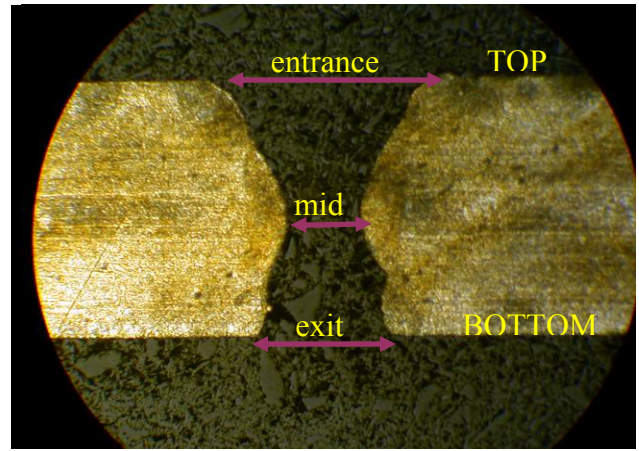
a)   b)

Fig. 4.31. Micrograph of typical shape and characteristic dimensions of the laser microdrilled hole cross section of hole profile in 760 μm thick 304 stainless steel obtained with pulsed laser beam transmitted through a single-mode fiber, pulse width t_p=1.9 ms, energy E=7.5 J, laser beam diameter $2\omega_0$=330 μm, and power P=4.2 kW: a) SEM image of the hole, entrance, b) cross section of the hole along z-axis.
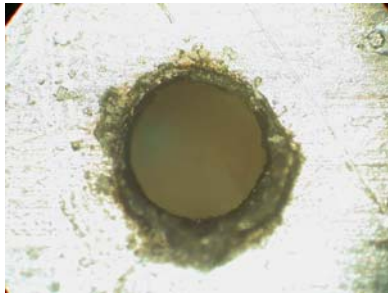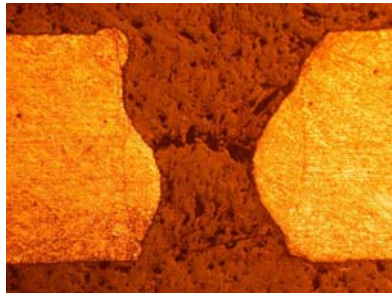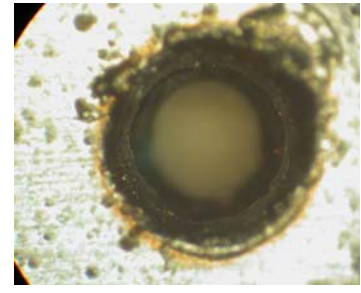
a)   b)   c)

Fig. 4.32. Micrographs of a typical hole profile drilled in 760 μm thick 304 stainless steel obtained with Nd:YAG pulsed laser beam transmitted through a single-mode fiber, pulse width t_p =1.8 ms, energy E=7 J, laser beam diameter $2\omega_0$ =300 μm, and power P=2.12 kW: (a) image of the exit of hole, (b) optical image of the cross section, (c) image of the entrance of hole.
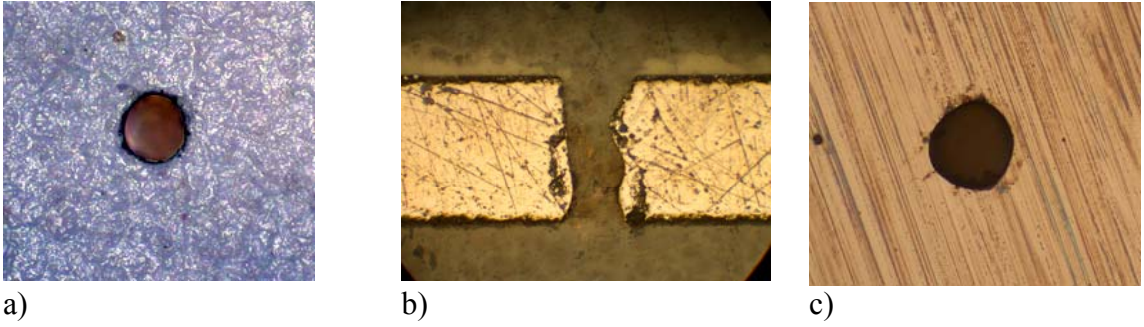
a)　　　　　　　　　　b)　　　　　　　　　　c)

Fig. 4.33. Micrographs of a typical hole profile drilled in 300 μm thick single crystal silicon obtained with single Nd:YAG pulse: pulse width t_p =0.5 ms, energy E=1.5 J, laser beam diameter $2\omega_0$ =58 μm: (a) image of the exit of the hole, (b) optical image of the cross section in axial direction, (c) image of the entrance of the hole.

More illustrations of microdrilled holes of 304 stainless steel and single crystal silicon can be found in Appendix B.

4.3.5. Effect of laser energy

The amount of laser energy required for laser microdrilling process depends on the optical and thermal properties of the workpiece material. When energy delivered to the workpiece exceeds the threshold energy, defined earlier, than the microdrilling process will occur.

In order to study the effect of laser energy on the resultant dimensions of the hole, continuously increased laser energy was applied to the samples ranging from 0.6 J to 5.7 J, with a constant pulse width of 0.8 ms, and the laser beam waist position (*lbwp*) was below the surface, i.e., the laser was focused 1/3 below the surface of the workpiece. Preliminary results are shown in Fig. 4.34 which shows that the power at the beam breakthrough (i.e., the onset of a through hole) was 2.1 J. For the hole entrance diameter,

at the top surface, designate as *entrance*, as the laser energy increased, *entrance* also increased. For the exit diameter, designate as *exit*, as the laser energy increased, *exit* also increased as the power increased from 2.1 J to 5.7 J. For the higher power densities the hole dimensions did not change much.
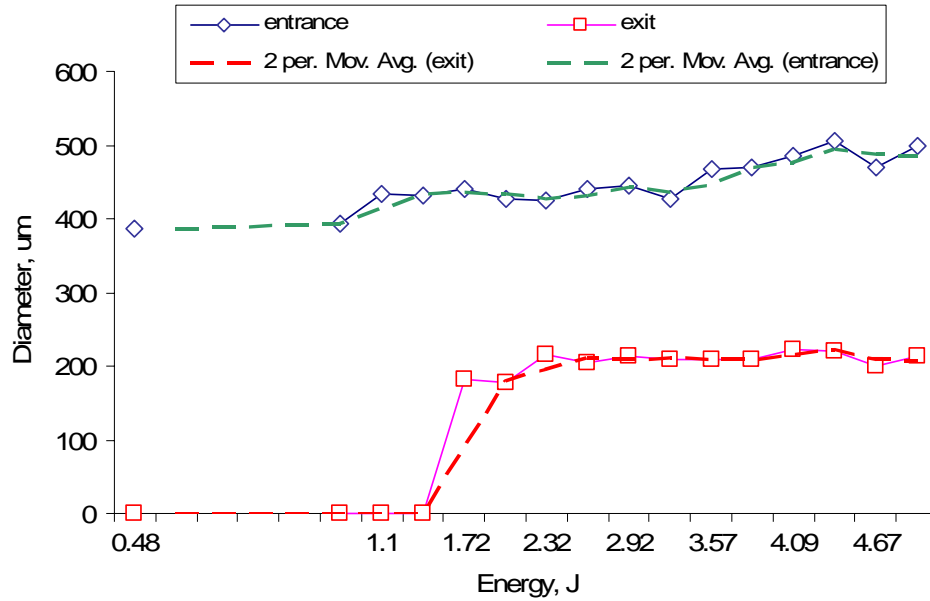
Fig. 4.34. Effect of laser energy on dimensions of laser drilled microholes in stainless steel 304 sheets: $N = 1$ and const voltage = 300V.

4.3.6. Effect of laser beam waist position (lbwp)

Position of the focal plane is known to have an effect on final shape of the hole as well as degree of penetration. As the laser focusing spot moves up and down, the laser material interaction varies too, Fig. 4.35.

The local beam radius as a function of depth, z, can be calculated using the following relationship (Zhao and DebRoy, 2003)

$$\omega(z) = n\omega_0 \left[1 + \left(\frac{z - z_W}{2 \cdot \omega_0 f / D} \right)^2 \right]^{\frac{1}{2}} , \qquad (414)$$

where ω_0 the laser beam radius at the beam waist position as is illustrated in Fig. 4.35.

The numerical values of Eq. 414 are represented graphically in Fig. 4.36. Focal plane

position, from now called laser beam waist position, lbwp, is negative when the focal

plane is above the workpiece and positive when it is below the surface of the workpiece,

because $z=0$, position is located at the top surface of the workpiece, Fig. 2.12.
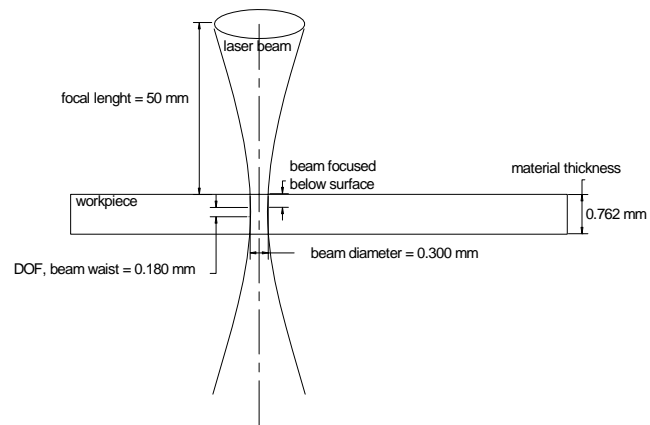
Fig. 4.35. The laser beam focused on the workpiece and cross section of the laser
penetrating the workpiece.
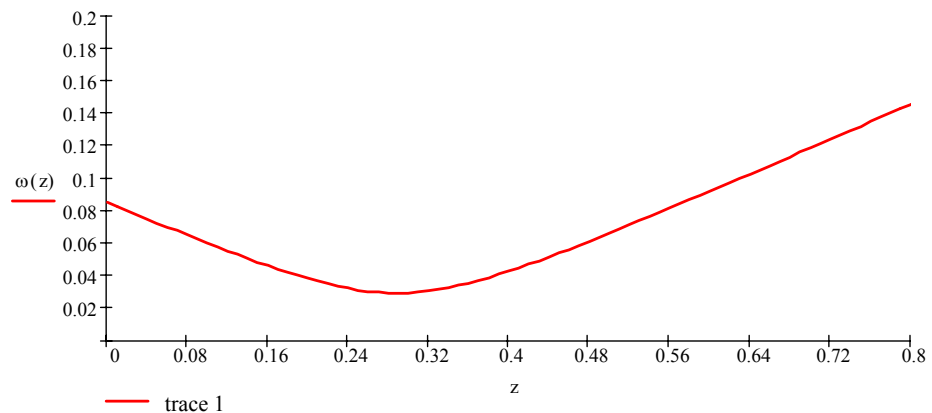
Fig. 4.36. Change of radius of the beam as position of focal plane with depth changes
with *z*, when *lbwp = 0.288 μm*.

Intensity of the laser beam at the material surface is one of the most important processing parameters in laser micromachining. The maximum irradiance of the laser beam (the most important parameter of laser micromachining) is obtained at the beam waist plane, Fig. 4.35. Beam waist of the laser beam or the depth of focus (DOF), defined in Eq. 10, is a distance over which the focused beam has approximately the same intensity, and is defined as a distance over which the focal spot size changes by 5%. For our Nd:YAG system manufacturer gives us value of 0.18 mm for DOF (Lasag, 1990). In macro scale this number can be considered small, and in this case lbwp can be considered as one plane (or a point). In microscale applications, is actually a function defined by Eq. 414, which is implemented by FDM in this Dissertation.

Looking closely at that problem, there are at least two reasons why a lens will not focus to a theoretical point; one is the diffraction limited problem discussed in Section 2.4.7.1, and the other is that a spherical lens is not a perfect shape. Lenses are made with more or less accuracy by different manufacturers. The more ideal spherical shape of the lens is the more expensive it gets. The other "lens faults" occur when mechanical and optical axis are not correctly aligned.

In some cases, spherical aberration was taken advantage of, and used in positive way Karnakis et al., 2005. They intentionally introduced more aberration in the system, Fig. 4.37 at first to correct the problem, later to obtain different shape of the beam, which increased efficiency of the laser drilling and in some cases quality of drilled holes.

Summarized factors that influence the size of the focal spot and *lbwp* are the imperfections of the optical components and diffraction effects, which limit the size of the obtainable focal spots.
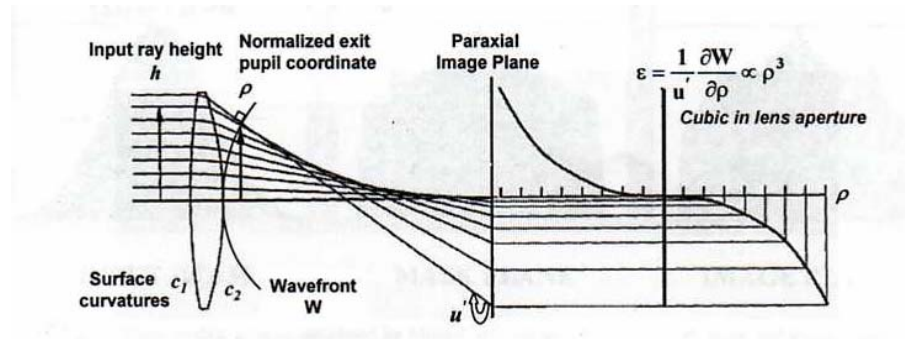
Fig. 4.37. Ray of beam tracing analysis describing spherical abberration
(Karnakis et al., 2005).

The reason that this was brought up is that knowledge is going to be helpful later in the discussion section of this Dissertation.

Next issue is directly related to the quality of the incoming beam, which can be quantified by the divergence of the beam. The smaller divergence the smaller spot size one can obtain. The diameter of the incoming laser beam affects the focal spot size. Focal spot size is influenced by diffraction.

Hole shape is a sensitive function of the position of the beam waist relative to the sample surface, Fig. 4.36. Let us define, that when the focal plane position, *lbwp*, is set on the workpiece top surface, than *lbwp* is considered to be zero.

In the experiments, the sample of stainless steel 304 sheet with the thickness of 0.762 mm was used, the *lbwp* was varied between +3.0 mm (above the workpiece surface) and -3.0 mm (below the workpiece surface) where the constant laser energy of

3.0 J, and 0.8 msec pulse width, and pulse frequency of 1 Hz was applied. The

characteristic dimensions of laser drilled microholes were measured designated as

follows: for the diameters of the laser beam at the TOP of the workpiece as D_entrance,

mid section of the hole as MID, and D_exit as the beam exits the workpiece, Fig. 4.31.

Holes were drilled using single pulses and a plano-convex lens was used with 50

mm focal length (note: there is a huge difference between a plano convex lens mounted

one way or the opposite way around).
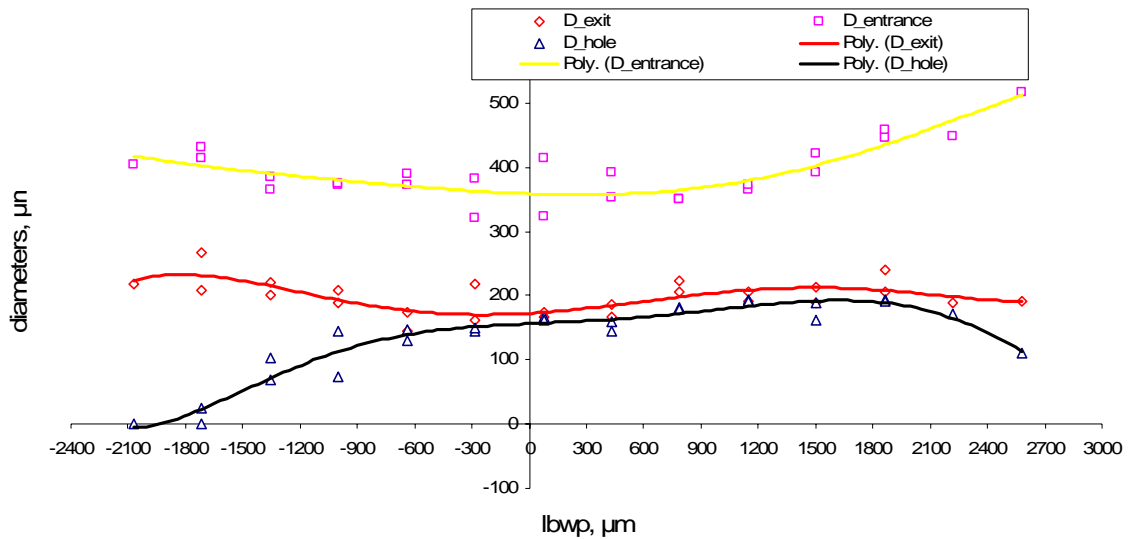
Fig. 4.38. Typical function of diameters of D_entrance, D_mid, and D_exit for various
lbwp, impinging on 304 stainless steel workpiece, one pulse, and energy *E=7.5 J*.
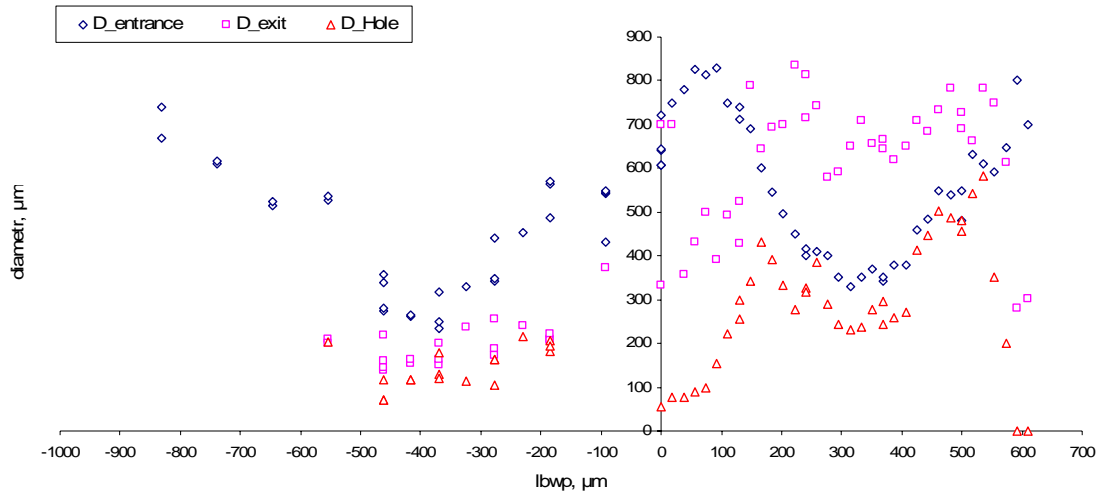
Fig. 4.39. Typical function of diameters of D_entrance, D_hole, and D_exit for various *lbwp*, impinging on single crystal silicon workpiece, one pulse, and energy *E=0.5 J.*

The laser beam waist position, *lbwp,* was moved vertically by constant amount of displacements, step in *z*-direction, ranging from 89 μm to 1,200 μm between holes. Laser drilling process was performed at every time step of *z*-micro-stage. After drilling process was accomplished, holes were measured (if any) and samples were cross-sectioned for further analysis, Fig. 4.40 and Fig. 4.41. Representative quantitative and qualitative results for cross-section measurements are shown in Fig. 4.42 and Fig. 4.44, for single crystal silicon and for stainless steel respectively.

Qualitatively, as the waist is moved away from the original surface in either direction, the spot size at that surface increases. Thus, at the start of drilling, material is removed over a larger area and at a slower rate due to the reduced intensity. Expended drilling an enlarged entrance, leaving less laser energy (or laser intensity) for deepening the hole.

When the waist is below the surface, experimental results are shown in Fig. 4.42, the spot size at the exposed surface, (after material is removed) decreases as drilling progresses deeper into material. This causes the hole to narrow relatively rapidly, so hole walls are not very steep. If *lbwp* is not too large, it also tends to produce narrow, rather pointed hole bottoms, Fig. 4.42a. Conversely, when *lbwp* is above the surface, the spot size at the exposed surface, increases steadily as drilling progresses inside the material. This tends to produce holes with relatively less steep walls and broad, rounded bottoms, Fig. 4.42a1-3. When the beam waist position lies above the workpiece surface, the beam represents a "smaller target" for the ejected matter.. The calculations found in literature show that the narrowest hole entrance occurs when the beam waist is at the workpiece's surface, because the smallest size of the laser beam has a contact directly with the material surface.

SET A, E=1.2 J

$\overline{100\ \mu m}$
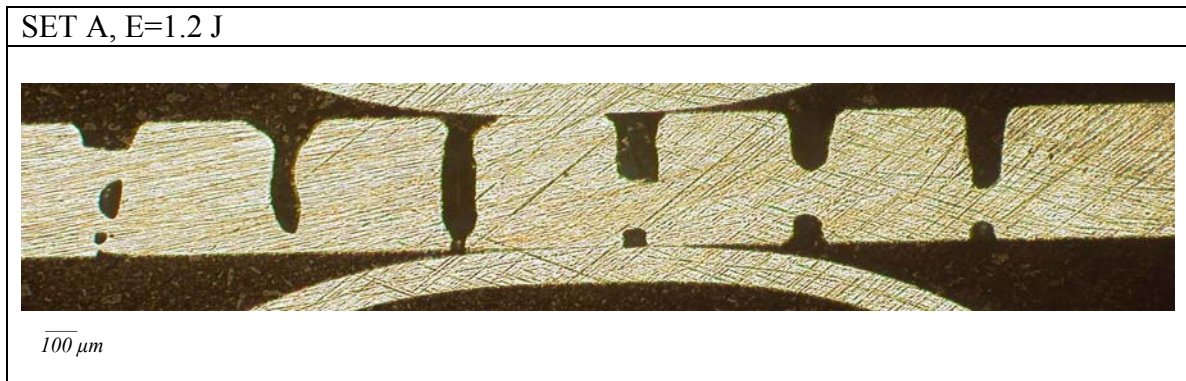
Fig. 4.40. Experimental results of microdrilling in 304 stainless steel workpiece. Effect of laser beam waist position on hole profiles. Holes were drilled with a beam diameter of 59 μm, 1.2 J energy. The waist was moved vertically by 89 μm between holes.

SET B, E=3 J
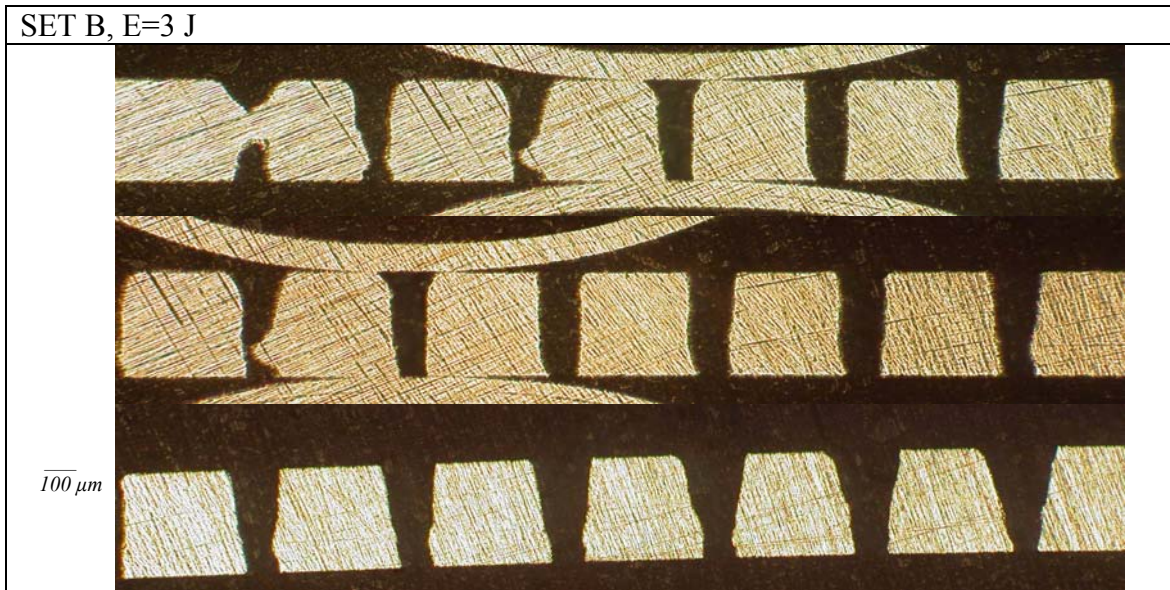
Fig. 4.41. Experimental results of microdrilling in 304 stainless steel workpiece. Effect of laser beam waist position on hole profiles. Holes were drilled with a beam diameter of 59 μm, 3.0 J energy. The waist was moved vertically by 89 μm between holes.

SET A

a) focused above the top surface | b) focused below the top surface
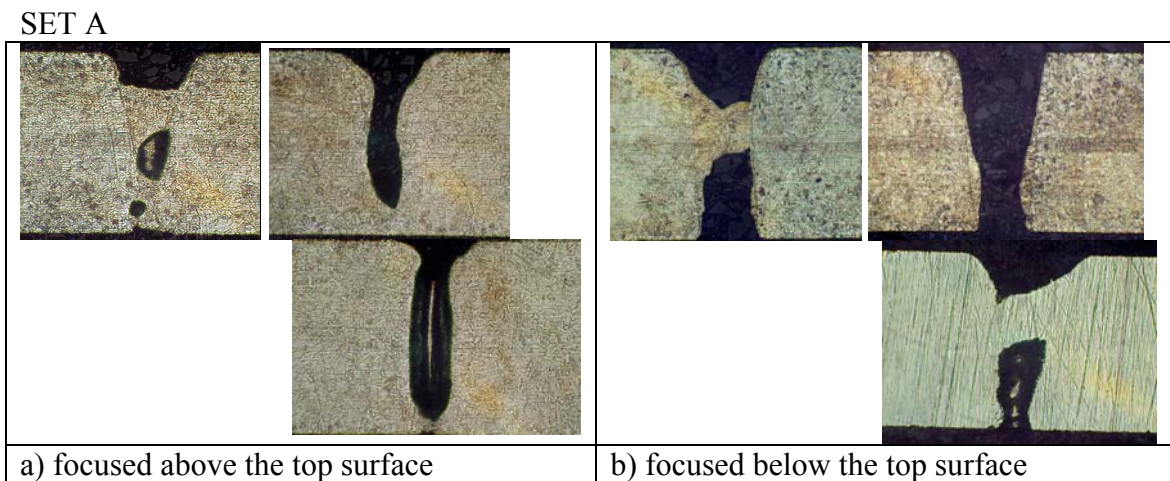
Fig. 4.42. Effect of laser beam waist position on experimental hole profiles drilled in 304 stainless steel. Holes were drilled with a 59 μm, 1.8 J pulse using the 50 mm lens. The waist was moved vertically by 89 μm between holes.

SET B

a) focused above the top surface	b) focused below the top surface

Fig. 4.43. Effect of laser beam waist position on experimental hole profiles drilled in 304 stainless steel. Holes were drilled with a 59 μm, 3.0 J pulse using the 50 mm lens. The waist was moved vertically by 189 μm between holes.
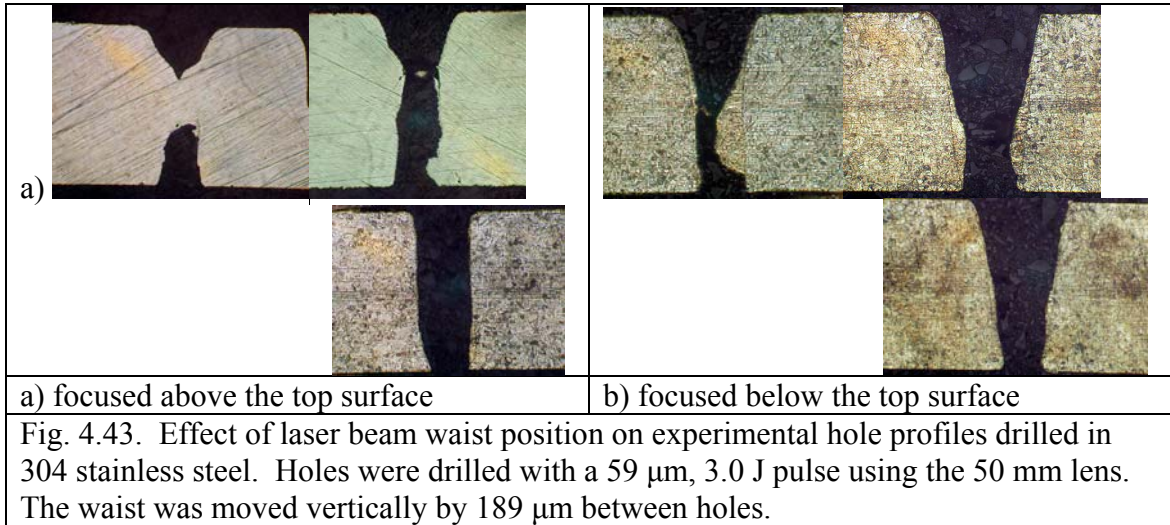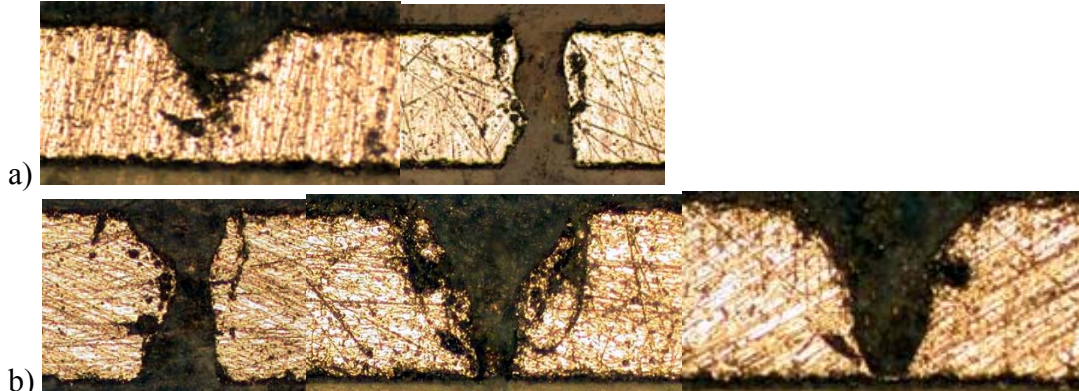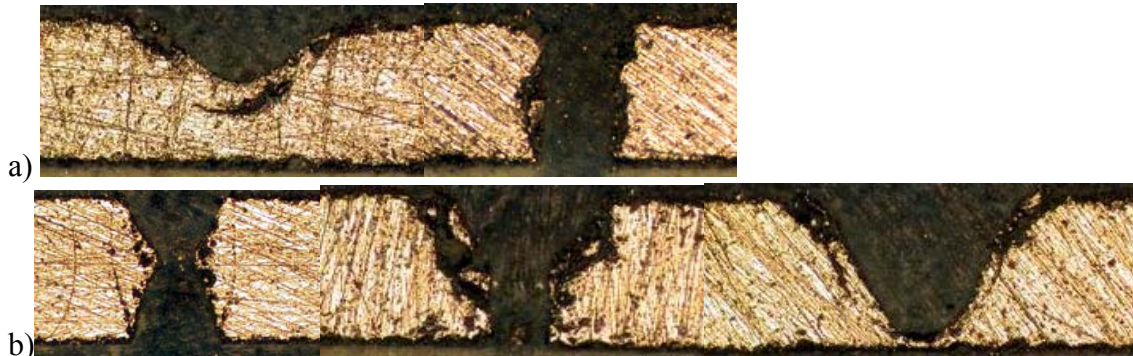
SET A

SET B

a) focused above the top surface   b) focused below the top surface

Fig. 4.44. Effect of laser beam waist position on experimental hole profiles drilled in single crystal silicon. Holes were drilled with a 59 μm diameter beam with 0.8 J (SET A) and 1.5 J (SETB) pulse using the 100 mm lens. The waist was moved vertically by 189 μm between holes.

5. Correlation between computational and experimental investigations

The model of the laser beam experimentally determines the shape through which the hole evolves, as beam propagates through the workpiece. Below there is summary of experimental results presented in previous chapters. Comparison of theoretically determined computer simulations of laser microdrilling with experimentally obtained ones is summarized in Fig. 5.1 to Fig. 5.4.

Despite limitations of the model mentioned above, determination of profiles of holes agreed well with the experimental data, although there are some regions of better agreement for example for intensities close to the threshold from liquid ejection. If intensity of laser beam is below threshold, then laser beam will not penetrate the workpiece through but only to a certain depth. Despite using a simple representation of beam aberration and treatment of the material being drilled, calculated hole profiles agree very closely with experimentally drilled holes. Most important is that the model correctly reproduces experimental changes in the hole size and shape with the beam waist position relative to the sample surface and beam divergence, which is illustrated in Fig. 5.1 to Fig. 5.4.
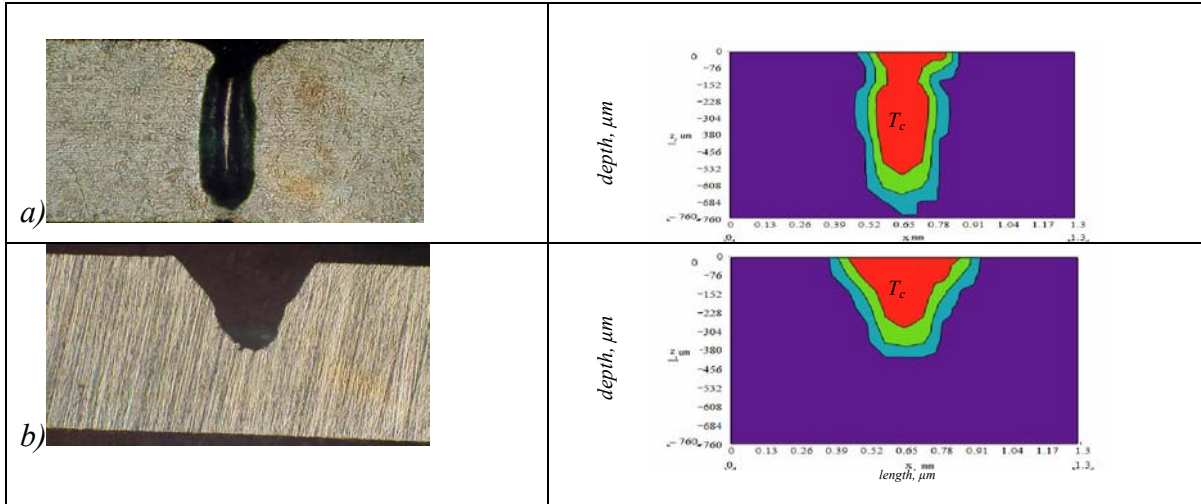
Fig. 5.1. Comparison of computer simulated results with experimental data of cross-sections of a microdrilled holes in 304 stainless steel material with a single pulse of Nd:YAG measured and focused above the top surface, a) *lbwp = 70 μm*, b) 189 *μm*.
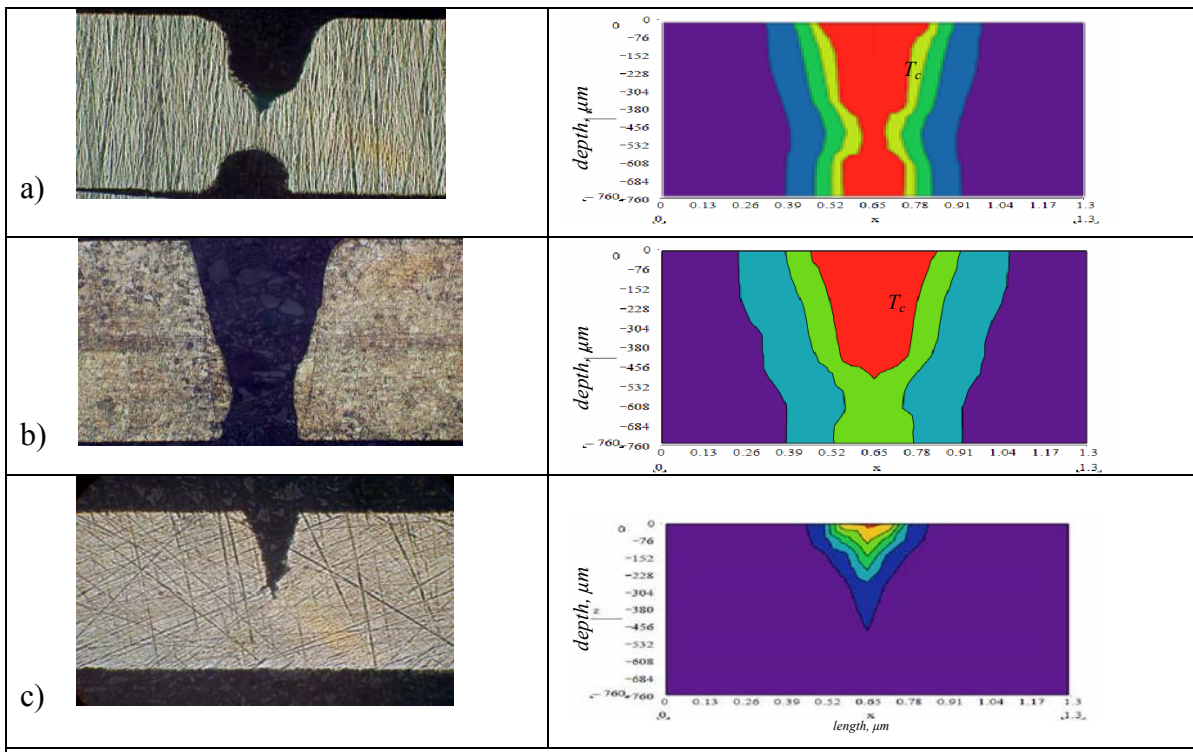
Fig. 5.2. Cross section of a micro machined sample of a 304 stainless steel material with a single pulse, *E=3.0 J*, focused to:a) z=500 μm below the top surface, b) *lbwp =700 μm*, c) 900 *μm*.
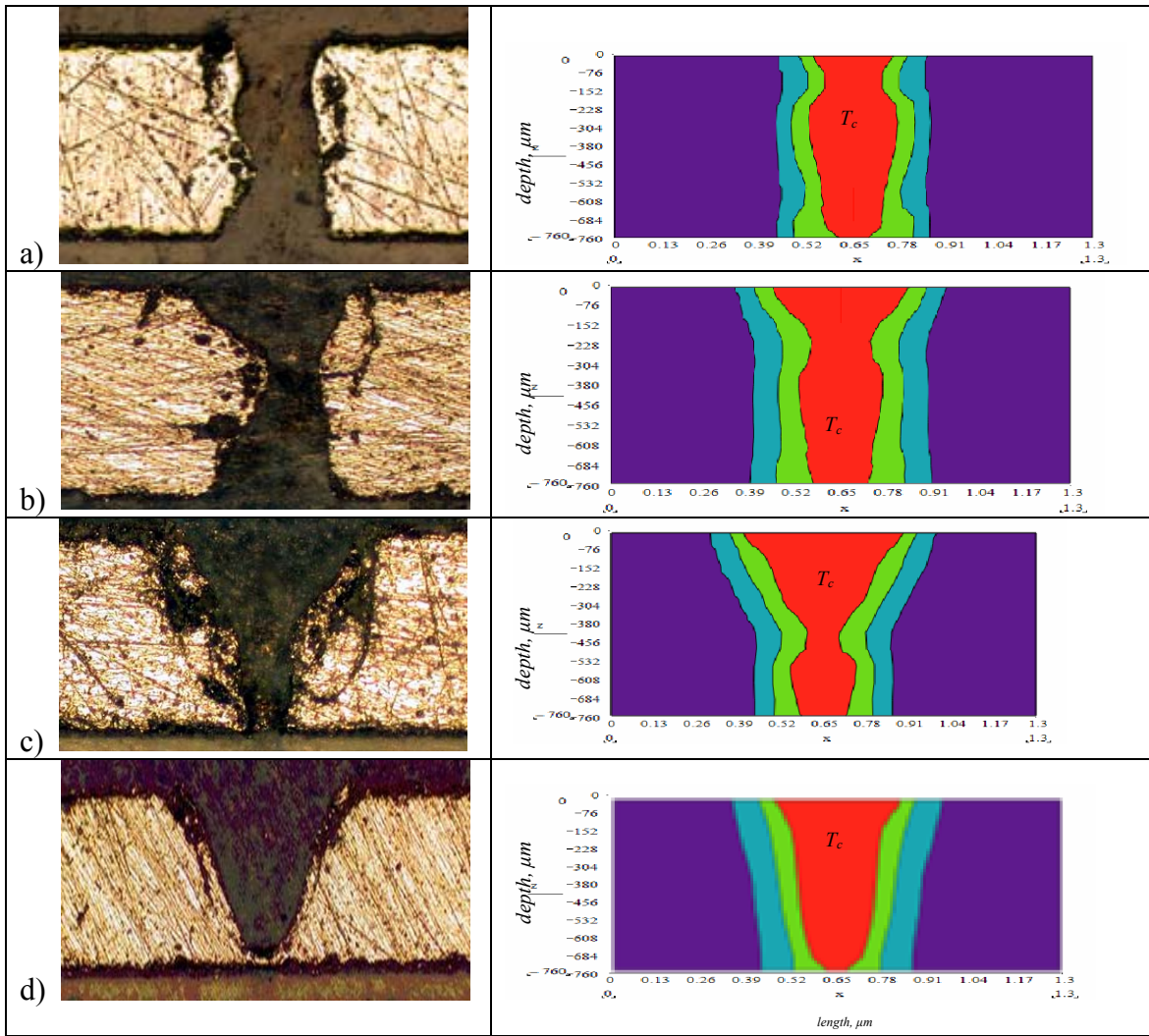
Fig. 5.3. Computer simulated cross section of a microdrilled sample of a single crystal silicon material with a single pulse of Nd:YAG measured laser beam focused below the top surface, a) *lbwp = 70 μm*, b) *lbwp = 300 μm*, c) 460 *μm*, d) 800 *μm*.
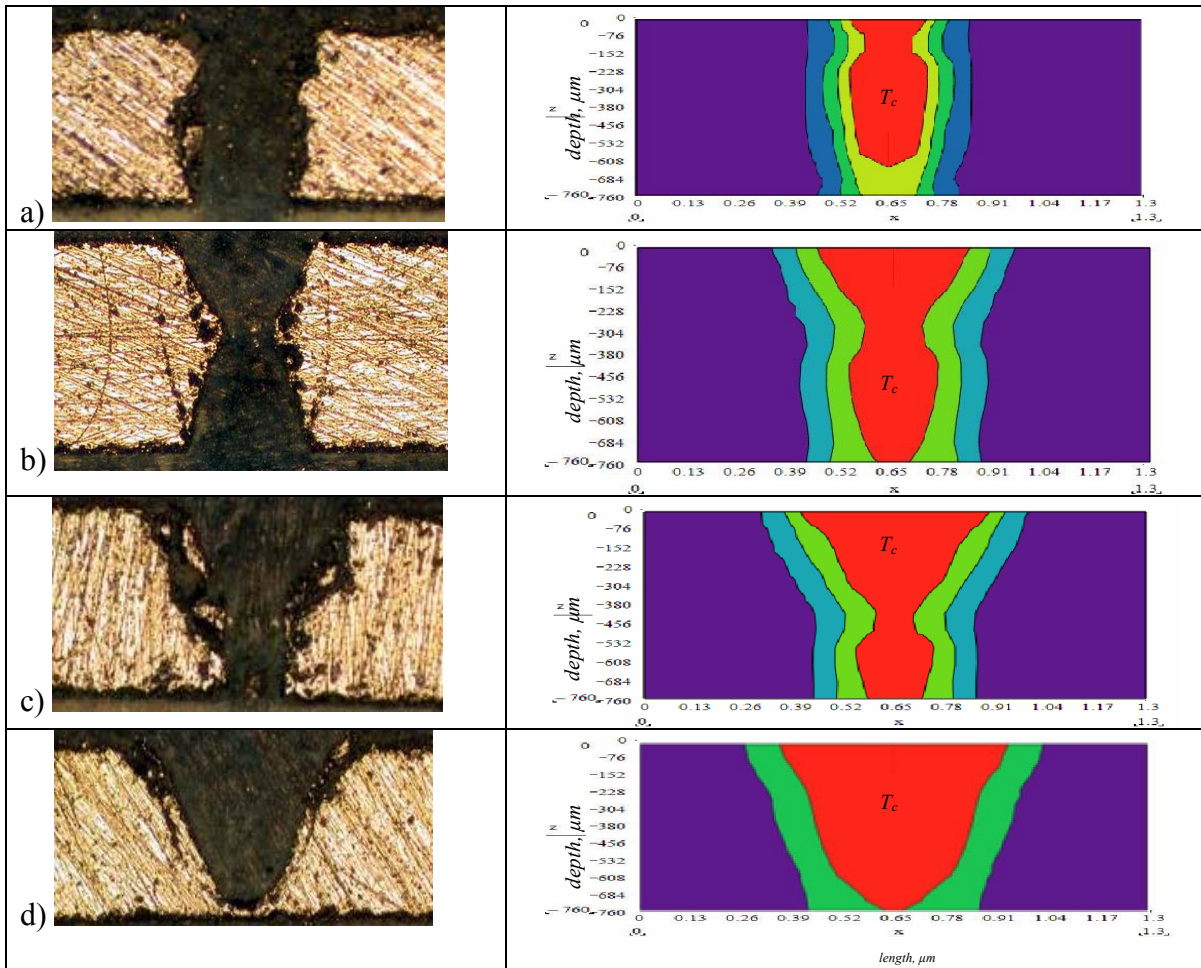
Fig. 5.4. Computer simulated cross section of a microdrilled sample of a single crystal silicon material with a single pulse of Nd:YAG measured laser beam focused below the top surface, a) *lbwp = -100 μm*, b) 300 *μm* , c) 400 *μm,* d) 700 *μm*.

5.1. Effect of critical temperature and absorption coefficient

In the area where the critical temperature is reached there is no more absorption of

the laser energy. Metallic material in this area becomes dielectric and transparent to the

beam. So the absorption is concentrating in the places just below the area with the

critical temperature. Material is being removed by evaporation at the top of dielectric

layer, and at the sidewalls material is being removed by the plasma pressure on the

364

existing liquid in the keyhole. At the end of the pulse, when the pressure suddenly drops, material is being removed by boiling of superheated liquid. As one can notice, to establish values for critical temperature is essential for predicting profile of the hole.

A good value for T_c is difficult to ascertain. First, because the silicon is a semitransparent material. The 304 stainless steel, on the other hand, is an alloy, comprised of a few metals each with a different properties. Meijer (2002) stated that "the value of the critical temperature T_c (of about 1.4 times the boiling temperature) is reached very fast and then remains constant". Other literature is giving different numbers for T_c, ranging from 4,000 to 9,000 K, determined experimentally (Beck et al., 1995; Bruggemann, 1996; Bulgakova and Bulgakov, 2001a; Christensen and Tillack, 2003, Craciun et al., 2002). Let us use two different numbers for T_c, run our computer program and determine how significant the value for T_c is. Results of this determination are shown in Fig. 5.5 and Fig. 5.6.
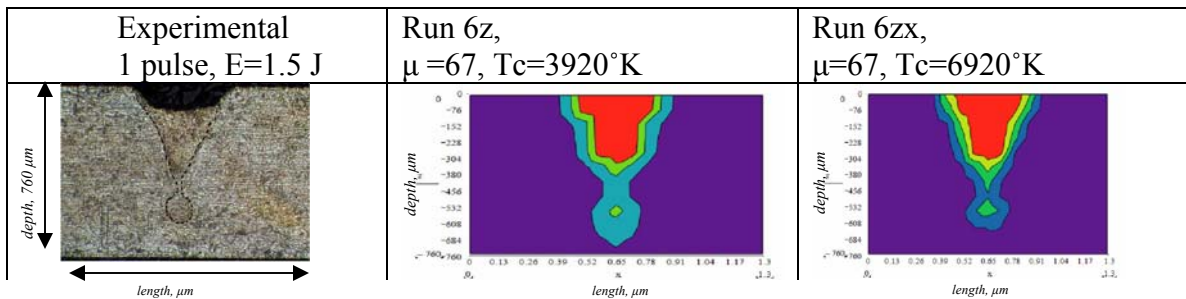
Fig. 5.5. Effect of critical temperature on the hole profile inside the 304 stainles steel with $T_c = 3920$°K and $T_c = 6700$°K.

Experimental 1 pulse, E=1.5 J	Run 6zr-800, μ =33.5, Tc=6920˚K	Run 6zv-800, μ=6.7, Tc=6920˚K
	6zt μ =67,Tc=6700˚K	Ssa, μ =70,Tc=6700˚K
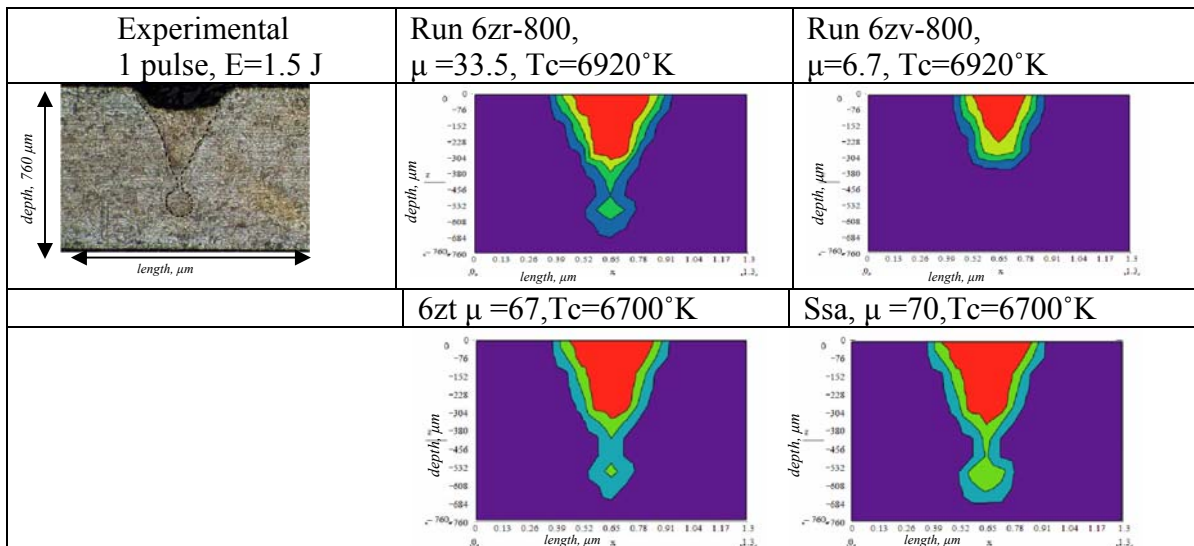
Fig. 5.6. Effect of absoption ceofficient μ, on the hole profile inside the 304 stainles steel
with μ = 6.7, μ=33.5, μ=67.0, μ=70, and T$_c$ = 6,700˚K.

In this Dissertation, the value for critical temperature was established based on
comparing the values from the literature and numerically obtained hole profile with the
experimental results. At the end of a few simulations, the value of critical temperature
obtained in this way was assumed to be 6,700˚K, and the absorption coefficient to be
70/mm. Please note that all other variables of the model were kept constant during
computer simulations.

Chapter 6 provides more conclusions based on quantitative and qualitative figures
presented herein.

6. Observations and recommendations

Laser microdrilling process shows material modifications around the hole which can be either of thermal (HAZ), mechanical (MAZ), or chemical (CAZ) nature. Depth, diameter, and amount of material damage as well as geometry depend on pulse energy, laser pulse characteristics, power density, and intensity distribution across the beam on the target and optics involved in the process.

Our FDM computer model is very broad and considers many issues, including: interfacing of the actual measured laser beam spatial and temporal distribution, Lambert-Beer's law of absorption of the laser light using Drude-Zener theory, temperature dependence of thermo-physical properties of the material under consideration and also accounts for expulsion of the melt ejection process during microdrilling process.

In spite of all of this, the model has some limitations. Model does not include however, workpiece related effects like light scattering in the sample, reflectivity of the hole wall, and abrasion of the hole wall by ejected material. The model also does not include the scattering and interruption of incoming laser beam by the material ejected from the hole.

In addition, the micromachining process depends on technical limitations like the pulse-to-pulse stability, as well as temporal development of the pulse, homogeneity of the material, and energy coupling into the material.

To control the microdrilling process it is essential to know the laser radiation reflectivity and location of the workpiece with respect to the focal plane of the optics used. Tilting and moving of the workpiece, movements of the melt by capillary force or

acoustic waves, and changes of the absorptivity during processing stimulates relaxation oscillations, laser beam mode instabilities or chaotic temporal behavior resulting in stochastic fluctuations of the spatial and temporal intensity distribution by optical feedback. Optical feedback is modulated by the lensing and absorption feature of laser modulated plasma (if present).

In conclusions we should mention that control of optical feedback is the main requirement for achieving reproducible processing with high repeatability and reliability. Consequently, a diagnostic of the laser beam must be performed on-line during processing, otherwise correlation between the laser parameters and the processing result will be uncertain.

For better understanding the microdrilling process time behavior of the material removal rate is essential. Most interesting to know is the drilling speed during the pulse and its dependence on the pulse power.

Analyzing a number of the experimental hole profiles (i.e., cross sections) we have observed that there is some re-melted or just melted material inside on the side wall of the hole.

Reading the articles of Basu and DebRoy (1992), in conclusions, they determined that when material is irradiated with single pulses, metal expulsion was observed only for larger values of pulse length. For multiple pulses, short pulses led to liquid metal expulsion only at high frequencies when the irradiated region could not cool sufficiently between pulses. It was established that the peak temperature must exceed the critical temperature for liquid metal expulsion to occur.

Basu and DebRoy (1992) also concluded by the observation that after the

expulsion of liquid metal commences, no residual liquid metal is observed in the cavity.

When the peak temperature at the center of the pool exceeds the critical temperature T_c

liquid expulsion takes place. When molten metal is expelled from the melt pool, the laser

beam gets defocused resulting in a decrease in the heat flux. As a result, the peak

temperature may drop below the critical value and no further expulsion may take place.

Thus, the extent of melting at the time when the critical temperature is reached

determines the amount of liquid metal expelled.

We had partially confirmed their statements in our fast filming experiments, but

additional experiments will have to be conducted (in the future) to fully understand why

and what type of re-melting occur on the wall of our experimental samples.

Examining Fig. 4.34 and Fig. C.2 it has been observed that while increasing

energy the hole diameter started to saturate. The reason for that is not yet clear.

Conditions necessary for initiation of liquid metal expulsion from laser-irradiated metals

were discussed in Section 2.7.1.2 and can be determined by balancing the vapor recoil

force with the surface tension force at the periphery of the liquid pool. Experimentally

observed velocities in liquid metal expulsion during laser irradiation of stainless steel

samples with single pulse were consistent with the calculated results. Intuitively

speaking, the amount of ejected material depends on the viscosity of the melt (which was

neglected in the calculations) and the thickness of the molten layer. This thickness is

proportional to the thermal diffusivity and to the temperature difference between

vaporization and melting of the material. The larger the viscosity of the molten layer, the

369

smaller amount of ejected material. From certain depth and upwards, a large amount of molten material deposits on the wall, Fig. 3.25, Fig. 4.31, Fig. 4.32, because it can not leave the hole anymore, and to remove the rest of the material on the wall the use of another pulse should be considered.

Experiments involving usage of a fast speed CCD camera, Section 4.3.3, confirmed results obtained in Section 4.3.2. In addition, experiments allowed us to determine and confirm our analytical calculations as well as already published results of velocity of expelled material during laser drilling process. In preliminary results, recession velocity of vaporization was determined to be on the range of 20-37 m/s, and velocity of ejected molten particles on the order of 3-6 m/s.

Optimizing the focal position is most important when welding with laser close to the minimum laser power. In this case, even small dislocations of the focal plane may interrupt the deep welding process.

It is apparent that in micromachining processes, as the energy flux reaches the threshold value, the ablation transitions from normal vaporization to some very aggressive mechanisms. This threshold depends on the material physical and thermal properties, the energy source, and the focusing parameters. If plasma is present then based on experimental data from the literature, plasma defocuses the beam and produces larger beam spot size then initial laser beam spot size before beam interacts with the material. Plasma acts like a lens, causing to defocus more and enlarge dimensions of the beam spot size.

The beam can also be broadened by diffraction due to beam truncation by the lens pupil. Value of this broadening of beam was calculated by Dickson (1970). Considering parameters of lenses used in the optics, size of the aperture, and input beam spot size used in experiments, the amount of diffraction will not be sufficient to cause much deviation from Gaussian beam shape alone, but together with the other effects of aberrations and plasma deformations plays significant role in the beam distortion. This fact is already considered in this Dissertation and mathematical model is compensated for it. In our FDM computer program model an artificial theoretical focusing correction factor, *fcf*, which can cause enlargement of the laser beam was introduced and assumed to be about 10 to 15 % (this value is based on the experimental evidence reported in literature by Beck et al. (1995) and Craciun et al. (2002). To confirm those data, more detailed study is recommended to determine the value for the focusing correction factor in the future work.

Experimental investigations show instability of the process. Since the plasma-affected focusing diameter depends on this temperature, it obviously also fluctuates during processing. Whenever the plasma temperature varies within the temperature range 6,000 to 22,000 K, the focus diameter can temporarily change even by a factor as large as eight. This might also be a cause for process instabilities. To increase process stability, therefore, the temperature-dependence of the focusing diameter should be suppressed as much as possible. This can be achieved by applying appropriate gas shielding to reduce the temperature-dependence of the optical properties of plasma. To avoid the temperature-dependence of the focus diameter, the lensing effect of the plume must not

be dependent on temperature; that is, the gradients of the refractive index in the radial direction have to remain constant within the plume.

Plasma defocusing and not plasma absorption, therefore, is assumed to be the main cause of the so-called 'plasma shielding' observed in laser micromachining.

Examining some of the silicon initial results obtained during the experimentation for this Dissertation indicate that, in the ablation process of silicon, a spalling was observed. It is occurring in brittle materials when the elastically stored energy allows unstable crack growth. There are two mechanisms distinguished: (i) spalling is due to an external force resulting from the ablation pressure, and (ii) it is due to internal force resulting from volumetric energy source. The latter mechanism is preferred in materials with low absorption coefficient, where a fraction of absorbing laser pulse is not absorbed in a thin surface layer, but within an extending volume. Consequently, thermal expansion of the material is causing high internal stress. This mechanism is strongly dependant of optical properties of the material and is recommended to be further studied in the future.

This concludes this chapter and now is a time for summarized conclusions and recommendations for future work, which follow in Chapters 7 and 8.

7. Conclusions

The objective of this Dissertation was to investigate and develop a better understanding of the fundamental processes during laser interaction with materials for microscale applications.

Study included analytical, computational, and experimental investigations of the interaction of a laser beam with oblique and opaque workpieces of finite size in dimensions. Then, a model was developed to optimize and better control the overall characteristics of the laser micromachining processes. Both qualitative and quantitative correlations of theoretical and experimental results were good with successful determination of the hole shape.

General models of the laser micromachining processes were developed based on the properties of the laser system, the workpiece, effects of melt expulsion, and the environmental conditions. Particular concentration in analysis was placed on laser energy description, including non-linear optical effect and physical laser beam characteristics and focal spot size considerations.

Energy transportations in multiple phases were investigated in detail for laser micromachining with concentration on laser microdrilling processes and dynamic behavior of the liquid and vaporized metals in laser micromachining were characterized.

Furthermore, detailed investigations were performed to determine the effects that laser beam properties, energy absorption at the surface of the workpiece, recoil forces, forced convection cooling by shielding gas mechanisms, and how plasma formation and absorption influence the quality of laser micromachining.

Studies in analytical consideration were focused on development of equations governing interaction of laser beam with materials, where analytical solutions of those equations are based on Fourier heat conduction using Laplace integral transform.

Analytical solutions of the governing heat transfer equation were found in four different cases: i) with spatial dependent laser beam heating, ii) with time dependent Gaussian laser pulse heating, iii) with time dependent Gaussian laser pulse heating with convective boundary conditions, and iv) considering transfer evaporation case. All those closed form solutions were based on Fourier heat conduction theory.

New technology in microelectronics requires pulses on the order of picoseconds, requiring one to look into microscale applications, where Fourier theory has some limitations, so a new approach to a solution has to be developed, called kinetic theory approach. As a result, development of a new analytical model using kinetic-phonon theory approach was conducted in this Dissertation. In this Dissertation electron-phonon analytical solution to the governing heat conduction equation was also examined and compared with both Fourier and kinetic theory approaches.

In the first part of computational investigations a finite element method (FEM) was used based on the TAS software to solve the thermal problems, such as temperature distributions of interaction of laser beam with materials under consideration.

The numerical computational investigations included development of own computer interface based on finite difference method (FDM) to solve the nonlinear governing heat transfer equations developed in this Dissertation. This model can be applied to various types of laser micromachining processes, such as laser annealing, laser

374

microdrilling, laser microwelding, etc. The program has capabilities and advantages of taking into calculation experimentally measured laser beam power intensity distributions, coefficient of energy absorption, and includes the variation of front of vaporization (i.e., recession velocity), phase changes occurring during micromachining, as well as convection and radiation heat losses during laser micromachining process. FDM has the capabilities of adjusting the nonlinear material properties of the workpiece, i.e., material properties as functions of temperature, various power distributions of the laser beam, and the energy absorption coefficient due to position and temperature change.

The experimental analysis performed in the course of this Dissertation included:

1) development of laser beam diagnostics technique, temporal and spatial laser beam characteristic supported with written software for interfacing operations and after diagnosis was done, to analyze the data.

2) experimental investigation concentrated also on measurement amounts of material being removed during laser beam interaction with the 304 stainless steel, and how much of that material has been vaporized and/or how much was being expelled in form of a liquid out of the molten material.

3) experimental investigation of the laser beam interaction with materials was also done by using fast camera to record microdrilling process, especially to measure speed of liquid expulsion and their effect on laser micromachining process.

4) microdrilling and analysis of holes in the 304 stainless steel and the single crystal silicon was processed by a pulsed Nd:YAG laser, which had the typical spot diameter of about 58 μm.

5) the experimental investigations of the laser microdrilling processes include the SEM characterization of surface topography of laser micromachined areas and parametric investigations of the effects of systematic parameters on microdrilling results.

6) parameters considered in experimental analysis of laser microdrilling included transverse mode and divergence of the laser beam, laser beam waist position, and energy per pulse characteristics.

7) quantitative analysis of the experimental data consisted of measurement of characteristic dimensions of the laser drilled holes (such as: entrance, mid diameter, and exit hole diameters, eccentricity, and taper).

The results from computational investigations were then compared with experimental data showing good correlations, although some discrepancies were identified. Reasons for these discrepancies were discussed and methods of how to improve the results were proposed.

Additional experiments will have to be conducted to fully understand why and what type of re-melting occurs on the wall of our experimental samples and study more thoroughly the recoil mechanisms and expulsions of the material (there was some evidence of small solid material of being ejected as well).

8. Future work

Based on observations regarding the theoretical and experimental results in this Dissertation, the following is advocated for the future work:

To control the microdrilling process it is essential to accurately know the laser radiation reflectivity and location of the workpiece with respect to the focal plane of the optics used. Tilting and moving of the workpiece, movements of the melt by capillary force or acoustic waves, and changes of the absorptivity during processing stimulates relaxation oscillations, laser beam mode instabilities or chaotic temporal behavior resulting in stochastic fluctuations of the spatial and temporal intensity distribution by optical feedback. Control of optical feedback is the main requirement for achieving reproducible processing with high repeatability and reliability. Consequently, diagnostics of the laser beam and in-process measurement of physical state of the irradiated workpiece (i.e., workpiece temperature and reflectivity) must be performed on-line during processing, otherwise correlation between the laser parameters and the processing results may not be possible.

Further, theoretical work should concentrate on modifying current problem statement by adding to the model effects of melt dynamics in radial direction (add velocity of the melt in x and y direction), improve modeling of interaction of the laser beam within the walls of a hole during the hole formation process, and more complete description of the propagation of the laser beam in semi- or transparent materials.

Development of a computer code written in more powerful PC based language (e.g., C++), in new graphical representation of data output, and with fully automatic link

377

to diagnostic equipment, which could feed information about the laser system or physical characteristic of the material back to the program.

Hypothesis of plasma defocusing, rather than plasma absorption, was assumed in this Dissertation to be the main cause of the so-called 'plasma shielding' observed in laser micromachining; to prove this statement additional work has to be perfumed in the future. In addition, an artificial theoretical focusing correction factor, *fcf*, which can cause enlargement of the laser beam and was introduced to FDM computer program's model developed in this Dissertation should be further studied to determine more realistic value.

For the future work, better resolution of diagnostic equipment, including CCD fast speed camera, is needed to accurately determine the problems related to expulsion of the materials during laser beam interaction, including identifying moments of initiating a plasma formation and its duration time.

References

Adams, M. J., 1970, ''Introduction to Gas Jet Laser Cutting,'' *Metal Const. British Weld. J.*, **2**, pp. 1–8.

Afanasiev, Yu. V., and O. N. Krokhin, 1967, *Sov. Phys, JETP* 25, 639.

Allmen, von M., 1976, "Laser drilling velocity in metals," *J. Appl. Phys.*, 47(12):5460-5463.

Andrews, J. G., and D. R. Atthey, 1975, "On the motion of an intensity heated evaporating boundary", *J. Inst. MATHS. Applics.,* 15:59-72.

Anthony, T. R., and H. E. Cline, 1977, "Surface rippling induced by surface-tension gradients during laser surface melting and alloying," *J. Appl. Phys.,* 48(9):3888-3894.

Anisimov, S. I., Y. A. Imas, G. S. Romanov, and Yu. V. Khodyko, 1971, *Action of high power radiation on metals,* National Tech. Inform. Service, Springfield, VA.

Anisimov, S. I., and V. A. Khokhlov, 1995, *Instabilities in laser-matter interaction*, CRC, Boca Raton, FL.

Arata, Y., N. Abe, and T. Oda. 1984, "Beam hole behavior during laser beam welding", *Proc. ICALEO'83*, Laser Institute of America, Orlando, 38:59-66.

Armon, E., Y. Zvirin, G. Laufer, and A. Solan, 1989a, "Metal drilling with a CO_2 laser beam. I. theory", *J. Appl. Phys.*, 65(12):4995-5002.

Armon, E., M. Hill, I. J. Spalding, and Y. Zvirin, 1989b, "Metal drilling with a CO_2 laser beam. II. Analysis of aluminum drilling experiments," *J. Appl. Phys.*, 65(12):5003-5006.

Armon, E., Y. Zvirin, and A. Solan, 1991, "Numerical simulation of metal drilling with CO_2 laser beam", *Numerical Heat Transfer*, Part B, 19:85-104.

Barin, I., and O. Knacke, 1973, *Thermochemical properties of inorganic substances*, Springer, Berlin.

Basu, S., and T. DebRoy, 1992, "Liquid metal expulsion during laser irradiation", *J. Appl. Phys.*, 72:3317-3322.

Batanov, V. A., F. V. Bunkin, F. V. Prokhorov, and A. M. Fedorov, 1973, *Sov. Phys. JETP* 36, 2.

Batteh, J. J., M. M. Chen, and J. Mazumder, 2000, "Stagnation flow analysis of the heat transfer and fluid flow phenomena in laser drilling," *J. Heat Transfer*, 122:801-807.

Beck, M., P Berger, and H Hiigel, 1995, "The effect of plasma formation on beam focusing in deep penetration welding with CO2 lasers", *J. Phys. D: Appl. Phys.*, 28:2430-2442.

Bejan, A., 1993, *Heat transfer*, Wiley, New York, NY.

Boulmer-Leborgne, C., J. Hermann, and B. Dubreuil, 1993, "Plasma formation resulting from the interaction of a laser beam with a solid metal target in an ambient gas," *Plasma Sources Sci. Technol.* 2:219-226.

Bronski, M., T., 2003, *Development of a process characterization of Nd:YAG crystals*, MS Thesis, Center for Holographic Studies and Laser micro-mechaTronics, Mechanical Engineering Department, Worcester Polytechnic Institute, Worcester, MA

Bruggemann, G. T., 1996, "Prediction of weld data using process control based on surface temperature measurement for high power energy flow processes," *Proc. SPIE*, 2888:168-177.

Bulgakova, N. M., and A. V. Bulgakov, 2001a, "Pulsed laser ablation of solids: transition from normal interaction," *Mat. Sci. and Eng.,* A292:162-168.

Bulgakova, N. M., and A. V. Bulgakov, 2001b, "Pulsed laser ablation of solids: transition from normal vaporization to phase explosion", *Appl. Phys. A,* 73:199–208.

Carslaw, H. S., and J. C. Jaegar, 1969, *Conduction of heat in solids*, Oxford Press, Great Britain.

Chan, C., and J. Mazumder, 1987, "One-dimensional steady state model for damage by vaporization and liquid expulsion due to laser –material interaction," *J. Appl. Phys.*, 62(12):4579-86.

Cheng, F., Y. C. Tsui, and T. W. Clyne, 1998, "Application of 3D heat flow model to treat laser drilling of carbon fiber composites," *Acta Metall. Et Mater.,* 46:4273-4285.

Christensen, B., and M. S. Tillack, 2003, "Survey of mechanisms for liquid droplet ejection from surface exposed to rapid pulsed heating," University of California, *UCSD-ENG*-100.

Chryssolouris, G., 1991, *Laser machining, theory and practice*, Springer-Verlag, New York, NY.

Chun, M. K., and K. Rose, 1971, *J. Appl. Phys*. 11, 2.

Columbia, 2005, "www.mrl.columbia.edu", Laser micromachining, last visited November 10, 2005.

Craciun, V., D. Craciun, M. C. Bunescu, C. Boulmer-Leborgne, and J. Hermann, 1998, "Subsurface boiling during pulsed laser ablation of Ge," *Phys. Rev. B*, 58, 11:6787-6790.

Craciun, V., N. Bassim, R. K. Singh, D. Craciun, J. Hermann, and C. Boulmer-Leborgne, 2002, "Laser induced explosive boiling during nanosecond laser ablation of silicon," *Appl. Surf. Sci.*, 186:288-292.

CRC Handbook of Chemistry and Physics, 1983, 64th edition, CRC Press, Boca Raton.

Cytrynowicz, D., M. Hamdan, P. Medis, H. T. Henderson, and F. M. Gerner, 2003, "Test Cell for a Novel Planar MEMS Loop heat pipe based on coherent porous silicon," edited by M. S. El-Genk, *Proc. Space Technology and Applications Internat. Forum*, Albuquerque, NM, pp. 230 - 232.

Dabby, F. W., and U. C. Paek, 1972, "High intensity laser induced vaporization and explosion of solid material," *IEEE J. of Quantum Electronics*, QE-8, 2:106-111.

Dausinger, F., H. Hugel, and V. Konov, 2003, "Micromachining with ultrashort laser pulses: from basic understanding to technical applications", Stuttgart University, Institut fur strahlwerkzeuge (IFSW), Pfaffenwaldring 43, D-70569 Stuttgart, Germany.

DebRoy, T., S. Basu, and K. Mundra, 1991, "Probing laser induced metal vaporization by gas dynamics and liquid pool transport phenomena", *J. Appl. Phys.* 70(3):1313-1319.

Dickson, L. D., 1970, "Beam waist location and measurement in dual laser Doppler," *Appl. Opt.*, 9:1854-1861.

Dobrovolskii, I. P., and A. A. Uglov, 1974, "Analysis of the hating of solids by laser radiation allowing for the temperature dependence of the absorptivity", *Kvant Elektorn, I*, 1423-1327.

Dowden, J. M., 2001, *The mathematics of thermal modeling*, Chapman & Hall/CRC, Boca Raton, FL.

Dowden, J., P. Kapadia, and R. Ducharme, 1994, Temperature in the plume in penetration welding with a laser, Colorado Springs Conf., Colorado, Transport Phenomena in Materials Processing and Manufacturing (ASME), pp 101.

Ducharme, R. M., H. Glowacki, P. Kapadia, and J. Dowden, 1994, "Sustained plasma burning using continuous and pulsed lasers operating at different infra-red and optical frequencies and various pulse repetition rates", ICALEO '93, Orlando: Laser Institute of America, pp. 97-105.

Duley, W. W., 1985, "Laser materials interactions of relevance to metal surface treatment," *Proc. NATO Advanced Study Institute on Laser Surface Treatment of Metals, Milano,* Italy.

Duley, W. W., 1999, *Laser welding,* Wiley, New York, NY.

Einstein, A., 1917, "Zur quantentheorie der Strahlung," *Physika Zeitshrift*, 18:121-128.

El-Batahgy, A. M., 1997, "Effect of laser welding parameters on fusion zone shape and solidification structure of austenitic stainless steels," *Materials Letters*, 32:155-163.

EMIS, Data review series No. 4, 1988, "Properties of Silicon," An INSPEC The Institute of Electrical Engineers.

Fieret, J., and B. A. Ward, 1986, ''Circular and non-circular nozzle exits for supersonic gas jet assist in CO_2 laser cutting,'' *Proc. 3rd Int. Conf. Lasers Manufact.*, pp. 45–54.

Finke, B. R., and G. Simon, 1989, "On the gas kinetics of laser-induced evaporation of metals," *J. Phys. D: Appl. Phys.*, 23:67-74.

Furlong, C., and R. J. Pryputniewicz, 2000, "Absolute shape measurements using high-resolution optoelectronic holography methods," invited paper, special issue on optical shape measurement techniques, *Opt. Eng.,* 39(1):216-223.

Furlong, C., R. J. Pryputniewicz, and J. S. Yokum, 2002, "Sensitivity, accuracy, and precision considerations of quantitative optical metrology based on high-spatial and high-digital resolution cameras," *Proc. SPIE*, 4777:74-82.

Ganesh, R. K., W. Bowley, R. R. Bellantone, and Y. Hahn, 1996, "A model for laser hole drilling in metals," *J. Comp. Phys.,* 125:161-176.

Golosnoy, I. O., K. T. Voisey, and T. W. Clyne, 2003a, "Finite difference simulation of melt ejection during laser drilling," *Int. J. Heat Mass. Trans.*

Golosnoy, I. O., S. A. Tsipas, and T. W. Clyne, 2003b, "An analytical model for simulation of heat flow in plasma sprayed thermal barrier coatings," *J. Ther. Spray Techn.,* 1-24.

Gordon, R. and J. Cobonpue, 1961, "Heat transfer between a flat plate and jets of air impinging on it," *Heat Transfer*, Pt. II, 454-460, ASME, New York, NY.

Grad, L., and J. Mozina, 1998, "Laser pulse shape influence on optically induced processes," *Appl. Surf. Sci.*, 127:999-1004.

Han, W., 1999, *Theoretical and experimental investigation of laser drilling of small holes in metals*, MS Thesis, Worcester Polytechnic Institute, Worcester, MA.

Han, W., and R. J. Pryputniewicz, 2001, "Study of a laser microwelding process for microelectronics and packaging," *Proc. 2001 IMAPS International Symposium on Microelectronics*, pp. 713-716.

Han, W., and R. J. Pryputniewicz, 2003a, "Study of thermal stresses in laser microwelding processes for microelectronics industry," *Proc. 2003 SEM Spring Conference*, pp. 546-552.

Han, W., and R. J. Pryputniewicz, 2003b, "Mechanical characterizations of laser microwelds for MEMS packaging," *Proc. 2003 MRS Fall Meeting*, in process.

Han, W., J. S. Yokum, and R. J. Pryputniewicz, 2004, "Parametric study of laser microdrilling process for MEMS fabrication," *Proc. 2004 SEM International Congress & Exposition*, in progress.

Harrington, R. E., 1967, "Application of the theory of heat conduction to the absorption of blackbody radiation," *J. Appl. Phys.*, 38:3266-3271.

He, X., T. DebRoy, and P. W. Fuerschbach, 2003, "Alloying element vaporization during laser spot welding of stainless steel", *J. Phys. D: Appl. Phys.* 36:3079-3088.

Herziger, G., 1986, "Physics of laser materials processing," *Proc. SPIE*, 650:188-194.

Herziger, G., E. W. Kreutz, and K. Wissenbach, 1986, "Fundamentals of laser processing of materials," *Proc. SPIE*, 658:2-10.

Ho, J. R., C. P. Grigoropoulos, and J. A. C. Humphrey, 1995, "Computational model for heat transfer and gas dynamics in the pulsed laser evaporation models,", *J. Phys.,* 78,7:4696-4709.

Hunter, B. V., K. H. Leong, C. B. Miller, J. F. Golden, R. D. Glesias, and P. J. Laverty, 1996, "Understanding high power fiber optic laser beam delivery," *J. Laser Appl.* 8, 6.

Ivarson, A., J. Powell, and C. Magnusson, 1991, ''The Role of Oxidation in Laser Cutting Stainless and Mild Steel,'' *J. Laser Appl.*, 3, pp. 41–45

Jin, X., and L. Li, 2003, "An experimental study on the keyhole shapes in laser deep penetration welding," *Optics and Lasers in Engineering*, 40:239-246.

Kabasawa, M., M. Ono, K. Nakada, and S. Kosuuge, 1992, Laser treatment of materials, edited by B. L. Mordike, p. 667.

Kahn, A. H., 1954, "Theory of the infrared absorption of carriers in Germanium and Sillicon," *Phys. Rev.,* 97, 1647.

Kandlikar, S. G., Shoji M., and V. K. Dhir, 1999, *Handbook of phase change: boiling and condensation*, Taylor and Francis, Philadelphia, PA.

Kaplan, A., 1994, "A model of deep penetration laser welding based on calculation of the keyhole profile ", *J. Phys. D.*, 27:1805.

Kaplan, A., 1997, "Surface processing with non-Gaussian beams," *Appl. Phys. Lett.*, 70, (2), 13:264-266.

Kar, A., and J. J. Mazumder, 1990, "Two-dimensional model for laser induced materials damage due to melting and vaporization during laser irradiation," *J. Appl. Phys.*, 68, 8:3884-3891.

Kar, A., and J. Mazumder, 1995, Mathematical modeling of keyhole laser welding", *J. Appl. Phys.,* 78:6353–6360.

Kar, A., T. Rockstroh, and J. Mazumdar, 1991, "Two-dimensional modal for laser induced materials damage: Effects of assist gas and multiple reflections inside the cavity," *J. Appl. Phys.*, 71, 6:2560-2569.

Karnakis, D. M., J. Fieret, P. T., Rumsby, and M. C., Gower, 2003, Microholedrilling using reshaped pulsed Gaussian laser beams, Exitech Ltd., Hanborough Business Park, Long Hanborough, UK.

Kittel, C., 1987, *Quantum theory of solids*, Wiley, New York, NY.

Knight, C. J, 1979, "Theoretical modeling of rapid surface vaporization with back pressure," *AIAA J.*, 17(5):519-523.

Korner, C., R. Mayerhofer, M. Hartmann, and H. Bergmann, 1996, "Physical and material aspects in using visible laser pulses of nanosecond duration for ablation," *Appl. Phys. A,* 63:123-31.

Lasag, 1997, *Operator's manual for KLS 126 laser source*, LASAG Corporation, Switzerland.

Liu, X., D. Du, and G. Mourou, 1997, "Laser ablation and micromachining with ultrashort laser pulses," IEEE *J. Quantum Electronic*s, 33, 10:1706-1716.

Low, D. K. Y., L. Li, and P. J. Byrd, 2002, "Hydrodynamic physical modeling of laser drilling," *J. Manuf. Scien. and Engin.*, 124, 4:852-862.

Luft, A., U. Franz, A. Emsermann, and J. Kaspar, 1996, "A study of thermal and mechanical effects on materials induced by pulsed laser drilling," *Appl. Phys. A*, 63:93-101.

Maiman, T. H., 1960, "Stimulated optical radiation in Ruby," *Nature,* 187:493-494.

Marley, C., 2002, "Laser welding photonic devices," *Industrial Laser Solutions*, pp. 9-14.

Mazumder, J., and W. M. Steen, 1980, "Heat transfer model for cw laser material processing," *J. Appl. Phys.*, 51:941-947.

Meijer, 2002, *Micromachining of engineering materials*, McGeough, Marcel Dekker, Inc., New York, NY.

Miotello, A., and R. Kelly, 1995, "Critical assessment of thermal models for laser sputtering at high fluencies," *Appl. Phys. Lett.*, 67 (24):3535-3537.

Mitchener, M., and C. H., Kruger Jr., 1973, *Partially ionized gases,* Wiley, New York, NY.

Miyamoto, I., 1986, "Beam absorption mechanism in laser welding," *Proc. SPIE*, 668:11-18.

Miyamoto, I., and Y. Arata, 1984, "The role of assist gas in CO_2 laser welding", *ICALEO'94*, ed.: T. D. McCay et al., Orlando, FL., Laser Institute of America, pp. 68.

Modest, M. F., 1996, "Three-dimensional transient model for laser machining of ablation decomposing materials," *Internat. J. Mass Transfer*, 39(2):221-234.

Moon, D. W., and Metzbower, E. A., 1983, *Weld. J.* 62 53.

Moon, D. W., S. G., Lambrakos, R. J., Wong, and E. A., Metzbower, 2003, "Temperature, macrostructure and hardness in high strength low alloy steel welds", *Science and Technology of Welding & Joining,* 8, 5:334-330.

Murthy, J., R. E. Mueller, V. V. Semak, and M. H. McCay, 1994, "Investigation of drilling dynamics in Ti-6Al-4V using high speed photography," Laser Materials Processing Conference ICALEO'94, San Diego, *Laser Institute of America*, 79:61-69.

News, 2004, http://news.thomasnet.com/Stainless steel pressure sensors measure hostile media, accessed June 15, 2004.

Niedrig, R., and O. Bostanjoglo, 1996, "Imaging and modeling of pulse laser induced evaporation of metal films," *J. Appl. Phys.*, 81 (1):480-485.

Nowak, T., 1990, *Theoretical and experimental investigation of laser drilling in a partially transparent medium*, MS Thesis, Center for Holographic Studies and Lasermicro-mechaTronics, Mechanical Engineering Department, Worcester Polytechnic Institute, Worcester, MA.

Nowakowski, K. A., 1990, *Computer simulation and experimental investigation of laser beam interaction with metals*, MS Thesis, Worcester Polytechnic Institute, Worcester, MA.

Nowakowski, K. A., and R. J. Pryputniewicz, 2004, "Fundamentals of laser microdrilling for MEMS applications", *Proc*. 15th *Internat. Invitational UACEM Symposium*, Springfield, MA, pp. 295-322.

Nowakowski, K. A., J. S. Yokum, W. Han, and R. J. Pryputniewicz, 2004, "State-of-the-art in laser micromachining for microelectronics and packaging," *IMAPS New England, 31st Annual Symposium & Exhibition*, Boxboro, Massachusetts

Nowakowski, K. A., W. Han, and R. J. Pryputniewicz, 2005, "Laser micromachining for microelectronics and packaging using fiber optic cable," *Proc.of the 32nd IMAPS-NE Annual Symposium & Exhibition*, Boxboro, MA.

Olson, R. W., and W. C. Swope, 1992, "Laser drilling with focused Gaussian beams," *J. Appl. Phys.*, 72:3686-3696.

Paul, A., and T. Debroy, 1988, "Modeling of weld metal convection from fundamentals of transport phenomena," *Metall. Trans.*, 19B:851-863.

Peak, U., and F. P. Gagliano, 1972, "Thermal analysis of laser drilling processes," *IEEE J. Quantum Electronics*, QE-8, 2:112-119.

Postacioglu, N., P. Kapadia, and J. M. Dowden, 1989, "Capillary waves on the weld pool in penetration welding with a laser," *J. Phys. D: Appl. Phys.*, 22:1050-1061.

Pryputniewicz, R. J., 1993, *Engineering experimentation*, Center for Holographic Studies and Laser micro-mechaTronics, Mechanical Engineering Department, Worcester Polytechnic Institute, Worcester, MA.

Pryputniewicz, R. J., 1998, *Laser engineering, science, and applications*, Mechanical Engineering Department, Worcester Polytechnic Institute, Worcester, MA.

Pryputniewicz, R. J., 2004, *Thermodynamics of microsystems*, Center for Holographic Studies and Laser micro-mechaTronics, Mechanical Engineering Department, Worcester Polytechnic Institute, Worcester, MA.

Pryputniewicz, R. J., C. Furlong, G. C. Brown, and E. J. Pryputniewicz, 2001, "Optical methodology for static and dynamic measurements of nanodisplacements," *Proc. of International Congress on Experimental and Applied Mechanics for Emerging Technologies*, Portland, OR, pp. 826-831.

Ready, J. F., 1971, Effects of High Power Laser Radiation, Academic, New York.

Reid, R. C., and T. K. Sherwood, 1966, *The properties of gases and liquids,* McGraw-Hill, New York, NY.

Rockstroh, T. J., and J. Mazumder, 1987, "Spectroscopic studies of plasma during CW laser materials interaction", *J. Appl. Phys.* 61, 917.

Rodden, W. S. O., S. S. Kudesia, D. P. Hand, and J. D. C. Jones, 2000, "Suitability of laser drilling models containing melt ejection mechanisms", *ICALEO,* Dearborn, MI, Section B, pp. 68-77.

Root, R. G., 1989, "Laser induced plasmas and applications", Radziemski and Cremers, New York, Marcel Dekker.

Rosato, D. A., 2004, *Thermal analysis system: user's manual,* Harvard Thermal, Harvard, MA.

Sami, M., and B. S. Yilbas, 1997, "Liquid ejection and possible nucleate boiling mechanism in relation to the laser drilling process," *J. Phys. D: Appl. Phys*, 30:1996-2005.

Schultz, W, D. Becker, J. Franke, R. Kemmerling, and G. Heniger, 1993, Heat conduction *losses* in laser cutting of materials *J. Phys. D: Appl. Phys.* 26 1357.

Seeger, K., 1997, *Semiconductor Physics*, Springer, Berlin, Germany.

Semak, V., and A. Matsunawa, 1997, "The role of recoil pressure in energy balance during laser materials processing," *J. Phys. D: Appl. Phys.*, 30:2541-2552.

Semak, V., B. Damkroger, and S. Kemka, 1999, "Temporal evaluation of the temperature filed in the beam interaction zone during laser material processing," *J. Phys. D: Appl. Phys.*, 32:1819-1825.

Semak, V., G. A. Knorovsky, and D. O. MacCallum, 2003, "On the possibility of microwelding with laser beams," *J. Phys. D: Appl. Phys.*, 36:2170-2174.

Shen, Z-H., and S.Y Zhang, 2001, "Laser heating of thin plate with time dependent absorbtance", *Microwave and optical technology letters,* 28, 5, pp. 364-367.

Solana, P., P. Kapadia, J. M. Dowden, and P. J. Marsden, 1999, "An analytical model for the laser drilling of metals with absorption within the vapor," *J. Phys. D: Appl Phys,* 32:942-952.

Solana, P., J. Kapadia, W. S. O. Dowden, S. S. Rodden, D. P. Kudesia, J. D. Hand, and J. D. C. Jones, 2001, "Time dependent ablation and liquid ejection process during the laser drilling of metals," *Opt. Commun.,* 191: 97-112.
Solan 1997

Solana, P., and Ocana, O., 1997, "A mathematical model for penetration laser welding as a free-boundary problem", *J. Phys. D: Appl. Phys.*, 30**:**1300–1313.

Sparks, M., 1975, "Theory of laser heating of solids: metals," *J. Appl. Phys.*, 47, 3: 837-849.

Steen, W. M., 2003, "Laser material processing ─ an overview," *J. Opt. A: Pure Appl. Opt.*, 5:3-7.

Tabor, D., 1991, *Gases, liquids and solids and other states of matter,* 3rd Ed, p. 272. Cambridge University Press, Cambridge.

Tannenbaum, B. S*.,* 1973, *Plasma physics,* McGraw-Hill, New York, NY.

Thompson, A., 2003, "Investigation into applications of light in technology", *users.netconnect.com.au,* accessed: June 20, 2004.

Tokarev, V. N., and A. F. H. Kaplan, 1999, "An analytical modeling of time dependent pulsed laser melting," *J. Appl. Phys.*, 86(5):2837-2846.

Tokarev, V. N., J. G. Lunney, W. Marinea, and M. Sentis, 1995, "Analytical thermal model of ultraviolet laser ablation with single-photon absorption in the plume," *J. Appl. Phys*. 78(2):1241-1246.

Towns, C. H., 2002, *How the laser happened: adventure of scientists*, Oxford University Press.

Treusch, H. G., and G. Herziger, 1986, "Metal precision drilling with lasers," *Proc. SPIE*, 650:220-225.

Ursu, I., I. N. Mihailescu, A. M. Prokhorov, V. N. Tokarev, and V. I. Konov, 1986, "High intensity laser irradiation of metallic surfaces covered by periodic structures," *J. Appl. Phys.*, 61,(7):2445-2457.

Xie, J and A. Kar, 1997, "Melting and vaporization for large-area film removal with a chemical oxygen–iodine laser", *J. Appl. Phys.,* 82:4744–4751.

Xu, X., and D. A. Willis, 2002, "Non-equilibrium phase change in metal induced by nanosecond pulsed laser irradiation," *J. Heat Transfer*, 124:293-298.

Yilbas, B. S., 1995, Study of liquid and vapor ejection processes during laser drilling of metals, *J. of Laser Applications*, 7:147-152.

Yilbas, B. S., 2001, "Electron kinetic theory approach-one and three dimensional heating with pulsed laser," *Internat. J. of Heat and Mass Transfer*, 44:1925-1936.

Yilbas, B. S., and M. Sami, 1997, "Liquid ejection and possible nucleate boiling mechanism in relation to the Laser drilling process," *J. Phy D: Appl. Phys*, 30:1996-2005.

Yilbas, B. S., and S. Z. Shuja, 1999, "Laser short-pulse heating of surfaces," *J. Phys. D: Appl. Phys.*, 32:1947-1954.

Yilbas, B. S., and A. F. M. Arif, 2001, "Material response to thermal loading due to short pulse laser heating," *Internat. J. Heat and Mass Transfer*, 44:3787-3798.

Yilbas, B. S., Z. Yilbas, and N. Akcakoyun, 1996, "Investigation into absorption of the incident laser beam during Nd:YAG laser processing of metals," *Optics & Laser Technology*, 28(7):503-511.

Yilbas, B. S., Z. Yilbas, and M. Sami, 1996, "Thermal processes taking place in the bone during CO_2 laser irradiation," *Optics & Laser Technology*, 28(7):513-519.

Yilbas, B. S., S. A. Gbadebo, and M. Sami, 2000, "Laser heating: an electro-kinetic theory approach and induced thermal stresses," *Optics and Laser Engineering*, 33:65-79.

Yoo, J. H., S. H. Jeong, X. L. Mao, R. Greif, R. and E. Russo, 2000, "Evidence for phase-explosion and generation of large particles during high power nanosecond laser ablation of silicon," *Appl. Phys. Letters*, 76(6):783-785.

Veiko, V. P., 1980, "Two-phase mechanism of laser induced removal of thin absorbing films: I. Theory," *J. Phys. D: Appl. Phys.*, 13:1565-1570.

Veiko, V. P., S. M., Metev, K. V. Stamenov, H. A. Kalev, B. M. Jurkevitch, and I. M. Karpman, 1980, "Two-phase mechanism of laser induced removal of thin absorbing films: II. Experimentt," *J. Phys. D: Appl. Phys.*, 13:1571-1575.

Verwaerde, A., R. Fabbro, and G. Deshors, 1995, "Experimental study of continuous CO_2 laser welding at subatmospheric pressures", *J. Appl. Phys.*, 78 (5):2981-2984.

Voisey, K. T., C. F. Cheng, and T. W. Clyne, 2000, "Quantification of melt ejection phenomena during laser drilling", *Mat. Res. Soc. Symp.,* 617:J5.6.1-J5.6.7.

Voisey, K. T., and T. W. Clyne, 2004, "Laser drilling of cooling holes through plasma sprayed thermal barrier coatings," *Surface and Coating Technology*, 176:296-306.

Wagner, R. E., 1974, "Laser drilling mechanics," *J. Appl. Phys.,* 45(10):4631-4637.

Wang, H., and X. Chen, 2003, "Three-dimensional modeling of the laser-induced plasma plume characteristics in laser welding," *J. Phys. D: Appl. Phys.*, 36:628-639.

Wang, H., 2004, "Thermal and themomechanical phenomena in picoseconds laser copper interaction," *J. Heat Transfer*, 126:355-364.

Willis, D. A., and X. Xu, 2000, "Transport phenomena and droplet formation during pulsed laser interaction with thin films," *J. Heat Transfer*, 122:763-770.

Zacharia, T., S. A. David, J. M. Vitek; and T. DebRoy, 1989, "Weld Pool Development during GTA and Laser Beam Welding of Type 304 Stainless Steel Part 2- Experimental Correlation," *Welding J.* 68, 499.

Zhang, W., and A. Faghri, 1999, "Vaporization, melting, and heat conduction in the laser drilling process," *Int. J. of heat and mass transfer,,* 42:1775–1790.

Zhang, W., Y. L., Yao, and K. Chen, 2001, "Modeling and analysis of UV laser micro-machining of copper," ICALEO, *Int. J. Adv. Manuf. Technol.,* 18:323–331.

Zhao, H., and T. DebRoy, 2003, "Macroporosity free aluminum alloy weldments through numerical simulation of keyhole mode laser welding," *J. Appl. Phys.*, 93(12):10089-10096.